Fischer-Tropsch Synthesis via Co-MOF-74-derived Catalysts and Catalytic Membranes

Michael Robert Rawlins

Doctor of Philosophy

Aston University

April 2022

Aston University

Fischer-Tropsch Synthesis via Co-MOF-74-derived Catalysts and Catalytic Membranes

Michael Robert Rawlins

Doctor of Philosophy

2022

Abstract

Natural gas and biomass offer alternative carbon feedstocks for the production of liquid fuels. The low-temperature Fischer-Tropsch (FTS) synthesis process is a well-known method of converting these resources into liquid fuels, but currently the process suffers from high operating costs. Developing more active and selective reactors through novel catalyst design and reactor configurations will contribute to lowering operating costs.

Pyrolysis of metal-organic frameworks is a recent technique used to prepare highly loaded and dispersed catalysts, for more active and selective performance. Catalysts derived from Co-MOF-74 were prepared and tested in a fixed-bed reactor, whilst chemical vapour deposition of acetylene was applied to improve performance. Loading the catalyst exclusively into the reactor resulted in very significant heat effects due to the highly exothermic nature of FTS, which was extremely detrimental to performance. Diluting the catalyst with inert particles showed significant improvement, whilst chemical vapour deposition of acetylene suggested further improvement. Comparing these catalysts to a conventionally prepared cobalt-based gamma-alumina supported catalyst, higher C_{7+} yields were obtained when the activity and local heat effect were considered.

Two novel catalytic membrane reactors were prepared. A phase-inversion and sintering technique was used to prepare two uniquely micro-structured ceramic flat-disc membranes, with micro-channel diameters of around 50 to 200 µm, for the purpose of reducing transport limitations which may negatively impact selectivity and activity. The membranes were impregnated with cobalt and tested alongside a pellet-based and ground gamma-alumina supported cobalt catalysts. The membranes did not exhibit superior performance compared to the ground and pellet-based catalysts, likely due to intense heat effects in the micro-channel and poor dispersion of the Co active phase. The Co-MOF-74-derived catalyst was loaded into the membrane, however extremely high methane selectivity was observed.

Acknowledgements

Firstly, I would like to sincerely thank my supervisor, Dr Zhentao Wu, whose patient supervision, support and knowledge has been vital in ensuring the completion of the project. I would like to extend my gratitude to my co-supervisor, Dr Qingchun Yuan, whose knowledge and experience has been very valuable. I would like to acknowledge the funding from the IEC\NSFC\201014, Horizon-2020-INNOMEM_862330, KL18-10 projects

Also, I would like to thank Dr Jinesh Manayil for his help and support in the lab, including training for the porosimeter, XRD, CHNS, TGA and GC-FID, and also for the operation of the SEM microscope. A word of thanks to Dr Daniel Nowakowski, whose patient supervision of the labs was needed to complete the project. I would also like to acknowledge Jiaojiao Zheng for her assistance in the lab. A word of thanks to my fellow colleagues in EBRI, who's encouragement was important during some difficult periods.

Outside of the lab, I would like to thank my friends, Tom and Becca, for hosting me after many late nights of working. And finally, I would like to thank my partner, Ann-Marie, whose support and encouragement was vital and much-appreciated.

Contents

List of Figures

List of Tables

List of Abbreviations

BET - Brunauer–Emmett–Teller

FCC – Face-centred cubic

FID – Flame ionisation detector

FT-IR – Fourier transform – Infrared spectroscopy

FTS - Fischer-Tropsch Synthesis

GC – Gas chromatography

HCP – Hexagonal close-packed

MOF – Metal-organic framework

TCD – Thermal conductivity detector

TGA – Thermogravimetric analysis

WGS – Water-gas shift

XRD – X-ray diffraction

Chapter 1

Introduction

1.1 Background

Presently, crude oil accounts for a vast amount of the world's fuel and chemical production. Worldwide, petroleum and other liquid fuels account for approximately 96 % of transport energy. This is predicted to remain high, approximately 88 % by 2040 [1, 2]. Liquid fuels remain the largest source of primary energy and are predicted to do so into the mid-21st century, resulting in an increasing oil consumption as a result of population and economic growth, particularly in non-OECD countries [2]. At the same time, oil prices have shown severe growth since 1970, with the price increasing from approximately US$ 15 per barrel to increase from to US$ 73 per barrel at the end of 2019, when adjusted for inflation [3]. This growth in oil price is expected to continue well into the 21st century [2]. Therefore, the development of alternative, sustainable fuel and chemical sources is important to meet the increasing global demand and offset increasing oil prices.

Alternative fuel sources include the conversion of syngas derived from coal, natural gas or biomass to liquid fuels. Such processes are known as gas-to-liquids (GTL), coal-to-liquids (CTL) and biomass-to-liquids (BTL) processes. The Fischer-Tropsch synthesis (FTS) process is the most eminent of such processes, named after F. Fischer and H. Tropsch, who discovered in 1923 that syngas could be converted catalytically into a wide range of hydrocarbons and alcohols. The process was used applied extensively in Germany in the 1930s to make CTL fuels. Crude oil abundance after the World War II meant that FTS processes became uncompetitive, however the process has been use in on a commercial scale in coal-rich South Africa since the 1950s to reduce the dependence on imported oil [4].

In order to meet the challenge of future energy security through alternative fuel sources, the utilisation of large and growing natural gas reserves presents a huge potential fuel source. Proven world reserves of natural gas jumped from 138 to 190.3 trillion cubic metres between 2000 and 2019 [3]. However, large amounts of natural gas are located in remote locations considered too small for liquified natural gas or pipeline projects. Much GTL interest is motivated by the desire to monetise stranded gas reserves [5]. Most of the world's FTS plants use natural gas as the carbon feedstock, with the largest of such plants operated by Shell, in Ras Laffan, Qatar, producing 140,000 barrels per day [6]. Coal is also still used as carbon source. The plant operated by Sasol in Secunda, South Africa, is based on both

coal and natural gas and has the largest production capacity of any FTS plant of 160,000 barrels per day. Similarly, BTL from FTS fuels may provide an alternative energy source. There is a growing desire to across the world to substitute fossil fuels with renewable energy source and biomass provides a renewable carbon source to be used as a feedstock for the FTS process [7]. However, opportunity for scale-up is affected by the availability of biogenic feedstocks and there are currently no commercial FTS plants producing BTL products [6, 8]. Furthermore, synthetic diesel produced via FTS is cleaner, due to the low concentrations of nitrogen, sulphur and aromatics [7].

Currently, FTS still faces challenges. GTL technology is too expensive to compete with crude oil products and natural gas as fuels in the transportation sector. Therefore, GTL must be less costly and more efficient in order to develop as an industry [9]. Likewise, BTL processes also suffer from high capital and operating costs [8]. In order to meet these challenges, process intensification of FTS is necessary. Recent studies have proposed innovative reactor configurations, such as monolithic loop, membrane reactors, and micro-channel reactors in order to improve performance in low-temperature Fischer-Tropsch (LTFT) [10]. Also, the performance of existing reactor configurations can be improved by developing novel, more efficient catalysts.

1.2 Project Aims

Low-temperature Fischer-Tropsch synthesis (LTFT) is carried out on either fixed bed reactors, or slurry reactors. Slurry reactors offer optimum performance, but requires a costly catalyst separation step whilst scale-up of these reactors is a major challenge, requiring costly and time-consuming pilot plant studies [11]. Therefore, a more efficient fixed-bed reactor to improve performance is desirable.

Much work has been undertaken for LTFT researching fixed-bed reactors using cobalt, a commonly used catalyst in LTFT supported on metal oxides. A recent novel method of preparing highly loaded, and highly dispersed Co catalysts is through the decomposition of metal-organic frameworks (MOFs). Only a handful of studies currently exist investigating the performance of Co catalysts for FTS based on MOFs. In this project, MOF-based catalysts were prepared from Co-MOF-74, and the performance of the catalyst was investigated by comparing directly to conventionally prepared metal-oxide supported Co catalysts, using the same reactor system. Also, improvements to the MOF-based catalyst were investigated using chemical vapour deposition. Aims were to investigate whether MOF-derived catalyst can provide enhanced performance over conventionally prepared catalysts in afixed-bed reactor for FTS.

Another method of improving the performance of LTFT in a fixed-bed reactor is the application of alternative reactor designs. One such design is the use of forced through contactor membranes, but currently only two studies exist. Ceramic membrane technology is largely studied in the context of separation processes. However, in this project, this technology will be applied to FTS to investigate whether a performance improvement can be feasible.

1.3 Thesis Structure

Chapter 2 – Literature Review

This chapter gives a brief overview of the core aspects of the FTS process, such as the reactions, mechanisms and catalysts. Reactors for LTFT are then discussed, and the remainder of the review discusses the limitations of the fixed-bed reactors for LTFT using a cobalt catalyst and how they can be overcome.

Chapter 3 – General Methods and Equipment

This chapter outlines the methods consistently used throughout the thesis, including the FT reactor system, preparation of the catalysts, and how characterisation was performed.

Chapter 4 – Investigation of Co-MOF-74-derived catalysts in FTS

This chapter details the characterisation of the Co-MOF-74, the characterisation of the catalysts derived from the Co-MOF-74 and investigates the performance of directly loaded Co-MOF-74-based catalysts in FTS.

Chapter 5 – Improvement and Comparisons of Co-MOF-74-derived Catalysts

Chapter 5 shows how the performance of Co-MOF-74-derived catalysts can be improved. The effect of bed dilution is investigated, as well as chemical vapour deposition of acetylene applied to the Co-MOF-

74-derived catalyst. These catalysts were then compared to a conventionally prepared, γ-alumina supported, ground cobalt catalyst.

Chapter 6 – Investigation of Fixed-Bed Reactor Designs for FTS

Chapter 6 outlines the fabrication and characterisation of ceramic flat disc membranes and their functionalisation using cobalt to obtain a catalytic membrane. The catalytic membranes were tested in FTS, along with a conventionally prepared, pellet-based γ-alumina supported cobalt catalysts, in order to see how the different reactor configurations and catalyst geometries perform in FTS. A Co-MOF-74-derived catalyst was also deposited into the membranes and tested in FTS.

Conclusion, Future Work and Recommendations

The thesis will be rounded off with the conclusions in Chapter 7 and the future work and recommendations in Chapter 8.

Chapter 2

Literature Review

2.1 Introduction to Fischer-Tropsch Synthesis Process

2.1.1 Fischer-Tropsch Process

The overall process requires an organic feedstock such as coal, biomass or natural gas, to be converted into syngas, mainly comprised of CO (35% - 45%), H_2 (27% - 30%), CO_2 (10% - 15%), H_2O (15% - 25%), and H_2S and COS (0.2% - 1%), although the composition will vary depending on the source [12]. The syngas will be used as the feedstock for FTS, where it is converted into a mixture of hydrocarbons through a series of reactions. Refining and upgrading is then required to process the hydrocarbon mixture into separate products. For a coal and biomass feedstock, gasification is usually required to produce the syngas. Syngas can also be produced from natural gas through steam reforming [13]. The economics of this process differ depending on the feedstock used [14]. An overview of the overall processes and products are shown in Figure 2.1

The composition of the syngas varies depending on the source, with syngas derived from coal and biomass generally having a lower H_2/CO ratio, between 0.45-1.03 for biomass derived syngas and approximately 1 for that produced via high temperature coal gasification [15, 16]. The desired ratio would be above 2, in order to bring the stoichiometry in line with the FTS reactions [17]. Coal was previously the most common feedstock for producing syngas, but despite the low prices of coal, the investment in a coal-based syngas plant is about three-times higher than that for a natural-gas-based plant [18].

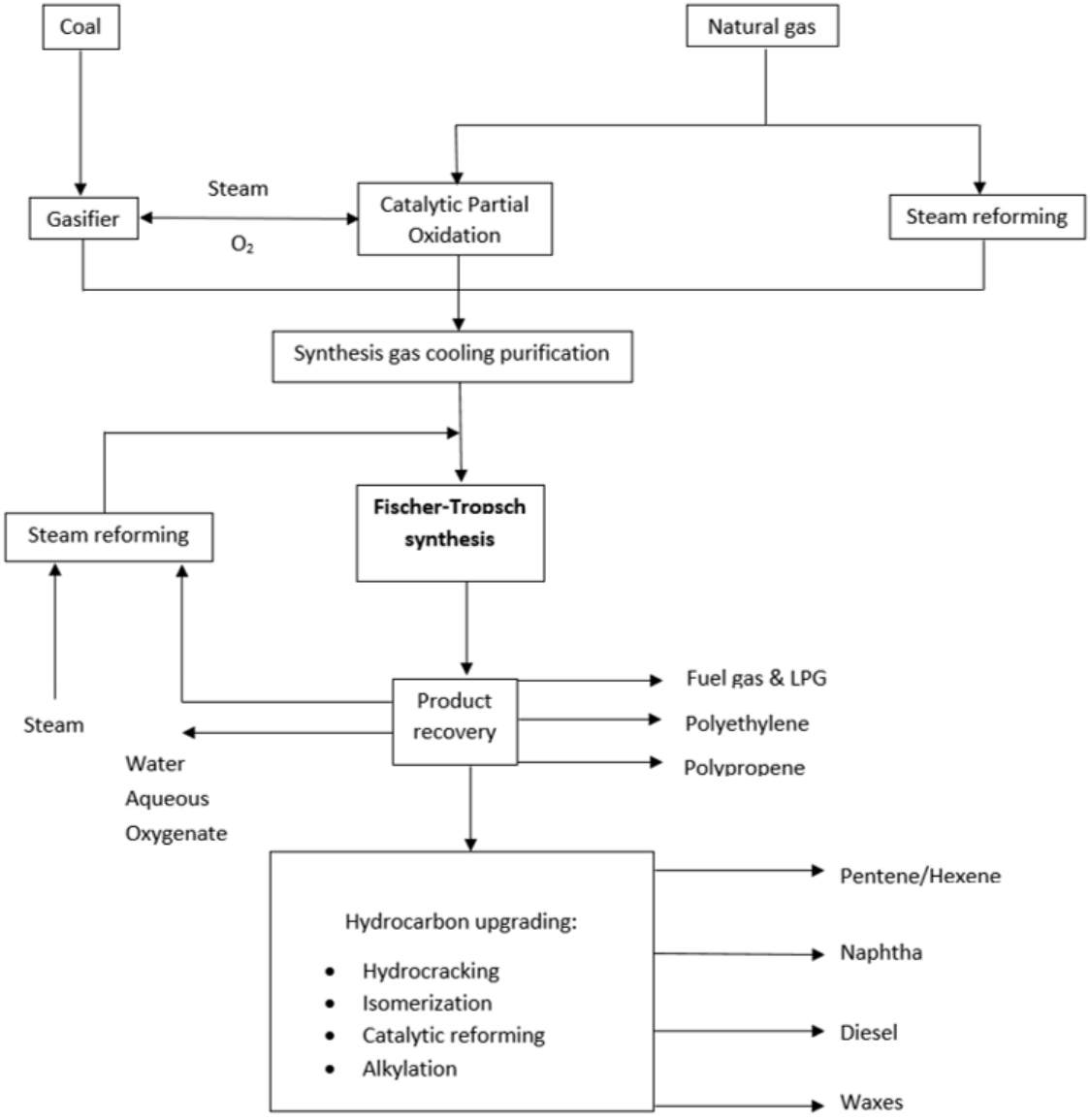

Figure 2.1 – Overall Process of GTL and CTL fuels using FT synthesis adapted from [19]

2.1.2 Fischer-Tropsch Synthesis Reactions and Mechanisms

The FTS reactions are considered highly exothermic surface polymerisation reactions, which produce a mixture of hydrocarbons including a range of alkanes, alkenes and alcohols and water, shown in Equation 2.1-2.3 [19, 20]. The formation of 1 mole of $-CH_2-$ is accompanied by the heat release of 165 kJ, shown in Equation 2.4 [6].

Alkanes: $(2n + 1)\ H_2 + n CO \rightarrow C_nH_{2n+2} + nH_2O$ (Equation 2.1)

Alkenes: $2nH_2 + nCO \rightarrow C_nH_{2n} + nH_2O$ (Equation 2.2)

Alcohols: $2nH_2 + nCO \rightarrow C_nH_{2n+2}O + (n-1)H_2O$ (Equation 2.3)

$CO + 2H_2 \rightarrow -CH_2- + H_2O$ $-165\ kJ\ mol^{-1}$ (Equation 2.4)

Other side-reactions include the water gas shift reaction (Equation 2.5), which can alter the H_2/CO ratio to fit the stoichiometry of the reactions. The Boudouard reaction (Equation 2.6) is an unwanted side reaction, which can lead to the build-up of carbon deposits. The water – gas shift (WGS) reaction also releases 42 kJ mol^{-1} [6].

Water-gas shift reactions: $CO + H_2O \leftrightarrow CO_2 + H_2$ $-42\ kJ\ mol^{-1}$ (Equation 2.5)

Boudouard reaction: $2CO \rightarrow C + CO_2$ $+172\ kJ\ mol^{-1}$ (Equation 2.6)

The products formed in FTS are produced through a polymerisation process, which consists of the following main steps [21]:

1. Reactant adsorption
2. Chain initiation
3. Chain growth
4. Chain termination
5. Product desorption
6. Re-adsorption and further reactions

Multiple reaction mechanisms for FTS reactions have been proposed, many of them are based on a chain growth process, consisting of initiation, propagation and termination steps. They can generally be separated into two distinguished paths. One path involves the cleavage of the C-O bond of CO before incorporation into the growing hydrocarbon chain [22]. The carbide mechanism was originally proposed by Fischer and Tropsch [23]. It entails the dissociative adsorption of CO onto the metal atom which forms a carbide species. Hydrogen is then inserted into the carbide species, forming an active CH_2 intermediate. Hydrogen could react either in a molecular state or by dissociative adsorption. The propagation step involves further growth of the hydrocarbon chain, which eventually terminates via hydrogenation or beta scission, forming a paraffin or olefin, respectively [23-25]. An example of the "surface carbene" mechanism, a typical example of a type of a surface carbide mechanism, is shown in Figure 2.2.

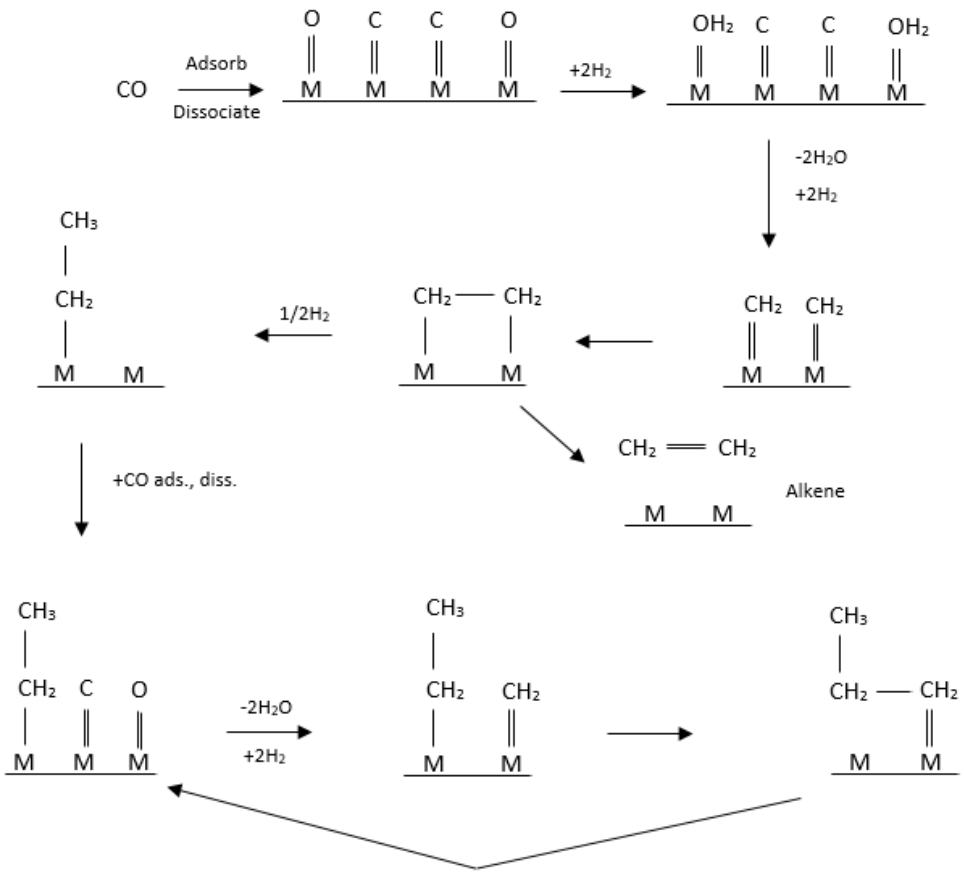

Figure 2.2 Surface “carbene” mechanism (redrawn from [26])

The other mechanistic pathway involves the dissociation of CO after incorporation into the hydrocarbon chain, known as the Pichler-Schulz mechanism. The enol mechanism, proposed by Storch et al, is related to this pathway as it is proposed that a HCOH species becomes inserted into the growing chain, and chain growth continues by the cleavage of the C-O after the insertion of the HCOH species into the growing chain [22]. An example of the enol mechanism can be seen in Figure 2.3.

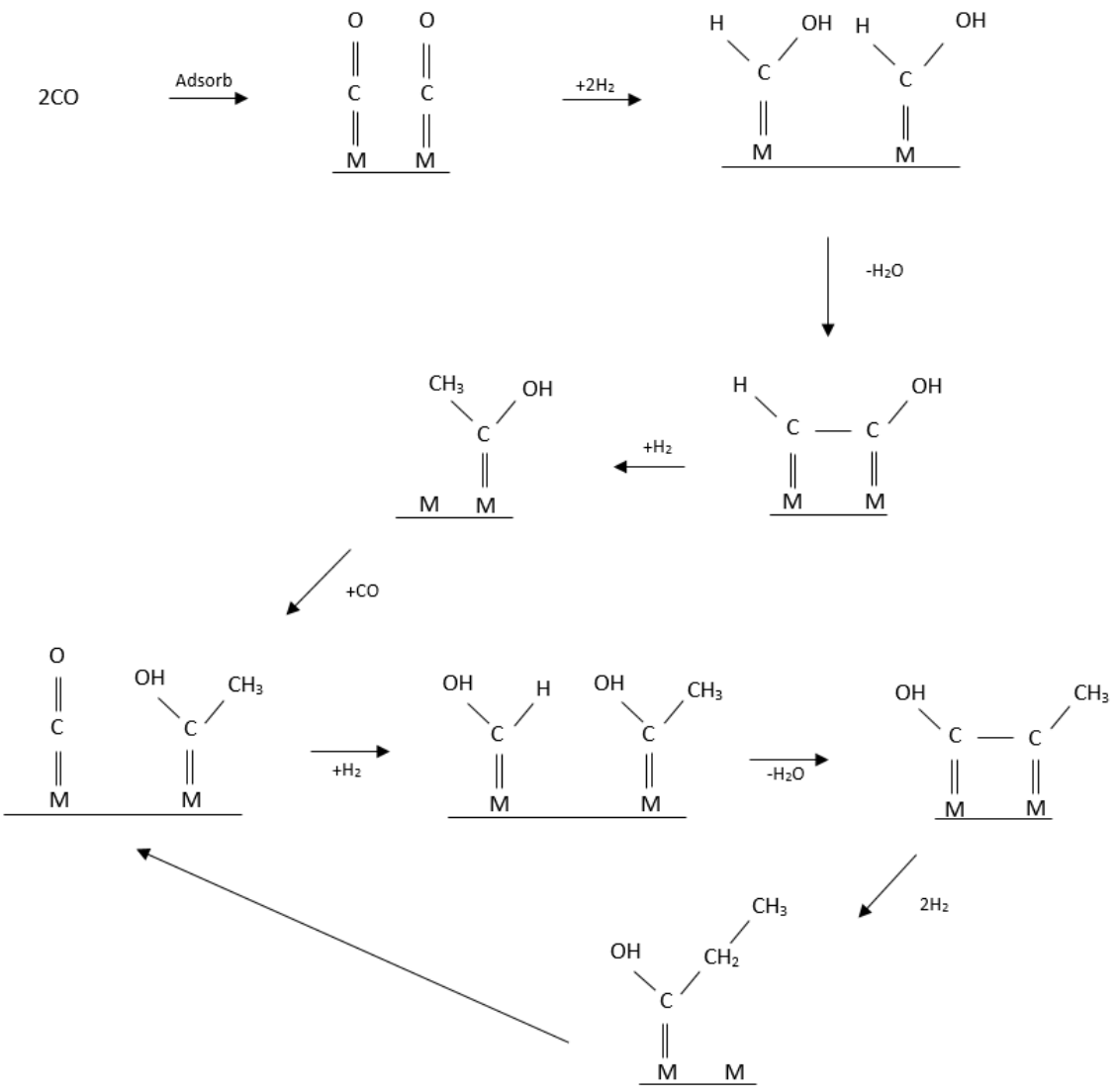

Figure 2.3 Enol mechanism (redrawn from [26])

FTS normally results in a wide range of hydrocarbon products, depending on the extent of the propagation step. The Anderson – Flory – Schulz distribution (ASF) is a model developed to predict the distribution of the hydrocarbon products based on their molecular weight. In the model, the weight fraction of the product is related to the chain growth probability, α, shown in equation 2.7. α is determined by the rates of propagation and termination, shown in Equation 2.8 [27].

$\frac{Wn}{n} = (1-\alpha)^2(a)^{(n-1)}$ (Equation 2.7) $\frac{\mathrm{Wn}}{\mathrm{n}}$ = weight fraction of product with n^{th} carbons

$\alpha = r_p/(r_p + r_t)$ (Equation 2.8) $\mathrm{r_p}$ = rate constant of propagation

$\mathrm{r_t}$ = rate constant of termination

A schematic example of the distribution can be seen in Figure 2.4. Operating at a greater chain growth probability means a higher fraction of heavy hydrocarbon products. An appropriate choice of catalyst, temperature, pressure and H_2/CO ratio can shift the chain growth probability (α), which can alter the product range [4]. It is often more desirable to operate at higher α values, as lighter hydrocarbon products, such as methane, have lower cost value [14, 28]. However, the distribution does have its limitations. For example, a well-known flaw is the fraction of methane produced does not obey the ASF equation [29].

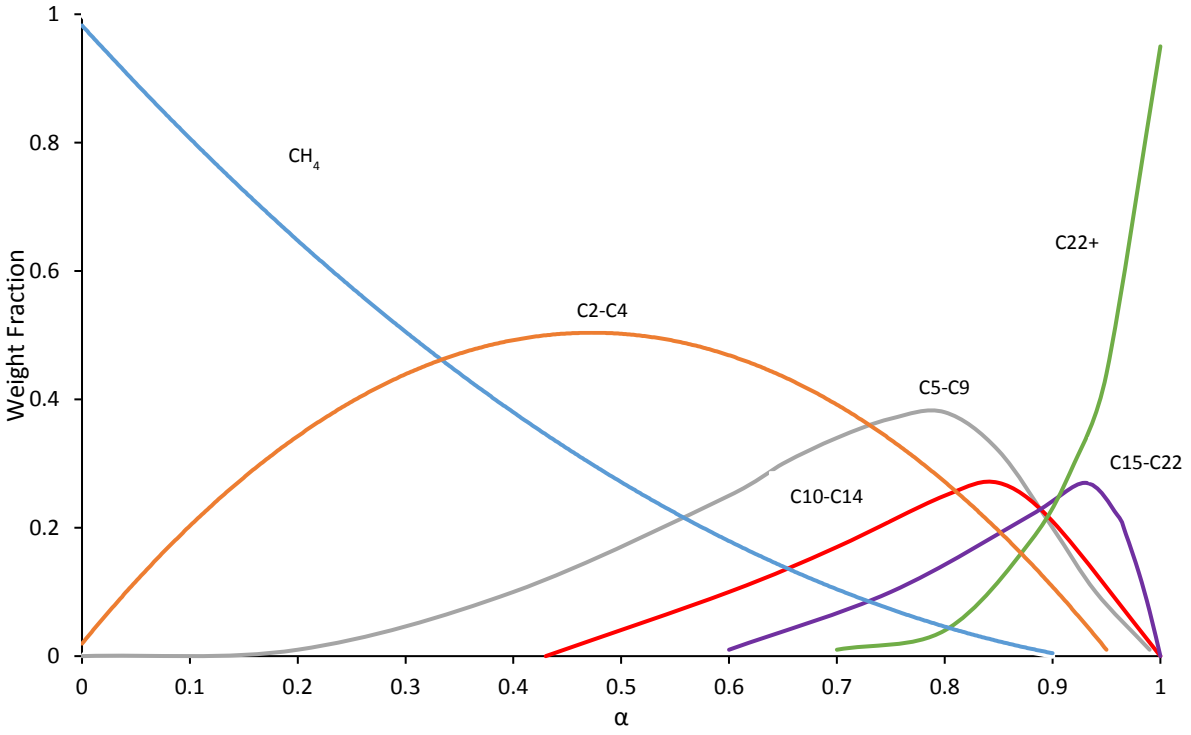

Figure 2.4 Schematic adaption of an ASF distribution from [27]

2.1.3 Fischer-Tropsch Synthesis Catalysts and Operation

Several catalysts have been tested for FTS activity, with Fe, Co, Ni, Ru and Os generally thought to be the best catalytic materials, with ruthenium commonly accepted as being the most active. However, high cost makes it economically unfeasible, whereas Ni only forms methane at reaction temperatures sufficiently high to suppress nickel carbonyl formation, therefore Co and Fe are most popular for industrial application [6, 14]. Generally, Fe catalysts produce more olefins and oxygenates than Co, which may be related to the lower hydrogenating ability of Fe. Whilst Co catalyst are active in the metal state, Fe catalysts change under FTS conditions to a more complex mixtures of iron carbides and oxides [6]. Co catalysts generally exhibit higher activity and relatively larger chain growth probability, therefore making them more suitable for the production of diesel and waxes. Using Fe catalysts at high temperature is the best option for producing gasoline or linear alkenes. As Fe catalysts are active for the WGS reaction, it is preferred for coal-derived syngas. Coal-derived syngas has a lower H_2/CO ratio, in the region of 0.7 to 1, and activity from the WGS can raise the ratio closer to 2. Conversely, Co catalysts do not show the same activity for the WGS reaction, meaning they must operate at higher H_2/CO ratios, making them more suitable for syngas obtained from natural gas [4].

Generally, FTS processes can be classified into the modes of operation, namely high temperature Fischer-Tropsch (HTFT) and low temperature Fischer-Tropsch (LTFT). The HTFT process uses operating temperatures in the range of 320 – 350 ^{o}C, with products essentially only in the gas phase during reaction, resulting in a gas-solid system without any liquid phase. Circulating fluidized bed and fixed fluidised bed are commonly used for this process. Co catalysts would only produce methane at these temperatures, making alkali-promoted Fe catalysts the only option for this process. The low temperature process (LTFT) is operated at temperatures between 200 – 250 ^{o}C. Co and Fe catalysts can be used for this process, with Co typically used towards the lower half of this temperature range. The product spectrum includes heavy waxes which are liquid under reaction conditions, and the presence of a bulk liquid phase results in a three-phase, gas-liquid-solid system. For the remainder of this thesis, the focus will be concerned with the low-temperature process using a Co catalyst. The low-temperature synthesis is ideally suited for the production of high-quality middle-distillates (diesel and jet fuel) and hydrocracking of long-chained waxes [6]. A shift in interest towards the low temperature process has been indicated by the most recent construction of FTS process plants, which can be seen in Table 2.1, along with their specifications.

Table 2.1 Current FTS plants (adapted from [6])

Company	Location	Syngas Source	Catalyst	Reactor	Start-up date	Approximate Plant Capacity (barrels per day)
Sasol	Sasolburg, South Africa	Originally coal, currently natural gas	Fused Fe/K	HTFT circulating fluidized bed	1955 - 1985	
			Precipitated Fe/K	LTFT multitubular fixed-bed	1955	5,000
			Precipitated Fe/K (spray dried)	LTFT slurry phase	1993	
Sasol	Secunda, South Africa	Coal and natural gas	Fused Fe/K	HTFT circulating fluidized bed	1980 - 1999	160,000
				HTFT SAS reactor	1995	
Shell	Bintulu, Malaysia	Natural gas	Co/SiO_2 Co/TiO_2	LTFT multitubular fixed-bed	1992	14,500
Petro SA	Mosselbay, South Africa	Natural gas	Fused Fe/K	HTFT circulating fluidized bed	1993	22,000
Sasol-QP (Oryx)	Ras Laffan, Qatar	Natural gas	Co/Al_2O_3	LTFT slurry	2007	34,000
Shell (Pearl)	Ras Laffan. Qatar	Natural gas	Co/TiO_2	LTFT multitubular fixed-bed	2011	140,000
Chevron-Sasol	Escravos, Nigeria	Natural gas	Co/Al_2O_3	LTFT slurry	2013	34,000

2.2 Fischer – Tropsch Synthesis Reactor Design

2.2.1 Contemporary Fischer-Tropsch Reactors

Mainly fixed-bed reactors have been used for this process, however recently slurry bubble-column reactors have been used [6]. For example, in both Shell MDS Bintulu and Pearl GTL, multi-tubular fixed bed technology is used for the Heavy Paraffin Synthesis [30]. Whereas slurry reactors are used in SASOL's SPD process [31]. Multi-tubular fixed-bed reactors are widely used in exothermic reactions, as they are easy to handle and design as all of the reactor tubes should behave in the same way, and there is no need for catalyst separation. One major drawback of using the multi-tubular fixed-bed reactor is the limitations imposed on catalyst particle size. It would be desirable to use very small catalyst particles, with diameters in the range of 0.2 mm. However, as this will incur high pressure drops, catalyst particles in the range of 1 to 3 mm must be used, which leads to decreased catalyst utilization and to undesirable effects on the product selectivity. Also, in tubes with diameters of several centimetres, hot-spot formation may occur. To prevent damage to the catalyst, the feed and cooling medium need to be set lower than the actual maximal temperature, which can decrease reactor productivity [11]. A simple schematic diagram of the multi-tubular fixed-bed reactor is shown in Figure 2.5.

The industrially prevalent alternative reactor is the slurry bubble column reactor. A simple schematic diagram of a slurry reactor is shown in Figure 2.5. The most attractive advantage of the slurry bubble column reactor is the ability to use fine catalyst powder, with particle diameters of less than 0.2 mm, eliminating the negative effects related to internal mass transfer limitations. Despite the achievable catalyst volume only being up to 25% of reactor volume, compared to 60 % for the fixed-bed, the greater catalyst utilization and higher reaction temperature should allow for higher productivity.

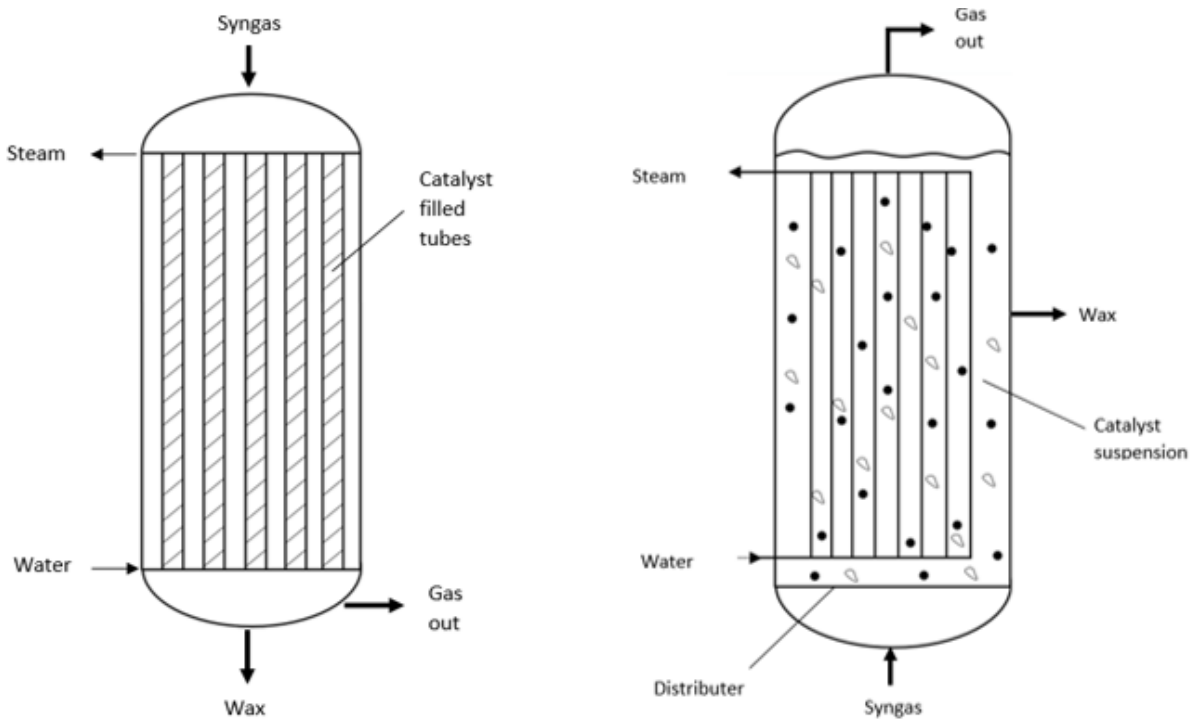

Figure 2.5 Reactors for LTFT (left: multitubular fixed-bed reactor, right: slurry bubble column reactor. Adapted from [11, 32])

Slurry reactors allow for efficient heat removal allowing for better isothermal operation [11]. Unfortunately, separation of the solid catalyst from the liquid products and the scale-up of these reactors are major challenges for industrial operation. Often, costly pilot-plant studies have to be done for successful scale-up. Also, slurry bubble column reactors have raised concerns over having uneven residence time behaviour of the syngas, however it has been thought that a reactor with a sufficiently high length to diameter ratio will behave similar to an ideal plug flow reactor [11]. In order to circumvent the issues related to catalyst separation of the slurry reactor, alternate reactor designs, such as microchannel reactors, have been developed in order to retain the advantages of the fixed-bed reactor without the negative affects related to diffusional limitations and heat transfer [6]. A general comparison of the advantages and disadvantages of both general reactor designs can be seen in Table 2.2.

Table 2.2 Advantages and disadvantages of established reactors for FTS (recreated from [11])

	Fixed Bed Reactor	Slurry Bubble column reactor
Pore diffusion	−	+
Catalyst content in the reactor	+	−
Gas-liquid mass transfer	+	−
Isothermal behaviour	−	+
Catalyst exchange	−	+
Catalyst attrition	+	−
Need for liquid-solid separation	+	−
Scale-up	+	−
Reactor costs	−	+

2.2.2 Diffusion in Fischer-Tropsch Reactors

Typical multi-tubular fixed-bed reactors in FTS consist of tubes with a diameter of 5 cm, with over 2000 of these tubes in a reactor with a height of around 12 m [4]. Some efforts have been made to improve the fixed-bed reactor for FTS, and therefore avoid the difficulties related to the slurry reactor, especially concerning catalyst separation. Currently, many limitations of fixed-bed reactors in FTS are related to the diffusional phenomena that occurs in the large catalyst particles. Many of the diffusion-related effects that can alter the activity or selectivity of FTS catalysts occurs at the catalyst particle level. The effects on the activity and selectivity based on catalyst particle diameter in FTS have been observed in a number of research papers. For example, in research conducted by Post et al, a variety of different catalysts with different support materials, sizes and active metal were tested in a 9 mm ID packed micro-flow reactor [33]. It was concluded that the larger diameter catalyst particles across all catalyst types consistently resulted in lower reaction rate. For instance, an impregnated, alumina-supported, Th and Mg promoted Co catalyst were tested with catalyst particle sizes of 2.3 mm and 0.22 mm, which showed space-time yields of 105 and 230 Kg C_{1+} m_{cat}^{-3} h^{-1}. Similar effects were

observed for Fe catalysts, as impregnated, silicon supported, Cu and K promoted Fe catalyst were tested with average catalyst particle diameters of 2.2 mm and 0.64 mm, giving values of 80 and 105 Kg C_{1+} m_{cat}^{-3} h^{-1} for the same conditions. Further investigation into diffusional effects on reaction rate, by calculation of the reaction rate constant for a variety of cobalt catalysts also confirmed this occurrence. It was determined that any effects due to the support material were negligible, as TPR results showed equal completion of reduction of Co between the all support materials. There was an excellent fit of the experimental data to the classical relationship between the Thiele modulus and effectiveness factor, and effectiveness factors of approximately 1 were found for the smallest of catalyst particles of 0.38 mm, compared with effectiveness factor values around 0.33 to 0.58 for particles of 2.4 mm. This is strong evidence to show that the retardation of reaction rates in larger particles is related to the accessibility of the reactants to the active phase. The greater diffusion distance means reactants and products take longer to diffuse in and out of the particles and in many cases reactants are consumed before they can access the active phase. This problem can be eliminated by using smaller catalyst particles, which is reflected by the greater effectiveness factors.

The other important effect related to the catalyst particle diameter is the effect on selectivity. It is consistently reported that the pores of the catalyst particles in FTS are filled with fluid consisting of the long-chained hydrocarbon product [34]. As H_2 has a much higher diffusion coefficient than CO, H_2 will diffuse much faster through the porous network leading to a higher local H_2/CO ratio, which can lead to higher methane selectivity [35]. In addition to slowing the arrival of reactants, intrapellet diffusion can also affect the removal of products leading to secondary reactions, which can modify the final product distribution even further. Madon and Iglesia showed this by testing a TiO_2 supported Ru catalyst in a stainless-steel multi-tubular packed-bed reactor (inner diameter 0.77 cm) [36]. Pellet sizes of 0.85-1.7 mm were produced and a portion of these were crushed and sieved to retain sizes of 0.1-0.18 mm, therefore ensuring that all catalyst parameters were identical apart from the catalyst particle diameter. The smaller particles consistently displayed higher C_{5+} selectivity throughout the time on stream and lower methane selectivity through a variety of initial H_2/CO feed ratios. This was attributed to the concentration gradients of reactants that develop in the pores of the large catalyst pellet as they become filled with hydrocarbon liquid products. The C_{5+} selectivity is more similar near the start of reaction on both catalyst particle sizes, both exhibiting values of approximately 80 and 88 % for the larger and smaller catalyst particles, respectively, as there little diffusion resistance to the arrival of reactants due to the absence of the liquid phase inside the pores. However, as the liquid phase builds up inside the pores, larger particles start to exhibit selectivity towards lighter products due to the CO concentration gradient that develops, with C_{5+} selectivity of approximately 67 % and 88 % for the large and smaller catalyst particles. Steady state is reached at about 20 h on stream when all pores in the

large pellets are filled with liquid. The pores within the smaller pellets also fill with liquid quickly, but the intrapellet liquid phase does not present any significant diffusion restrictions because of the short path to access the active metal sites, which is shown by maintaining the high C_{5+} selectivity.

It is not only the catalyst particle diameter that can have an effect on the FTS reaction. Other factors, such as pore radius, can also have an effect on the FTS product by introducing diffusion restriction, whilst these restrictions may have further consequences. Iglesia detailed some of these effects, like the effect on secondary reactions such as olefin reabsorption [37]. Whilst diffusional restrictions can negatively impact the rate and selectivity, they can also have some potentially positive effect with regards to the diffusion out of the product. The growing hydrocarbon chains can terminate through beta-hydrogen abstraction to form linear alpha olefins, or hydrogen addition to form n-paraffins on Co catalysts. Olefin re-adsorption onto the active metal site can occur, leading to re-initiation of chain growth and the desorption of longer chain hydrocarbons. This well-known secondary reaction can lead to an increase in C_{5+} selectivity and decrease in CH_4 selectivity when olefin concentration is increased, whilst the rate of this reaction is also increased the more olefins that are retained in the liquid-filled catalyst pellets. To better estimate the effect that internal diffusion restrictions may have on the product as a result of olefin readsorption, Iglesia introduced the dimensionless parameter Φ_n shown in Equation 2.9, which reflects the maximum diffusion rates to the maximum reaction rates for an alpha olefin with n carbons [37].

$$\phi_n = \left(\frac{k_{r,n}}{D_n}\right) \times \left(\frac{R_o^2 \varepsilon \theta_{Co}}{r_p}\right) = \psi_n \times (\chi) \qquad \text{(Equation 2.9)}$$

The first term, ψ_n, contains the rate constant of olefin readsorption and effective diffusivity inside the pellet, which reflects mainly the molecular properties of olefins and accounts for the effect of chain size on termination probability and olefin diffusivity inside the liquid-filled medium. This term is only weakly affected by porous structure of the support. However, χ term depends only on the number of sites available for chain desorption and readsorption, and on the average distance that molecules must diffuse within the intrapellet liquid phase before they are removed. It is based on the structural parameters of the catalyst pellet and the Co site density: the average radius of the catalyst pellet (R_o), the density of Co sites per unit area (θ_{Co}), the void fraction (ε) and the average pore radius (r_p) of the metal oxide support. The χ term contains properties that can be independently measured, and more importantly, altered by careful catalyst design. In the case of olefin readsorption, at low χ values the

selectivity to C_{5+} products increases and CH_4 selectivity decreases as χ increases, as diffusional restrictions increase intrapellet olefin concentrations. This leads to a higher reaction rate of the olefin readsorption secondary reaction, increasing selectivity towards C_{5+} hydrocarbons. An increase in the χ parameter leads to an increase in C_{5+}, which peaks values of around 100 x 10^{-16}. CH_4 selectivity also exhibits the same trend in reverse. This is also supported by simulations. As the χ parameter increases past this point, CO monomer depletion occurs due to the restricted diffusion through the intraparticle and high Co site density, resulting in a decline in C_{5+} selectivity and increase in CH_4 selectivity [37]. Although this parameters is thought of in terms of olefin readsorption, as it based on properties related to diffusion, it can perhaps be used more generally to gauge the point at which point serious diffusional restrictions occur.

Another important point referred to by Iglesia is the effect that water can have on the diffusional process [37]. It has been recognised that water seems to have an autocatalytic effect. It is thought that the presence of water increases the reaction rates and C_{5+} selectivity. CO and H_2 diffusion coefficients are about 3 times larger in water than in typical FTS liquids. Iglesia suggested that capillary effects occurring due to the narrow pores diameter can lead to condensation of water, to form either a separate water phase or form an emulsion together the hydrocarbon liquid, stabilized by minor alcohol components among the FTS products. This may enable water to form a liquid phase at concentrations well below the saturation vapour pressure at reaction conditions. The higher diffusion coefficient of the reactants in the water phase or emulsion would reduce diffusional restrictions allowing for greater reaction rate and less methane selectivity [37].

To circumvent the diffusional limitations of larger catalyst particles required for the fixed-bed reactor, alternate catalyst particle designs have been attempted. One such innovation is egg-shell catalysts, which was proposed many years ago to avoid negative effects of diffusion on rate and selectivity [38]. Since, a number of studies have investigated the effect of eggshell catalysts in FTS. By locating the active phase near the outer pellet surface, the negative effects of transport restrictions, such the depletion of CO deep inside the pellet can be avoided, whilst the larger pellet size can maintain acceptable pressure gradients [39]. Iglesia et al prepared an eggshell catalyst for FTS using a molten cobalt nitrate impregnation technique. By controlling the viscosity of the impregnating melt, and controlling the contact time between the SiO_2 support and the melt during the impregnation process, the active layer thickness could be controlled, with shell thickness of less than 0.2 mm on a catalyst pellet of about 2.7 mm diameter. The following catalyst particles contain 10 - 13 % Co loading, with a local Co content in the active phase shell area of 40 - 50%, and about 75 % of the total pellet volume contains no Co crystallites. The eggshell pellets showed an improvement in synthesis rate and C_{5+}

selectivity compared to uniformly impregnated large pellets, however Co-time yield and C_{5+} selectivity become slightly higher when these eggshell catalyst are crushed to form catalyst particles of 0.143 mm, suggesting that the reaction is still partially limited by the reactant arrival on the eggshell catalyst [39]. More recently, Fratalocchi et al used a new impregnation method to create γ-Al_2O_3 supported Co eggshell catalysts [40]. Catalyst particles with a diameter of 600 µm with an active shell region 75 µm thick were tested in a fixed bed reactor, whilst the eggshell catalysts were also ground and sieved to a powder with a particle size of 150 µm, before testing in the reactor. The larger eggshell catalyst displayed slightly higher conversion and selectivity to C_{15+} products. It is suggested that the eggshell catalyst is affected by weak mass transport limitations, as the higher C_{15+} selectivity is a result of slow olefin removal, resulting in olefin readsorption leading to higher weight products. This is supported by the fact that the eggshell catalyst products are less olefinic compared to the powdered catalyst. The increase in conversion witnessed in the eggshell catalyst is also suggested to arise from weak mass transport limitations. Fischer-Tropsch kinetics are positive order with respect to H_2 and negative order with respect to CO, and the higher H_2 diffusivity results in a higher local H_2/CO ratio at the active phase surface [40].

Another method of reducing diffusional limitations in large catalyst particles is the introduction of transport pores with larger diameters. Small pores are necessary to achieve a high surface area which is required for the high dispersion of the active phase, however this introduces the aforementioned diffusion limitations. The introduction of additional transport pores with larger diameters may be a way to combine high mass transfer within the pores with high surface area required for a more active catalyst [41]. Becker et al investigated the introduction of transport pores using a mathematical model [42]. They found that additional transport pores enhance the mass transport but reduce the amount of active phase, which requires a balance by optimizing the fraction of transport pores and catalyst pellet layer thickness. They showed that the catalyst layer with an ideal amount of transport pores and ideal thickness exhibits a productivity that is about 47 % higher than that for the best layer without transport pores [42]. A study by Li showed that introducing macropores can alleviate some internal diffusion restrictions in larger cobalt-based catalyst particles [35]. Two porous silica supports were produced through a sol-gel method and one sample was ground to destroy the macropores, whilst the other sample contained both macropores and mesopores, before undergoing impregnation with a cobalt nitrate precursor. The two samples were separated into 10-20 mesh and 60-80 mesh portions and tested in the reactor. It appeared that the larger pellet catalyst showed poor performance in comparison to the smaller pellets, due to the existence of internal diffusional restrictions in larger pellets. However, when comparing the 10-20 mesh samples, it was observed that the unground samples containing macropores had higher conversion, C_{5+} selectivity and TOF. Also, it was shown that,

although there was an increase in performance for the smaller 60-80 mesh pellets over the larger 10-20 mesh pellets for both sizes of the unground sample containing macropores, the difference is very small. For example, the difference in C_{5+} selectivity was only 3.38 % when operated at 220 ^{o}C, suggesting that macropores may be beneficial in larger particles. However, there was a 16.07 % difference in CO conversion. Despite the advantages in regards to diffusion limitations offered by using macropores, it was still evident smaller pellets offered better FT performance than larger ones.

2.2.3 Alternative Reactors for Fischer-Tropsch Synthesis

Fixed-bed reactors utilising the appropriate catalyst particle size have been shown to exhibit some degree of diffusional limitations, despite some improvements through the introduction of transport pores and eggshell catalysts. Alternative reactor designs may negate internal diffusion limitations of fixed-bed catalyst particles and avoid the need for catalyst separation required for slurry reactors. Multiple reactor design types have been considered for this purpose, such as reactors with micro-structured catalysts (monoliths and foams), coated microchannel reactors, and micro and milli fixed-bed reactors with small catalysts particles that are loaded into the packed bed [43]. For example, some reactors consist of structured catalyst geometries that are characterised by a non-randomly ordered fixed bed of catalysts. These may be honeycomb or foam shaped catalysts. Honeycomb monolith catalysts consist of a large number of identical, parallel tubes with a cell density of up to 1200 channels per square inch [11].

Another example of such reactor types is micro-structured reactors. They contain a large number of small channels or tubes with diameters in the micrometer region. For example, a typical channel with a diameter of 100 μm and with a length of 20,000 μm (2 cm) results in a high surface area to volume ratio of 10,000 m^2/m^3 [44]. These kinds of reactors can almost eliminate mass transport limitations caused by intraparticle diffusion. The short reactant diffusion length can improve catalyst efficiency by minimizing the negative effects on activity and selectivity [43-45]. The intensification of heat transfer also facilitates easier isothermal operation, even with very exothermic reactions [44]. However, the low catalyst inventory of these reactors reduces productivity per reactor volume [45]. There are also technical challenges involved in fabricating a reactor structure with uniform channel morphology. However, recent advancements in ceramic and monolith technology have managed to circumvent this problem.

Almeida et al used an Al-alloyed stainless-steel micro-reactor block coated in with a cobalt catalyst to test in FTS [46]. The micro-structured reactor block consisted of channels with a 56 mm^2 geometric surface and 0.7 mm hydraulic radius which was wash coated with a cobalt catalyst. Two blocks were tested with catalyst loads of 2.9 and 7.3 mg cm^{-2}. The average thickness of the catalyst coating inside the microchannel could be estimated from the catalyst loading, alumina density, specific pore volume of the catalyst and the void fraction between catalyst particles, giving values of 32 and 80 µm, respectively. The reaction data showed consistently high C_{5+} selectivity, especially in block 1 where the values stayed between 80.4 and 80.7 for a range of different space velocities at 20 bar and 220 ^oC. By comparing results from the two blocks at the same operating conditions, it was noted that whilst conversion was similar, the C_{5+} selectivity and olefin/paraffin ratio was higher for block 1. It was suggested that as block 1 has the lower catalyst loading and therefore lower coating thickness, the lower diffusion resistance reduces the effect of the unequal diffusion coefficient of H_2 and CO which results in a CO deficit at the active site. A H_2/CO ratio closer to the feed stoichiometric ratio will result in greater C_{5+} selectivity compared to a CO deficit at the active site. Olefins that are diffusing away from the active site back into the bulk also meet less resistance in the thinner catalyst film, meaning there is a reduction of the olefin readsorption side-reaction, which was shown by the higher olefin/paraffin ratio when using the thinner catalyst layer. Another effect that was noted was that increased conversion resulted in lighter hydrocarbon production. This was explained by the increase in reactants and products throughout the liquid-filling of the catalyst pores increasing diffusional resistance to reactants and leading to a lower H_2/CO ratio. Overall, it was shown the microchannel reactor can still be affected by the thickness of the washcoated catalyst layer. Although the elementary particles of catalyst were ball-milled to very small sizes (<10 µm), which shouldn't result in any transport limitation, the porosity of the layer is not only controlled by the size of the catalyst particle, but by the additives used in the washcoating process. Although generation of a very packed layer favours adhesion of the coating, it can impair diffusion and therefore reaction selectivity [46].

Cao et al used a microchannel reactor system with a packed alumina supported cobalt catalyst bed inside the channel [47]. The microchannel slot had a width of 0.508 mm, which was sandwiched by two oil cooling channels to take advantage of the high potential for efficient heat transfer offered by the system. The catalyst had particle sizes of 45 and 150 µm with a surface area of 60 $m^2\ g^{-1}$. 0.2 g of the catalyst was packed into the microreactor. It was observed that the 45 µm sized catalyst particles exhibit better performance with higher conversions, productivity and lower methane selectivity. Productivity as high as 2.14 g $C_{2+}\ g_{cat}^{-1}\ h^{-1}$ was observed at 200 ^oC, 35 atm and a GHSV of 22,886, which are higher than those typically reported in the literature (0.5 g $C_{2+}\ g_{cat}\ h^{-1}$). It is noticeable here that diffusional limitations still play a significant role between particle sizes of 150 to 45 um, which

corresponds to Post and co-workers' earlier assertion that diffusional limitations are negligible only below around 100 um. 63% CO conversion was achieved with a methane selectivity of 10.5% when the reactor is operated at a GHSV of 60,000 h^{-1}, 20 atm and 235 ^{o}C. This GHSV is about 15 times faster than that in Shell's conventional fixed bed technology [47].

Membrane reactors have also been investigated for use in FTS. Membrane reactors in FTS are used in multiple different configurations and for different purposes. These included distributed feed of reactants, in-situ removal of water, forced-through membrane contactor, and zeolite encapsulated catalysts. Distributed feed of reactants through a membrane allows for better temperature control. Also, the methane selectivity can be influenced as it depends on the H_2/CO ratio, therefore a distribution of H_2 in a stream of CO may increase the yield of heavier products [11]. The in-situ removal of water using membranes can prevent the re-oxidation of catalysts and can shift the equilibrium of the WGS reaction to convert CO_2 to CO, increasing the hydrocarbon yield [11, 48]. Encapsulated catalysts have been studied that coat a thin layer (around 10 μm) of zeolite on to catalyst pellets. The zeolite layer acts as a membrane reactor, as the FTS products diffusing out undergo hydrocracking and isomerization due to the acidic sites in the zeolite [49].

In this work, the interest is centred on forced-through contactor membranes. These types of reactors serve similar purposes to micro-channel reactors, which is to reduce problems associated with diffusion whilst preventing the need for a catalyst separation step. A study by Khassin et al looked into using a permeable composite monolith (PCM) membrane in FTS to solve the problems associated with diffusion whilst maintaining a high concentration of the active component [50]. The PCM membrane was prepared by mixing the powders of the Co-Al co-precipitated catalyst, a pore-producing agent and dendritic metallic copper powder as a reinforcing heat-conductive agent, and pressing the mixture into a hollow cylinder which was calcined in the inert gas flow and then in the flowing hydrogen at 620 ℃. The PCM membrane formed a three-modal porous structure where the larger pores, with an effective radius of >2-3 μm, are the transport pores, which are almost completely gas filled and are responsible for the gas permeation. The smaller pores are flooded with liquid products due to capillary forces and are not permeable. The most narrow pores, with an effective radius of <0.5 μm, are located inside the catalyst particles. Two PCM membranes exhibiting these characteristics were prepared; PCM 17 with an outer diameter of 17 mm and an axial hole of 7 mm, and PCM 42 with diameters of 42 mm and 9 mm. The catalytic properties of the PCM membranes were studied in a radial flow membrane reactor at 484 K at 0.1 and 0.6 MPa. Considering the high loading of the catalyst, at 0.1 MPa the PCM17 membrane managed to produce space-time yields of greater than 27 mg_{C5+} cm^{-1} h^{-1}, which is close to the space-time yield of the slurry bed reactor operating at 2 MPa (SASOL SSPD) [50]. The productivity

of the PCM42 membrane at 0.1 MPa is worse than that of the PCM17. This is suggested to be due to the wider pore size distribution of the PCM42 membrane, which results in bypass through the wider pores and flow stagnation in the narrow pores. Conversely, the PCM42 membrane showed significantly greater C_{5+} selectivity and lower methane selectivity at similar catalyst space velocities, however no explanation was provided by the authors [50]. Bradford et al tested a tubular ceramic membrane reactor [51]. A stainless steel reactor designed to house a mesoporous 1 cm x 25 cm commercially available tubular Al_2O_3 membrane was coated with a 200 µm layer of P/Pt-Co/γ-Al_2O_3 catalyst. The feed gas was fed into the shell side of the reactor and was forced to flow through the catalytic layer and support in order to exit the reactor. The catalyst was also prepared and tested in a fixed-bed reactor configuration. A comparison of results showed that the C_{2+} hydrocarbon selectivity in the membrane reactor is lower than that observed in the fixed-bed reactor, although the conversion and C_{2+} yield (moles of CO converted to C_{2+} per mole of CO in the reactor inlet) are higher in the membrane reactor, as well as a lower olefin to paraffin ratio. It was suggested that diffusion resistances in the membrane and catalyst layers imposed by the membrane reactor structure create an increase in the local H_2/CO ratio that leads to an increase in selectivity to methane, a decrease in selectivity to C_{2+} species, an increase in reaction rate, and a decrease in the olefin to paraffin ratio [51]. This is to be expected as the catalyst particles in the fixed-bed reactor were less than 45 µm, where should be no significant diffusion resistance [33]. Also, the production potential of a monolith loop ceramic membrane reactor was calculated based on a simplified reactor model, which was based on experimental results. The maximum C_{2+} production rate for a honeycomb membrane module (0.25 m × 1.524 m) with 11,470 channels coated with a 300 µm catalyst layer is given as 270 kg m^{-3} h^{-1} at 200 °C and 2 MPa [49, 51].

2.3 Ceramic Membrane Development for Microstructured Reactor

One such method that may help in the fabrication of a suitable membrane reactor is the development of phase-inversion assisted ceramic membranes. Ceramic membrane fabrication via a phase-inversion assisted process allows for the fabrication of a precise and adjustable structure which, by supporting a suitable catalyst, can form a micro-structured reactor capable addressing current issues with FTS reactors, such as the previously mentioned intraparticle diffusional limitations on activity and selectivity.

Ceramic membranes are often used in filtration processes. The unique thermal, chemical and mechanical properties of ceramic membranes give them significant advantages over polymeric membranes, stainless steel membranes and conventional filtration techniques such as rotary-drum filtration, decantation, centrifugation and media filtration, in many applications. The membranes can withstand high temperatures, extreme acidity or alkalinity and high operating pressures, making them suitable for many applications where polymeric and other inorganic membranes cannot be used. They have increasingly been used in a broad range of industries, including biotechnology and pharmaceutical, dairy, food and beverage, as well as chemical, microelectronics, metal finishing and power generation. Within the food and beverage industry, specific applications include fruit juice clarification, cane sugar juice filtration, and spent caustic or acid recovery [52]. A growing area of interest for such membranes is the water treatment industry, especially for microfiltration and ultrafiltration processes. Currently, the water and wastewater industry is dominated by polymeric membranes, which have been extensively investigated since the 1990s for water and municipal wastewater treatment. However, poor stability against chemicals as well as high fouling propensity of polymeric membranes due to their hydrophobic nature can not only affect their performance but also impact sustainability for long-term operation [53].

Ceramic materials such as γ-Al_2O_3 and α-Al_2O_3, ZrO_2, TiO_2, SiO_2 and SiC are used to fabricate the membranes. Various configurations of membranes can be formed, such as flat disc membranes, single-channel and multi-channel cylindrical membranes, and hollow-fibre membranes. The membrane cross-section can also be symmetrical, where a uniform cross-sectional structure is exhibited throughout the whole membrane. Conversely, asymmetrical membranes exhibit two distinct cross-sectional structure. Often, for filtration processes, a thin separation layer is combined with a porous sub-layer, allowing for higher permeation fluxes due to the thinner separation layer. A variety of fabrication techniques can be used which are generally broken down into several stages, including preparation of the ceramic powder, paste or suspension, shaping of the ceramic into the desired geometry, followed by heat treatment such as calcination or sintering [54]. This work will be primarily concerned with the combined phase-inversion and sintering fabrication technique. This technique can produce a both symmetric and a wide range of asymmetric membranes in a single step for both flat sheet and hollow-fibre geometries. This technique results in the formation of a large amount of finger like voids, which can reduce mass transfer resistance for permeation fluxes similar to membranes formed from conventional methods [54]. Although this structure may be useful for filtration applications, membranes containing these finger-like voids may have use as membrane reactors, especially considering the variety of structures that can be formed. These membranes are produced by preparing a suspension of ceramic particles and a polymer binding agent in a solvent, and through

solvent – non-solvent exchange induced phase inversion of the polymer binder, the ceramic particles are immobilized in the desired geometry through casting (flat membrane) or spinning (hollow fibre). The preparation parameters of the suspension can affect the viscosity and density of the suspension and the rate of polymer precipitation, which can greatly influence the morphology of the finger-like voids. The sintering step removes the organic components in the membrane precursor suspension, such as the polymer binding agent, and at high temperatures (usually over 1000 ^{o}C) the final structure of the membrane is consolidated with improved mechanical strength. Higher sintering temperatures can lower porosity but further improve the mechanical strength [54].

Choi et al prepared ultrathin hollow fibres using a phase inversion and sintering method [55]. Al_2O_3 (30 wt%) was dispersed, with the help of a dispersing agent, in DMAc and 1,4-dioxane solvent mixtures and polysulfone (10 wt%), was added and dissolved as a polymer binding agent. A spinneret with an orifice diameter/inner diameter of 3/2 was used to spin hollow fibre membranes which were solidified in a water bath, before sintering at 1300-1400 ^{o}C. They showed that by introducing 1,4-dioxane as an additive in the polymer solution, a closely packed sponge structure is created instead of macrovoids, which usually result from fast phase separation.

Kingsbury and Li further investigated how the preparation of the ceramic precursor suspension can affect the structure [56]. Ceramic hollow fibre membranes were prepared from suspensions of Al_2O_3, NMP (N-methy-2-pyrrolidone) and polyethersulfone (PESf) using a phase-inversion assisted spinning/sintering process. They showed that finger-like voids, separated by sponge-like layers, could be formed on both the inner and outer surface of the hollow fibre membrane which were mostly retained after calcination. By changing the air-gap between spinning and the coagulant bath, it was shown that the length of the fingers from the inner surface and outer surface of the hollow fibre membrane can be altered. Also, by adding water as a non-solvent additive to the precursor suspension to increase viscosity, it is possible to reduce the length, as well as change the morphology of the finger-like voids. It was suggested that hydrodynamically unstable viscous fingering, a phenomenon that occurs at the interface of two fluids of different viscosities, can explain the formation of the finger-like like voids. At the first moments of mixing between the precursor suspension and non-solvent, a steep concentration gradient results in solvent/non-solvent exchange, causing a rapid increase in viscosity and the precipitation of the polymer phase. The interfacial instability that arises at the interface between the solvent and non-solvent lead to the occurrence of viscous fingering and the formation of the finger-like voids. Increasing the precursor suspension above a critical viscosity can prevent viscous fingering occurring, which leads to a sponge-like structure throughout the membrane [56].

Lee et al showed that the morphologies of the finger-like voids could be modified significantly by altering the solvent in the ceramic precursor suspension [57]. Precursor suspensions were separately prepared using DMSO, NMP, DMAc, DMF and TEP, with PESf as the polymer binding agent. They were then poured into a mould and placed in a coagulation bath of de-ionized water to create flat membranes, afterwards being sintered at to 1350 ^{o}C. Membranes prepared using DMSO, NMP and DMAc resulted in asymmetric membranes containing finger-like voids separated by sponge-like layers, whereas membranes prepared with DMF and TEP resulted in symmetric membranes with a sponge-like layer exhibited through the whole membrane cross-section. However, a major difference in the finger-like void structures were present between DMSO, NMP and DMAc membranes. DMSO membranes exhibit thin, densely packed finger-like voids in the cross-section. NMP cross-sections of the membranes show larger, pear-shaped structures. The cross-section of DMAc membranes shows finger-like voids that are more similar to that of DMSO, however they are noticeably broader. It was suggested that the reason for such a difference in the structure of the finger-like voids is linked to the solubility of the polymer binding agent, PESf, in each of the solvents. DMSO, the weakest solvent for PESf, allows for a faster precipitation of the polymer which causes a rapid viscosity increase at the wall of the void, constraining its growth and producing narrower channels. The precipitation rate of polymer in NMP, the strongest of the three solvents for PESf, is much slower and therefore a slower rate of increasing viscosity at the wall of the void allows for greater radial growth [57]. The finger-like voids formed from the phase-inversion assisted fabrication technique exhibit voids with a diameter of approximately 10 – 100 µm, depending on fabrication parameters [57]. These channels provide an opportunity for process intensification of FTS by potentially removing debilitating transport limitations. The catalyst could be applied directly, or on a substrate through wash coating which can improve surface area to create a catalytic micro-structured reactor.

2.4 MOF Catalysts in FTS

The catalyst used FTS obviously has a very important role and good catalyst design can greatly improve performance. Heterogeneous catalysts face many longstanding challenges, especially with regards to metal nanoparticle-based catalysts, such achieving the desired particle sizes and metal loadings. One method for addressing such challenges is MOF-mediated synthesis, which utilises a MOF (metal organic framework) as the catalyst precursor which has the potential to achieve higher metal loading, ideal nanoparticle size and good metal particle dispersion. The combination of such properties is currently difficult to achieve using traditional methods such as impregnation and deposition-

precipitation [58, 59]. Since about 2003, MOF related research has experienced almost unparalleled growth, with the number of papers escalating in the last ten years [60]. MOFs are crystalline solids consisting of infinite lattices, made up from inorganic secondary building units (metal ions or clusters) and organic linkers, connected by coordination bonds of moderate strength. MOFs exhibit very high porosity. However, MOFs suffer from low thermal and chemical stability, especially compared to other inorganic porous solids, such as zeolites [58, 61]. Catalytic activity can exist within the material itself, as the metal ion in the structure can be active [62]. Also, MOFs can be utilized in catalysis by introducing an active component into the pore network [63]. A more recent method of using MOFs is as a catalyst precursor, where the MOF acts as a sacrificial structure which gives way to the active material under certain conditions. Under certain atmospheres at high temperature, the framework collapses and the organic linker is completely or partially burnt away, if oxygen is present, or carbonised in the case of an inert atmosphere. The metal ions/clusters become mobile within the newly created matrix or just evaporate.. This process allows for several different approaches which can create many different kinds of materials, and depending upon the heat treatment and post-treatment, MOF precursors can form bulk and supported catalysts with unprecedented properties [58].

MOF-derived catalysts for FTS have only been investigated within the last 5-6 years, to develop both Fe and Co-based catalysts. In this case, the focus will be on Co containing catalysts derived directly from the pyrolysis of MOFs. Currently only 5 studies have documented FTS performance of Co-based MOF-derived catalysts formed from direct pyrolysis. Luo et al experimented with the controlled pyrolysis of ZIF-67 to create carbon supported Co catalysts for the purpose of studying the effect of nanoparticle size on FTS performance [64]. Pyrolysis in Ar was performed at a variety of temperatures between 450 and 900 ^{o}C and different dwell times between 4 and 12 hours. TGA results showed that decomposition of the framework starts to occur around 350 ^{o}C and a significant weight loss occurs around 490 ^{o}C. XRD results showed a face-centred cubic (FCC) structure of Co^{o}, showing an increasing metal nanoparticle size with increasing pyrolysis temperature. Nanoparticle sizes in the region of 5.8 to 11.7 nm were observed for pyrolysis at 500 ^{o}, whilst BET results showed that the surface area decreased from 1761 $m^2 g^{-1}$ to 177-332 $m^2 g^{-1}$. It was concluded that pyrolyzing ZIF-67 above 500 ^{o}C resulted in metallic Co entrapped in a partially graphitized carbon matrix, polished by a certain amount of pyridinic and graphitic N and a small quantity and adsorbed oxygen. Catalyst performance was tested in FTS at 235 ^{o}C, 1 MPa, H2/CO = 2 and GHSV of 5550 mL g^{-1} h^{-1}. Pyrolysis conditions of 500 ^{o}C for 8 hours resulted in the highest conversion of 57 %, highest C_{5+} selectivity of 58 % and the lowest methane selectivity of 28 %. With regards to metal nanoparticle particle size effect studies, it was found that turnover frequencies increased and plateaued at about 11 nm, whilst a selectivity dependence was also observed, with larger particles between approximately 30 nm to 78 nm showing

an increase C_{5+} selectivity, whilst nanoparticles between 10 and 30 nm exhibiting almost the same selectivity.

Li et al investigated the carbon-supported Co catalysts from MOFs for FTS from Co-BDC through chemical vapour deposition in order to prepare core-shell Co in carbon catalysts [65]. Co-BDC MOF precursors were heated in either an Ar atmosphere or a 2 % C_2H_2/Ar atmosphere at 5 $^oC\ min^{-1}$ to 550 ^oC for 1 hour, before reduction in hydrogen at 240 ^oC. The TGA results showed that a large mass loss occurs between approximately 410 and 550 ^oC in an Ar atmosphere. However, in a 2 % C_2H_2 atmosphere, part way through this decomposition there is a large weight gain which brings the sample back to over 100 % of its original weight. HR-TEM suggested the formation of a graphited carbon shell with a Co core from pyrolysis of the MOF in Ar. After pyrolysis in C_2H_2, where carbon was constantly deposited on the surface of the cobalt nanoparticles during the carbonization process, a thin layer of carbon was formed with low graphitization degree. The surface content of carbon was higher in a 2 % C_2H_2 atmosphere (83.15 %) than that in a pure Ar atmosphere (75.78 %), suggesting the decomposition acetylene deposits additional carbon. FTS tests of the two catalysts were run at 220°C and 3.0 MPa, by using syngas with a H_2/CO molar ratio of 2 and a GHSV of 3000 h^{-1}. The catalyst prepared under pyrolysis with 2 % C_2H_2 showed higher conversion, around 11 % compared to 7 %, and higher C_{5+} selectivity, with values around 80 % compared to 68 %. Lower methane selectivity was also noticed, with values of around 15 % compared to 22 %. It was suggested this may be due to the acetylene-prepared catalysts exhibiting higher porosity. The authors also suggest that metallic Co in the catalyst had been transformed into Co_2C during reaction. As the catalyst maintained stable activity, the authors suggest Co_2C may be an active phase for FTS.

Qiu investigated FTS with nitrogen free Co-MOF-74 and nitrogen-containing ZIF-67 [66]. Both MOFs underwent pyrolysis at 550 ^oC for 2 hours under an Ar atmosphere and tests were carried out at 230 ^oC and 30 bar. The Co-MOF-74 derived catalyst showed a higher conversion, 30 % compared to 10 %, with the higher conversion attributed to the higher Co loading (52 % based on ICP-OES) and higher porosity than the catalyst derived from ZIF-67. C_{5+} selectivity was higher with the Co-MOF-74 derived catalyst, with 65 % compared to 31 % from the ZIF-67 based catalyst. The lower selectivity of the ZIF-67 derived catalyst was attributed to the smaller pore size which impedes transportation of longer chain hydrocarbons, whilst it was suggested that nitrogen species, which were present in the catalyst after pyrolysis, act as electron donors and can change the valence state of Co and promote the synthesis of short-chain hydrocarbons.

Pei et al prepared a FTS catalyst through the pyrolysis of Co-MOF-71. By doping the MOF with a Si species before pyrolysis, they showed the FCC Co nanoparticles can be partially transformed into the

hexagonal close-packed (HCP) phase via a Co_2C intermediate. FTS reactions were performed in a stainless-steel fixed-bed micro-reactor. In-situ pyrolysis of the precursor MOF occurred at 600 ^oC for 8 hours in He to generate the MOF-derived catalyst, before FTS reaction at 30 bar and 300 ^oC. The catalyst precursors doped with Si showed slightly higher activity and selectivity to C_{5+}, with a selectivity of approximately 80 % compared to 50 %.

Zhang and colleagues also investigated the effects of chemical vapour deposition using acetylene to create core-shell catalysts [67]. Co-MOF-74 was used as a precursor, which underwent in-situ pyrolysis at a variety of temperatures between 400 and 600 ^oC for 1 hour in a 2 % C_2H_2/He atmosphere. HR-TEM images show Co^o nanoparticles encapsulated in a carbon shell. The carbon shells at lower temperatures (400-450 ^oC) are amorphous, while at higher temperatures (500-600 ^oC) layered graphene of 2-12 layers are shown, with Co nanoparticles appearing in the range of 2-10 nm. Catalytic testing was done at 30 bar and a variety of temperatures. . The catalyst showed excellent performance at a temperature 260 ^oC, which is just above the normal LTFT operating range of 200-250 ^oC, with high activity of 242.3 10^{-6} mol g_{Co}^{-1} s^{-1}, good C_{5+} selectivity of 75.4 % and low CO_2 selectivity of 4.8 %. Also, an improvement over the same MOF prepared by simple pyrolysis under inert gas was shown, which contained Co nanoparticles with a diameter of 10-12 nm, and showed C_{5+} selectivity of 65 % and CO_2 selectivity of 8 % at a reaction temperature of 230 ^oC. Another study focused on the effect of the Co-MOF-74 pyrolysis temperature was done. It was shown that for catalysts generated at a pyrolysis temperature of 500 ^oC and above, C_{5+} selectivity increased but activity declined with increasing pyrolysis preparation temperature up to 600 ^oC. It was suggested this was due to the less permeable, highly graphitized carbon shells, which may also cause the greater selectivity of $C_{5+,}$ as it may affect diffusion out of the reactants.

2.5 Conclusion

In order to improve the efficiency of the FTS reaction, there are several unresolved challenges that need to be addressed. Many of these challenges are related to the fixed-bed reactor design, which has the advantage of discarding a catalyst separation step, however suffers from transport limitations which can have detrimental effects on activity and selectivity. Several alternative reactor designs have been proposed, such as micro-structured and membrane reactors which can address these problems. An innovative technology which may be used for such reactor design is the fabrication of suitable ceramic membranes. Through the use of a phase-inversion assisted and heating technique, it may be

possible to fabricate membranes with the desirable properties for a micro-structured reactor. Also important in improving FTS is the nature of the catalyst. The FTS synthesis process can be improved by using tuneable MOF-derived catalysts which can display high activity and selectivity. In this project, a membrane is prepared using a phase-inversion assisted and heating technique and the membrane is functionalised with Co to create a catalytic membrane. The catalytic membrane is thought to address the detrimental mass transport effects observed in fixed-bed reactors. A MOF-based catalyst derived from the pyrolysis of Co-MOF-74 is produced, where the performance benefits over conventionally prepared impregnated cobalt catalysts is investigated. Applying the MOF-derived catalyst to the membrane is also attempted.

Chapter 3

General Methods and Equipment

3.1 Introduction

This chapter provides a general overview of the equipment and methodology which has been used consistently throughout the experimental work. Some of parts of the methodology may have minor alterations, which are acknowledged in the experimental section of each results chapter. The detailing of the main pieces of equipment and the corresponding method of operation are shown in this chapter, as well as catalyst preparation methods, synthesis of the Co-MOF-74 and preparation of the ceramic membrane.

3.2 20 cm^3 Fixed-Bed Reactor Operation

FTS Reactor System

All FTS reactor work was carried out using a 20 cm^3 fixed-bed automated Autoclave Engineers Fischer-Tropsch reactor system. The outside shell of the reactor system can be seen in Figure 3.1. The reactor tube itself is a stainless-steel tube with inner diameter of approximately 7.5 mm and a length of 43.5 cm. The reactor tube was placed in a ceramic heating jacket inside the reactor oven chamber (Figure 3.2).

Figure 3.1 FT reactor system

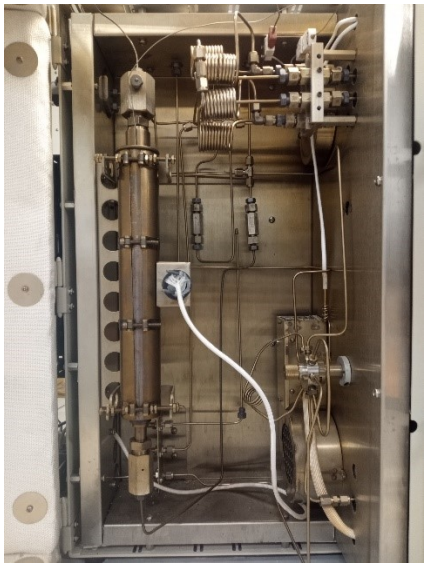

Figure 3.2 FT reactor system oven

A schematic diagram of the reactor system can be seen in Figure 3.3. Three mass flow controllers (Brooks Instrument Model number 5850TRG) regulate the inlet flowrate of H_2, CO and N_2 which are piped into the reactor from external cylinders. The inlet gases to the reactor can be directed away from

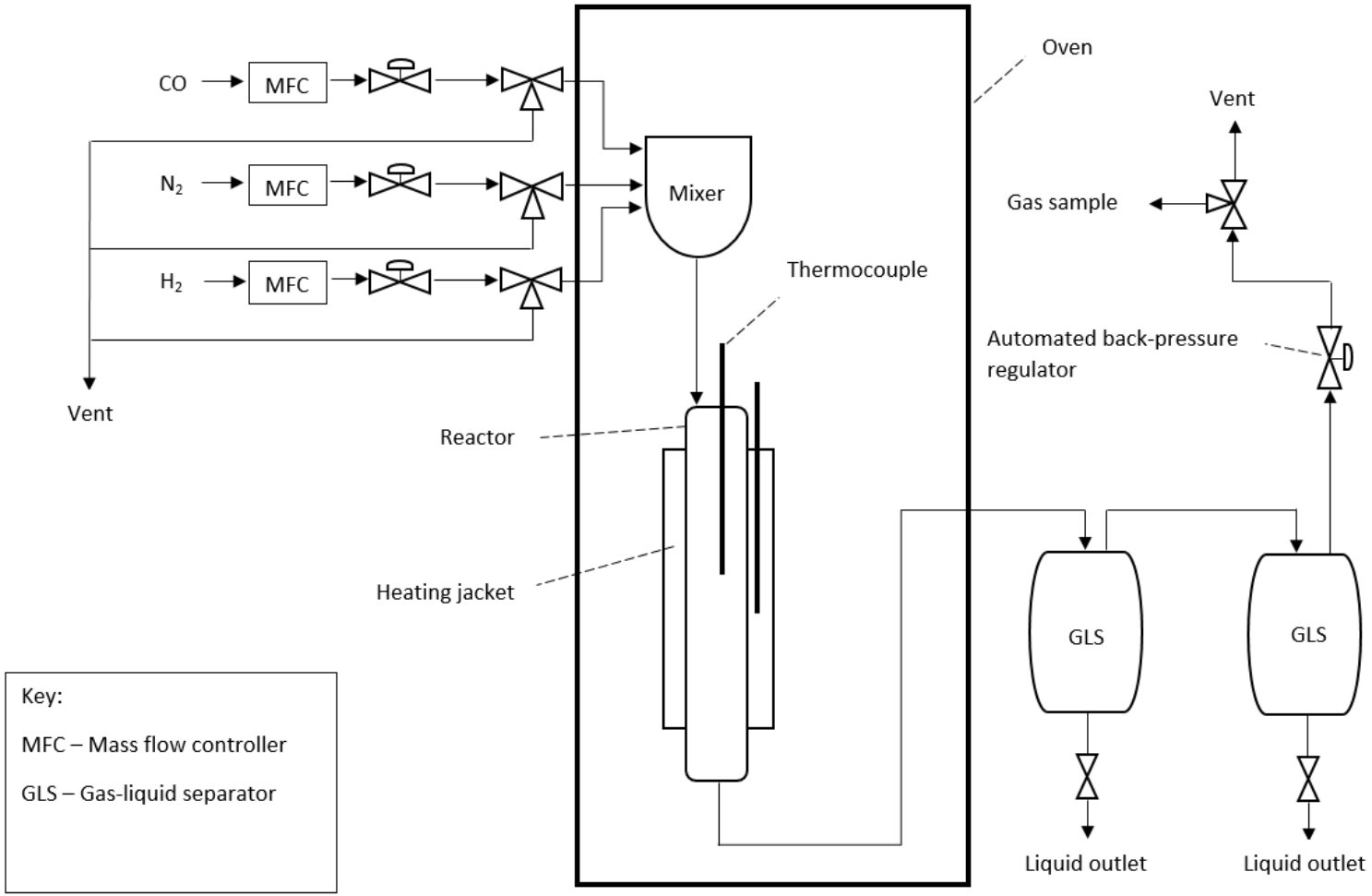

Figure 3.3 Simple schematic diagram of the FTS reactor system

the system before mixing using a vent valve, if necessary. The mass flow controllers express flowrate in standard cubic centimetres per minute (SCCM). The mass flow controllers were calibrated based on the volumetric flowrate at room conditions (T = 20 ^{o}C, P = 100 kPa). In this work, volumetric flowrates relating to the inlet flow of reactants will be expressed as the volumetric flowrate at room conditions. The gases enter a mixer before entering the reactor tube. The reactor tube is heated by the ceramic heating jacket connected to an electrical heater. A thermocouple is located inside the reactor tube itself, as well as on the outside of the tube, between the tube wall and ceramic heating jacket. The reactor is housed in an insulated, stainless-steel oven that can be heated up to 250 ^{o}C to prevent condensation of the products exiting the reactor. Products are then separated in two 150 ml gas-liquid separators (GLS), located outside of the reactor oven. Gases from the reactor that are not condensed pass through a back-pressure regulator before exiting the reactor system through the vent. GLS 1 and GLS 2 can be set at 200 and 80 ^{o}C respectively, to create a hot and cold trap. A sampling valve was fitted to the external pipe leading to the vent, to enable gas sampling. The reactor flowrates, temperatures and pressure is automatically controlled by software, which can be seen in Figure 3.4. All valves were operated pneumatically, with a nitrogen supply of 5 bar.

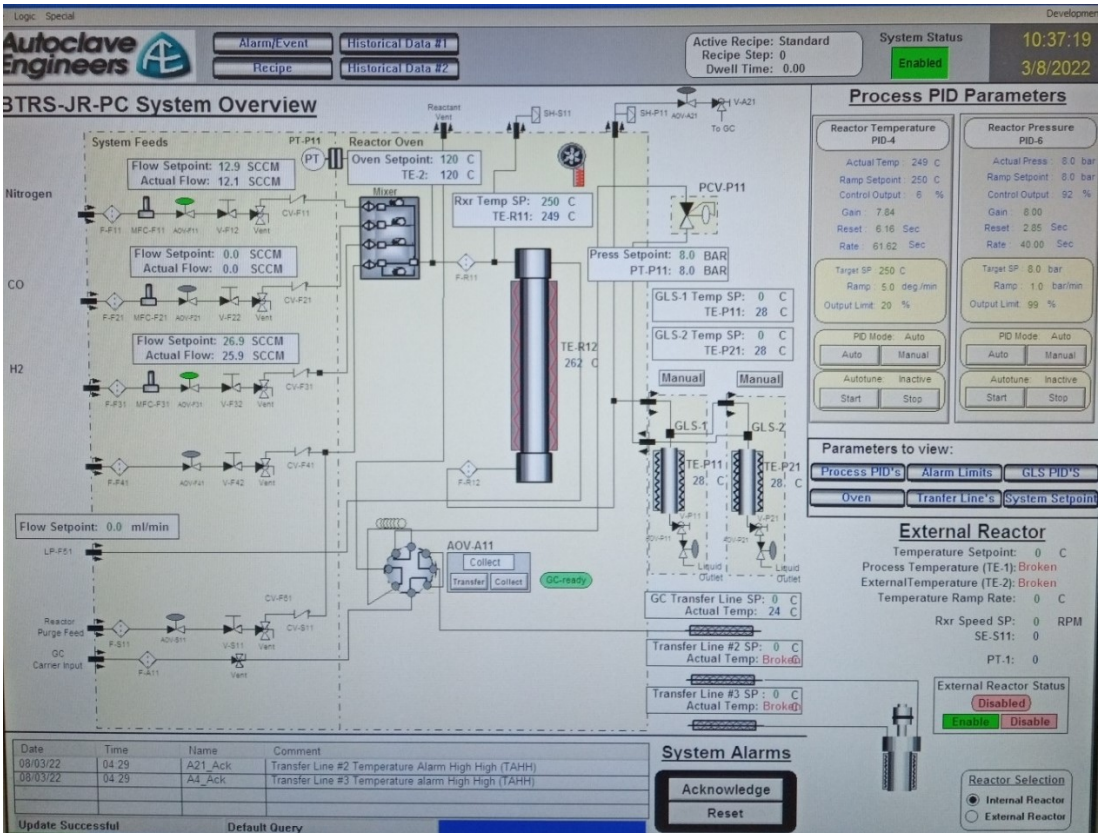

Figure 3.4 Reactor operating software

Packing Catalyst inside the Reactor

The ceramic heating jacket can be disconnected from the system, and the reactor tube extracted. The reactor tube was packed according to the layout in Figure 3.5. Quartz wool was stuffed at the bottom of the reactor tube which was filled with borosilicate glass balls (1 mm diameter), before stuffing another layer of quartz wool above the glass balls to hold the catalyst bed. The catalyst bed varied between approximately 0.27 – 4 cm, depending on the type of catalyst used and desirable space velocity. Another layer of quartz wool was stuffed above the catalyst bed. By estimating the bed height, the reactor tube was packed in such a way that the thermocouple tip is surrounded by the quartz wool, which will measure the temperature inside the reactor.

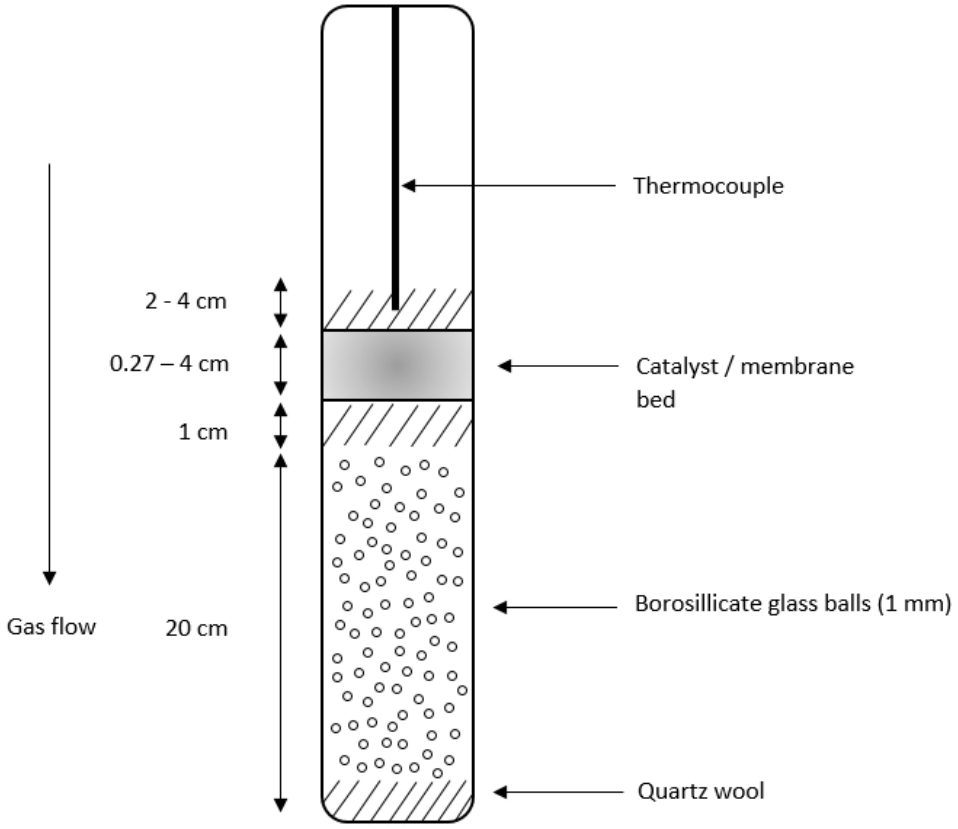

Figure 3.5 Schematic diagram of reactor catalyst packing

Some work included the packing of a catalytic membrane bed. This packing consisted of 15 flat disc membranes packed directly on top of each other, with the same packing format shown in Figure 3.5. An example of the stacked membranes can be seen in Figure 3.6, which may give some idea as to the

configuration inside the reactor tube. During the preparation of the membranes, the edges of each membrane were sanded to fit snug inside the reactor tube. An example of a membrane, before application of the catalyst, can be seen inside the entrance to the reactor tube in Figure 3.7.

Figure 3.6 Stacked membranes outside of the reactor tube

Figure 3.7 Membrane inside the entrance to the reactor

Reduction of Catalysts

For reduction of the catalyst or decomposition of the Co-MOF-74, the system was purged with the reducing or inert gas, to remove air and attain the reduction or pyrolysis atmosphere. The reduction temperature heating rate and set point were entered into the operating system software. The oven was also set to 200 ^{o}C to prevent condensation in the pipework. Once the desired reduction temperature was reached, it was left to dwell for a specified amount of time before switching off the power output to the reactor and oven heating systems. After the dwell time was reached, the reactor system was purged with nitrogen and isolated from the atmosphere until reaction.

Catalytic Reaction

The GLS was emptied to collect water which may have condensed from reduction. The system was then heated and pressurised using nitrogen until the pressure and temperature remained stable at the desired set point. The oven was heated to 120 ^{o}C to prevent condensation before the reactants entered the GLS, but set sufficiently low enough to allow for the reactor to cool effectively to maintain isothermal operation. The reactant gases were then let in, at which point the time for the beginning of the reaction was recorded. After running the reaction between 4 and 12 hours, the reactor heating was switched off, the system purged with nitrogen and depressurised. In operation, both GLS were left at room temperature, in order to condense as much of the liquid as possible. The catalyst was left in the reactor tube and isolated under a N_2 atmosphere until starting the next reaction, or the catalyst was removed from the tube for characterisation.

Measurement of Reactor Outlet Gas Flowrate

The outlet gas flow was measured using a Supelco bubble flowmeter column shown in Figure 3.8. The external gas sample valve was connected to the bubble flowmeter column, and a soap bubble was generated by pumping soap water through bottom of the column into the flowing outlet gas coming in from the side of the column. The time for a bubble to fill 100 ml of the column was recorded, and this was repeated at least 5 times and the average time was used to measure the flow rate of gaseous product, which was further used to calculate the mass balance, conversion and selectivity of the reaction. The flowrate was recorded after at least 3 hours of reaction and was assumed to represent steady-state operation.

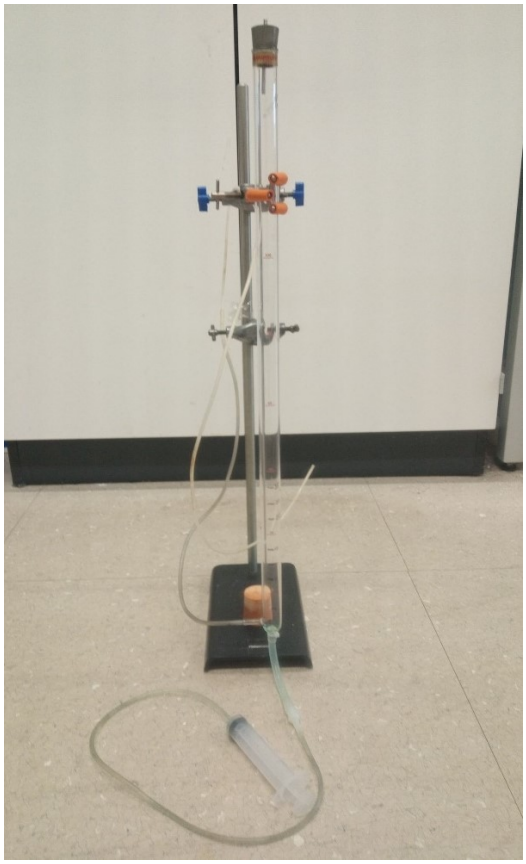

Figure 3.8 Supelco bubble flowmeter

Sampling and Analysis of Gaseous Products

The outlet gases were analysed offline using a Varian CP-4900 Micro-GC with a Molsieve 5A column connected to a TCD detector to detect H_2, O_2, N_2, CH_4 and CO, and a PPQ column connected to a TCD detector to detect CH_4, CO_2, C_2H_6, C_2H_4, C_3H_8, C_3H_6 with He as the carrier gas. When analysing H_2 with He as a carrier gas, although the thermal conductivity of H_2 is greater than that of He, the thermal conductivity of the H_2-He binary mixture is not a simple monotonic increasing function of H_2 concentration [68]. Using the current GC method, H_2 can form a negative peak at concentrations above 8 % when using He as a carrier gas. Therefore, the sample needed to be diluted to ensure H_2 concentrations remained below 8 %. To collect the gas sample, an empty sampling bag of 500 ml was first filled with 450 ml of nitrogen to dilute the gas sample, using the reactor system vent valve before the reactants mix (Figure 3.3) and the automated mass flow controller. After measuring the outlet product gas flowrate, the remaining 50 ml of the sample bag can be filled with reactor product gas

based on the product gas outlet flowrate. The sample bag was then connected to the micro-GC for analysis, which was run with a column temperature of 90 °C and injector temperature of 42 °C for the PPQ column, and a column temperature of 80 °C and injector temperature of 35 °C for the Molseive 5A column. The gas sample was taken after at least 3 hours after the start of the reaction, and it was assumed that the gas sample analysis represented steady-state operation.

Analysis of Liquid Products

Liquid products were emptied from the GLS after each reaction run and the mass of liquid was measured and recorded. When the liquid was collected, it was often present as two immiscible phases, with the water and oxygenates at the bottom, and the hydrocarbons on the top, shown in Figure 3.9.

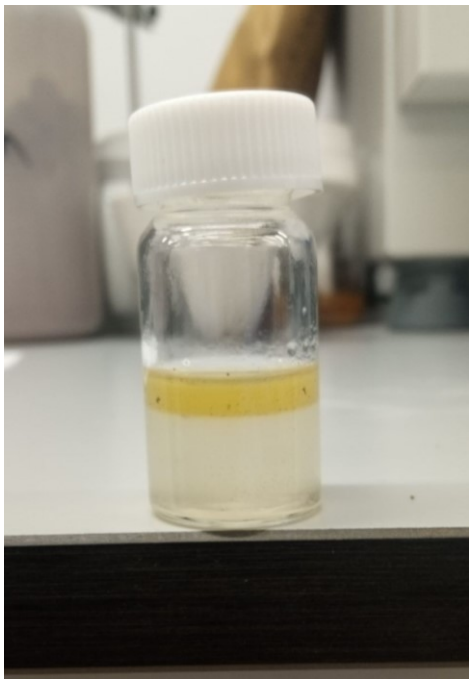

Figure 3.9 Liquid product emptied from the GLS

After weighing the total mass of liquid, the lower water and oxygenate phase was extracted using a syringe, and the vial was weighed again to determine the separate masses of the oil phase and the water and oxygenates. A few drops of the upper hydrocarbon phase was then dissolved in toluene and analysed using a Shimadzu GC-2010 Plus equipped with an FID detector using a 30 m ZB-1HT

Inferno column and He carrier gas. A sample of the water and oxygenates was put into a sample vial and analysed neat using the same method. 1 µl of the sample was injected using a split ratio of 80 with an injector temperature of 280 °C. The column oven temperature was held at 40 °C for 1 minute and then ramped at 5 °C min^{-1} to 330 °C and held for 20 minutes at 330 °C. The FID temperature was set to 340 °C. The FID spectrum of each sample was compared to a standard, run using the same method. Two standards were used, a C_8 – C_{20} straight chain alkane standard (Supelco – 40 µg each in hexane) and a C_7 – C_{40} straight chain alkane standard (Supelco – 1000 µg each in hexane). The retention time of each alkane from the standard can be seen from the GC-FID spectra in Figure 3.10. Molecules with an identical number of carbon atoms will elute at the same or very similar retention times. Each peak area from the FTS liquid samples eluting at, or around, the same retention time of each separate straight chain alkane from the standards, was added together and grouped as the same carbon number. This was done by taking the midpoints between the retention times of each alkane. From this, the mass ratio of the products based on the carbon number can be calculated, and by using the mass of the hydrocarbon fraction measured from the FTS liquid product, the mass of each carbon number in the FTS sample can be calculated, which can be used to calculate the mass ratio of products. The amount of moles of each carbon product was then calculated in the same way as Schafer et al, using Equation 3.1[69].

$$\text{Moles of } C_n = \frac{MF_n \times m_{oil}}{mm_n} \qquad \text{(Equation 3.1)}$$

Where C_n is the carbon product with n carbons, MF_n is the mass fraction of products with the carbon number n, m_{oil} is the mass of oil, and mm_n is the molecular mass of the straight-chain alkane with the chain being n carbons in length. The calculation was only performed for the oil phase of the FTS liquid product. Some carbon-containing compounds were observed in the water and oxygenate phase, however many of them had carbon products below C_5, and almost all of them had all of the carbon-containing products with carbon numbers below C_7.

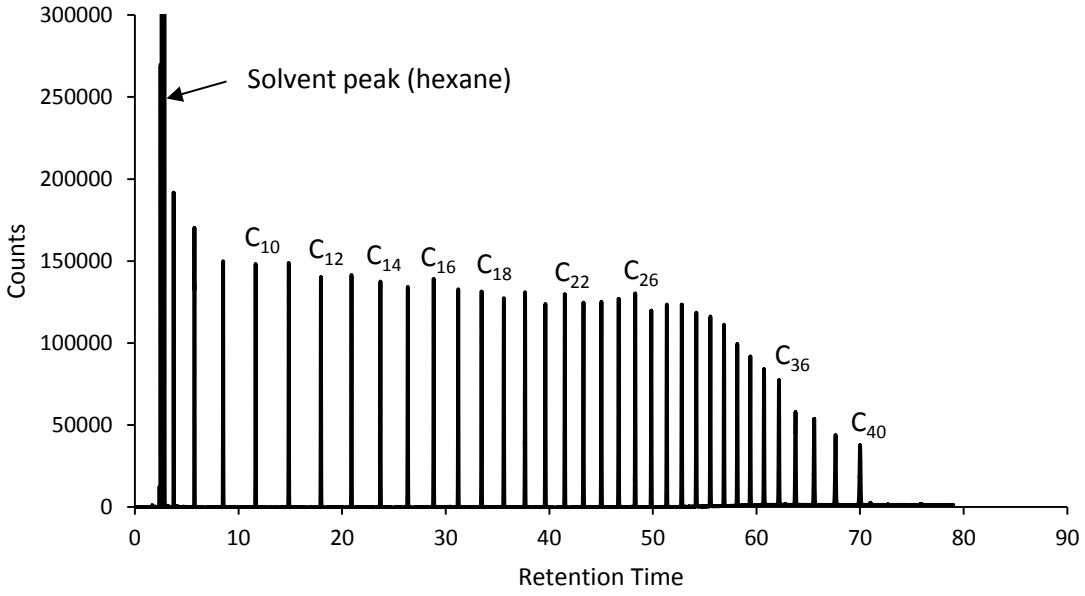

Figure 3.10 GC-FID chromatogram of standard saturated C_7 – C_{40} alkane solution

Factors Affecting Catalyst Performance Evaluation

Unfortunately, as there is no water-cooling system, temperature control relies mostly on the heating of the heating jacket surrounding the reactor tube. As FTS is a highly exothermic reaction, this can occasionally make isothermal control difficult. Also, as overnight working is not allowed, the reaction needs to be completed between the hours of 8 am and 6 pm. This meant that the reaction could only be run for a maximum of 9 hours, if possible. This is a challenge for running FTS reactions. Firstly, in some cases FTS catalysts have shown that steady-state operation is only achieved after 10 hours or more [70]. This means the reaction may have run at conditions that are not steady-state, and therefore will affect calculation of performance. Secondly, if the selectivity to C_{5+} products is low, it may be difficult to accumulate enough liquid product during the reaction time for feasible analysis. Even when the oil product is clearly visible and separate from the water, if the amount of oil product is low, when the water and oxygenates are extracted any small error in extraction can affect the measurement of oil product mass. The absence of an online GC also made operation challenging, as usually only one data point can be collected making it difficult to measure conversion over time and estimate steady-state operation.

Calculation of Catalyst Performance

The performance of the catalyst was measured by calculating the CO conversion (expressed as a fraction, Equation 3.2), activity (expressed as moles of CO converted per gram of Co per hour, Equation 3.3), CH_4 selectivity (Equation 3.5), C_{2+} selectivity (Equation 3.4), and CO_2 selectivity (Equation 3.6), expressed as percentages). C_{7+} and C_{10+} selectivity was also calculated in the same way as the CH_4 selectivity, except the moles of C_{7+}/C_{10+} exiting the reactor replaces the moles of CH_4 out in the numerator of Equation 3.5. The yield percentage can be obtained from equation 3.7.

$$\text{CO converted} = \frac{\text{mol CO}_{\text{in}} - \text{mol CO}_{\text{out}}}{\text{mol CO}_{\text{in}}} \quad \text{(Equation 3.2)}$$

$$\text{Activity} = \frac{\text{mol}_{\text{CO converted}}}{\text{g}_{\text{Co}} \times \text{h}} \quad \text{(Equation 3.3)}$$

$$\text{C}_{2+}\text{ Selecitivity} = \left(\frac{\text{mol CO}_{\text{in}} - \text{mol CO}_{\text{out}} - \text{mol CH}_{4\text{ out}} - \text{mol CO}_{2\text{ out}}}{\text{mol CO}_{\text{in}} - \text{mol CO}_{\text{out}}}\right) \times 100 \quad \text{(Equation 3.4)}$$

$$\text{CH}_4 = \left(\frac{\text{mol CH}_{4\text{ out}}}{\text{mol CO}_{\text{in}} - \text{mol CO}_{\text{out}}}\right) \times 100 \quad \text{(Equation 3.5)}$$

$$\text{CO}_2\text{ Selectivity} = \left(\frac{\text{mol CO}_{2\text{ out}}}{\text{mol CO}_{\text{in}} - \text{mol CO}_{\text{out}}}\right) \times 100 \quad \text{(Equation 3.6)}$$

$$\text{Yield (\%)} = \text{Conversion} \times \text{Selectivity} \quad \text{(Equation 3.7)}$$

3.3 Co-MOF-74 Synthesis

Co-MOF-74 was consistently used as the catalyst precursor for the MOF-based catalyst throughout the experimental work. In each case it was prepared through a variation of a hydrothermal synthesis method previously reported by Dietzel et al [71]. A solution of 0.298 g of 2,5-dihydroxyterephthalate (2,5 DHTP) in 5 ml tetrahydrofuran (THF) (Fischer chemical, assay >95.5 %) was mixed with a solution of 0.786 g cobalt(II) acetate tetrahydrate (Alfa Aesar, 98 % purity) in 5 ml deionized water inside a Teflon-lined steel autoclave of 50 ml, shown in Figure 3.11. The variation in the synthesis procedure in this work was a higher concentration of 2,5-dihydroxyterephthalate and cobalt(II) acetate in their respective solutions. In comparison, in the work reported by Dietzel et al, cobalt(ii) acetate (187 mg, 0.75 mmol) in water and 2,5-dihydroxyterephthalic acid (149 mg, 0.75 mmol) in THF (10 mL) was used [71]. The autoclave was placed in an oven (Thermo Scientific Heratherm oven) at 110 °C for 72 hours. The crystals were filtered under vacuum using filter paper (Whatmann 4.25 cm, 11 µm retention) and a Buchner flask and left to dry at room temperature. The crystals were filtered and washed in THF and left again to dry at room temperature.

Figure 3.11 Teflon-lined steel autoclave

3.4 γ-alumina Supported Co-based Catalyst Preparation

To compare against the FTS performance of the MOF-based catalyst derived from Co-MOF-74 and the catalytic membrane, a conventionally prepared Co-based catalyst was prepared by impregnation on a γ-alumina support. 4.219 g (1 g Co equivalent) of cobalt (II) acetate tetrahydrate (Alfa Aesar, 98 % purity) was dissolved in 50 ml of de-ionized water. 10 g of γ-Al_2O_3 pellets (Alfa Aesar, 1/8 “) were degassed and the cobalt acetate solution was added. The mixture was gently stirred with the container

open at approximately 75 ^{o}C until all the water had vaporised. The sample was then dried at 120 ^{o}C for 2 hours. The sample was calcined inside a muffle furnace and heated from room temperature to 500 ^{o}C at 2 min^{-1} and allowed to dwell for 1 hour before cooling naturally inside the oven. The catalyst then underwent reduction with H_2 inside the reactor at 3 ^{o}C min^{-1} to 450 ^{o}C for 5 h under 120 ml min^{-1} hydrogen flow.

3.5 Ceramic Flat Disc Membrane Preparation

Ceramic flat disc membranes were fabricated as part of the catalytic membrane. The composition of the membrane suspensions can be seen in Table 6.2, Table 6.3, Table 6.4 in Chapter 6, Milling balls (Inframat 12mm Yttrium stabilized zirconia) were placed inside a 250 ml glass bottle and the solvent (NMP, VWR International, purity > 99.5% / DMSO, VWR International, assay 100%) was measured and added. The required amount of A135 dispersant was weighed and added to the bottle. The bottle was then put on a roller (Gladstone Engineering Co. LTD.) for approximately 15 minutes to allow for the dispersant to dissolve. Afterwards, the required amount of α- Al_2O_3 powder (1 µm, Inframat Advance Materials LLC) was weighed out and added to the bottle. The mixture was then milled for approximately 48 hours. Afterwards, the polymer binding agent (Polyethersulfone (PESf) or Polyethylene methacrylate (PMMA, Sigma-Aldrich)) was weighed and added to the bottle, which was milled for another 48 hours. About 50 ml of the milled suspension was then transferred to a beaker and degassed in an air-tight vessel under vacuum whilst being stirred by an electronic stirrer to remove trapped air in the suspension that could cause defects in the final structure. After degassing for approximately 3 hours, the suspension was poured into an aluminium mould with a disc diameter of either 10.4 or 11.4 mm and height of 3 mm, taped to glass plates (Figure 3.12). Shortly afterwards, the mould was placed horizontally in a water bath at room temperature and left for approximately 24 hours. The mould would be removed and left to dry for at least 24 hours. The dry membranes would then be sintered at 1500°C to remove the polymer binder and improve the mechanical strength of the membrane. The sintering profile used was:

1. From room temperature to 600 ^{o}C at 5 ^{o}C min^{-1}
2. Hold for 2 h at 600 ^{o}C
3. From 600 ^{o}C to 1500 ^{o}C at 5 ^{o}C min^{-1}
4. Hold at 1500 ^{o}C for 4 hours
5. From 1500 ^{o}C to room temperature at 5 ^{o}C min^{-1}

Figure 3.12 Aluminium mould and glass plate

3.6 Preparation of Catalytic Membrane

After the sintered membrane was prepared, the top and bottom surface of the membranes was sanded off to expose the opening of the micro-channels. The membranes were sanded to expose as many micro-channels as possible whilst keeping the membrane thickness between 1.3 and 1.7 mm, from the original 3 mm, to retain a reasonable degree of mechanical strength. The membrane diameter decreased by approximately 20 % of its original after sintering. However, all membranes had diameters slightly larger than the inner diameter of the reactor tube, and were also sanded at the side to fit snugly inside the inner diameter of the reactor tube. This was achieved by rotating the membrane at the edge of a surface and sanding using sand-paper attached to a metal file, to ensure the membrane retained a circular shape as best possible. The membranes were then cleaned using an ultrasonic bath and dried in an oven at 100 ^{o}C. The prepared membranes were then functionalised by Co impregnation or the application of the Co-MOF-74-based catalyst.

Cobalt Acetate-Based Catalytic Membranes

To prepare catalytic membranes from a cobalt acetate solution using an impregnation method, the membranes were degassed in a conical flask and a concentrated solution of 3 g of cobalt (II) acetate tetrahydrate (Alfa Aesar, 98 % purity) dissolved in 10 g of de-ionized water was inserted into the flask under vacuum to cover the membranes, which were left in the solution for 10 minutes and removed and left to dry at room temperature. This step was repeated 2 more times. Calcination was done by heating the membranes to 500 ^{o}C at 2 ^{o}C min^{-1} a muffle furnace for 1 hour, where they were allowed

to cool naturally in the furnace. After the cobalt oxide had formed on the membranes from the calcination, the membranes were then packed into the reactor and reduced under flowing hydrogen with a ramp of 3 ^{o}C min^{-1} to 450 ^{o}C for 5 h under 120 ml min^{-1} hydrogen flow.

CO-MOF-74-Based Membranes

Co-MOF-74-based membranes were prepared by dispersing 1.633 of Co-MOF-74 in methanol, placing the membranes into the beaker, stirring the suspension with membranes inside, and leaving the suspension to settle overnight. The excess methanol was extracted from the suspension using a syringe until the level was just above the settled suspension, and the remaining suspension was allowed to dry naturally. The Co-MOF-74 was retrieved, whilst some of the Co-MOF-74 gathered on the membrane surface was scraped off, although some was retained in order to retain enough Co required for the reaction to proceed at a conversion of over 10 %.

3.7 Characterisation Techniques

Powder X-RAY Diffraction (XRD)

Powder X-ray diffraction (XRD) was performed on a Bruker D8 Advance operated at 40 kV and 40 mA using copper radiation ($\lambda_{CuK\alpha}$ = 1.54060), with a 2θ range of 5-80 ^{o}, a step size of 0.020 ^{o} and a time per step of 192 s. Nanoparticle grain size was calculated from the Scherrer equation shown in Equation 3.8.

$$\tau = \frac{k\lambda}{\beta cos\theta} \qquad \text{(Equation 3.8)}$$

τ is the mean size of the ordered crystalline domains, K is the dimensionless shape factor (0.9), λ is the X-ray wavelength (1.54060), β is the peak width at half height, and θ is the Bragg angle.

Specific Surface Area, Pore Volume and Pore Diameter

Specific surface area, pore volume and pore diameter measurements were performed on a Quantachrome Nova 4200e porosimeter. Samples were degassed at 130 ^{o} overnight before being connected to the sampling port and immersed in liquid nitrogen. N_2 adsorption/desorption isotherms were recorded with 25 adsorption points up to a relative pressure of 1 with 21 desorption points. Specific surface area was calculated from multipoint Brunauer-Emmett-Teller (BET) analysis from 7 points between relative pressures of 0.01816 and 0.19119. Average pore diameter, pore volume and pore size distribution were calculated using the Barrett–Joyner–Halenda (BJH) method from the desorption branch of the isotherm.

Scanning Electron Microscope and Energy Dispersive X-Ray Analysis (SEM-EDX)

SEM and EDX images were taken using a JEOL 7800F Prime Field Emission SEM equipped with an energy dispersive X-ray spectrometer (EDX) detector. SEM images were also taken using Hitachi S-4800 SEM.

Thermogravimetric Analysis (TGA)

TGA analysis was undertaken using a Perkin Elmer Pyris 1 TGA and a Mettler-Toledo TGA/DSC 2 STAR System. TGA analysis was performed on Co-MOF-74 in pure N_2. A heating profile from room temperature to 800 ^{o}C with a heating ramp of 10 ^{o}C min^{-1} was used. Another heating profile from room temperature to 500 ^{o}C, held for 1 hour, with a heating ramp of 8 ^{o}C was also performed.

Elemental Carbon, Hydrogen, Nitrogen and Sulphur (CHNS) Analysis

CHNS analysis of solid samples was performed on a ThermoFischer Scientific Organic Elemental Analyser to determine carbon, hydrogen, nitrogen and sulfur content. Approximately 2.5 mg of sample and 5 mg vanadium pentoxide (V_2O_5), an oxidant to assist combustion, was loaded into a tin foil holder which was pressed shut. The tin capsules were inserted into a furnace where they underwent combustion in a quartz furnace at 900 ^{o}C. The gases passed through a copper catalyst and GC column and CO_2, H_2O, NO_x and SO_2 concentrations were analysed by a TCD detector. Liquid samples were analysed using the same procedure, however approximately 1.3 mg of liquid was placed onto an adsorbent pad, which was inserted into the tin foil holder with the vanadium pentoxide.

Fourier-Transform Infrared Spectroscopy (FT-IR)

FT-IR was performed on a PerkinElmer Frontier FT-IR spectrometer between wavenumbers of 400 and 4000 cm^{-1} and 20 scans min^{-1}.

Digital Microscope and Optical Microscope

Optical microscope images were taken with Motic BA310 microscope. Digital microscope images were taken using a Dino-Lite Basic AM2111 hand-held USB microscope. Scale bars were added using ImageJ. Calibration was done by taking an image of a 30 cm ruler at comparable magnification and measuring the distance of 1 mm on ImageJ to set as the standard.

Mercury Intrusion

Mercury intrusion was performed on a Micromeritics Autopore IV. The samples were analysed between pressures of 0.1 to 60,000 psia with an equilibrium time of 10 s and a contact angle of 130^{o}.

Chapter 4

Investigation of Co-MOF-74-derived Catalysts in FTS

4.1 Introduction

MOF-derived catalysts for FTS have only been investigated within the last 5-6 years. In the case if catalysts derived directly from the pyrolysis of Co-MOF-74, only 2 studies have been found, which consist of those completed by Qiu et al and Zhang et al [66, 67]. More studies exist covering FTS using other Co-containing MOFs [64, 65, 72]. The espoused advantages of the direct pyrolysis of MOFs for FTS catalysis is the ability to achieve high metal loading with small Co nanoparticle size, enable complete reduction of the Co metal, and limit sintering and oxidation due to the spatial confinement caused by nanoencapsulation [73]. Conversely, conventional methods of catalyst preparation for FTS usually involve the cobalt precursor (often an oxide or nitrate) supported on an oxide of Si, Ti, Al or Zr. One shortcoming of such methods are undesirable metal-support interactions which can hamper reducibility and negatively affect catalyst performance in FTS [74]. Carbon-based supports, such as activated carbon, have been suggested as good catalyst supports as they have been reported to minimize the metal-support interaction [73]. However, traditional methods such as impregnation fall victim to the interdependence of metal loading and particle size, as larger nanoparticles will form when high metal loadings are used [59]. It is in this area that MOFs can excel as catalyst precursors due to the simple, one-step pyrolysis process that can achieve both high metal loading and small nanoparticle size, whilst being supported on a porous carbon structure. The typical preparation of such catalysts involves the controlled pyrolysis in an inert atmosphere at a temperature high enough for the MOF framework to decompose, leaving behind carbon from the organic ligand and previously co-ordinated metal ions [58].

4.1.1 Objectives

The purposes of the experiments contained in this chapter were related to method development and testing of the reactor system, to provide some confirmation of the Co-MOF-74 structure, give information about the properties of the catalyst once it has undergone decomposition and reduction,

and the performance of Co-MOF-74 in FTS when decomposed in a nitrogen atmosphere. The reaction tests in this chapter were limited by laboratory and health and safety constraints and were consequently run at a lower pressure compared to similar studies, which may give different results and findings compared to some literatures. Also, the results of this chapter act as a guide as to how the decomposition parameters can be changed to prepare a more desirable catalyst.

4.2 Experimental

The methods for the preparation of Co-MOF-74, reaction testing, and characterisation outlined in Chapter 3 were used in this chapter. One variation from the methods in Chapter 3 was that the reactor bed was packed in such a way that the thermocouple was estimated to be inside the reactor bed, instead of just above it, to gain and accurate reading of temperature. The list of experiments performed in this chapter, as well the conditions of reaction and pyrolysis, are shown in Table 4.1. The Co-MOF-74 underwent in-situ pyrolysis inside the reactor under different heating rates and dwell times, whilst the reaction was run at a variety of temperatures and pressures with comparable heating rate and dwell times.

Table 4.1 List of reaction experiments in Chapter 4

Sample	Pyrolysis Conditions				Reaction Conditions		
	Mass of Co-MOF-74 (g)	Heating Rate ($^{o}C\ min^{-1}$)	Dwell Time (h)	Temperature (^{o}C)	Pressure (Bar)	Temperature (^{o}C)	Space Velocity ($cm^{3}\ min^{-1}\ g_{Co}^{-1}$)
Run 1	1	2	1	500	7	260	752
Run 2	1	2	1	500	5	200	652
Run 3	1	8	1	500	5	200	652
Run 4	1	8	1	500	7.5	250	652
Run 5	1	8	5	500	7.5	250	652
Run 6	1	8	5	500	7.5	250	1629
Run 7	1	8	5	500	3.1	250	652
Run 8	0.5	8	1	500	7.5	200	534
Run 9	0.5	8	1	500	7.5	200	3493
Run 10	0.25	8	1	500	7.5	210	6860
Run 11	1	8	1	500	10	250	652
Run 12	1	8	1	500	10	220	652
Run 13	1	8	1	500	10	200	652

4.3 Characterisation

4.3.1 Co-MOF-74 Characterisation

The Co-MOF-74 was analysed using XRD, TGA, and FT-IR, CHNS, as well as some microscope images to confirm the formation of the Co-MOF-74 crystal. Often in studies involving Co-MOF-74, removing all solvent residue is important as the crystal structure is often directly involved in the research, therefore clearing the pore network can be very important. In this case, the Co-MOF74 will act as a sacrificial template, where any remaining solvent and impurities in the MOF will most likely be vaporised in the pyrolysis process.

XRD

Figure 4.1 shows the XRD spectra for a Co-MOF-74 sample after washing with THF and before pyrolysis. According to literature sources, the strongest diffraction peaks occur at about 2θ = 6.5° and 2θ = 11.5° [62]. These values correspond to the lattice plane (2-10) and (300), and both the 6.5° and 11.5° peaks are observed in the spectrum in Figure 4.1. Other weaker peaks observed in both the literature and Figure 4.1 are those at 2θ = 26°, 2θ = 31° and 2θ = 41. The intensity of all the major peaks are consistent with spectra in the literature [62].

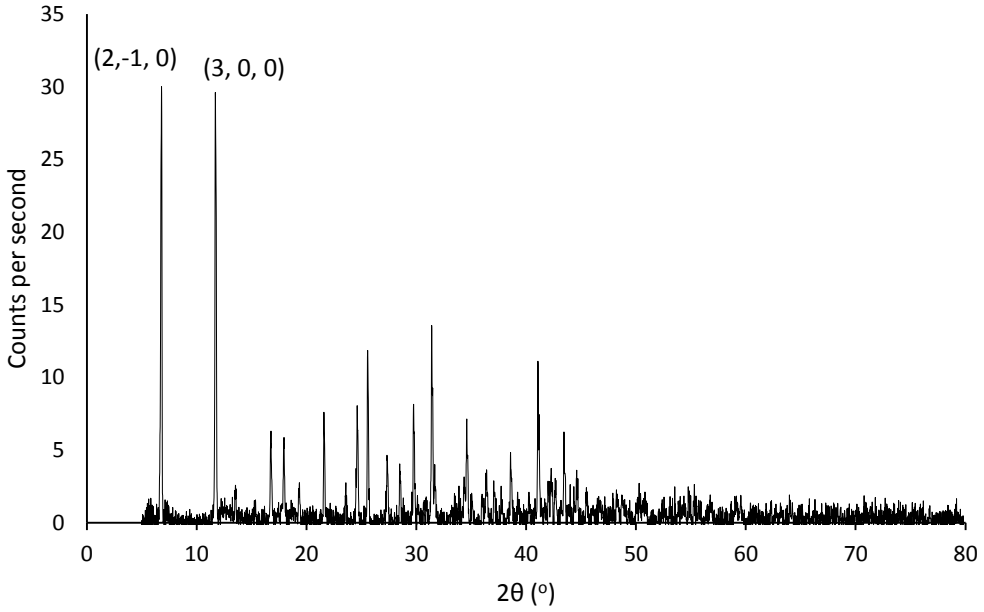

Figure 4.1 XRD spectrum of Co-MOF-74

FT-IR

Fourier Transform Infrared Spectroscopy (FT-IR) was used to assess the bonds present in the Co-MOF-74 sample. The wavenumber at which peaks occur in a previous study by Jiang et al are given in Table 4.2 [75]. Although there are slight differences in transmission from previous literature, the spectra obtained from Co-MOF-74 in Figure 4.2 compares well with data from literature with respect to the wavenumber at which transmission loss occurs. The broad band at wavenumber 3255 cm^{-1} due to the stretching vibration of hydroxyl or water, which indicates solvent water adsorbed on the surface of the Co-MOF-74 or within the pore structure. The peak at approximately 1556 cm^{-1} can be attributed to C=O bonds. The small peak around 1460 cm^{-1} and larger one about 1412 cm^{-1} represent the C=C bonds of the benzene ring. This shows that the organic ligand is present, which contains the benzene ring.

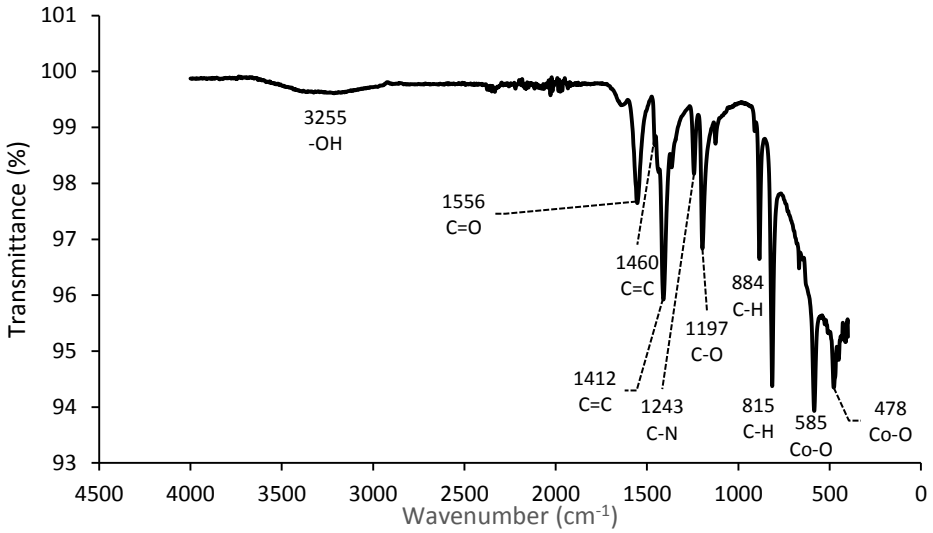

Figure 4.2 FT-IR spectra of Co-MOF-74

The peak at 1243 cm^{-1} is thought to represent vibration upon absorption of C-N, however, it is not clear where such bonds are located within the MOF. This peak was also noted by Jiang et al, who suggested it originated from DMF absorbed on the surface or in the channel, however DMF was not used in this work [62]. Another sharp peak at 1197 cm^{-1} is thought to represent the absorption of the C-O bond. The peaks at 884 cm^{-1} and 815 cm^{-1} are attributed to the C-H bending vibration of the inner and outer plane of the benzene ring. The smaller, but noticeable, peaks at 585 cm^{-1} and 478 cm^{-1} are thought to be the result of Co^{2+}-O and Co^{3+}-O bonds. This indicates the presence of the Co ion in the framework

to which the organic ligands are bonded. The FT-IR spectra obtained in this work compares well with that of Jiang et al and further suggests the correct Co-MOF-74 has been synthesized [75].

Table 4.2 Positions and assignments of FT-IR peaks (adapted from Jiang et al [75])

Bond	**Wavenumber (cm^{-1})**
-OH	3423
C=O	1557
C=C	1453, 1410
C-N	1244
C-O	1196
C-H	886, 817
(Co^{2+}-O) or (Co^{3+}-)	585, 481

TGA

It is evident from the curve in Figure 4.3 that two different mass losses occur. The first mass loss occurs below 200 ^{o}C, with a mass loss of about 30% of the original value of the sample. This first mass loss can be attributed to the removal of physically and chemically bonded water and THF solvent. The second mass loss is due to the decomposition of the MOF framework. Part of the organic ligand decomposes and evaporates into the gas phase, whereas some of it becomes carbonized in the framework. In this stage, the formation of cobalt nanoparticles is thought to occur, either on or within the carbon matrix [58].

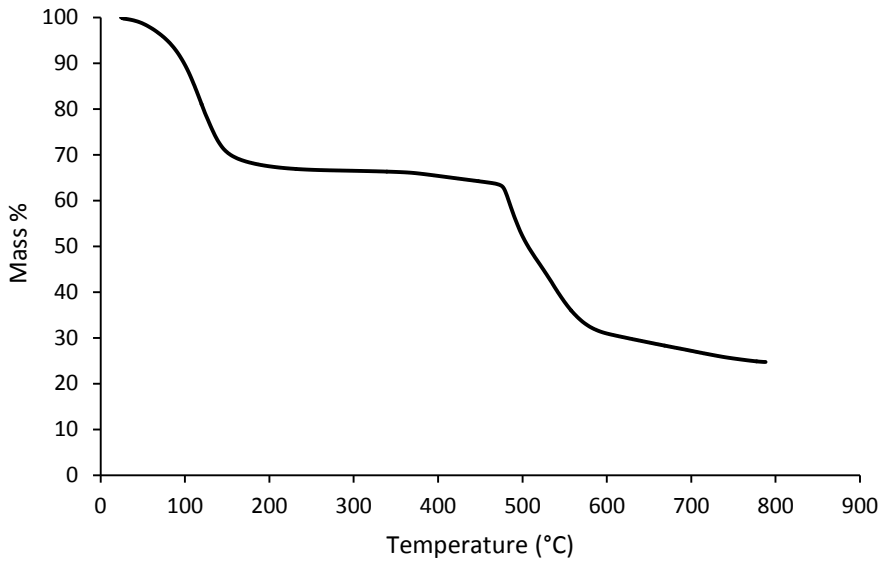

Figure 4.3 TGA analysis of Co-MOF-74 (Heating rate of 10 ^{o} min^{-1} to 800 ^{o}C in pure N_2)

Optical and SEM Microscope Images

Rod shaped crystals can be observed from the image in Figure 4.4. This shape for the Co-MOF-74 crystal corresponds to those found in study by Qiu et al [66]. The similar crystal geometry indicates that Co-MOF-74 has been synthesized. Although it is noticeable that significant agglomeration can occur, this is not likely to affect performance in catalytic reactions, as the MOF undergoes pyrolysis before the reaction. However, SEM images in Figure 4.5 of another batch of crystals prepared in the same way show that the morphology is slightly different, showing larger crystals.

Figure 4.4 Microscope image of Co-MOF-74 crystals

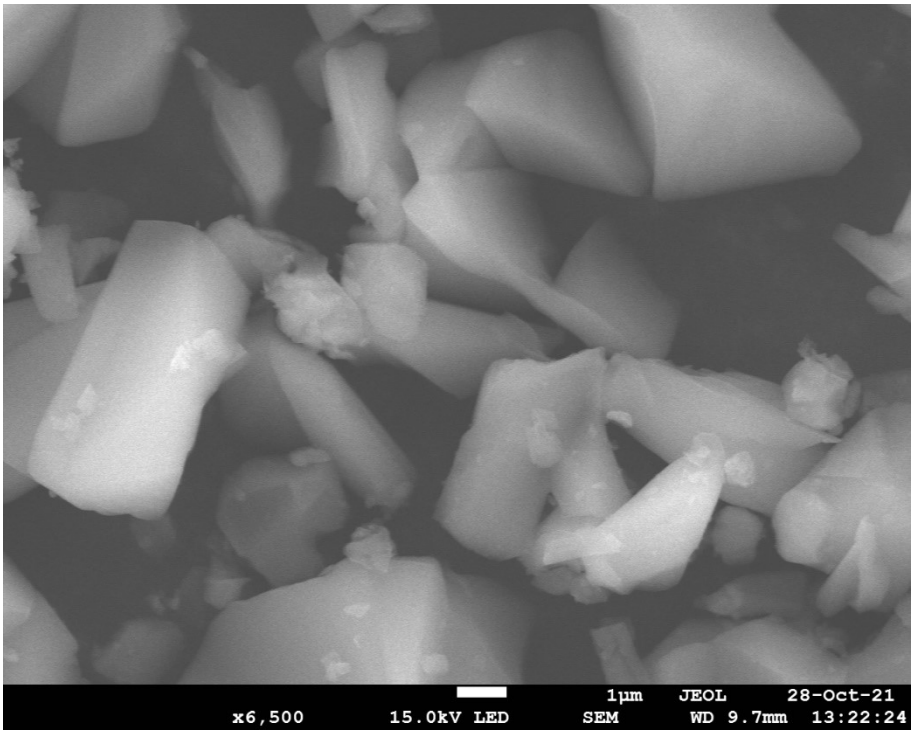

Figure 4.5 SEM image of Co-MOF-74 crystals

4.3.2 Catalyst Characterisation

Powder XRD, N_2 adsorption, SEM-EDX and CHNS were used to characterise the catalyst. The information obtained from XRD can provide information about the size and crystalline phase of the nanoparticles present. N_2 adsorption and SEM and provide structural information about the catalyst, whilst CHNS and EDX can provide information about the elemental composition. Prepared catalysts underwent pyrolysis in the reactor system and were removed for characterisation without starting a reaction. The spent catalyst underwent pyrolysis in the reactor system and was removed after the reaction experiments.

XRD

Figure 4.6 shows the XRD spectra of the prepared MOF-derived catalyst after common pyrolysis conditions used in this chapter. The Co-MOF-74 sample underwent pyrolysis at 500 ^{o}C for 1 hour at a heating rate of 8 ^{o}C min^{-1}. A broad peak with very low intensity is noticeable at 2θ = 44.3 ^{o}. Pei et al also recognised a very similar peak after pyrolysis of Co-MOF-70 at 600 ^{o}C for 8 hours at a heating rate of 5 ^{o}C min^{-1} in He [72]. In this case, the peak was assigned to the FCC phase of metallic Co. In the study by Pei et al, the Scherrer equation was used to calculate the grain size as 14.5 nm whilst the particle diameter measured from TEM was 12.3 nm. Qiu et al observed a sharper peak at 2θ = 44.3^{o,} as well as two more peaks located at 2θ = 51 ^{o} and 77 ^{o}, after pyrolysis of Co-MOF-74 at 550 ^{o}C for 2 hours at a heating rate of 5 ^{o}C min^{1} in Ar [66]. All peaks were considered obvious signs of the lattice planes of the FCC crystal phase of Co. Nanoparticle sizes of 8 nm were estimated using TEM in their study.

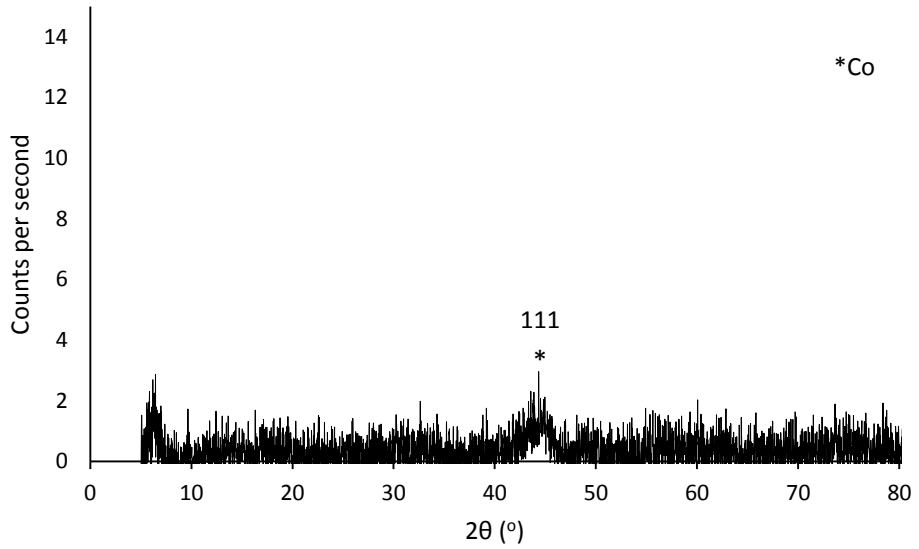

Figure 4.6 XRD spectrum of prepared catalyst after pyrolysis of Co-MOF-74 in the reactor (without reaction) (temp. = 500°C, dwell = 1 h, ramp = 8 °C min^{-1})

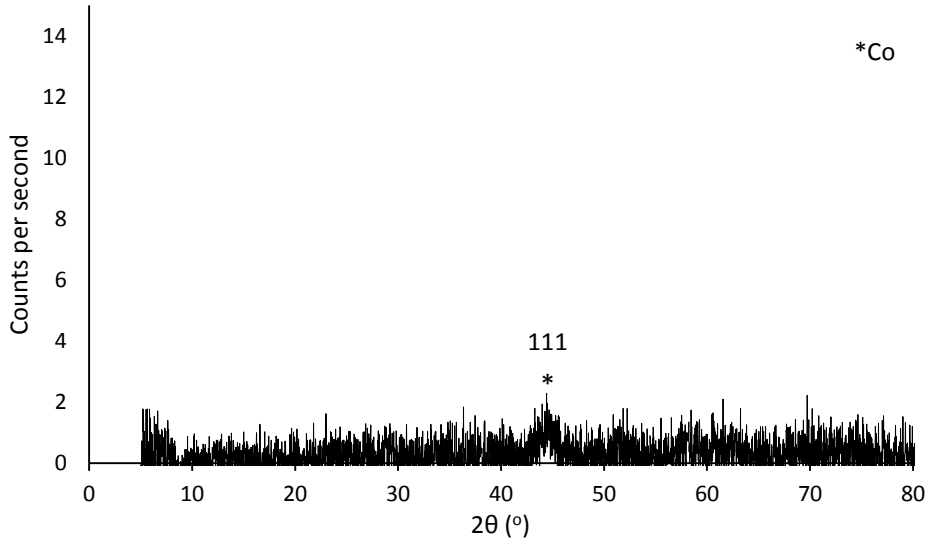

Figure 4.7 XRD spectrum of the spent catalyst after reaction (Co-MOF-74 Pyrolysis conditions: temp. = 500°C, dwell = 1 h, ramp = 8 °C min^{-1})

Zhang et al also heated Co-MOF-74 to 500 °C for 1 hour in He [67]. The powder XRD spectrum obtained showed traces of Co in the original Co-MOF-74 precursor and signals of CoO, including a CoO peak at 2θ = 42.5 °. Metallic Co peaks were observed at 52.2 ° and 59.8 °. This indicates incomplete decomposition of the MOF during pyrolysis and only partial reduction of the Co with some being oxidised to CoO. They used the Scherrer equation to estimate the grain sizes of the Co nanoparticles to be 4.1 nm. After FTS reaction, any trace of the Co-MOF-74 framework has disappeared, but the intensity of Co metal and CoO peaks increases, with the metallic Co nanoparticle size estimated to be 18.8 nm. In the case of prepared and spent catalyst spectra shown in this work in Figure 4.6 and Figure 4.7, the broad, low-intensity peak at 2θ = 44.3 ° is likely due to metallic Co of the 111 face-centred cubic (FCC) plane, which is very comparable to that shown by Pei et al [72]. Metallic Co formation usually occurs with another two FCC phase peaks that are present at 2θ values of approximately 2θ = 51 ° and 76 ° representing the 200 and 220 lattice planes [76]. However, only the most intense peak at 2θ = 44.3 ° is observable, most likely due to the small size of the cobalt nanoparticles. This peak is unlikely to be that of Co_3O_4, as the most intense peak for the FCC arrangement of Co_3O_4 is not present at around 2θ = 44.3, instead being present at approximately 2θ = 36.6 ° [77]. The FCC arrangement of CoO does have the largest peak around 2θ = 42.39 °, however this should show a noticeable difference in 2θ value from the metallic Co peak at 2θ = 44.3 [78]. The HCP arrangement of CoO has its strongest peak around 2θ = 36 °, therefore this can also be ruled out [79]. Considering the previous literature examples, it is reasonable to consider the sole peaks shown in the spectra in Figure 4.6 and Figure 4.7 belong to the 111 plane of the FCC metallic Co phase. Also, as no other obvious peaks seem to be present, it is likely that Co has been reduced mostly to the FCC phase with no noticeable presence of cobalt oxide. Using the Scherrer equation, the Co nanoparticle grain size for the prepared catalyst from XRD spectrum in Figure 4.6 is estimated to be 7.5 nm. The spent catalyst after FTS had a Co nanoparticle grain size estimated at 8.5 nm from the XRD spectrum in Figure 4.7. This is in a similar range to the aforementioned studies, which estimate grain sizes between 4.1 to 14.5 nm for prepared catalyst using either the Scherrer equation or TEM. Also, based on the XRD spectra, there seem to be no obvious signs of oxidation or sintering during reaction.

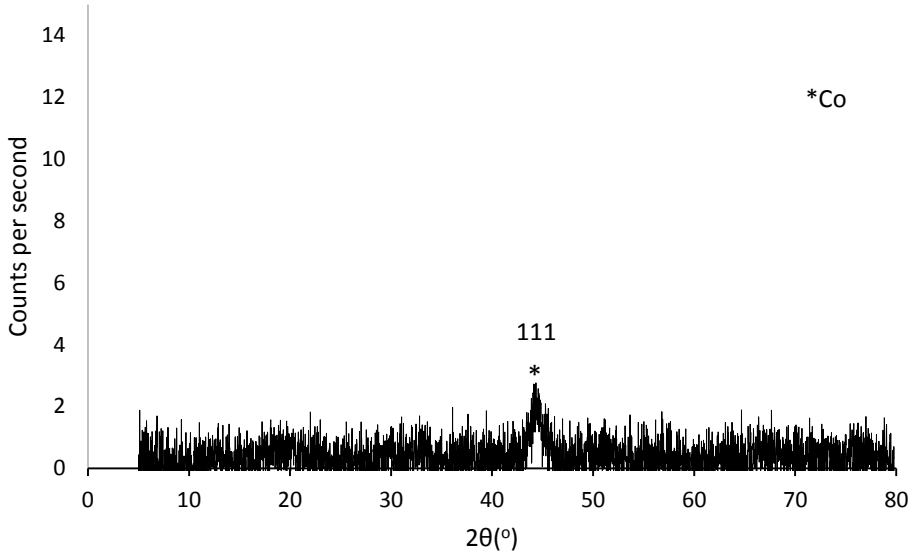

Figure 4.8 XRD spectrum of spent catalyst (Co-MOF-74 Pyrolysis conditions: temp. = 500°C, dwell = 5 h, ramp = 8 °C min^{-1})

Figure 4.8 shows the spent catalyst after reaction, after the original precursor Co-MOF-74 underwent pyrolysis for 5 h. The metallic Co peak is present at 2θ = 44.3 ° and using the Scherrer equation the grain size was estimated to be 8.9 nm, which is similar to that observed in the catalysts after 1 hour of pyrolysis and in the literature [72]. Based on the estimation of nanoparticle grain size using the Scherrer equation, no significant increase was observed indicating the extra dwell time did not cause sintering.

N_2 Adsorption

N_2 adsorption analysis was performed on the spent samples after reaction for the catalysts that underwent pyrolysis at 500 °C, with a ramp of 8 °C min^{-1} and dwell times of 1 and 5 h. BET surface areas, as well as BHJ pore volume and pore diameter, can be viewed in Table 4.3. The original Co-MOF-74 precursor is also included.

Table 4.3 N_2 adsorption analysis results (T = temperature (^oC), R = heating ramp ($^oC\ min^{-1}$), D = dwell time (h))

Sample	BET Surface Area ($m^2\ g^{-1}$)	Pore Volume ($cm^3\ g^{-1}$)	Average Pore Diameter (nm)
Co-MOF-74	60.2	-	-
T500 R8 D5 spent	262.4	0.50	4.42
T500 R8 D1 spent	194.6	0.27	3.87

Figure 4.9 shows the adsorption isotherm for the spent catalyst that underwent pyrolysis at a temperature of 500 ^oC, with a heating rate of 8 $^oC\ min^{-1}$ and dwell time of 5 h. The isotherm exhibits something approaching a type 4 isotherm, indicating the presence of a mesoporous material with pore diameters between 2-50 nm [80]. The increase in N_2 uptake at higher relative pressure indicates capillary condensation in the mesopores or the presence macropores [80, 81]. The type H3 hysteresis loop observed is also observed in similar Co-MOF-74 derived catalysts in literature and suggests a large amount of mesoporous cavities with slit-shaped pores [66, 82]. The BET surface area was given as 262.4 $m^2\ g^{-1}$, confirming the porous nature of the carbon after decomposition of the Co-MOF-74 and showing that it retains a porous structure after reaction. The BET surface area measurement is also in a comparable range to those observed in literature, with a values of 341 $m^2\ g^{-1}$ observed for a similar pyrolysis experiments involving Co-MOF-74 [66]. Also, a BJH pore volume of 0.5 $cm^{-3}\ g^{-1}$ and an average pore diameter of 4.42 nm was obtained for spent catalyst after an original pyrolysis dwell time of 5 hours. An average pore diameter of 7 nm and pore volume of 0.58 $cm^3\ g^{-1}$ was observed in a similar pyrolysis of Co-MOF-70 [66]. This is in a comparable range to the spent catalysts in this work, with a slightly larger average pore diameter. Figure 4.10 shows the isotherm of another spent catalyst, where the original Co-MOF-74 underwent pyrolysis with a dwell time of 1 h. The isotherm is a similar type 4 isotherm to that in Figure 4.9, which slightly less N_2 uptake in the higher relative pressure range, suggesting decreased capillary condensation due to fewer mesopores or the absence of macropores. The sample has a lower BET surface area of 194.6 $m^2\ g^{-1}$, slightly lower than the T500 R8 D5 spent sample, whilst having a comparable average pore diameter of 3.87 nm but lower pore volume of 0.272 $cm^3\ g^{-1}$. This may suggest that a longer pyrolysis time can alter the physical properties of the catalyst. Luo observed that increasing the pyrolysis time of a ZIF-67 MOF from 4 to 8 to 10 to 12 h at 500 ^oC

decreased the elemental composition of carbon, hydrogen and nitrogen, suggesting a gradual decomposition of organic ligands to the condensed carbonaceous substance, along with the release of gases [64]. However, there wasn't the same correlation in BET surface area, pore volume or average pore diameter. In this case, without further study, it is difficult to conclude that the dwell time significantly affected the physical property of the catalyst, especially considering the similar range of values, which could be a result of natural variation of the data.

Also noticeable is the very low surface area of the Co-MOF-74, which recorded a BET surface area of only 60.2 $m^2 g^{-1}$ after degassing at 160 ^oC overnight, as opposed to 130 ^oC for all other samples. After degassing at 130 ^oC, the surface area was even lower, at 30.3 $m^2 g^{-1}$. Normally, MOFs exhibit a very large surface area, and a value of 1025 $m^2 g^{-1}$ has been recorded in the literature [66]. However, other researchers had difficulty obtaining this value, with a value of 107 $m^2 g^{-1}$ recorded for one study involving Co-MOF-74 for FTS [67]. Also, a value of 0.2 $m^2 g^{-1}$ has been recorded for Co-MOF-71 in a FTS study [72]. MOFs are very sensitive, and great care needs to be taken in order to obtain the expected surface area. The fact that surface area increases with degassing temperature indicates there may be some solvent or water trapped within the pore network of the MOF. However, as the Co-MOF-74 itself is not involved in the reaction as it undergoes pyrolysis, and considering confirmation of the Co-MOF-74 in XRD and the presence of the expected bonds in FT-IR, obtaining the expected surface area was not considered important.

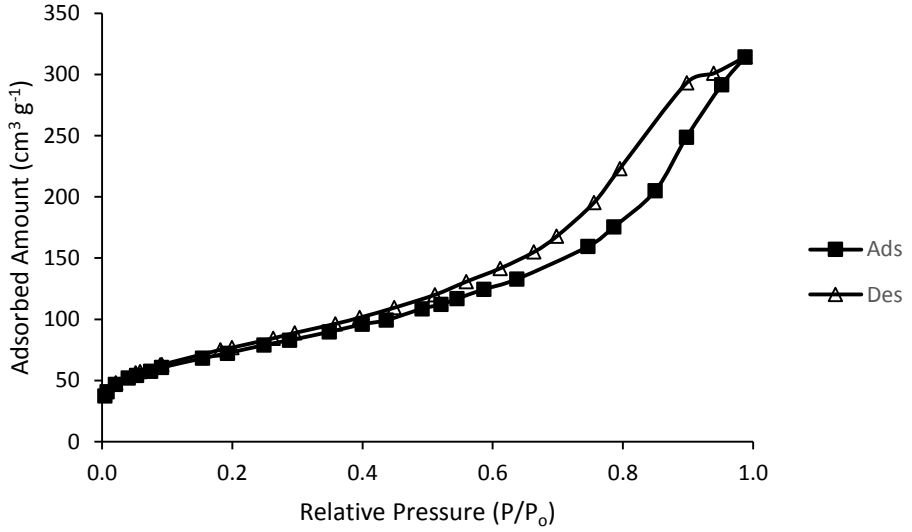

Figure 4.9 N_2 adsorption isotherm of the spent catalyst formed from the pyrolysis of Co-MOF-74 at a temperature of 500 ^oC, heating rate of 8 $^oC\ min^{-1}$ and a dwell time of 5 h

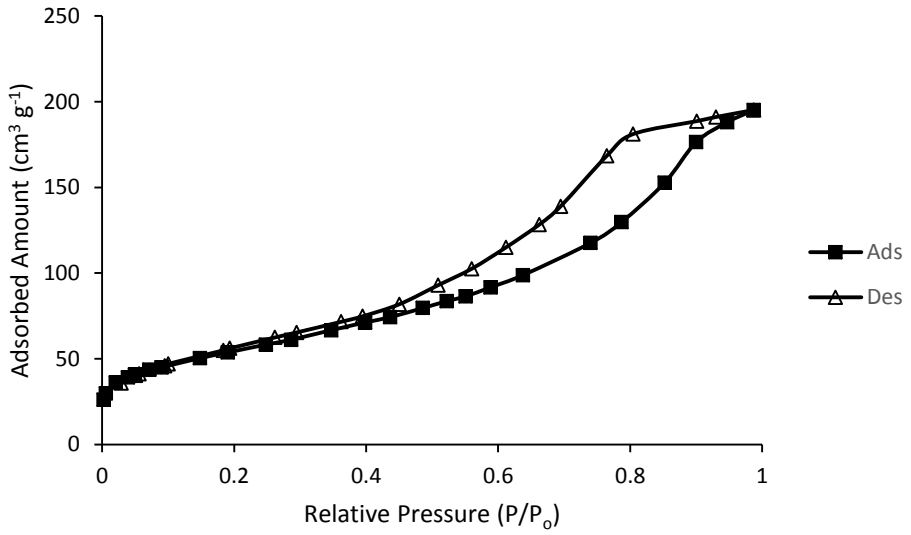

Figure 4.10 N_2 adsorption isotherm of the spent catalyst formed form the pyrolysis of Co-MOF-74 at a temperature of 500^{o}C, heating rate of 8 ^{o}C min^{-1} and a dwell time of 1 h

CHNS

Table 4.4 shows the CHNS analysis results for the spent catalyst after pyrolysis at a temperature of 500 ^{o}C, heating rate of 8 ^{o}C min^{-1} and dwell time of 5 h, showing the weight percentage of C, H, N and S. As expected, the amount of nitrogen and sulfur was 0 %. As there was no nitrogen or sulfur in the Co-MOF-74 precursor or the FTS reactants. The results confirm that the carbon from the Co-MOF-74 ligand is still present in the final catalyst. The result shows that some of the hydrogen is retained. One potential source is the residue of FTS products. It is possible that some O may remain in the sample, either through oxidation during decomposition or from adsorbed O molecules on the surface after removal from the reactor.

Table 4.4 Elemental CHNS analysis for the spent catalyst after pyrolysis at a temperature of 500 ^{o}C, heating rate of 8 ^{o}C min^{-1} and dwell time of 5 h.

Sample	**C (wt%)**	**H (wt%)**
T500 R8 D5	35.1	0.65

SEM-EDX

Figure 4.11 shows and SEM image of the spent Co-MOF-74-derived catalyst. The catalyst exhibits a rectangular morphology. A similar image with the EDX mapping in Figure 4.12 shows the elemental composition of the catalyst, which composes of carbon, oxygen and cobalt. Large amounts of carbon and cobalt are expected, oxygen is also shown, which has most likely been adsorbed onto the surface after removal from the reactor. It is possible that oxygen in the organic ligand from the original Co-MOF-74 caused a level of oxidation, but it cannot be detected from the XRD spectra.

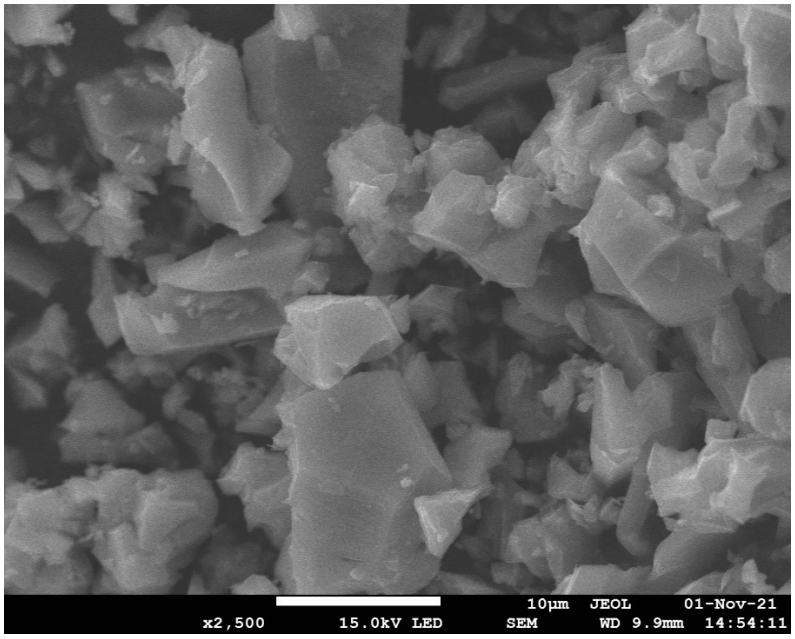

Figure 4.11 SEM image of spent catalyst after pyrolysis at a temperature of 500 ^{o}C, heating rate of 8 ^{o}C min^{-1} and dwell time of 1 h.

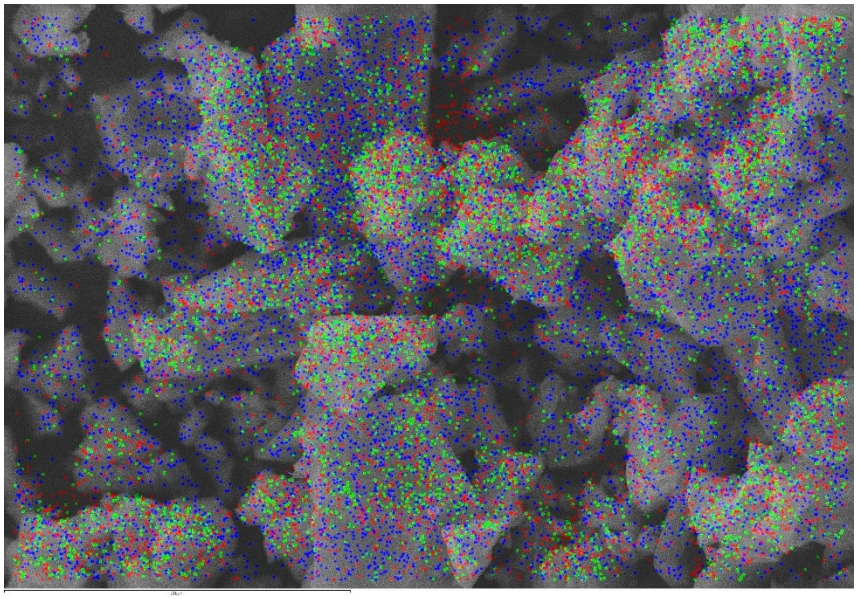

Figure 4.12 SEM-EDX image of spent catalyst after pyrolysis at a temperature of 500 ^{o}C, heating rate of 8 ^{o}C min^{-1} and dwell time of 1 h (C = red, O = green, Co = blue)

4.4 Reaction Results and Discussion

Table 4.5 shows the FT reaction results and the corresponding reduction conditions for the experiments previously listed in Table 4.1. From this data it is possible to investigate the performance of the Co-MOF-74 derived catalyst in FTS, as well as compare the performance at different reaction conditions and MOF decomposition conditions.

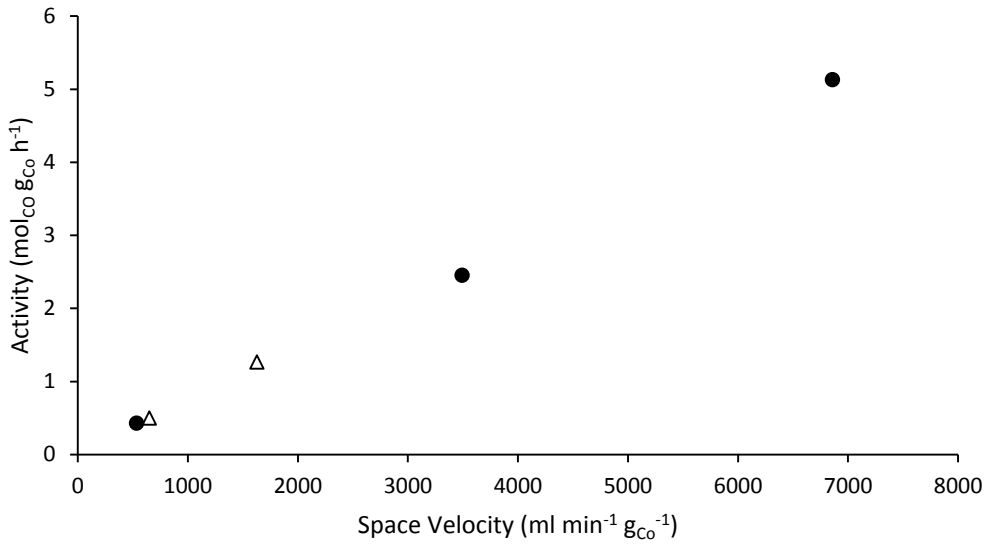

Figure 4.13 The effect of space velocity on activity. ● : T = 200 °C, P = 7.5 bar, pyrolysis dwell time = 1 h, pyrolysis ramp = 8 °C min^{-1}. △ : T = 250 °C, P = 7.5 bar, pyrolysis dwell time = 5 h, pyrolysis ramp = 8 °C min^{-1}

Table 4.5 Chapter 4 FTS reaction results

Experiment	**Run 1**	**Run 2**	**Run 3**	**Run 4**	**Run 5**	**Run 6**	**Run 7**	**Run 8**	**Run 9**	**Run 10**	**Run 11**	**Run 12**	**Run 13**
Pyrolysis													
Mass of Co-MOF-74 (g)	1	1	1	1	1	1	1	0.5	0.5	0.25	1	1	1
Heating Rate ($^{o}C\ min^{-1}$)	2	2	8	8	8	8	8	8	8	8	8	8	8
Dwell Time (h)	1	1	1	1	5	5	5	1	1	1	1	1	1
Temperature (^{o}C)	500	500	500	500	500	500	500	500	500	500	500	500	500
Reaction													
Pressure (Bar)	7	5	5	7.5	7.5	7.5	3.1	7.5	7.5	7.5	10	10	10
Temperature (^{o}C)	260	200	200	250	250	250	250	200	200	210	250	220	200
Space velocity ($cm^3\ min^{-1}\ g_{Co}^{-1}$)	752	652	652	652	652	1629	652	534	3493	6860	652	652	652
X_{CO}	0.97	0.99	0.98	0.99	0.92	0.93	0.94	0.96	0.84	0.90	1	0.73	0.76
Activity ($mol_{CO}\ g_{Co}^{-1}\ h^{-1}$)	0.610	0.535	0.532	0.540	0.498	1.264	0.511	0.429	2.454	5.131	0.542	0.395	0.412
C_{2+} Selectivity (%)	9.6	0.0	0.0	9.3	6.2	2.2	1.6	16.2	0.0	12.3	15.3	7.6	14.3
CH_4 Selectivity (%)	61.6	71.1	73.7	63.4	67.0	69.3	67.3	61.6	73.7	62.4	60.9	69.1	64.2
CO_2 Selectivity (%)	28.8	32.0	33.1	27.3	26.7	28.5	31.1	22.2	29.2	25.4	23.7	23.2	21.5

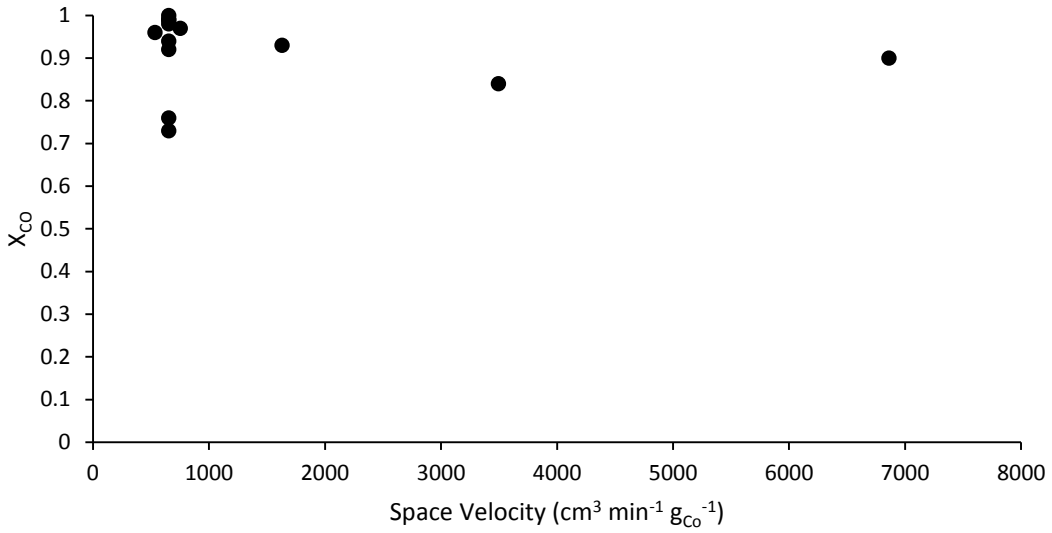

Figure 4.14 Effect of space velocity on conversion for all reaction results in Table 4.5.

Based on the reaction result data in Table 4.5, a very striking feature of the catalyst is the extremely high conversion. Most conversion values are consistently in the region of around 0.9, with a range of values between 0.73 and 1, which can be seen in Figure 4.14. Also noticeable, is that conversion is maintained in the region of 0.9, despite increasing space velocity to almost 6860 cm^3 min^{-1} g_{Co}^{-1}. Therefore, as space velocity increases, the activity of the catalyst will increase in a linear fashion, which is demonstrated in Figure 4.13. This trend seems to occur in both data sets in Figure 4.13, despite there being a difference in reactor temperature of 50 ^oC, indicating little or no effect of temperature on the conversion. This is backed up by the data in Table 4.5, where by comparing the Run 4 and Run 8 reaction results, it can be seen that there is little difference in conversion despite a temperature difference between 200 and 250 ^oC, whilst other conditions remain very similar. The only instance that there is a notable change in conversion is between the Run 11 to Run 13 reactions in Table 4.5, where total conversion was achieved at 250 ^oC, whilst conversion values of 0.76 and 0.73 were achieved for temperatures of 200 and 220 ^oC, respectively, with all other conditions remaining identical.

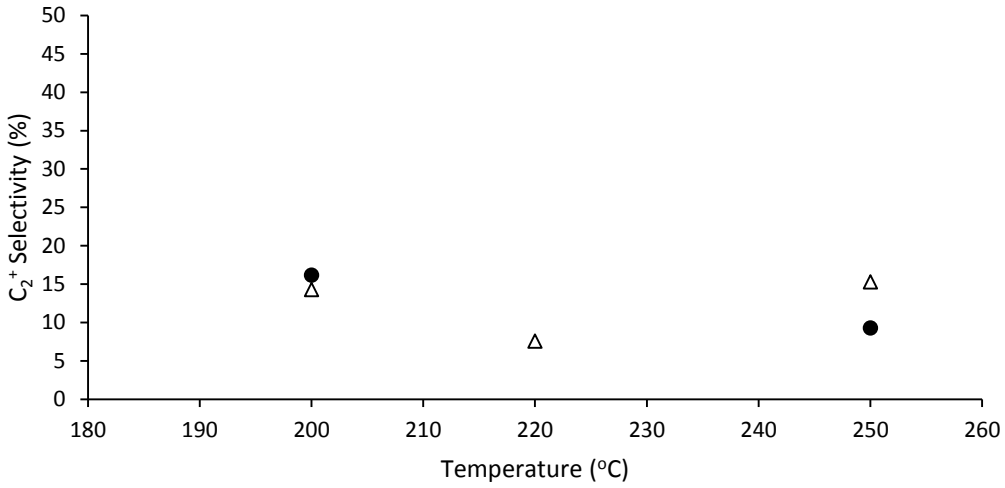

Figure 4.15 Effect of temperature on C_{2+} Selectivity. ● : P = 7.5 bar, space velocity = 652 cm^3 min^{-1} g^{-1}_{Co}, pyrolysis dwell time = 1 h, pyrolysis ramp = 8 °C min^{-1}. △ : P = 10 bar, space velocity = 652 cm^3 min^{-1} g^{-1}_{Co}, pyrolysis dwell time = 1 h, pyrolysis ramp = 8 °C min^{-1}

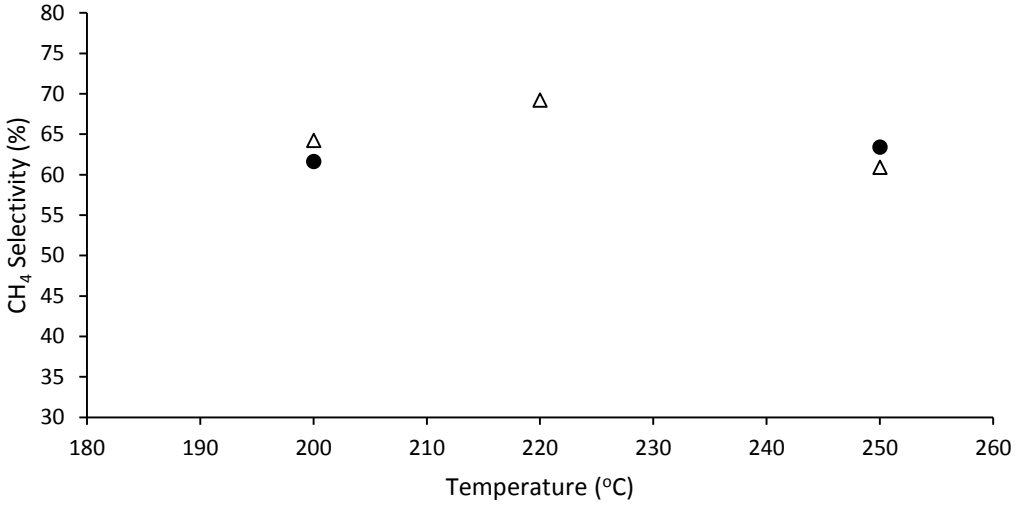

Figure 4.16 Effect of temperature on CH_4 selectivity. ● : P = 7.5 bar, space velocity = 652 cm^3 min^{-1} g^{-1}_{Co}, pyrolysis dwell time = 1 h, pyrolysis ramp = 8 °C min^{-1}. △ : P = 10 bar, space velocity = 652 cm^3 min^{-1} g^{-1}_{Co}, pyrolysis dwell time = 1 h, pyrolysis ramp = 8 °C min^{-1}

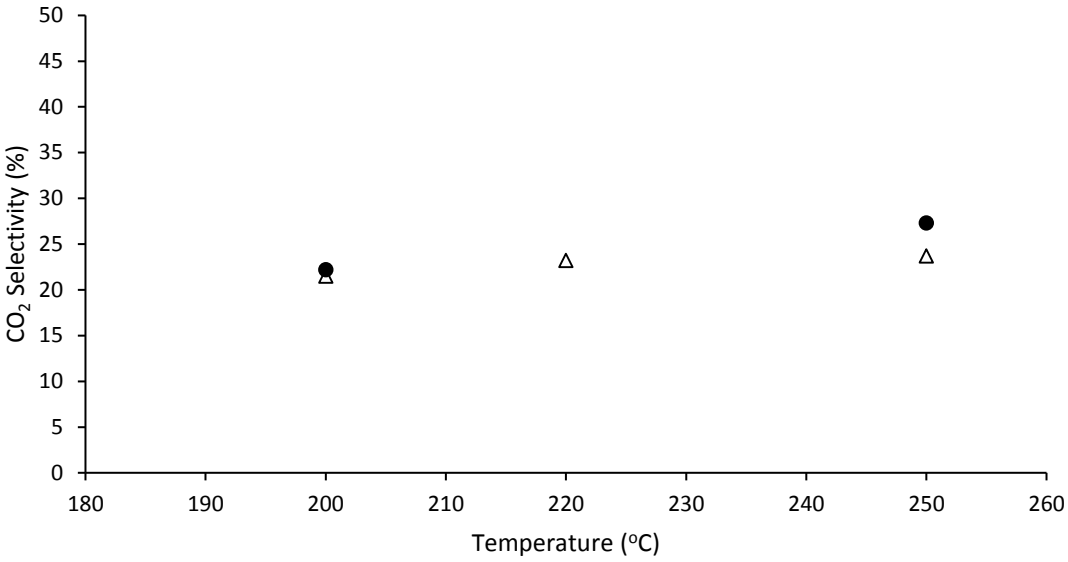

Figure 4.17 Effect of temperature on CO_2 selectivity. ● : P = 7.5 bar, space velocity = 652 cm^3 min^{-1} $g^{-1}_{Co,}$ pyrolysis dwell time = 1 h, pyrolysis ramp = 8 ^oC min^{-1}. △ : P = 10 bar, space velocity = 652 cm^3 min^{-1} g^{-1}_{Co}, pyrolysis dwell time = 1 h, pyrolysis ramp = 8 ^oC min^{-1}

Figure 4.15, Figure 4.16 and Figure 4.17 show the effects of temperature across two different pressures on the C_{2+} selectivity, CH_4 selectivity and CO_2, respectively. It is very clear from Figure 4.15 that the C_{2+} selectivity is extremely low for Fischer-Tropsch reactions, whilst increasing the temperature had a very negligible effect. From Table 4.5, the range of C_{2+} selectivity across all reaction results ranges from 0 to 15.3 %. Conversely, Figure 4.16 shows the CH_4 selectivity is consistently very high, with almost no effect shown with changing temperature. This is also shown in Table 4.5, with methane selectivity in the range of 60.9 to 73.7 % across all reaction results. Figure 4.17 also shows CO_2 selectivity levels around 20 % for the two data sets, with no significant variation with increasing temperature. Table 4.5 shows a range of values between 23.1 and 33.5 %. This is unusual, as high water-gas shift activity is not expected when using a Co catalyst in FT reactions [83].

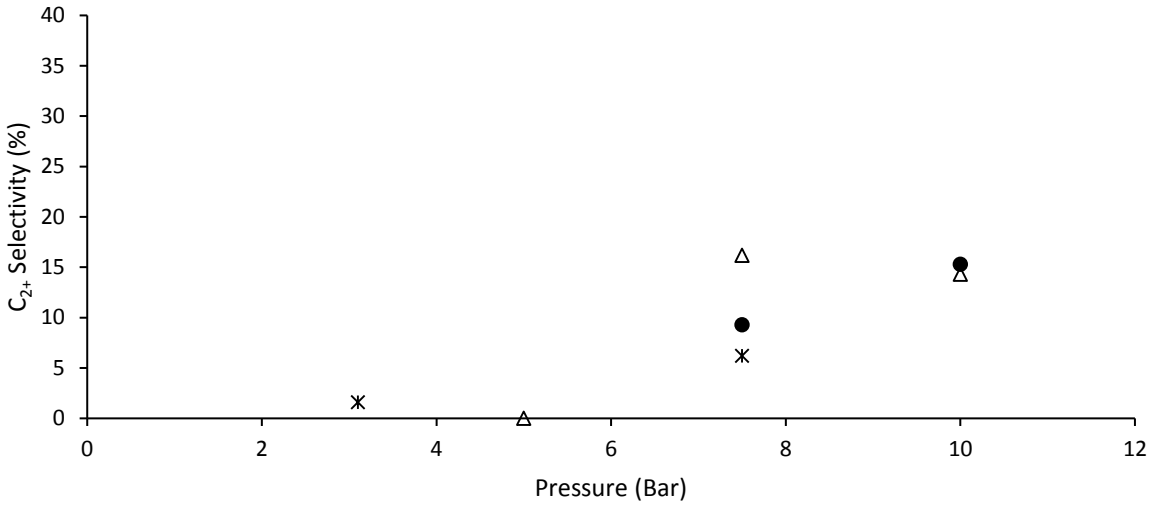

Figure 4.18 Effect of pressure on C_{2+} selectivity. ● : T = 250 °C, space velocity = 652 cm^3 min^{-1} $g^{-1}_{Co,}$ pyrolysis dwell time = 1 h, pyrolysis ramp = 8 °C min^{-1}. △ : T = 200 °C, space velocity = 534 - 652 cm^3 min^{-1} g^{-1}_{Co}, pyrolysis dwell time = 1 h, pyrolysis ramp = 8 °C min^{-1}. ✳ : T = 250 °C, space velocity = 652 cm^3 min^{-1} $g^{-1}_{Co,}$ pyrolysis dwell time = 5 h, pyrolysis ramp = 8 °C min^{-1}

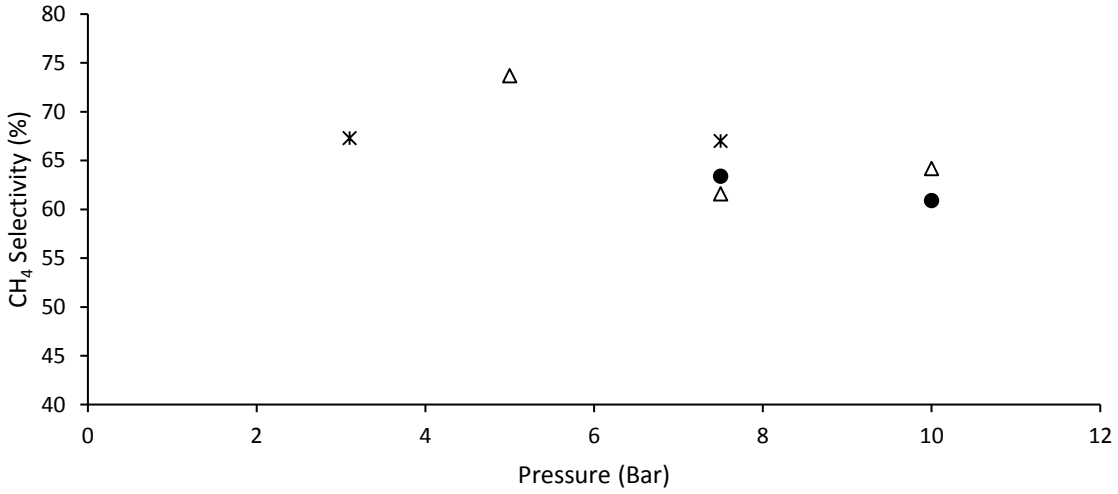

Figure 4.19 Effect of pressure on CH_4 selectivity. ● : T = 250 °C, space velocity = 652 cm^3 min^{-1} $g^{-1}_{Co,}$ pyrolysis dwell time = 1 h, pyrolysis ramp = 8 °C min^{-1}. △ : T = 200 °C, space velocity = 534 - 652 cm^3 min^{-1} g^{-1}_{Co}, pyrolysis dwell time = 1 h, pyrolysis ramp = 8 °C min^{-1}. ✳ : T = 250 °C, space velocity = 652 cm^3 min^{-1} $g^{-1}_{Co,}$ pyrolysis dwell time = 5 h, pyrolysis ramp = 8 °C min^{-1}

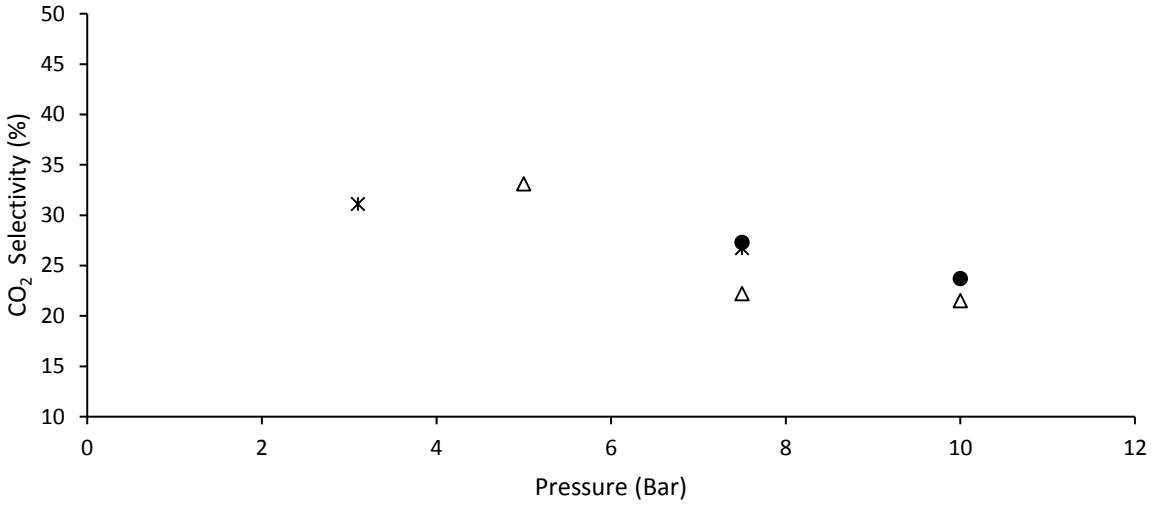

Figure 4.20 Effect of pressure on CO_2 selectivity. ● : T = 250 °C, space velocity = 652 cm^3 min^{-1} $g^{-1}_{Co,}$ pyrolysis dwell time = 1 h, pyrolysis ramp = 8 °C min^{-1}. △ : T = 200 °C, space velocity = 534 - 652 cm^3 min^{-1} g^{-1}_{Co}, pyrolysis dwell time = 1 h, pyrolysis ramp = 8 °C min^{-1}. ✱ : T = 250 °C, space velocity = 652 cm^3 min^{-1} $g^{-1}_{Co,}$ pyrolysis dwell time = 5 h, pyrolysis ramp = 8 °C min^{-1}

Figure 4.18, Figure 4.19 and Figure 4.20 show the effect of pressure on the selectivity of the catalyst. Figure 4.18 indicates a very mild C_{2+} selectivity increase with increasing pressure. Reactions run at a temperatures of 200 °C with space velocity between 534 – 652 cm^3 min^{-1} g^{-1}_{Co} and pyrolysis dwell time and ramp of 1 h and 8 °C min^{-1}, denoted by △, show almost 0 % selectivity to C_{2+} at 5 bar, whereas this rises to 16.2 % at 7.5 bar under similar conditions. However, increasing the pressure to 10 bar did not show any greater selectivity, with a similar selectivity value of 14.3 % achieved. Reactions run at 250 °C with a space velocity of 652 cm^3 min^{-1} g^{-1}_{Co} with dwell time of 1 h and a ramp of 8 °C min^{-1}, denoted as ● in Figure 4.18, also showed a jump in selectivity from 6.2 to 14.3 % when the pressure increased from 7.5 to 10 bar. Reactions run at 250 °C a with space velocity of 652 cm^3 min^{-1} g^{-1}_{Co} with dwell times of 5 h and a ramp of 8 °C min^{-1}, denoted as ✱, showed a jump in selectivity from 1.6 to 3.2 %, when running at pressures of 3.1 and 7.5 bar. Figure 4.19 displays the same data sets and their CH_4 selectivity with changing pressure. Naturally, the values here are somewhat analogous to the C_{2+} selectivity, and generally show a very mild decrease in selectivity towards CH_4 with increasing pressure in the range of

73.7 to 60.9 %. A similar case is present in Figure 4.20 with regards to CO_2 selectivity, with a slight decrease in selectivity with increasing pressure, in the range of 33.1 to 21.5 %. It is important to point out that the variation of selectivity with pressure and temperature is very minor, and despite the change in operating conditions, the values remain in a narrow range. In some cases, the differences may be due to normal variation in the reaction measurements.

Table 4.6 Reaction results comparison between different Co-MOF-74 pyrolysis conditions

Experiment	**Run 2**	**Run 3**	**Run 4**	**Run 5**
Reduction				
Mass of Co-MOF-74 (g)	1	1	1	1
Heating Rate ($^oC\ min^{-1}$)	2	8	8	8
Dwell Time (h)	1	1	1	5
Temperature (^oC)	500	500	500	500
Reaction				
Pressure (Bar)	5	5	7.5	7.5
Temperature (^oC)	200	200	250	250
Space velocity ($ml\ min^{-1}\ g_{Co}^{-1}$)	652	652	652	652
X_{CO}	0.99	0.98	0.99	0.92
Activity ($mol_{CO}\ g_{Co}^{-1}\ h^{-1}$)	0.535	0.532	0.540	0.498
C_{2+} Selectivity (%)	0.0	0.0	9.3	6.2
CH_4 Selectivity (%)	71.1	73.7	63.4	67.0
CO_2 Selectivity (%)	32.0	33.1	27.3	26.7

Table 4.6 is a comparison of reaction results which shows the effect of pyrolysis dwell time and pyrolysis ramp. By looking at the results of Run 2 and Run 3, a comparison can be drawn between altering the pyrolysis ramp from 2 ^{o}C min^{-1} and 8 ^{o}C min^{-1}, with all other conditions remaining identical. The performance is almost identical based on the results obtained at a temperature of 200^{o}C, pressure of 5 bar and space velocity of 652 cm^{3} min^{-1} g_{Co}^{-1}. For instance, conversions of 0.99 and 0.98 are recorded for the catalysts with a 2 ^{o}C min^{-1} and 8 ^{o}C min^{-1} ramp, whilst the C_{2+}, CH_4 and CO_2 selectivity do not differ by more than 2.6 %. A similar observation is noted by comparing Run 4 and Run 5, where all conditions are kept similar aside from the dwell time, which is 1 h and 5 h for Run 4 and Run 5, respectively. In this case, pressures of 7.5 bar and temperatures of 250 ^{o}C were used. The results are generally very similar, although performance is marginally better when a pyrolysis dwell time of 5 h is used. For example, conversion is at 0.99 compared to 0.92, selectivity towards C_{2+} is 3.1 % higher and methane selectivity is 2.6 % lower, whilst CO_2 selectivity remains almost identical with values of 27.3 and 26.7 %. However, as the values are so similar, it is not possible to claim a clear improvement on performance by reduction of the dwell time from 5 h to 1 h, as the difference in performance indicating values may just be attributable to the natural variation of data.

The results obtained in this set of reaction experiments is vastly different to those shown in the most similar studies. Previously mentioned studies by Qiu et al [66] and Zhang et al [67] tested Co-MOF-74 derived catalysts which were obtained by a similar pyrolysis procedure. In the work by Qiu et al, Co-MOF-74 underwent pyrolysis at 550 ^{o}C for two hours under Ar at a heating rate of 5 ^{o}C min^{-1}. The catalyst was tested at 230 ^{o}C at 30 bar with a syngas H_2/CO ratio of 2. Based on the information given by the authors, a space velocity of 769.23 cm^{3} min^{-1} g_{Co}^{-1} was calculated. This was based on 52% of Co in a 50 mg catalyst sample, which was recorded by ICP-OES in the authors' work, with a flowrate of 20 cm^{-3} min^{-1}. A conversion of 0.3 was observed by the authors. Considering a similar flowrate is used in comparison to many of the results listed in Table 4.5 (and assuming the flowrate given was at room conditions), there is a significant difference in conversion and activity, with conversions of between 0.73 and 1 recorded in Table 4.5 compared to 0.3 recorded by the author. However, despite the much higher conversions shown in the results in Table 4.5, the selectivity is much less desirable. Qiu et al recorded methane selectivity of 18 %, compared to methane selectivity in the range of 60.9 to 73.7 % in Table 4.5. Furthermore, C_{5+} selectivity recorded by Qiu et al was 65 %, compared to selectivity in the range of 0 to 15.3 % for C_{2+} products in this chapter, which shows an immense difference in the selectivity towards higher hydrocarbons. CO_2 selectivity was also very different, with a value of 7 % in the work by Qiu et al, compared to values between 23.1 and 33.5 % recorded in Table 4.5. Zhang et al also provided a rare example of the performance test of a MOF-derived catalyst from Co-MOF-74. Co-MOF-74 underwent pyrolysis in He at 500 ^{o}C, and was tested with space velocities of 4000 and 8000 h^{-}

^{1} at 200 ^{o}C and 30 bar. Again, stark differences in conversion and selectivity were observed. For example, a conversion of 0.055 was achieved at a space velocity of 8000 h^{-1}, whilst a conversion of 0.143 was achieved at 4000 h^{-1}. For comparison, conversions of between 0.73 and 1 were recorded in Table 4.5. Many of the reactions in this chapter were run at 652 ml min^{-1} g_{Co}^{-1}, which is approximately 15,000 h^{-1} based on the volume of the catalyst bed, and assuming room conditions. The activities given by the author were 0.06084 and 0.0792 mol g_{Co}^{-1} h^{-1}, based on moles of CO converted, for the reactions run at 8000 and 4000 h^{-1}, respectively. Again, this is very different from values of around 0.5 mol g_{Co}^{-1} h^{-1} recorded in Table 4.5. In the work by Zhang et al, the two reactions at different space velocities produced a C_{5+} selectivity of between 65.9 and 69 %, CH_4 selectivity of between 17.2 and 18.6 %, and a CO_2 selectivity of 0. This selectivity given here is very similar to the work produced by Qiu et al, who recorded C_{5+} and CH_4 selectivity as 65 and 18 %. As previously mentioned, such values are significantly different to those given in Table 4.5 by a very large margin.

By comparing the reaction data with similar work by other authors, there are some large differences on performance. However, characterisation of the MOF-derived catalyst is not so dissimilar, which is not surprising, considering similar pyrolysis conditions were used. For instance, in the most similar previous research by Qiu et al [66] and Zhang et al [67], the MOF underwent pyrolysis under conditions of 550 ^{o}C for two hours and 500 ^{o}C for one hour in an inert atmosphere, similar to the 500^{o}C for one hour used for the majority of experiments in this chapter. Based on the reaction data from Table 4.5 and Table 4.6, small changes to the pyrolysis conditions in an inert atmosphere are unlikely to affect the result. The most notable deviation in experimental method arises from a change in the reaction conditions used. Whilst the temperature range remains similar (200-250^{o} C), pressures of 30 bar were used in the work by Qiu et al and Zhang et al, compared to pressure in the range of 3.1 and 10 bar used in this chapter [66, 67]. Therefore, it is possible that an increase in pressure contributes to the very different reaction results shown in this chapter. However, with some Co catalysts, it is quite possible to achieve high selectivity towards higher hydrocarbons using pressures as low as atmospheric pressure [84].

Effect of the Water-Gas Shift Reaction

It is important to note the very high CO_2 selectivity in particular, as this may provide some insight into the reason for such unexpected results. The only source of CO_2 production in FTS is the water-gas shift (WGS) reaction, which confirms the very high activity of this side-reaction. This is unusual for a Co-based catalysts, as Co is thought not be active for the WGA, unlike iron catalysts, except at

temperatures far exceeding those typical for Co-based FTS [85, 86]. However, high conversions can lead to higher partial pressure of H_2O in the reactor, which may induce greater WGS activity. Marion et al studied FTS at high CO conversion level. At these conditions, it was observed that a cobalt catalyst can develop a water-gas shift activity which may become significant at the expense of the Fischer-Tropsch reaction, as H_2 and H_2O are competing to react with CO. They showed that this undesired phenomena depends on a specific criteria based on the molar H_2O/H_2 ratio level in the Fischer-Tropsch reactor [87]. It was reported the Co catalyst would develop significant WGS activity if the ratio exceeds 1. They also observed that the process was both reversible and that the reversibility was close to instantaneous. This occurrence is also supported in a study by Gavrilovic et al, who ran FTS at a low H_2/CO ratio of 1.12 with added water to the feed [88]. At low conversions, CO_2 selectivity was negligible. After increasing the conversion until the H_2O/H_2 ratio reached unity, selectivity towards CO_2 increased rapidly, giving values of 12 % at a conversion of 0.466. The reversibility of this phenomenon was demonstrated, as CO_2 selectivity rapidly decreased shortly after reducing the conversion level. However, the CO_2 selectivity was still higher after lowering the conversion than before the H_2O/H_2 ratio had been brought to unity, which may suggest that a change in the catalyst properties is involved, such as the formation of cobalt oxides, as water is an oxidising agent [88].

For the results contained in Table 4.5, it is difficult to estimate the H_2O/H_2 ratio, as H_2O at the outlet was not directly measured. However, this can be roughly estimated by CHNS analysis of the liquid product along with the hydrogen composition measured at the reactor outlet. Using this method, it possible to obtain a very crude estimation of the amount of water produced in the FTS reaction, and therefore an estimation of the H_2O/H_2 ratio inside the reactor can be obtained, based on the composition at the reactor outlet. The moles of H_2 can be directly calculated based on the outlet flowrate and gas composition obtained from the analysis of the outlet gas from the gas chromatograph. If reaction Run 5 is considered, shown in Table 4.5, with an outlet flowrate of 44.4 cm^3 min^{-1} and H_2 composition of 14.7 %, the total moles of hydrogen eluted from the reactor over a reaction period of 5 h and 51 min is 0.095 mol. The mass percentage of H and C in the liquid, and therefore the mass ratios and mole ratios, can be calculated directly from the CHNS result of the liquid. As only C, H and O atoms are fed into the reactor but only C and H are detected in the CHNS analysis of the liquid product, it is assumed that the remaining mass in the liquid is composed of O, and therefore moles of each component in the liquid can be deduced by using the mass ratio and total liquid mass recorded over the 5 h and 51 minutes of reaction. It was calculated that the H to O ratio in the liquid was 2.18, with the total moles of O in the liquid equal to 0.22 mol. This is almost in a 2:1 H/O ratio, which indicates that the liquid from this reaction is largely made up of water. Considering the C_{2+} selectivity is very low, at 6.2 %, it is not absurd to make this assumption, especially as water is a primary product

of FTS. Therefore, if the moles of water produced over the period of 5 h 51 min is estimated to be equal to the moles of O in the liquid, the H_2O/H_2 ratio at the reactor outlet can be estimated as 0.220/0.095 = 2.3, which is well above a ratio of 1 thought to induce significant WGS reaction [87].

To induce WGS activity, high conversions are needed to raise the partial pressure of water. This suggests that the root cause of the high CO_2 and high methane selectivity is the very high activity of the catalyst. Usually, the conversion of the catalyst can be reduced by increasing the space velocity [89]. However, high space velocities have been used, up to 6860 $cm^3\,min^{-1}\,g_{Co}^{-1}$, but this had little effect on conversion. Further increasing the space velocity should eventually have the effect of lowering the conversion, which may prevent high partial pressure of water in the reactor. The high activity of the catalyst may be due to the very high cobalt loading, which is estimated at 66 % based on the TGA data in Figure 4.3, whereas Qiu et al recorded values of 52 % Co loading by ICP-OES in Co-MOF-74 derived catalysts that underwent pyrolysis at 550 ^oC [66]. With the very high loading of catalyst, depending on the dispersion, it would be expected to achieve very high activity.

Effect of Metal Oxide Formation

Potential WGS activity has been linked to cobalt oxide-based species, which may form from the active metallic Co during exposure to a H_2O-rich, high conversion environment. Particularly considered is the formation of CoO and metal-support compounds, which have been suggested drive this change in catalytic WGS activity. In the case of mixed metal oxides, the increased concentration of H_2O may induce oxidation or a solid state reaction between the active metallic Co and widely applied metal oxide carriers, such as Al_2O_3, SiO_2 and TiO_2 [86]. Wolf et al prepared a cobalt aluminate and showed no water-gas shift activity in the medium-shift temperature range, whilst a cobalt titanate sample was shown to catalyse the conversion of water and carbon monoxide to hydrogen and carbon dioxide after an extended activation period. However, this perovskite material underwent vast restructuring forming metallic cobalt, a known catalyst for the water-gas shift reaction at temperatures exceeding typical conditions for the cobalt-based Fischer-Tropsch synthesis [86]. In the case of Co-MOF-74, there is no traditional metal oxide support, however it may be possible that the formation of Co_2C occurred, either during the pyrolysis procedure or the reaction, which is shown to have WGS activity [90]. Although it is not thermodynamically feasible for the bulk of Co to be completely oxidised, it may be possible for some surface atoms, which allows for the high CO_2 selectivity [88]. Re-oxidation of cobalt metal to cobalt oxide has been shown to occur in studies by Schanke et al, who investigated the role of water on deactivation for alumina-supported cobalt catalysts [91]. They showed, using XPS studies,

that there was significant surface oxidation of cobalt even at low H_2O/H_2 ratios. Also, Ma et al showed that when CO conversion exceeds 80%, part of Co was oxidized [92]. XANES spectroscopy of used catalyst displayed spectra consistent with the presence of more CoO at higher conversion levels. It was speculated in this study that the high water partial pressure ($PH_2O/PH_2 > 0.9$) leads to the formation of cobalt oxide surfaces which may contribute to the enhanced WGS reaction and methane formation reactions.

Based on estimations, the H_2O/H_2 ratio in the reactor is very high and therefore a possibility for surface Co to oxidise. However, in the case of characterisation linked to this work, there is no evidence of cobalt oxide, which would normally show up on the XRD spectrum. But considering XRD is a bulk characterisation technique, observable peaks for cobalt oxide are unlikely to appear if the oxidation has only occurred on the surface. Furthermore, if post-reaction characterisation of the spent catalyst using another technique, such as XPS, did show the presence of cobalt oxides, it is difficult to prove that this formation occurred during the reaction and not oxidation from the atmosphere after removal from the reactor. Further to this point, it may be possible that some cobalt oxide was formed during the pyrolysis of the MOF itself, as O is present within the ligand of the Co-MOF-74 and both CoO and Co_3O_4 formation can occur at temperatures above 425 ^oC [93]. To prove the formation of cobalt oxides during reaction, all transferral of the catalyst sample to the characterisation equipment from the reactor must be carried out in an inert atmosphere, which is often not practical. Besides, previous studies have confirmed the presence of cobalt oxides when analysing post-reaction catalysts and did not see the same extreme activity for the WGS reaction, whilst cobalt oxide nanoparticles supported on TiO_2 have even shown more desirable FTS performance compared to Co metal at low pressures of 5 bar [94]. This suggests that the main cause of WGS activity is related to the high conversion.

Origin of High Methane Selectivity

It is possible that the high WGS activity may also explain the high methane selectivity shown in the results in Table 4.5. It is often observed that the methane selectivity will decrease with increasing conversion up to around 0.8, after which methane selectivity increases exponentially [95]. In the case of the results in this chapter, conversion is around the range of 0.9. As the WGS reaction produces H_2 and uses CO, the H_2/CO ratio may be distorted beyond the initial value of 2 in line with the stoichiometry for FTS. With the abundance of H_2 compared to CO, hydrogenation to methane is more likely, and may account for the very high methane selectivity observed.

Effect of Co Nanoparticle Size

Another feature of the catalyst which may contribute to the high activity needed to induce WGS, is the small Co nanoparticle size, which have average grain sizes the range of 7.5 to 8.9 nm, based on the Scherrer equation. High dispersion, as well as low active metal crystal size, has been shown in literature to provide higher activity [96]. In some reactions such as FTS, there is a slight deviation from this general observation. Iglesia showed that Co site-time yields are independent of Co particle size in the 10-210 nm range using Al_2O_3, SiO_2 and TiO_2 supports [97]. Luo et al used a similar MOF-derived catalyst based on ZIF-67 and found that turnover frequency increased with increasing Co crystallite size from 8.4 to 10.5 nm, and then remained constant in the range of crystallite sizes of between 10.5 and 74.8 [64]. A similar observation was also noted in other studies [98, 99]. Results from the study by Luo et al showed that productivity also increased from Co nanoparticle sizes of about 5 to 10.5 nm, whilst a sharp decrease was observed with Co nanoparticles over 10 nm, which is expected with a constant site-time yield and increasing particle size [64]. Some studies suggests that, from steady-state isotopic transient kinetic analysis (SSITKA), that lower CO consumption rates of small Co nanoparticles can be attributed to blocking of the active edge/corner sites by irreversibly adsorbed CO [99, 100]. Other research suggests that the disassociation of H_2 is difficult on small Co particles, and that CO activation is facilitated by the presence of hydrogen on Co nanoparticles, therefore the ability to dissociate hydrogen is the key parameter to determine FTS activity [99, 101, 102]. Based on previous literature data, enhanced activity is observed with Co crystallite sizes of about 10 nm, which is slightly larger than the Co crystallite sizes observed from the catalyst samples for reactions completed in Table 4.5, although not by much. As the nanoparticle sizes of 7.5 and 8.9 nm in this work are close to the optimum size of 10 nm, it is possible that the high turnover frequency and small Co nanoparticle grain size (suggesting high dispersion) have contributed to the high activity of the catalyst, which may induce significant WGS activity.

Also, product selectivity can also be influenced by Co nanoparticle size, where small nanoparticle size has been associated with higher methane selectivity. A common observation is increasing C_{5+} selectivity with increasing nanoparticle size. For example, Borg et al showed that C_{5+} selectivity increased and sharply and peaked at an optimum Co nanoparticle size of 8 nm, before a slight decrease and levelling off, using a Co based, γ-Al_2O_3 supported catalyst [103]. This occurrence is also backed up in a study by Rane et al [104]. Melaet et al showed that C_{5+} selectivity increased with nanoparticle size from 3.2 and 11 nm on a silica support at 250 ^{o}C, with a particle size of 11 nm exhibiting the highest selectivity, however this effect was not as pronounced at lower temperatures [105]. In the aforementioned study by Luo et al using similar MOF-derived catalyst based on ZIF-67, the relationship

between nanoparticle size and selectivity is different. High methane selectivity was shown, with values around 48 % observed in the Co nanoparticle size range of around 8 to 30 nm [64]. However, a significant decrease in methane selectivity, from approximately 48 % to 32 %, was observed as the particle size increased from 30 to 74.8 nm. It was suggested that methane is generated from the hydrogenation of the intermediate species of $HCHO^*$ and CH_X^*, according to the H-assisted CO dissociation mechanism for FTS reaction. It is suggested adsorbed H over the catalyst surface is the key factor in determining methane selectivity. The decreased methane selectivity with large Co nanoparticle size may be related to the lower H coverage, as Co dispersion and accessible sites are expected to decrease with increasing Co nanoparticle size. Therefore adsorption and activation may be weakened, meaning less hydrogen coverage and lower methane selectivity. Furthermore, the presence of a small amount of Co^{2+} from cobalt oxides also have the ability to activate and dissociate hydrogen, and although CO dissociation cannot occur on Co^{2+}, activated H on Co^0 may be transferred to adjacent cobalt oxides through hydrogen spillover, which facilitates the formation of methane [64]. It has been suggested that an increased localised H/CO ratio may be achieved by H spillover, which has been linked to an increase in reaction rate [106]. It may also be possible that an increase in the ratio may lead to increased methane formation [107]. Also, when considering carbon supports in FTS, a high surface area and a carbon surface functionalization, generally through the introduction of surface oxygen groups or defects, is required to increase spillover. However, there are currently no studies showing the direct involvement of hydrogen spillover on FTS activity and selectivity on unpromoted carbon-supported cobalt catalysts [107]. These phenomena may be pertinent to the results generated in Table 4.5, as the particle size for the catalyst is around 7.5 and 8.9 nm which, according to the study by Luo, is in the particle size range for high methane selectivity and low C_{5+} selectivity [64]. Although other studies may suggest that this is approaching the range of optimum C_{5+} selectivity, many of these studies are based on more conventional alumina and silica supports, rather than a carbon, MOF-derived carbon support which is used in this work, whilst the nanoparticle size range studied was not as extensive [103, 108]. The small nanoparticle size may be a contributing factor to the high methane selectivity observed in Table 4.5. However, if this is the case, it is likely to be co-contributor to the abnormal results observed, as selectivity effects related to nanoparticle size alone cannot account for such high CO_2 selectivity.

As well as particle size effects, activity and selectivity have also been linked to differences in the particle crystal phase. The different morphologies and surface topologies of each crystal phase can expose different concentrations of active sites which can affect performance. Bulk Co adopts a HCP structure under ambient conditions, however phase transformation to FCC occurs at 400 ^oC. The occurrence of either HCP or FCC can depend on the particle size, support, presence of promoters and pre-treatment

conditions used [99]. As shown from the previous XRD results in this chapter, the dominant phase for the current Co-MOF-74 derived catalyst is FCC, with no evidence of HCP. This is to be expected, as the pyrolysis of the MOF occurred at temperatures of 500 ^{o}C. It has been reported that the HCP crystal phase exhibits greater activity in FTS than FCC [99]. It is unlikely that any crystal phase effects have contributed to the high activity needed to induce significant WGS activity. However, it has been reported that the HCP phase exhibits a lower rate of CH_4 formation compared to FCC [99]. Considering the exclusive presence of the FCC crystal phase, it may be responsible for a portion of the high CH_4 selectivity observed.

4.5 Conclusion

MOF-derived catalysts were prepared form Co-MOF-74, used as a precursor. Characterisation of the spent catalysis seemed to be comparable to characterisations found in the literature. However, reactor testing of the catalyst showed very high methane selectivity, very low C_{2+} selectivity, and very high CO_2 selectivity, whilst showing extremely high activity. Conversion of around 0.9 were often observed. This occurrence was present across all the reaction results, despite altering the reaction conditions and MOF pyrolysis conditions, where the only observable trend was a slight increase in C_{2+} selectivity when pressure was increased. The high CO_2 selectivity indicates the high WGS activity, which is thought to be the main reason behind the high methane selectivity and low selectivity to higher hydrocarbons. Very high conversions lead to high partial pressure of water which increases WGS activity, and H_2 and H_2O compete to react with CO. The result is a distorted H_2/CO ratio, much higher than the original ratio of 2, which favours the hydrogenation and methane formation. Other factors that may have contributed is the formation of cobalt oxides. Whilst the high catalyst loading and Co nanoparticle size effects contribute to the high activity of the catalyst and possibly the formation of methane. One method to improve the performance of the catalyst may be to dilute the MOF-derived catalyst with inert particles, to lower the loading of the catalyst.

Chapter 5

Improvements and Comparisons of Co-MOF-74-derived Catalysts

5.1 Introduction

Results from Chapter 4 showed unexpected performance of the Co-MOF-74-derived catalyst across a range of conditions. The very high CO_2 selectivity suggests very high WGS activity, which can also explain the very high methane selectivity observed. Two previous studies have looked at improving the performance of Co-MOF derived catalysts through chemical vapour deposition of acetylene in order to prepare core-shell catalysts, which has been shown to provide a degree of graphitization in the carbon shell. Li et al investigated carbon-supported Co catalysts from MOFs for FTS from Co-BDC through chemical vapour deposition in order to prepare core-shell Co catalysts [65]. After pyrolysis in C_2H_2, a thin layer of carbon was formed with low graphitization degree. The catalyst prepared under pyrolysis with 2 % C_2H_2 showed higher conversion, around 11 % compared to 7 %, and higher C_{5+} selectivity, with values around 80 % compared to 68 %, compared to the same catalyst that underwent pyrolysis in an inert atmosphere. Lower methane selectivity was also noticed, with values of around 15 % compared to 22 %. In another instance, Zhang and colleagues also investigated the effects of chemical vapour deposition using acetylene to create core-shell catalysts [67]. The catalyst showed excellent performance at a temperature 260 ^oC, which is just above the normal LTFT operating range of 200-250 ^oC, with good C_{5+} selectivity of 75.4 % and low CO_2 selectivity of 4.8 %. Also, there was an improvement over the same MOF prepared by simple pyrolysis under inert gas, which showed C_{5+} selectivity of 65 % and CO_2 selectivity of 8 % at 230 ^oC, a temperature more comfortably in the range of LTFT.

5.1.1 Objective

This chapter aims to improve on the results from Chapter 4. Unfortunately, the high CO_2 selectivity and methane selectivity suggest high WGS activity, which leads to very poor catalyst performance. Several possible reasons for this were suggested in Chapter 4. The extremely high loading of the Co catalyst causing increased bed temperature may have played a role. In this chapter, the effects of diluting the catalyst to attain better isothermal control of the reactor will be investigated. Also, the

supposed benefits of chemical vapour deposition with C_2H_2 will be studied in order to see an improvement in Co-MOF-74-derived catalyst performance. Advantages of the direct pyrolysis of MOFs to create FTS catalysts is the ability to achieve high metal loading with small Co nanoparticle size, enable complete reduction of the Co metal, and limit sintering and oxidation due to the spatial confinement caused by nanoencapsulation [73]. On the other hand, traditional methods of catalyst preparation using metal oxide supports have an interdependence of metal loading and particle size, as larger nanoparticles will form when high metal loadings are used, whilst undesirable metal-support interactions can hamper reducibility and negatively affect catalyst performance in FTS [59, 74]. Therefore, the effectiveness of the Co-MOF-74 catalyst was compared to that a conventionally prepared γ-Al_2O_3-supported Co catalyst.

5.2 Experimental

The experiments undertaken in this chapter can be seen in Table 5.1. Co-MOF-74 underwent pyrolysis in a 2% C_2H_2 and 98 % N_2 atmosphere at 500 ^oC at 8 ^oC min^{-1}, as opposed to a 100 % N_2 atmosphere, to investigate the effect of chemical vapour deposition using C_2H_2. This catalyst was denoted as MOF-C_2H_2. To investigate the effect of diluting the Co-MOF-74 catalyst bed, the MOF/Al_2O_3 catalyst was comprised of 0.5 g Co-MOF-74 sieved to 80 mesh, and 1 g of ground Al_2O_3 pellets sieved to 80 mesh and mixed with the Co-MOF-74. This catalyst underwent pyrolysis at 500 ^oC at 8 ^oC min^{-1} in pure N_2. In addition, to investigate the effect of chemical vapour deposition on the diluted Co-MOF-74 catalyst, the MOF/Al_2O_3-C_2H_2 was diluted with ground Al_2O_3 pellets that sieved to 80 mesh and mixed with the Co-MOF-74, and pyrolysis occurred at 500 ^oC at 8 ^oC min^{-1} in a 2 % C_2H_2 atmosphere. To compare the performance of the Co-MOF-74-based catalyst, a γ-Al_2O_3 supported Co catalyst was prepared using the methods in Chapter 3, and 1 g sieved to 80 mesh was loaded for testing and reduced at 450 ^oC in flowing H_2 with a ramp of 3 ^oC min^{-1} for 5 h. The spent catalysts were removed after reaction for characterisation. All other experimental work, including characterisation, was done according to the methods in Chapter 3.

Table 5.1 Chapter 5 experiment list

Catalyst	Composition	Reduction/Pyrolysis Atmosphere	Reduction Temperature (°C)	Reduction Time (h)
MOF-C_2H_2	0.5 g Co-MOF-74	2 % C_2H_2/98 % N_2	500	1
MOF/Al_2O_3	0.5 g Co-MOF-74 + 1 g inert γ-Al_2O_3	100 % N_2	500	1
MOF/Al_2O_3-C_2H_2	0.5 g Co-MOF-74 + 1 g inert γ-Al_2O_3	2 % C_2H_2/98 % N_2	500	1
Co/Al_2O_3	1 g impregnated Co/Al_2O_3	100 % H_2	450	5

5.3 Catalyst Characterisation

XRD

XRD was performed on all spent catalyst samples in this chapter. Figure 5.1 shows the XRD spectra of the MOF-C_2H_2 catalyst. Similar to the XRD spectra shown for the Co-MOF-74 after pyrolysis in Chapter 4, a broad peak with very low intensity is noticeable at 2θ = 44.3 °, whilst the Co-MOF-74 framework seems to have completely collapsed, as there is no trace of the two largest peaks observed at 2θ = 6.5 ° and 11.5 ° in the original Co-MOF-74 spectra. The peak at observed at 2θ = 44.3 ° is likely due to metallic Co of the 111 lattice plane of the FCC crystal phase, which is very comparable to that shown by Pei et al after the pyrolysis of Co-MOF-70 in an inert atmosphere [72]. The two peaks of the 200 and 220 FCC plane, usually observed at 2θ = 51 ° and 77 °, are not present, unlike in another previous study applying a similar pyrolysis procedure in inert atmosphere to Co-MOF-74 [66]. The absence of these two peaks could be explained by the extremely low intensity of the peaks due to the very small nanoparticle size, as the largest peak of the 111 FCC plane at 2θ = 44.3 ° is only just discernible. Another, very broad peak was observed at a 2θ value of approximately 13° in Figure 5.1. Considering the broad nature of this peak, it is likely that it represents an amorphous material, however this peak was not able to be identified accurately. Compared to two previous studies utilising chemical vapour

deposition using C_2H_2, the XRD spectrum observed in this work is quite different. Zhang et al also used a similar pyrolysis procedure to create Co-MOF-74-derived core-shell catalysts, by pyrolyzing the MOF in a flow of 2 % C_2H_2 at heating rate of 2 $^oC\ min^{-1}$ to temperatures between 450 ^oC and 600 ^oC for 1 h. The XRD spectrum of the prepared catalyst decomposed at 500 ^oC showed peaks appear at 2θ = 44.3 ^{o}, 52 ^{o} and 60 ^{o} which were assignable to CoO, the FCC Co^o phase and HCP Co^o phase, respectively. However, this was not observed in this work. Li et al prepared catalysts from Co-BDC MOF precursors which were heated in a 2 % C_2H_2/Ar atmosphere at 5 $^oC\ min^{-1}$ to 550 ^oC for 1 hour. The prepared catalyst showed diffraction peaks at 2θ values of 51.8 ^{o}, 60.6 ^{o}, 48.7 ^{o} and 55.7 ^{o} which were assigned to FCC Co^0 and HCP Co^o, and their spectrum showed very little difference to that of the same MOF pyrolyzed in pure Ar. However, the XRD patterns in the spent catalyst showed that the peak intensity of FCC Co is much lower and the peaks for HCP Co disappear, whereas new peaks appear at 2θ = 43.2°, 48.3°, 49.9°, 53.7°, 66.3°, 70.1° and 76.3°, which were ascribed to Co_2C. It was suggested that metallic Co, including all the HCP Co and part of the FCC Co, have been transformed into Co_2C [65]. In this work, these peaks were not observed.

Using the Scherrer equation, the nanoparticle grain size can be estimated to be 14.3 nm. This is slightly larger than that of the Co-MOF-74 decomposed in N_2 in Chapter 4, which showed a Co nanoparticle grain size in the range of 7.5 to 8.9 nm. The grain sizes here are larger than those reported by Zhang et al, who reported grain sizes of 2.5 nm, based on the Scherrer equation, after pyrolysis of Co-MOF-74 in 2 % C_2H_2 in He at 500 ^oC for 1 h. However, after reaction the Co nanoparticle size increased to 5 nm. Li et al reported an average nanoparticle size of 13.6 nm based on HR-TEM after pyrolysis of Co-BDC in 2 % C_2H_2 in Ar at 550 ^oC for 1 h. XRD results in this work show that the Co nanoparticle is slightly larger than those reported in Chapter 4 for catalyst prepared from Co-MOF-74 in a pure N_2 atmosphere, but the difference is not hugely significant, and the size is in a similar range to those reported in similar research. Although it is noteworthy that the grain size is slightly higher than that reported for the same procedure using exactly the same MOF [67]. A summary of the Co crystal phase information from this work and other studies utilizing Co-based MOFs for FTS can be seen in Table 5.2.

Table 5.2 Summary of Co crystal nanoparticle information from MOF-derived catalysts in Chapter 4 and Chapter 5

Sample	**Pyrolysis Temperature (°C)**	**Co XRD 2θ Peak Positions (°)**	**Pyrolysis Atmosphere**	**Grain Size (nm)**	**Co Crystal Phase**
T500 R8 D1 Spent (Chapter 4)	500	44.3	100 % N_2	8.5	FCC
T500 R8 D5 Spent (Chapter 4)	500	44.3	100 % N_2	7.5	FCC
MOF-C_2H_2 Spent (Chapter 5)	500	44.3	2 % C_2H_2/98 % N_2	14.3	FCC
[72]	600	44.3	100 % He	14.5	FCC
[66]	550	44.3, 51.0, 77.0	100 % Ar	-	FCC
[67]	500	52.2, 60.0	2 % C_2H_2/98 % He	2.5	FCC, HCP
[65]	550	51.8, 60.6, 48.7 55.7	2 % C_2H_2/98 % Ar	13.6	FCC, HCP

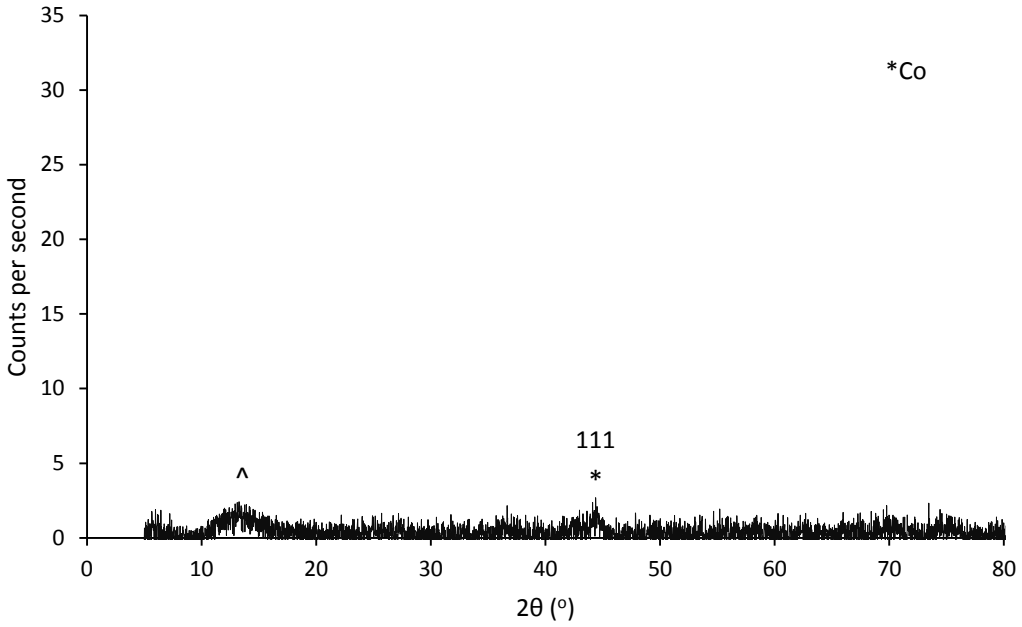

Figure 5.1 XRD spectrum of MOF-C_2H_2 spent catalyst

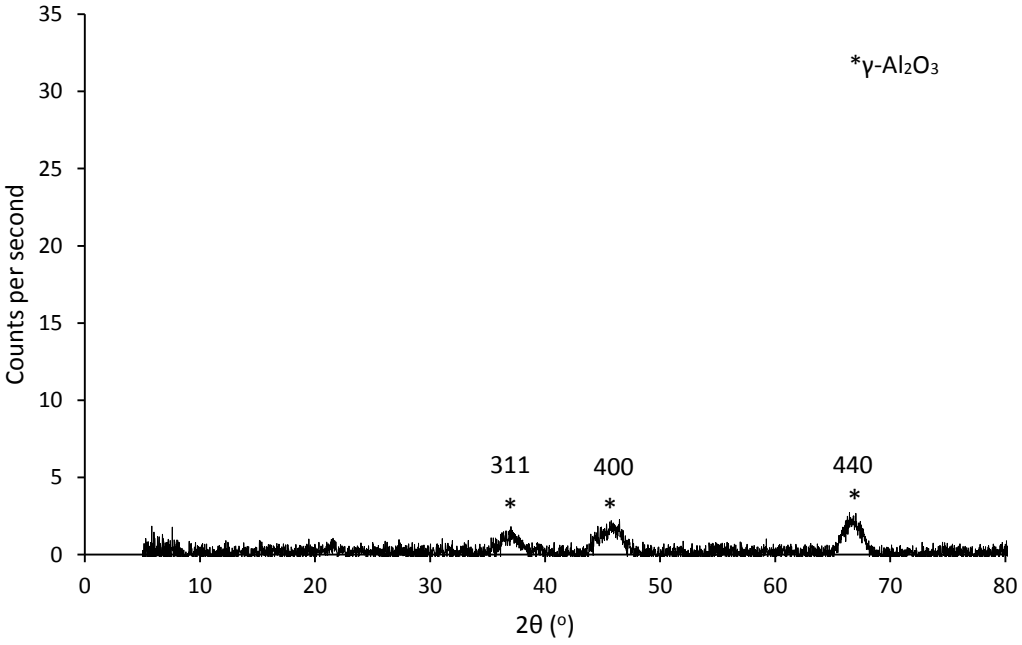

Figure 5.2 XRD spectrum of Co/Al_2O_3 spent catalyst

Figure 5.2 shows the XRD spectrum for the spent Co-Al_2O_3 catalyst. Three obvious peaks at 2θ = 37.8 °, 45.7 ° and 66.9 ° are obvious signs of 311, 400 and 440 reflections of γ-Al_2O_3 [109]. This is expected, due to the γ-Al_2O_3 catalyst support. Obvious signs of any other peaks are not present, especially the peaks of FCC Co^o at 2θ = 44.3 °, 51 ° and 77 ° [66]. This may be due to the small size of the Co nanoparticles, although it is likely that the most obvious peak of FCC Co^o at 2θ = 44.3 ° is obscured by that of γ-Al_2O_3 at 2θ = 45.7 °.

SEM

Figure 5.3 shows an SEM image of the MOF-C_2H_2 catalyst, which look very similar to those of the spent catalyst that underwent decomposition under a pure N_2 atmosphere in Chapter 4. The image shows similar angular blocks to those in Chapter 4. Previously, EDX mapping of the spent catalyst in Chapter 4 show carbon and cobalt, with some oxygen which must have been adsorbed after removal form the reactor. A similar composition is likely, although the carbon content may increase due to the chemical vapour deposition, which was shown by Li et al through elemental analysis [65].

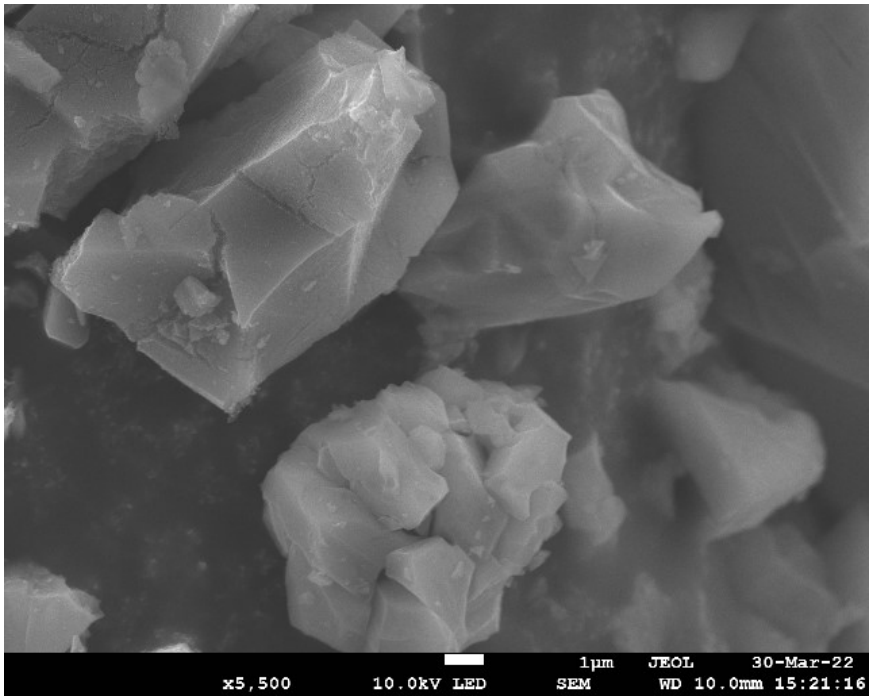

Figure 5.3 SEM image of spent MOF-C_2H_2 catalyst

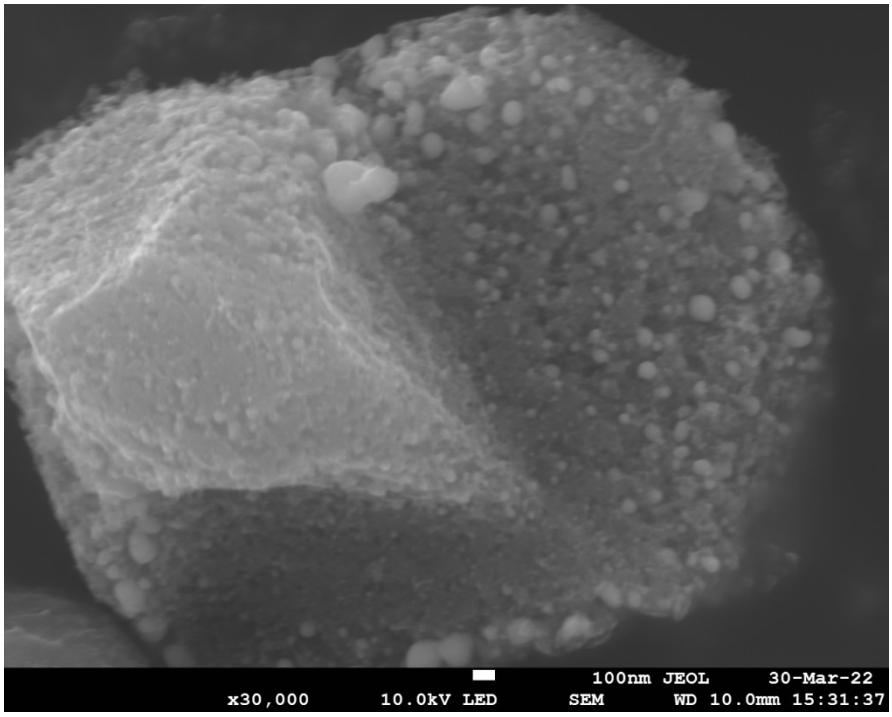

Figure 5.4 SEM image of spent MOF-C_2H_2 catalyst

Figure 5.4 shows the same MOF-C_2H_2 catalyst at a greater magnification. From this image, small spherical objects of varying sizes can be seen, which are a lighter colour than the main bulk of material. The lighter colour suggests a change in material. Considering the scale of the image, it is possible that these spheres show the Co nanoparticles, which are scattered on the surface of the carbon with varying size. Some of the supposed Co particles are around 100 nm in size, and even slightly larger. Whereas many of them are smaller, less than 20 nm, whilst are some are around 10 nm or less. Considering the smallest particles are difficult to detect in this image, the average grain size of 14.3 nm calculated from the Scherrer equation seems possible and reasonable. The image in Figure 5.4 suggests Co nanoparticles are present on the surface of the carbon. It is possible than some nanoparticles are embedded within the carbon, which has been shown in previous research [65, 67]. TEM images may reveal more information about encapsulated nanoparticles and give a better idea of the true average nanoparticle size, as well as the degree of graphitization that occurs in the carbon shell. Also, it is difficult to conclude any clear difference between the morphology of the MOF-based catalyst pyrolyzed in pure N_2 and an N_2/C_2H_2 atmosphere from the SEM images shown in Figure 5.3 and Figure 5.4.

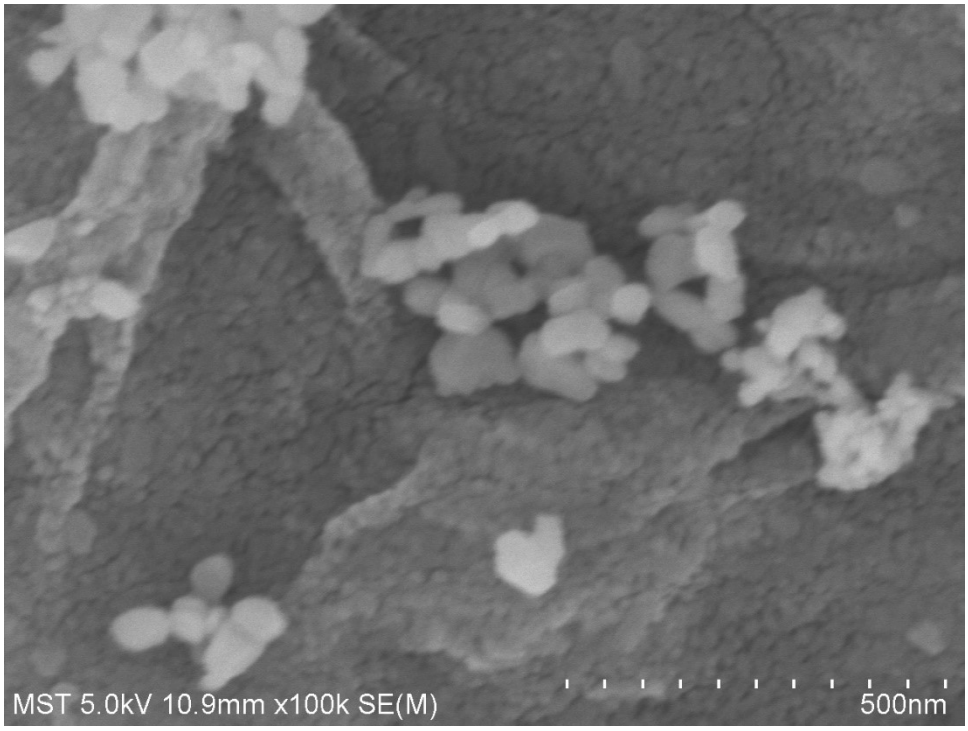

Figure 5.5 SEM of impregnated γ-Al_2O_3 pellet after calcination

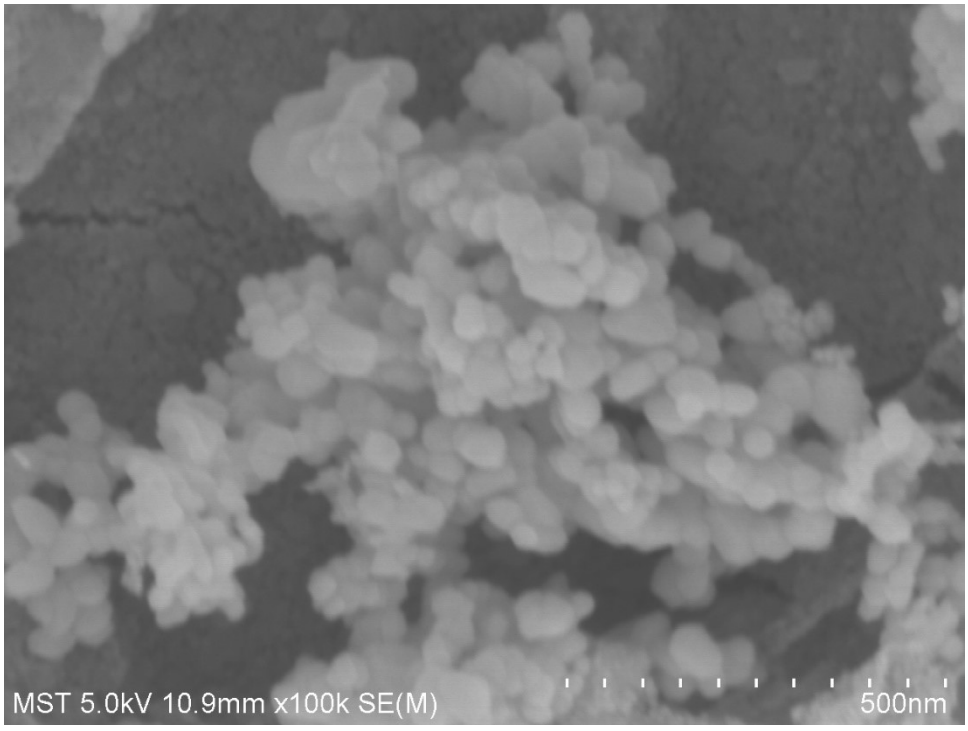

Figure 5.6 SEM of impregnated γ-Al_2O_3 pellet after calcination

Figure 5.5 shows an SEM of the impregnated Co/Al_2O_3 catalyst pellet after calcination, before grinding and reduction in the reactor. The lighter colour looks to represents a material change, which is likely to be Co_3O_4, as the catalyst has not undergone reduction at this stage. The darker background is likely to be the alumina. It can be seen that the crystallite size of the Co_3O_4 is around 50 nm or smaller, however there seems to be an agglomeration of the crystallites. A clearer example of this agglomeration can be seen in Figure 5.6, an image also taken of the impregnated pellet after calcination. Co_3O_4 particle diameter can be converted to the corresponding Co metal particle size according to the relative molar volumes of the metallic Co and Co_3O_4 [84]. The conversion factor can be seen in Equation 5.1.

$$d(Co^0) = 0.75d(Co_3O_4) \qquad \text{Equation 5.1}$$

Therefore, the Co_3O_4 nanoparticle of approximately 50 nm and be estimated as having a Co nanoparticle diameter of 37.5 nm.

N_2 Adsorption

The BET surface areas, BHJ pore volume and average pore diameter are listed in Table 5.3. Measurements were taken for the spent MOF-C_2H_2 and the original unimpregnated Al_2O_3 pellets, to show information about the structure of the γ-alumina catalyst and the MOF-derived catalyst after chemical vapour deposition of acetylene. The calcined pellets, containing the Co_3O_4 precursor, were ground before loading into the reactor, and plain γ-Al_2O_3 pellets were ground and mixed with Co-MOF-74 to make the MOF/Al_2O_3 and MOF/Al_2O_3-C_2H_2 catalysts. However, the surface area, pore volume and pore diameter of the original, plain Al_2O_3 pellet are assumed to apply to the ground pellet. As the γ-Al_2O_3 in the MOF/Al_2O_3 and MOF/Al_2O_3-C_2H_2 catalysts are inert particles, the morphological properties are considered irrelevant and only the properties of the spent the MOF/Al_2O_3 and MOF/Al_2O_3-C_2H_2 catalysts are considered.

Table 5.3 N_2 adsorption results of the MOF-C_2H_2 spent catalyst and γ-alumina pellet

Sample	BET Surface Area (m^2 g^{-1})	Pore Volume (cm^3 g^{-1})	Average Pore Diameter (nm)
MOF-C_2H_2 Spent	252.2	0.49	3.11
Al_2O_3 Pellet	249.5	0.85	6.71

Figure 5.7 shows the isotherm of the MOF-C_2H_2 spent catalyst. The isotherm exhibits a similar type 4 isotherm shown for Co-MOF-74-derived catalysts after pyrolysis in Chapter 4, with slightly larger deviation between the adsorption and desorption branches in middle relative pressure range. The type 4 isotherm indicates the presence of a mesoporous material with pore diameters between 2-50 nm [80]. The increase in N_2 uptake at higher pressure indicates capillary condensation in the mesopores or the presence macropores [80, 81]. The similar type H3 hysteresis loop seen from the series 7 prepared and spent samples in Chapter 4 is also observed. Similar isotherms have been reported in a previous study of Co-MOF-74-derived catalysts, where it was suggested this type of isotherm indicates a large amount of mesoporous cavities [66]. This kind of isotherm has been linked with slit-shaped pores [82]. From Table 5.3, the BET surface area of the MOF-C_2H_2 spent catalyst was given as 252.2 m^2 g^{-1}, which clearly shows a porous material with a surface area close to that measured for the series 5 spent catalyst in Chapter 4, where a BET surface area of 262.4 m^2 g^{-1} was obtained. This surface area is also comparable to other studies investigating the chemical vapour deposition of ethyne of Co-MOF-74. Zhang et al reported a BET surface area of 337 m^2 g^{-1} when pyrolysis was conducted at 500 ^oC for 1 hour, and showed that the surface area decreased slightly with increasing pyrolysis temperature, with BET surface areas of 325 and 271 m^2 g^{-1} for pyrolysis temperatures of 550 and 600 ^oC [67]. Li et al reported BET surface areas of 86 and 137 m^2 g^{-1} after pyrolysis of Co-BDC in pure Ar and 2 % C_2H_2/Ar atmospheres, respectively [65]. In this case, they suggest that the increase in BET surface area is the result of carbon deposition from C_2H_2, as acetylene may facilitate the pore formation in the graphite carbon shell and increase the surface area of the catalyst during pyrolysis. The BET surface area measurement is also in a comparable range to those observed in literature without C_2H_2 deposition, with values of 341 and 130.8 m^2 g^{-1} observed for similar pyrolysis experiments involving Co-MOF-74 [66, 72]. In this work, the chemical vapour deposition did not show any significant change in BET

surface area. A BJH pore volume of 0.49 cm^{-3} g^{-1} and pore diameter of 3.11 nm was obtained for the MOF-C_2H_2 catalyst, which is very similar to that of the series 5 spent catalyst in Chapter 4, which measured a pore volume of 0.5 cm^3 g^{-1} and an average pore diameter 4.42 nm.

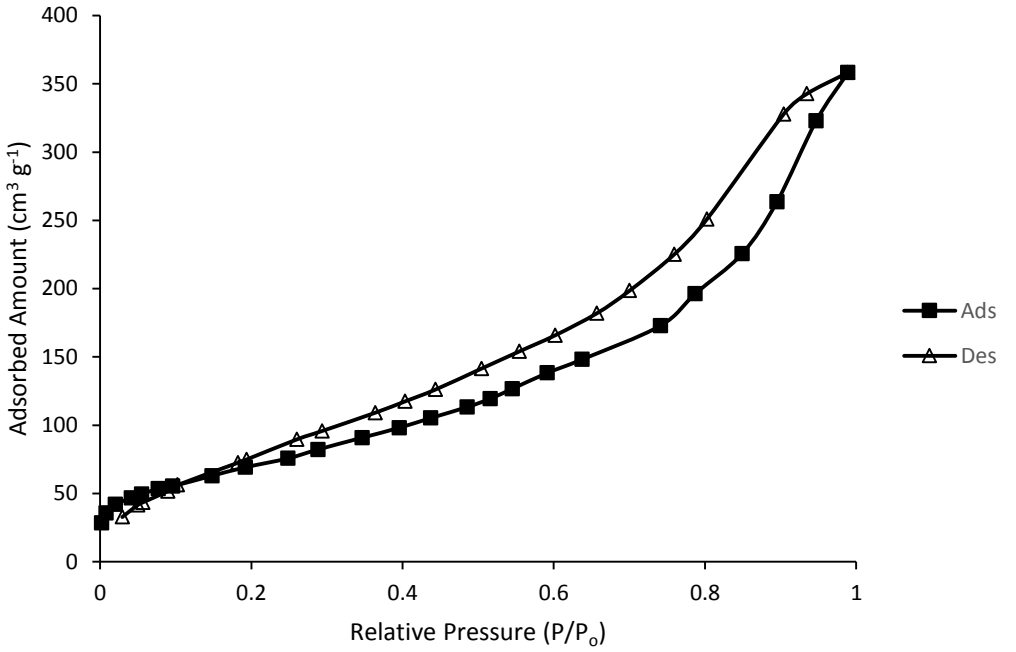

Figure 5.7 N_2 adsorption isotherm of MOF-C_2H_2 spent catalyst

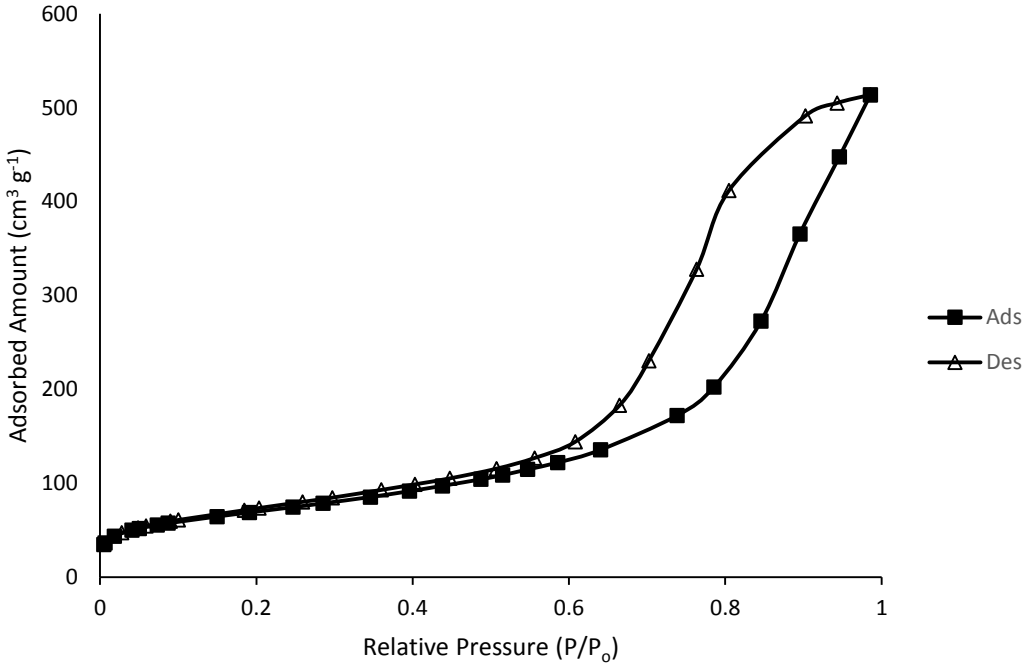

Figure 5.8 N_2 adsorption isotherm of plain Al_2O_3 pellets

The N_2 adsorption isotherm of the plain Al_2O_3 pellets can be seen in Figure 5.8. A clear fit to the type 4 isotherm is displayed with type 3 hysteresis. The BET surface area of 249.5 $m^2 g^{-1}$ was measured, which is almost identical to the manufacturer's specification of 250 $m^2 g^{-1}$. A pore volume of 0.85 $cm^3 g^{-1}$ and an average pore diameter of 6.71 nm was obtained from the BJH model, which seems to be reasonable compared to some other γ-alumina supports [110]. N_2 adsorption data shows that the surface area of both catalysts is similar, the γ-alumina catalyst seems to have a greater pore volume, about 73 % larger, and more than double the average pore diameter.

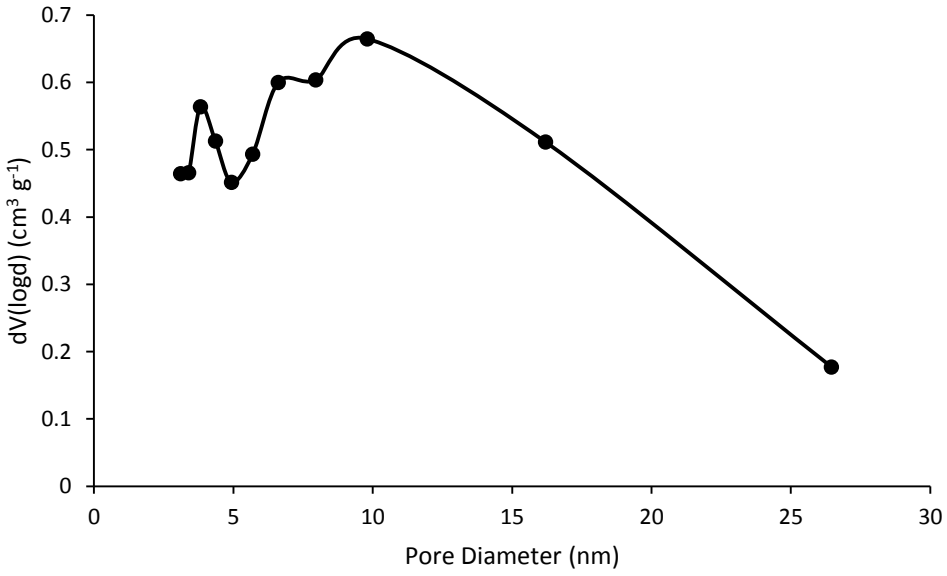

Figure 5.9 Pore size distribution on MOF-C_2H_2 spent catalyst

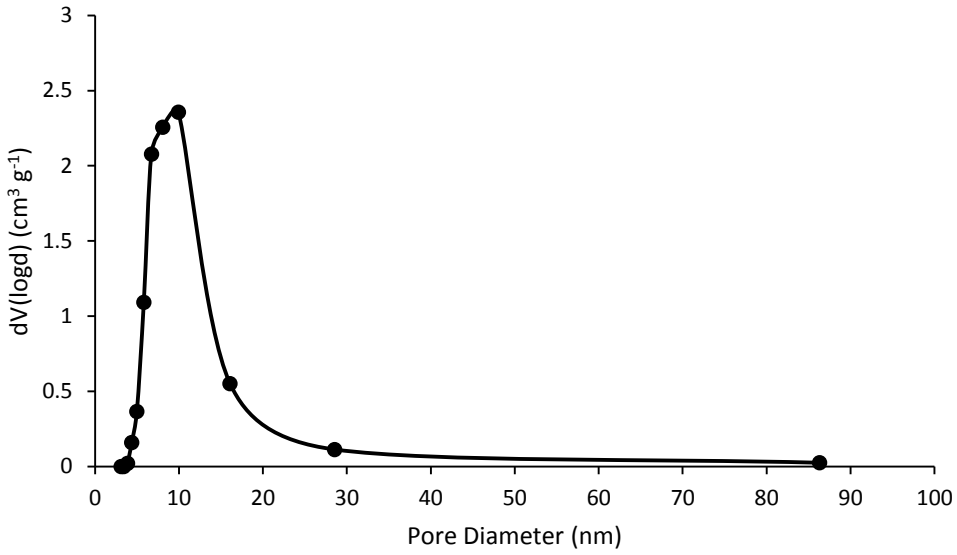

Figure 5.10 Pore size distribution of Al_2O_3 pellet

Figure 5.9 and Figure 5.10 show the pore size distribution of the MOF-C_2H_2 spent catalyst and γ-alumina pellet, respectively. The pore size distribution of the pellet shows a unimodal size distribution, where most of the pore volume concentrated in a large peak between 3 and 20 nm, with the peak around 10 nm. Whereas the MOF-C_2H_2 catalyst shows a very uneven distribution of the pore volume, which is spread over approximately 3 to 26 nm. It is interesting to recognise that the average Co nanoparticle size of MOF-C_2H_2, approximately 14.6 nm calculated from the Scherrer equation, is larger than the average pore diameter of 3.11 nm. Although estimating the average Co nanoparticle size of ground Al_2O_3 is difficult, the current evidence suggests a larger Co nanoparticle size than the 6.71 nm measured for the average pore diameter of the γ-alumina. This would suggest that most of the catalyst is dispersed on the catalyst particle surface, and not inside the porous network. This has been observed previously for both MOF-derived catalysts and γ-alumina supported Co catalysts [72, 110]. However, it may be completely possible that Co nanoparticles are located inside the pore system and the conflicting data may arise due to the choice of pore geometry model. As the BJH model assumes only the presence of cylindrical pores and the absence of pore networks, pore geometry is oversimplified [110]. 3D-TEM and HR-TEM has been used to visualise the pores and the cobalt-alumina interphase, and it has been shown that a simple pore structure with metal oxide impregnated onto the pore wall did not exist. Instead, it was that the alumina crystals were tangled into each other in a chaotic fashion and the cobalt agglomerates stretched over multiple alumina crystals and apparent pores [110].

Ultimately, the two catalysts exhibit similar overall surface areas, close to 250 m^2 g^{-1}, but a more uneven pore size distribution exists for the MOF-C_2H_2, which also shows a slightly lower pore volume and average pore diameter. XRD results show the MOF-C_2H_2 catalyst has a small Co nanoparticle diameter of 14.6 nm. Difficulty obtaining this information from the spent Co/Al_2O_3 catalyst means calculating an average Co nanoparticle size is challenging, however SEM images show that the nanoparticle size is in the range of 50 nm or below, with a large amount of agglomeration. Also important is the fact that the MOF-C_2H_2 catalyst does not seem to exhibit any significant difference compared to the Co-MOF-74 catalysts prepared in N_2 in Chapter 4. Chemical vapour deposition is thought to deposit a layer of carbon over the catalyst during pyrolysis, which may hinder or improve the level of graphitisation [65, 67]. However, this is difficult to confirm without the aid of TEM.

5.4 Results and Discussion

Table 5.4 shows the reaction results of the all the catalysts tested in Chapter 5. The ground Co/Al_2O_3 was used as a benchmark to compare against the MOF-based catalyst, as Al_2O_3-supported impregnated Co catalysts are commonly studied in FTS. In order to achieve enough amounts of liquid to analyse in a short reaction time, the reaction was run at 250 ^oC, which is at the high end of the LTFT temperature spectrum [6]. A low pressure of 10 bar was also used, compared to 20 – 40 bar commonly used for the operation of LTFT synthesis [111]. The performance of the Co/Al_2O_3 catalyst across three cobalt space velocities can be seen from Table 5.4. As expected, increasing the space velocity from 403 to 943 cm^3 min^{-1} g_{Co}^{-1} results in decreasing conversion of CO from 0.5 to 0.28. Equation 5.2 shows the relationship between conversion and the initial molar flow of a reactant for heterogenous catalytic fixed-bed reactor [44]. The conversion, X_A, is proportional to the catalyst weight, W, and inversely proportional to the initial molar flowrate, F_{A0}.

$$X_A = \frac{-r_a W}{F_{A0}} \qquad \text{Equation 5.2}$$

Table 5.4 Chapter 5 FT Reaction Results. S_{5+}, S_{C7+}, S_{C10+} are based on the hydrocarbons in the oil phase.

Catalyst	**Space Velocity ($cm^3\ min^{-1}\ g_{Co}^{-1}$)**	**X_{CO}**	**CTY ($mol_{CO}\ g_{Co}^{-1}\ h^{-1}$)**	**S_{CH4} (%)**	**S_{C2+}**	**S_{C2-C6} (%)**	**S_{5+} (%)**	**S_{C7+} (%)**	**S_{C10+} (%)**	**S_{CO2} (%)**
MOF-C_2H_2	652	0.85	0.461	64.3	2.00	-	-	-	-	33.7
MOF/Al_2O_3	403	0.59	0.197	56.3	36.5	12.6	25.51	23.9	15.4	7.2
	652	0.51	0.276	53.4	44.6	28.8	16.26	15.8	11.3	2
	943	0.42	0.328	60.1	39.3	18.9	21.0	20.4	14.2	0.63
MOF/Al_2O_3-C_2H_2	403	0.66	0.221	38.9	55.8	30.7	26.9	25.0	18.6	5.4
	652	0.52	0.283	58.6	37.9	15.2	23.0	22.7	17.6	3.5
	943	0.43	0.340	59.6	39.9	25.3	14.7	14.5	10.9	0.57
Co/Al_2O_3	403	0.50	0.169	33.1	66.6	26.9	41.1	39.7	28.0	0.3
	652	0.45	0.243	45.8	51.4	36.7	15.0	14.6	9.6	2.9
	943	0.28	0.223	44.4	55.7	27.6	28.9	28.0	18.3	<0.1

The methane selectivity is very high for FTS, at 33.1 % of moles of carbon converted, which rises to 45.8 and 44.4 % for space velocities of 652 and 943 $cm^3\,min^{-1}\,g_{Co}^{-1}$ for the Co/Al_2O_3 catalyst. Whereas many other studies show methane selectivity below 15 % when using γ-alumina-supported Co catalysts [88, 104, 110]. However, it is important to note in these typical examples that FTS was run at a temperature between 210 to 230 ^oC, with pressure of 20 bar, making it difficult to compare directly the results here to those in many published studies. However, some examples of FTS at similar conditions have been found in literature. For example, Bezemer et al studied a carbon nanofibre-supported Co catalyst at range of different conditions [108]. At conditions of 1 bar and 220 ^oC, running at conversions of around 2%, methane selectivity obtained for a number of different catalysts was generally in the range of 40-50 wt%, and C_{5+} selectivity mostly between 18-30 wt %, which were considered typical for unpromoted Co catalysts at such conditions. These values are very similar to the Co/Al_2O_3 catalyst in this work, which also showed a methane selectivity of 46 wt %. Melaet et al also ran FTS reactions at 5 bar and 250 ^oC to study particle size effects of carefully prepared Co nanoparticles on a silica support, MCF-17 [105]. Across nanoparticles sizes of 3.2, 5.5 and 8.6 nm, methane selectivities of around 41, 49 and 29 % were reported, similar to those reported in the Co/Al_2O_3 catalyst. However, a very dramatic drop in methane selectivity was observed for particle sizes of 11 nm, where the methane selectivity dropped to below 10 %. A similar story existed for the C_{5+} selectivity, where values of around 5, 20 and 38 % were reported for the particles sizes between 3.2 and 8.6 nm, before a large increase to around 80 % for particles sized at 11 nm. Very low C_{5+} selectivity has also been observed by Yang et al [70]. Although the Co/Al_2O_3 catalyst in this work produces relatively high methane selectivity, at these particular conditions there evidence from previous studies to suggest that these results are not that abnormal. At temperatures above 240 ^oC, Co catalysts do perform more actively in FTS, but simultaneously promote methanation resulting in lower selectivity to desired C_{5+} hydrocarbons [67].

Table 5.4 shows the reaction results for the MOF-C_2H_2 catalyst, where the Co-MOF-74 precursor was not diluted, and pyrolysis was undertaken in a 2 % C_2H_2/N_2 atmosphere, and reaction occurred at 10 bar and 250 ^oC. The results look similar to those presented in Chapter 4 for the Co-MOF-74 catalyst pyrolysized in pure N_2, at the same conditions and flowrate used in this experiment (S9R1, Table 4.5). The conversion for both catalysts is very high, however a value of 0.85 was measured for the MOF-C_2H_2 catalyst here, and a value of 1 shown in Table 4.5 in Chapter 4. Considering the same space velocity is used, it is expected that activity is slightly higher in the S9R1 experiment, with a value of 0.542 mol_{CO} converted $g_{Co}^{-1}\,h^{-1}$, compared to a value of 0.461. C_{2+} selectivity decreased to 2 % in the case of the MOF-C_2H_2 catalyst, from 15.3 % in the S9R1 experiment. Methane selectivity remained similar, with 63.4 % compared to 60.0 %, whereas there was a difference in the CO_2 selectivity, with

values of 33.7 % in the MOF-C_2H_2 catalyst compared to 23.7 % in the S9R1 experiment. Although there is some slight difference in the result, it seems clear that the MOF-C_2H_2 catalyst has been affected in the same way as the experiments in Chapter 4, which is evidenced by the very high CO_2 selectivity. High WGS activity has been induced, most likely through excessively high conversions which causes high water partial pressure in the reactor and therefore promotes methanation due to the much-increased H_2/CO ratio [87, 88]. This occurrence is evidenced by comparing the MOF-Al_2O_3 catalysts with the results from Table 4.5 in Chapter 4. The MOF-Al_2O_3 catalyst was composed of 0.5 g of Co-MOF-74 and 1 g of crushed γ-alumina pellets, which were both sieved to 80 mesh and mixed before pyrolysis inside the reactor at 500 ^oC for 1 hour. It is clear from the result in Table 5.4, and comparing those to the S9R1 result in Table 4.5, that diluting the MOF-derived catalyst with inert particles has a very large effect. For the same temperature, pressure and space velocity of 652 $cm^3\ min^{-1}\ g_{Co}^{-1}$ used for the S9R1 experiment in Table 4.5, the MOF-Al_2O_3 catalyst displays significantly lower conversion at 0.51. Also, dramatically reduced CO_2 selectivity of 2 % was shown, with C_{2+} selectivity of 44.6 %, significantly higher than 15.3 % recorded for the undiluted catalyst in experiment S9R1, and higher than all the experiments in Chapter 4, where the C_{2+} selectivity ranges from 0 to 16.2 %. This is clear evidence that the Co-MOF-74-derived catalyst is clearly affected by dilution with inert particles. The reason for this is likely related to the local bed temperature at the active site. FTS is a very exothermic reaction [4]. Considering the derived catalyst after pyrolysis of the MOF has a very high Co loading, around 66 % based on the TGA results in this work and 51 % based on ICP-OES of the same Co-MOF-74-derived catalyst a previous study [66], the high activity of the catalyst is likely to result in very high local reactor temperature. This may cause a dramatic increase in reaction rate leading to high conversions, which increases partial pressure of water in the reactor (as water is a main product of FTS), therefore promoting significant WGS reaction, evidenced by high CO_2 selectivity in undiluted MOF experiments. This is supported in observations in previous FTS studies [87, 88]. Due to high WGS activity, a high H_2/CO ratio is formed in the reactor, which promotes methanation, and accounts for the very high methane selectivity, usually over 60 %, shown in undiluted MOF-derived catalyst experiments in this work. The details of this hypothesis were explained in Chapter 4, and the results in Table 5.4 show evidence that this explanation is likely to be correct.

It is important to note that this may not always occur in directly packed MOF-derived catalysts. In all the Chapter 4 experiments, one methodical difference from this chapter was the placement of the thermocouple. The reactor in Chapter 4 was packed in such a way that the thermocouple was expected to be inside the packed bed. The temperature reading given by the reactor in the Chapter 4 experiments was no different from the setpoint at 250 ^oC, therefore it was assumed that the reaction was operating at the setpoint. However, it seems that the internal thermocouple cannot always give

an accurate local temperature reading inside the reactor bed, especially for highly loaded catalysts. Also, the high WGS activity was also witnessed at reaction temperatures of 200 ^{o}C in Chapter 4, suggesting that the temperature difference between the thermocouple reading and local bed temperature can be quite dramatic. The effect of diluting the catalyst with inert particles effectively reduces the Co loading, in this case from around 66 % to about 8 % for the MOF-based catalysts, which benefits temperature control and provides more isothermal operation. In previous studies of Co-MOF-74 derived catalysts from direct pyrolysis, this practice is sometimes, but not always, adhered to. For example, in the previous two studies using Co-MOF-74 as the catalyst precursor, the catalyst was packed directly into the reactor with no mention of dilution with inert particles [66, 67]. However, other researchers using different MOFs as catalyst precursors did dilute the catalyst [64, 72], although others did not [65]. In the previous studies using Co-MOF-74 as the catalyst precursor, it is likely that the reactor system had very good temperature control, in order to avoid such high local bed temperatures.

As it is clear that the performance of the MOF based catalyst used in this reaction system is severely impeded without dilution, a diluted Co-MOF-74 also underwent pyrolysis in a pure N_2 and 2 % C_2H_2/98 % N_2 atmosphere, to more accurately study the effect of the chemical vapour deposition of acetylene. From Table 5.4, the performance of the diluted MOF/Al_2O_3 catalyst can be compared against the Co/Al_2O_3 and diluted MOF/Al_2O_3-C_2H_2 across 3 cobalt space velocities. Figure 5.11 shows the conversion at the three cobalt space velocities between the MOF/Al_2O_3, MOF/Al_2O_3-C_2H_2 and Co/Al_2O_3 catalysts. All three catalysts show an almost linear decrease in conversion with space velocity. This decrease is expected and is commonly reported in FTS studies [89]. It is clear that the Co/Al_2O_3 exhibits the lowest conversion at all 3 space velocity points, with the conversion decreasing from 0.5 to 0.28 when the space velocity is increased from 403 to 943 $cm^3\,min^{-1}\,g_{Co}^{-1}$. The MOF-based catalysts exhibit higher activity at the same space velocity, with conversion being in the range of 0.06 to 0.14 higher for each space velocity point. This shows that both MOF-based catalysts are utilising the active Co metal more effectively in terms of converting CO. Both MOF-derived catalysts exhibit similar conversion, with the MOF/Al_2O_3-C_2H_2 showing slightly higher conversion at each space velocity point.

A similar story exists for the activity, shown in Figure 5.12. The MOF-based catalysts both show superior activity, about 0.04 to 0.12 mol_{CO} converted $g_{Co}^{-1}\,h^{-1}$ higher, which seems to increase linearly with space velocity, with the MOF/Al_2O_3-C_2H_2 showing marginally higher activity. However, the Co/Al_2O_3 productivity does not continue in a linear fashion and shows a stabilisation in activity at the space velocity of 943 compared to 652 $ml\,min^{-1}\,g_{Co}^{-1}$, showing that it is beginning to reach maximum activity. The higher activity of the MOF-derived catalysts may be explained by the very small nanoparticle size.

According to the XRD characterisation, the average nanoparticle size is in the range of 7.5 to 14.6 nm for the MOF-derived catalysts, whereas the nanoparticle size estimated from SEM for the Co/Al_2O_3 is larger, around 37.5 nm. In general, high dispersion and low active metal crystal size has been shown to provide higher activity [96]. Iglesia showed that Co site-time yields are independent of Co particle size in the 10-210 nm range using Al_2O_3, SiO_2 and TiO_2 supports [97].

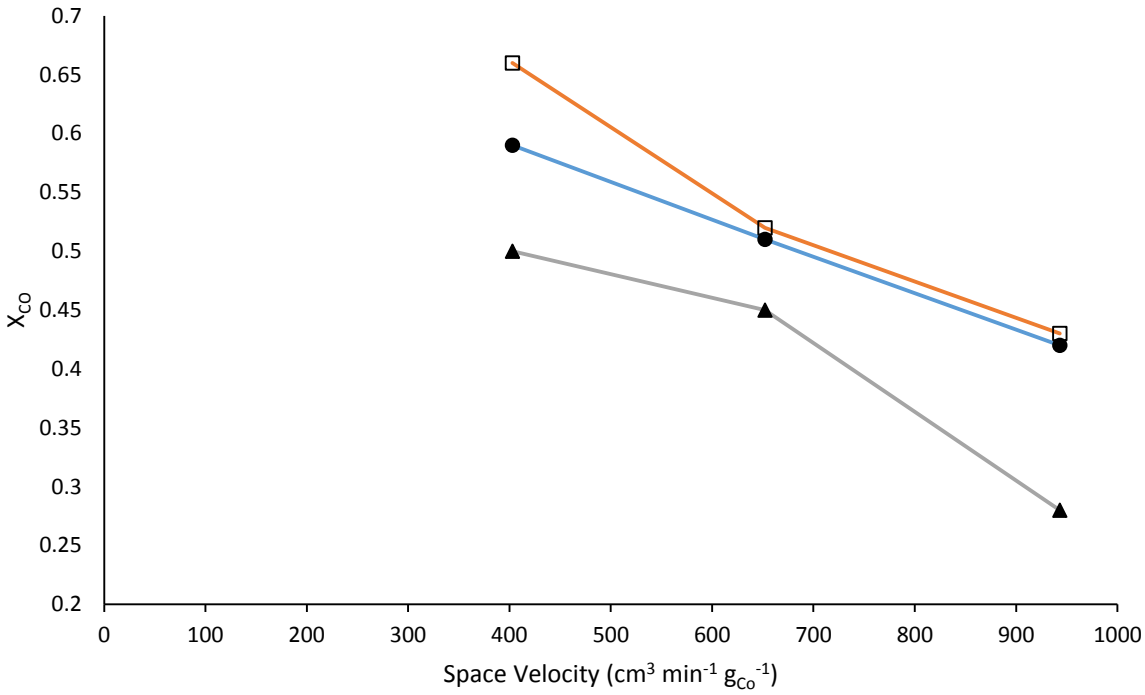

Figure 5.11 Space velocity and conversion. ● = MOF/Al_2O_3, □ = MOF/Al_2O_3-C_2H_2, ▲ = Co/Al_2O_3

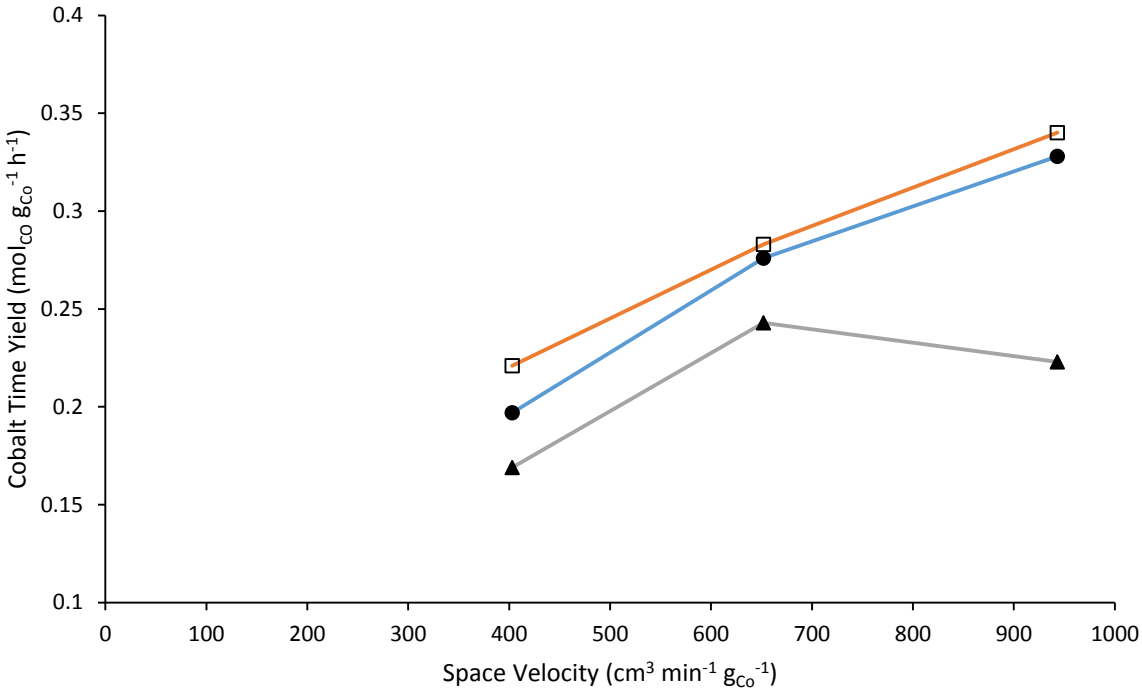

Figure 5.12 Space velocity and cobalt time yield. ● = MOF/Al_2O_3, □ = MOF/Al_2O_3-C_2H_2, ▲ = Co/Al_2O_3

Luo et al used a similar MOF-derived catalyst based on ZIF-67 and found that turnover frequency increased with increasing Co crystallite size from 8.4 to 10.5 nm, and then remained constant in the range of crystallite sizes of between 10.5 and 74.8 [64]. A similar observation was also noted in other studies [98, 99]. Results from the study by Luo et al showed that productivity increased from Co nanoparticle sizes of about 5 to 10.5 nm, whilst a sharp decrease was observed with Co nanoparticles over 10 nm, which is expected with a constant site-time yield and increasing particle size [64]. What has been shown in literature is that with increasing nanoparticle size, site-time yield seems to be constant at sizes greater than 10 nm with MOF-derived and metal oxide supported catalysts. Therefore, if site-time yield remains the same but the proportion of active sites reduces due to larger nanoparticles size, a drop in activity is expected.

Table 5.4 shows the C_{5+}, C_{7+} and C_{10+} selectivity for all reaction results for the MOF/Al_2O_3, MOF/Al_2O_3-C_2H_2 and Co/Al_2O_3. The selectivity is based on the moles of each hydrocarbon section in the oil phase. The FTS liquid existed in two phases, and only the oil phase was analysed for higher hydrocarbons. However, some carbon-containing compounds existed in the water and oxygenate phase, where almost all carbon-containing components had a carbon number of less than 7. Therefore, there may be some inaccuracies in the C_{5+} calculation due to carbon in the oxygenates, or carbon that escaped in

the gas phase as the GLS temperatures was often at around 27 °C, as there was no cooling mechanism present. However, Table 5.4 shows that the difference between the C_{5+} and C_{7+} is very small.

Figure 5.13 shows a plot of the C_{7+} selectivity for each catalyst at the three cobalt space velocities. The C_{5+} selectivity is generally low for cobalt catalysts. However, considering the conditions used, this does not seem abnormal. For example, Bezemer et al showed that testing a carbon nanofiber-supported Co catalyst at 220 °C and 5 bar, C_{5+} selectivity of around 20-30 wt% was observed [108]. Conversely, when the same catalysts were tested at at 210-250 ° at 35 bar, C_{5+} selectivity increased significantly. Xie et al have also shown a negative relationship between higher temperature and C_{5+} selectivity and a positive relationship between pressure and C_{5+} selectivity [112].

From Figure 5.13, it can be seen all three catalysts exhibit the highest selectivity at a space velocity of 403 $cm^3\ min^{-1}\ g_{Co}^{-1}$. It has been reported in multiple studies that, generally, higher conversions lead to reduced methane selectivity and higher C_{5+} selectivity until conversions around 0.8 are reached, after which methane selectivity increases exponentially due to WGS activity. This decrease in methane selectivity at higher conversion could possibly be explained by a decrease in surface H/CO ratio due to an increase in H_2O concentration. The adsorption of CO and intermediates such as O* and OH* from H_2O decomposition is relatively strong on the surface, which could reduce the adsorption of H [95]. At the lowest space velocity, conversion is at its highest, which may be the reason for the increase in C_{7+} selectivity.

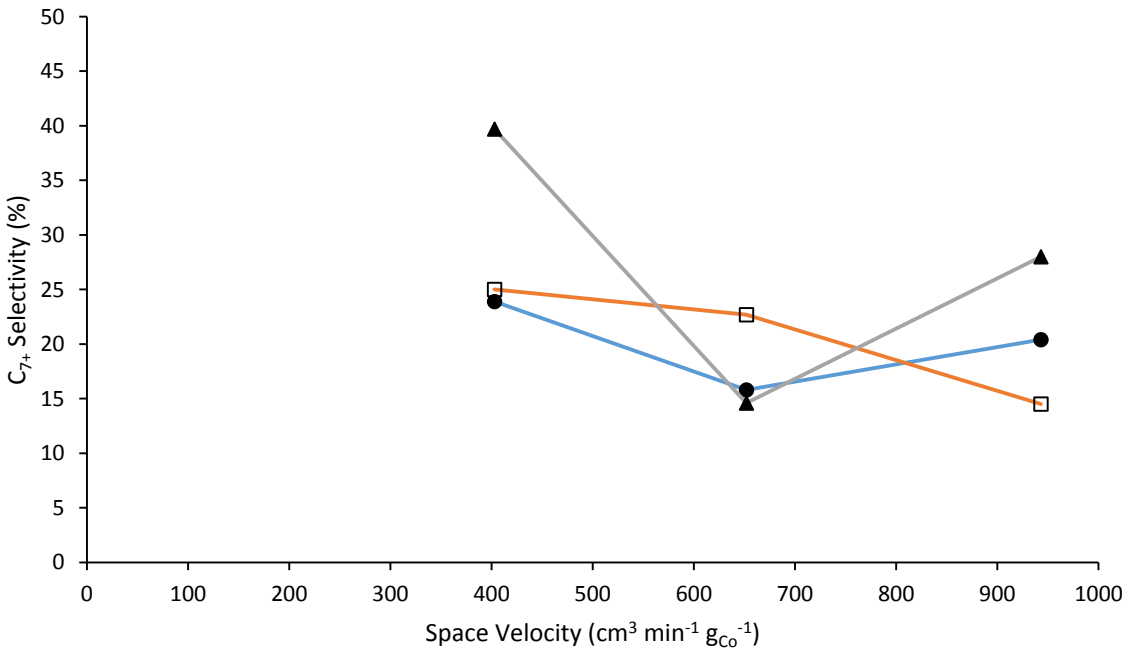

Figure 5.13 Space velocity and C_{7+} selectivity. ● = MOF/Al_2O_3, □ = MOF/Al_2O_3-C_2H_2, ▲ = Co/Al_2O_3

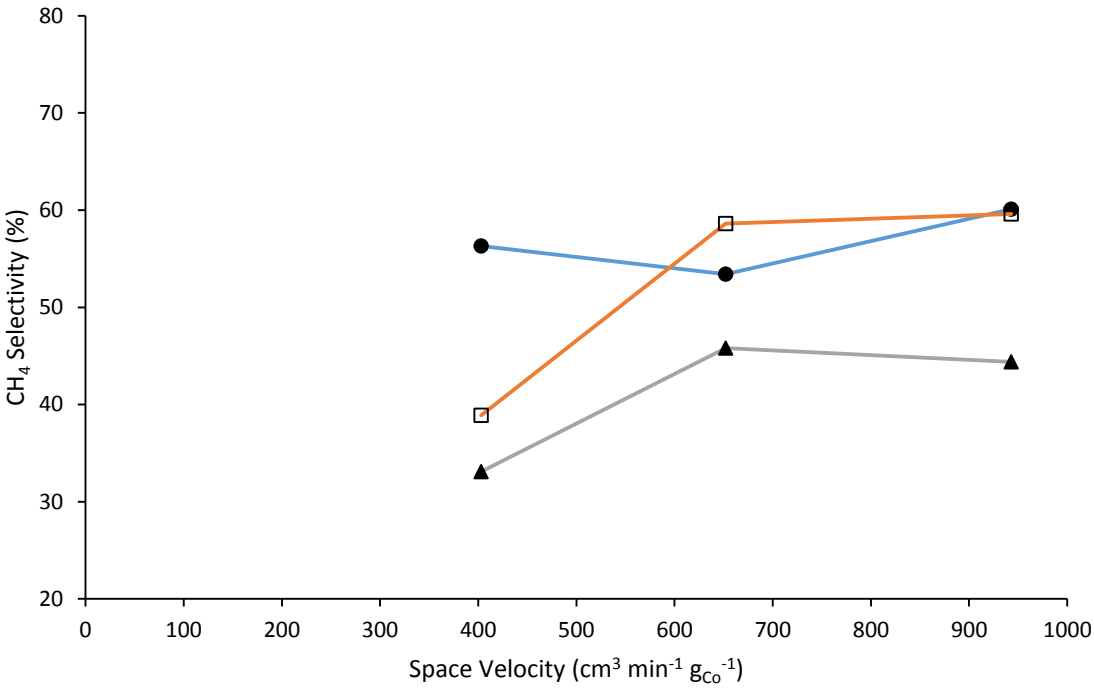

Figure 5.14 Space velocity and CH_4 selectivity ● = MOF/Al_2O_3, □ = MOF/Al_2O_3-C_2H_2, ▲ = Co/Al_2O_3

A consequent decrease in methane selectivity would also be expected, which is the case for the MOF/Al_2O_3-C_2H_2 and Co/Al_2O_3, which show the lowest methane selectivity at the lowest space velocity and can be seen in Figure 5.14. However, between 652 and 943 $cm^3\ min^{-1}\ g_{Co}^{-1}$, the methane selectivity stabilises. The MOF/Al_2O_3 seems to show less difference in the methane selectivity, but it is noteworthy that this catalyst shows the least radical decreases in conversion with space velocity, and also shows the highest WGS activity out of all the catalysts at the lowest space velocity, shown by a CO_2 selectivity of 7.2 %. Also, all catalysts show that an increase in C_{7+} selectivity and decrease in methane selectivity between the highest and lowest space velocity points.

It can be seen by comparing the selectivity of each catalyst in Figure 5.15 that the Co/Al_2O_3 converts more of the carbon to C_{2+} products, with the selectivity higher at all space velocity points by 6-16 %. At the space velocity of 652 $cm^3\ min^{-1}\ g_{Co}^{-1}$, a drop in C_{2+} selectivity is observed for the Co/Al_2O_3. However, unlike the C_{7+} selectivity, at this point the Co/Al_2O_3 catalyst still shows the highest selectivity to C_{2+}, and the drop in C_{7+} is due to higher conversion to C_2-C_6 products, where a C_2-C_6 selectivity of 36.7 % is observed. At the lowest space velocity of 403 $ml\ min^{-1}\ g_{Co}^{-1}$, the Co/Al_2O_3 clearly shows the

highest C_{7+} selectivity and lowest methane selectivity, with values of 39.7 and 33.1 %, respectively. In comparison, the two MOF-based catalysts show C_{7+} selectivity of around 25 %. The reason for the

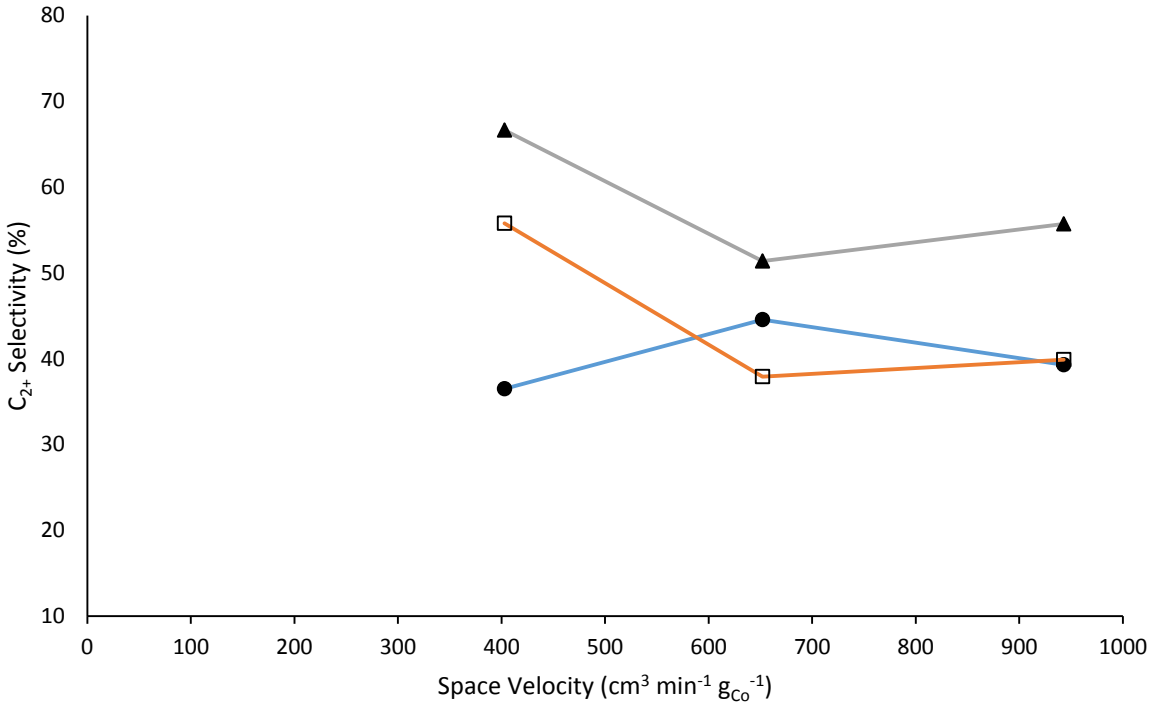

Figure 5.15 Space velocity and C_{2+} Selectivity. ● = MOF/Al_2O_3, □ = MOF/Al_2O_3-C_2H_2, ▲ = Co/Al_2O_3.

higher selectivity towards C_{2+} products and C_{7+} products, at least for two of the three space velocity points, may be linked to the nanoparticle size effect. As all the catalysts were sieved to 80 mesh, resulting in catalysts particle sizes of about 180 µm, the effect of diffusion limitations are likely to be negligible [33]. The effects of the nanoparticle size may present itself in two-ways. The product selectivity may be influenced directly by Co nanoparticle size, where small nanoparticle size has been associated with higher methane selectivity. In a study by Luo et al using similar MOF-derived catalyst based on ZIF-67, a relationship of a methane selectivity with small Co particle size was shown [64]. High methane selectivity was shown with smaller Co nanoparticles, with values around 48 % observed in the Co nanoparticle size range of around 8 to 30 nm [64]. However, a significant decrease in methane selectivity, from approximately 48 % to 32 %, was observed as the particle size increased from 30 to 74.8 nm. The Co nanoparticles of the MOF-derived catalysts in this work are in the range of 7.5 to 14.6 nm which, according to the study by Luo et al, is in the particle size range for high methane selectivity

and low C_{5+} selectivity [64]. However, other studies suggest that selectivity is independent on nanoparticle size above 8 nm, but the Co nanoparticle sizes studied are often in a smaller range [103, 108]. It was suggested that high methane selectivity is generated from the hydrogenation of the intermediate species of $HCHO^*$ and CH_X^*, according to the H-assisted CO dissociation mechanism for FTS reaction. Adsorbed H over the catalyst surface is the key factor in determining methane selectivity. The decreased methane selectivity with large Co nanoparticle size may be related to the lower H coverage, as Co dispersion and accessible sites are expected to decrease with increasing Co nanoparticle size. Therefore adsorption and activation may be weakened, meaning less hydrogen coverage and lower methane selectivity [64]. In the case of γ-Al_2O_3 supported catalysts in this work, the estimated Co nanoparticle size is around 37.5, based on SEM, whereas for the MOF-based catalysts it is much smaller, based on average grain size from XRD. Based on previous studies, it is difficult to state explicitly whether the Co nanoparticle size directly improves selectivity in the Co/Al_2O_3 catalyst, although work by Luo suggests in may be slightly favourable [64].

The other way in which Co nanoparticle size effects may lead to an increase in and C_{2+} and C_{7+} selectivity is linked to the size dependency on activity. As previously mentioned, the larger particle size of the Co/Al_2O_3 catalyst may explain the lower activity compared to the MOF-derived catalysts. Although previous studies show that higher conversion may be beneficial, once WGS activity begins to occur it can be detrimental to C_{5+} selectivity and favour methane selectivity. At the same space velocity, both MOF-derived catalysts do show higher conversions, but also show higher WGS activity, which is shown by the higher CO_2 selectivity in Table 5.4. This is most pronounced at the lowest space velocity, where the MOF/Al_2O_3 and MOF/Al_2O_3-C_2H_2, show CO_2 selectivity of 7.2 and 5.4 %, respectively, compared to 0.3 % for the Co/Al_2O_3 catalyst. This may explain the significantly higher C_{7+} selectivity of the Co/Al_2O_3 catalyst at the lowest space velocity. However, this cannot explain the selectivity difference at higher space velocity, as the conversion of all catalysts is low enough to limit the WGS reaction.

The MOF/Al_2O_3-C_2H_2 shows that the C_{7+} selectivity increases with conversion as the space velocity decreases, whilst methane selectivity decreases. This can be explained by the aforementioned trends in selectivity and conversion. However, the MOF/Al_2O_3 does not show the same trend. The main difference is the performance at the lowest space velocity, where there is significantly higher methane selectivity and lower C_{2+} selectivity for the MOF/Al_2O_3 catalyst. Otherwise, C_{2+} and C_{5+} selectivity remains fairly similar between the two catalysts at cobalt space velocities of 652 and 943 ml min^{-1} g_{Co}^{-1}, with selectivity not differing by more than about 7 %. At a space velocity of 403 ml min^{-1} g_{Co}^{-1}, a large difference in methane selectivity is present, about 18 %, whilst C_{2+} differs by about 19 %, where the

MOF/Al_2O_3-C_2H_2 shows a much greater selectivity towards C_2-C_6 products instead of methane compared to the MOF/Al_2O_3 catalyst.

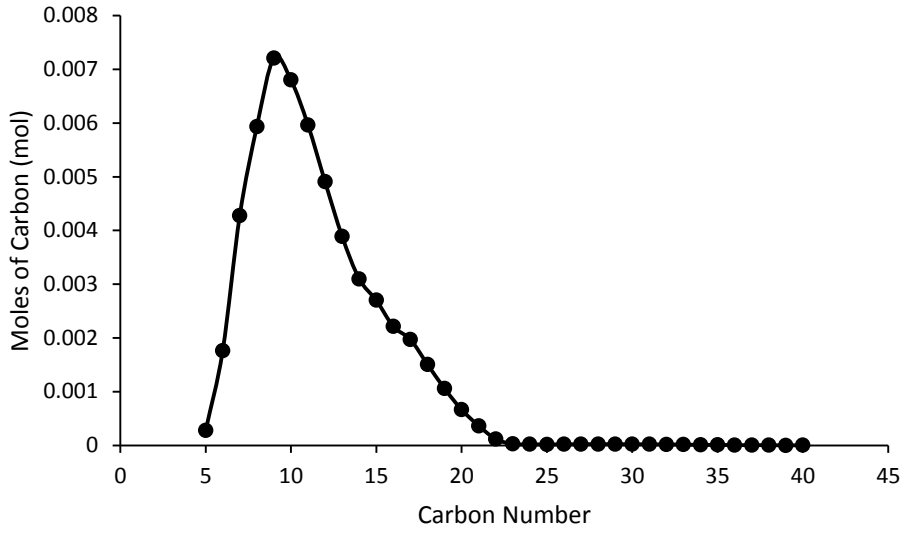

Figure 5.16 Carbon number distribution of the Co/Al_2O_3 oil phase at 403 ml min^{-1} g_{Co}^{-1}

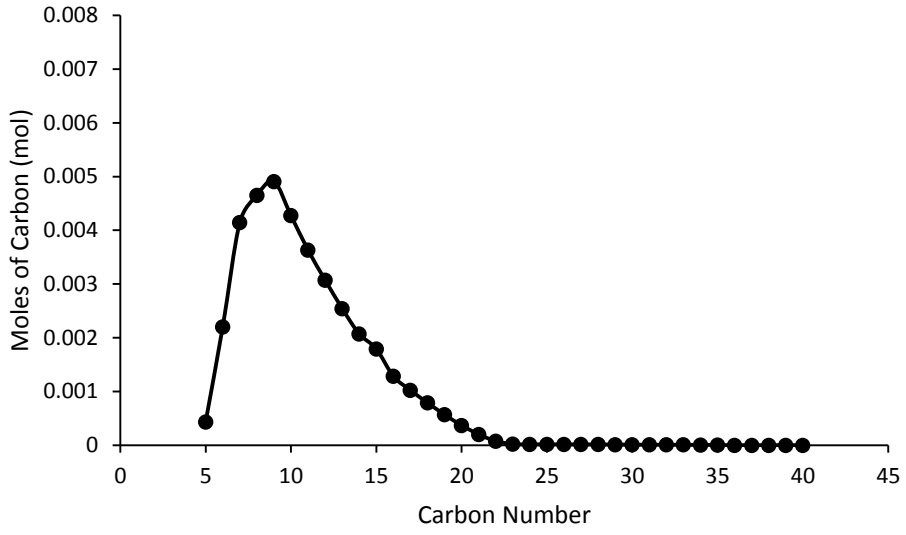

Figure 5.17 Carbon number distribution of the MOF/Al_2O_3 oil phase at 403 ml min^{-1} g_{Co}^{-1}

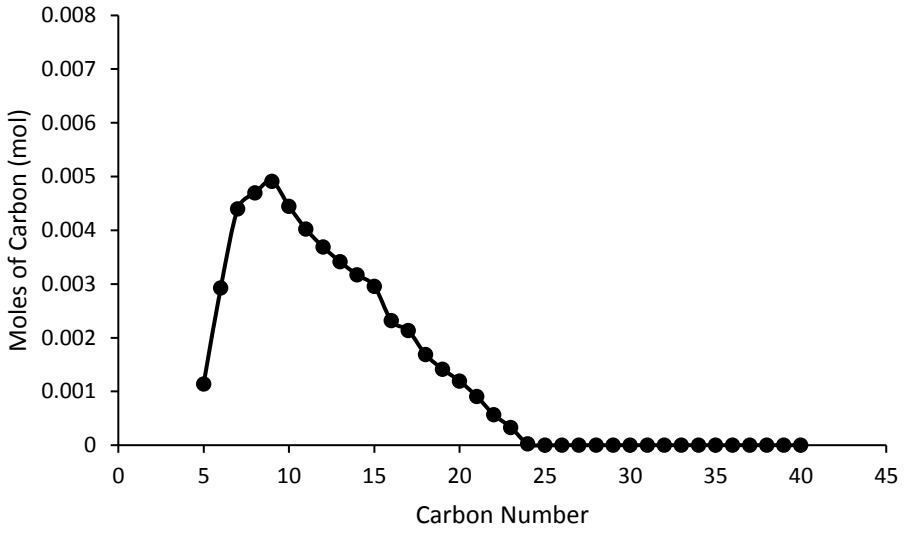

Figure 5.18 Carbon number distribution of the MOF/Al_2O_3-C_2H_2 oil phase at 403 ml ml min^{-1} g_{Co}^{-1}

Figure 5.16 - Figure 5.18 show the carbon number distributions of the oil liquid product for the three different catalysts at the lowest space velocity of 403 ml min^{-1} g_{Co}^{-1}. In all cases, the amount of product peaks around a carbon number of 10, and steadily declines. The three catalysts show comparable distributions. A very similar distribution is observed for most of the reactions in this chapter. This may be linked to the high temperature of reaction, which has been shown to favour lighter products in a Co catalyst [67].

Chemical vapour deposition of Co-MOF-74 for FTS has been previously studied by Zhang et al [67]. The Co-MOF-74 underwent pyrolysis in a pure He atmosphere and a 2 % C_2H_2 atmosphere at 500 ^oC. At gas hourly space velocity of 4000 h^{-1} and 8000 h^{-1}, the catalysts decomposed in C_2H_2 showed significantly higher conversion, reaching 100 % at 4000 h^{-1}, resulting in significant WGS activity. At 8000 h^{-1}, significantly greater conversion and C_{5+} selectivity was shown. Post reaction analysis using XRD showed that under pure He pyrolysis atmosphere, traces of CoO and the original MOF signal showed there was only a partial decomposition of the MOF and a partial reduction of cobalt species. In a C_2H_2 atmosphere, the metallic cobalt signals at 2θ = 52.2 and 59.8 ^{o} indicate the complete decomposition of MOF and the entire reduction of cobalt species, which may account for the higher activity. The effect of the chemical vapour deposition in this case was a greater extent of the reduction of the Co, which may be from the hydrogen released from the acetylene decomposition. Also, a comparison of the prepared and spent catalyst XRD samples in their work showed that the Co nanoparticle size increased from 2.5 nm to 5 nm after reaction, whereas for the sample that decomposed in a pure He atmosphere

showed an average nanoparticle size increase from 4.1 to 18.8 nm, suggesting that the chemical vapour deposition of acetylene plays a role in restricting particle sintering during reaction [67]. However, according to the XRD spectra in this work, it seems complete decomposition and reduction of the MOF occurred. However, it is possible that a slight increase in the extent of reduction occurred due to H_2 released from acetylene decomposition, which may account for the marginally higher activity shown by the C_2H_2 catalyst. Also, the average Co grain size size of the spent catalyst from the MOF-C_2H_2 after reaction was 14.6 nm, which is slightly larger than the average Co grain size calculated from the Scherrer equation in Chapter 4 of around 7.5-8.9 nm. In the work by Zhang et al, the effect of chemical vapour deposition was more apparent. It was shown from HR-TEM images that Co^o nanoparticles were encapsulated in a carbon shell. The carbon shells at lower temperatures (400-450 ^oC) are amorphous, while at higher temperatures (500-600 ^oC) layered graphene of 2-12 layers are shown. The catalyst showed excellent performance at a temperature 260 ^oC after pyrolysis in a 2% C_2H_2 atmosphere at 500 ^oC for 1 hour, which is just above the normal LTFT operating range of 200-250 ^oC. High activity of 242.3 10^{-6} mol g_{Co}^{-1} s^{-1} was recorded, with good C_{5+} selectivity of 75.4 % and low CO_2 selectivity of 4.8 %, at a GHSV of 60,000. Also, an improvement over the same MOF prepared by simple pyrolysis under inert gas was shown, which contained Co nanoparticles with a diameter of 10-12 nm, and showed C_{5+} selectivity of 65 % and CO_2 selectivity of 8 % at 230 ^oC . The other samples were tested at 260 ^oC and it was shown that for samples that underwent pyrolysis at 500 ^oC and above, C_{5+} selectivity increased but activity declined with increasing pyrolysis preparation temperature up to 600 ^oC. It was suggested that the lower activity of the samples that underwent pyrolysis at 550 and 600 ^{o} was due to the less permeable, highly graphitized carbon shells, which may also cause the greater selectivity of $C_{5+,}$ as it may affect diffusion of the reactants and products [67]. From Table 5.4, the MOF/Al_2O_3-C_2H_2 catalyst showed activity of 0.944 10^{-6} mol g_{Co}^{-1} s^{-1}, with a C_{5+} selectivity of 14.7 % and CO_2 selectivity of 0.57 % at a GHSV of 22,963, which shows significantly worse performance. However, it is important to note that in this work the reaction was carried out of a pressure of 10 bar, compared to 30 bar used by Zhang et al [67].

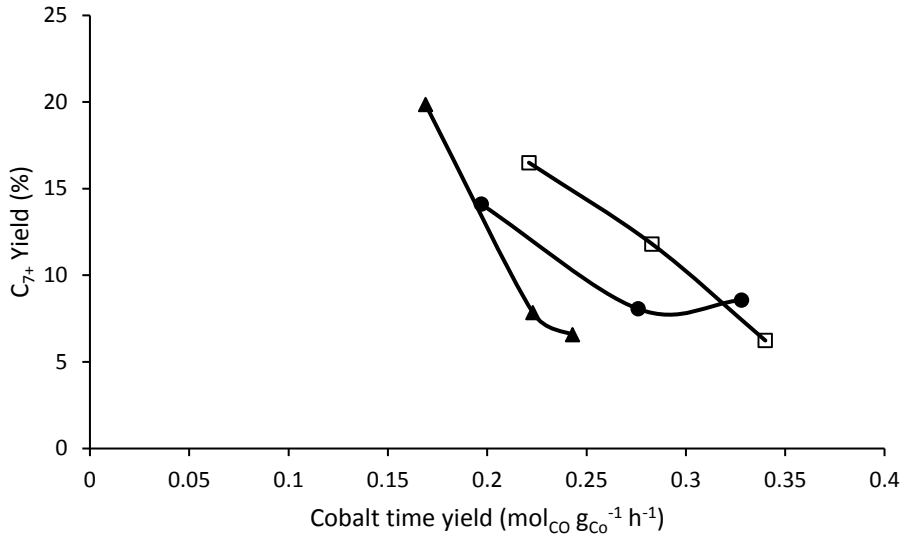

Figure 5.19 Effect of activity on C_{7+} yield. ● = MOF/Al_2O_3, □ = MOF/Al_2O_3-C_2H_2, ▲ = Co/Al_2O_3

Another way of analysing the result in Table 5.4 is displayed in Figure 5.19, which shows the effect of cobalt time yield on the yield of C_{7+} hydrocarbons. It can be seen that the yield of C_{7+} decreases with the cobalt time yield for the three catalysts. A larger cobalt time yield corresponds to more CO converted and more heat released from the conversion. If the reaction heat is not effectively removed, a larger cobalt time yield will result in a higher local temperature on the catalyst. As the local temperature increases, the long hydrocarbon formation reduces, as demonstrated by the yield of C_{7+}, whilst the catalyst activity increases, but the product starts to become dominated by the methane and more significant WGS activity begins to occur [67].

Looking up at a fixed cobalt time yield, i.e. at similar reaction local temperature, it is shown that the MOF-based catalysts exhibit a higher C_{7+} yield. For example, at a cobalt time yield of around 0.25 mol_{CO} g_{Co}^{-1} h^{-1}, the MOF/Al_2O_3-C_2H_2 catalyst gives a C_{7+} yield of 17 %, whereas the MOF/Al_2O_3 catalyst gives a yield of approximately 10 %, which is significantly higher than that of the Co/Al_2O_3 catalyst at 6 %. The MOF-based catalysts show greater selectivity at comparable local temperatures, suggesting that the MOF-based catalyst is actually more selective towards longer-chained hydrocarbons. Similarly, the highest C_{7+} selectivity of the Co/Al_2O_3 at the lower cobalt time yield, can be the result of a lower local temperature of the active site. Due to the lower local temperature, the catalyst showed lower activity in CO conversion and a higher selectivity towards long hydrocarbons.

Previous studies in the literature have extensively presented that the activity and selectivity of cobalt-based FTS catalysts are related to the nanoparticle size and more sensible reaction temperatures [64,

67, 103, 108]. Based on the facts shown in Figure 5.19, it can be concluded that the MOF-derived catalysts are more advanced for higher weight hydrocarbon formation at the temperature higher than 250 °C. The porous carbon support formed from the organic ligand from the original Co-MOF-74 in the catalyst may play a key role in changing the selectivity whilst chemical vapour deposition of acetylene can enhance the selectivity by forming graphene layers on the cobalt nanoparticles [67]. However, the occurrence is not explicitly discussed in the literature, an more findings need to be accumulated to explore in more depth the catalyst design for process intensification.

5.5 Conclusion

This chapter shows the comparison between Co-MOF-74-based catalysts derived directly from pyrolysis in N_2, and a similar catalyst that underwent chemical vapour deposition in a 2% C_2H_2 atmosphere, as well as a conventionally prepared Al_2O_3-supported Co catalyst. The effect of diluting the Co-MOF-74-based catalysts with inert γ-alumina particles was also investigated. It was shown that diluting the Co-MOF-74 with inert γ-alumina particles had a major effect on performance, showing greatly increased selectivity to higher hydrocarbons and significantly lower methane selectivity compared to undiluted catalysts in Chapter 4. This is likely due to the dilution reducing the extremely high bed temperature induced by having such a highly loaded MOF-based catalyst in a highly exothermic reaction, which causes very significant WGS activity detrimental to FTS performance. The conventionally prepared Co/Al_2O_3 showed lower activity but greater selectivity at comparable space velocity compared to the MOF-based catalysts. However, when the catalysts are running at comparable activity, the MOF-based catalysts show greater C_{7+} yields, suggesting that the MOF-based catalysts exhibit better selectivity at comparable bed temperatures. Whilst the improved selectivity of the Co/Al_2O_3 catalyst at comparable space velocity may be linked to the lower bed temperature as a result of lower activity caused by larger nanoparticles. The effect of the chemical vapour deposition of acetylene on the MOF-based catalyst was demonstrated with slightly higher C_{7+} yields at comparable activities, suggesting an improvement in the performance of MOF-based catalysts, however the exact reasons for this are still unclear.

Chapter 6

Investigation of Fixed-Bed Reactor Designs for FTS

6.1 Introduction

Previous chapters have focused on improving the nature of the catalyst for fixed-bed reactors in FTS, which is an important part of FTS research to avoid the awkward catalyst separation required in slurry reactors. Although features such as the catalyst loading, dispersion and metal nanoparticle size can be important, improvements to FTS can be made by altering the design of the reactor bed itself. It has been shown in previous research that the structure of the catalyst particle/pellets can have a significant effect on FTS performance. Mass transport restrictions, which are analogous to the morphology and size of the catalyst particle, have been shown to have a significant effect. For example, reports of smaller catalyst particle size have shown to improve activity and C_{5+} selectivity due to the removal or reduction of transport restrictions [33, 36]. Conversely, a certain level of transport restriction has been shown to improve C_{5+} selectivity [37]. For industrial operation of fixed-bed reactors, a large particle size is required in order to operate at sensible pressure drops [11]. Some solutions to this problem have come in the form of eggshell catalysts, which have shown performance improvement over uniformly dispersed larger particles [39]. Mild transport limitations in eggshell catalyst have even been suspected to improve selectivity to high molecular weight hydrocarbons [40]. The introduction of transport pores has also been shown to have a positive effect [35]. Also, alternative reactor designs such as microchannel and membrane reactors have been investigated as possible solutions to solving mass transport problems. By utilising reactor configurations with many small channels containing the active metal, it is possible to improve performance by removing diffusional restrictions. However, this kind of reactor design is hampered by the low catalyst inventory, requiring a larger volume of reactor [43, 45].

6.1.1 Objectives

The purpose of this chapter is to investigate the effect of a new, alternative membrane reactor design. Through the fabrication of flat disc ceramic membranes via a phase-inversion and sintering process, membranes with two distinct microstructure morphologies were prepared. These membranes were

coated directly with Co and their performance tested in FTS. The orientated micro-channels, often in the region of 80-200 µm diameter, can be used to support the active phase directly, and remove any transport effects that may occur in conventional fixed-bed reactors containing porous catalyst particles. To assess the performance of the membrane reactor, FTS experiments were also performed for the purpose of comparison with γ-Al_2O_3 supported Co catalysts in pellet form, with pellet diameter of 3 mm. Combined with the data collected for the same Al_2O_3 supported Co catalyst ground into fine particle form, a comparison of performance across different Co space velocities and conversions can be drawn. Following on from the experiments with a Co-MOF-74 derived catalyst in Chapter 5, the same catalyst was also tested with the catalyst inside the same ceramic membrane. Previous results in Chapter 5 showed that it is necessary for the Co-MOF-74 derived catalyst to be diluted with inert particles to reduce high bed temperatures that occur due to the highly exothermic nature of FTS, as a result of the extremely high Co loading of the catalyst. By inserting this catalyst into the membrane, it may serve as a suitable support for the Co-MOF-74, which is usually in powder form, as well as further control bed temperature to avoid negative effects on FTS performance. The performance of the Co-MOF-74-based membrane can also be compared to the performance of Al_2O_3 supported Co catalysts and Co based catalytic membranes.

6.2 Experimental

All methods for operation of the reactor, preparation of the Co-MOF-74, γ-Al_2O_3-based Co catalyst, preparation of the ceramic flat disc membranes and catalytic membranes that are outlined in Chapter 3 apply here. All characterisation methods outlined in Chapter 3 also apply. Table 6.1 shows the reaction experiment list for Chapter 6. The Co/Al_2O_3-P catalyst consisted of the 1 g of the calcined γ-alumina supported Co catalyst pellets, which were packed into the reactor and reduced in hydrogen atmosphere. The Co/Al_2O_3 consisted of 1g of the calcined Co/Al_2O_3-P pellets ground and sieved to attain particle sizes of less than 180 µm, which were loaded into the reactor before reduction with H_2. The Co/NMP-PMMA-56 and Co/NMP-PMMA-60 were made by taking the pre-made membranes which underwent an impregnation process describe in Chapter 3, before being calcined and loaded into the reactor for in-situ H_2 reduction. The MOF/NMP-PMMA-56 membrane was prepared by dispersing 1.633 of Co-MOF-74 in ethanol, placing the NMP-PMMA-56 membranes into the beaker, stirring the suspension with membranes inside, and leaving the suspension to settle overnight. The excess methanol was extracted from the suspension using a syringe until the level was just above the settled

suspension, and the remaining suspension was allowed to dry naturally. The Co-MOF-74 was retrieved, whilst some of the Co-MOF-74 gathered on the membrane surface was scraped off, although some was retained in order to retain enough Co required for the reaction to proceed at a conversion of over 10 %.

Table 6.1 Chapter 6 experiment list

Catalyst	**Type**	**Co Loading Wt (%)**	**Reduction/Pyrolysis Temperature (°C)**	**Reduction Time (h)**	**Reduction Atmosphere**
Co/Al_2O_3	Ground particle	9	450	5	H_2
Co/Al_2O_3-P	Pellet	9	450	5	H_2
Co/NMP-PMMA-56	Membrane	2.4	450	5	H_2
Co/NMP-PMMA-60	Membrane	2.1	450	5	H_2
MOF/NMP-PMMA-56	Membrane	1.2	500	1	N_2

6.3 Ceramic Membrane Preparation and Characterisation

Ceramic flat disc membranes were prepared using a phase inversion and sintering process using the procedure outline in Chapter 3 and characterised using a simple digital microscope and SEM microscope. The membrane fabrication technique has been reported in multiple studies previously to prepare hollow fibre and flat disc membranes containing finger-like voids, the morphology of which can vary depending on the preparation procedure [54, 56]. Previous examples of the fabrication of ceramic membranes using this technique were discussed in Chapter 2. Of particular interest is how the morphology of the finger-like voids can be altered significantly depending on the solvent used, which was reported by Lee et al [57]. Initially in this work, two membranes with distinct structures were prepared. One using NMP as a solvent and PMMA as the polymer binding agent, and the other using

a DMSO solvent and PESf as the polymer binder, denoted as NMP-PMMA-58 and DMSO-PESf-58, respectively. The preparation mixtures can be seen in Table 6.2. 150 g of α- Al_2O_3 was used as the base. The amount of polymer was based on one tenth of the amount of α-Al_2O_3, whilst the A135 dispersant was based on 1/1000th of the surface area of the α-alumina. The amount of solvent was adjusted to make the wt% of α-alumina to 58 %.

Table 6.2 Preparation mixture for the preparation of NMP-PMMA-58 and DMSO-PESf-58

Component	**g**	**Wt%**
NMP/DMSO	92.6	35.8
α-Al_2O_3	150.0	58.0
PMMA/PESf	15.0	5.8
A135	1.1	0.4

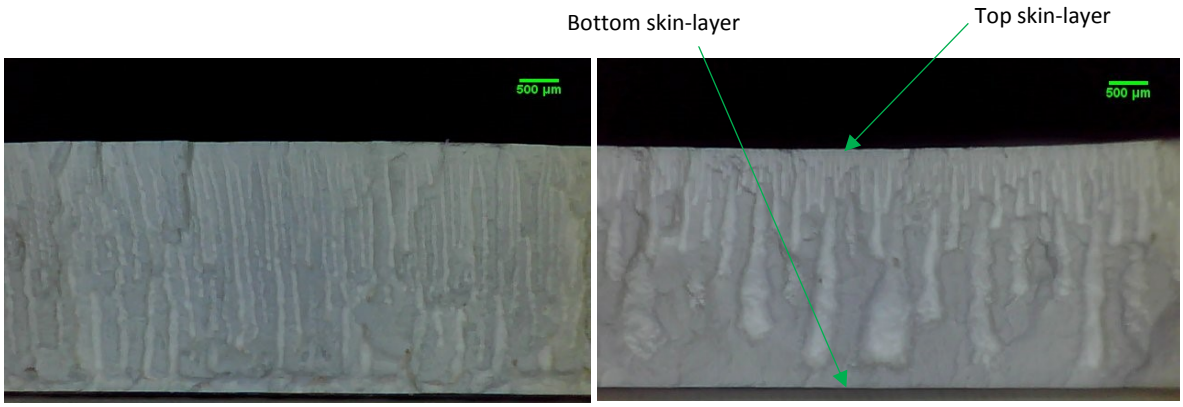

Figure 6.1 Membrane cross-section of DMSO-PESf-58 (left) and NMP-PMMA-58 (right) taken using digital microscope

Figure 6.1 shows the cross-section of the two flat disc membranes, and without sanding of the top and bottom skin-layer. Finger-like voids have formed, which are separated by a sponge-like layer. It is clear that the morphology of the finger-like voids in the two membranes is very different. The DMSO-PESf-58 membrane exhibits narrow straight channels that are densely packed. Conversely, the NMP-PMMA-58 membrane shows channels with a bell-like structure, with increasing channel diameter with increasing distance from the top-surface of the membrane. The channels in this case are less densely packed, and there is a noticeable reduction in the number of channels that are able to penetrate deep into the membrane. This phenomenon is similar to that reported by Lee et al, who showed that using NMP and DMSO solvents in Al_2O_3/PESf-based membranes exhibited similar results. The phase inversion process that leads to the formation of the channels is very complex. When the coagulant, in this case water, comes into contact with the suspension, it leads to instability at the interface between the two fluids. At this interface, there is a difference in viscosity, density and composition between the two fluids. At the moment of contact, the outflow of solvent and the inflow of coagulant cause the interface to accelerate rapidly towards the suspension side due to the extraction of solvent and contraction of polymer. The transfer of mass and heat cause significant disturbances at the interface. The disturbances that occur in the interface can grow and lead to finger-like void formation, whilst the extraction of the solvent leads to the precipitation of the polymer and the solidification of the finger-like void shape, separated by a sponge-like layer [57]. A simple schematic diagram shown in Figure 6.2 can help to display this occurrence. It is thought that the formation of the channels, or finger-like voids, can occur due to hydrodynamically unstable viscous fingering, a phenomenon that occurs at the interface of two fluids of different viscosities. At the first moments of mixing between the precursor suspension and non-solvent, the steep concentration gradient results in solvent/non-solvent exchange, causing a rapid increase in viscosity and the precipitation of the polymer phase. The interfacial instability that arises at the interface between the solvent and non-solvent lead to the occurrence of viscous fingering and the formation of the finger-like voids due to the viscosity difference between the two fluids [56]. It has also been suggested that the formation of the channels can be attributed to Rayleigh-Taylor instability, which occurs when there is acceleration of the interface between two fluids of different densities, from the lighter fluid to the heavier fluid [57].

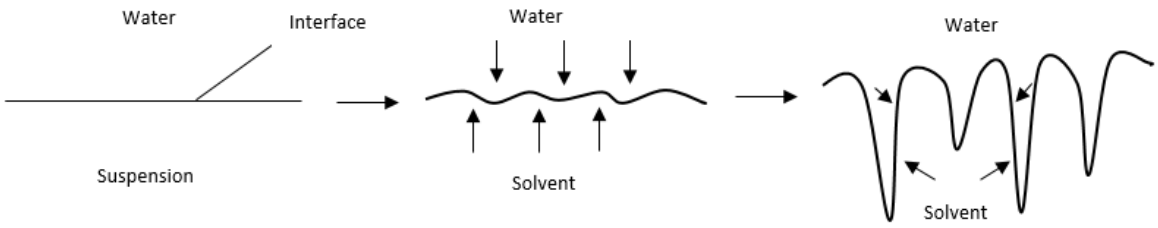

Figure 6.2 Schematic diagram of interfacial instability and channel propagation

There are many factors that can affect the morphology of the micro-channels, but mainly it is affected by the initial momentum of the inflowing coagulant, the rate of the increase of viscosity at the channel wall, and diffusional inflow of the solvent from the surrounding suspension into the micro-channel [57]. The difference in morphology of the finger-like voids between the two membranes in Figure 6.1 can be largely explained by the solubility of the polymer binder in the solvent. The viscosity of the micro-channel side wall increases faster than the head of the forming channel due to a more significant concentration gradient caused by shear flow, leading to faster solvent and coagulant exchange at the channel wall [57]. Also, DMSO is a weaker solvent for PESf compared to NMP for PMMA. This can be seen from ternary polymer phase diagrams shown in previous studies and demonstrated in the schematic diagrams in Figure 6.3 and Figure 6.4. When plotting the cloud points of a NMP-PMMA-water system, the points are located in line with a solvent to water percentage of about 90 %, until a tail is reached which shows a greater homogenous phase range. The extension of this tail means more water is needed to precipitate the polymer [113]. Whereas cloud point plots of DMSO-PES-water systems show a smaller homogenous phase range, with water percentages of less than 10 % leading to precipitation of the polymer, whilst no tail is present [114]. This shows the precipitation rate of the polymer is faster in a DMSO-PES-water system compared to an NMP-PMMA-water system, meaning a faster increase in viscosity at the channel wall, constraining the radial growth of the channel. This manifests as the narrow channels observed in Figure 6.1 for the DMSO-PESf-58 membrane. On the contrary, as the precipitation of PMMA in NMP is slower, greater radial growth of the channel occurs before the precipitation of the polymer causes the viscosity of the channel wall to increase and prevent further radial growth. As a result, the diameter of the channel increases with increasing length from the top surface. When the inflow of water loses its momentum, the growth of channels relies more on the diffusion of the solvent from the suspension into the channel. As this growth is not directed, the head of the channel will grow from all directions, leading to a rounded bottom, shown in the NMP-

PMMA-58 membrane [57]. This does not occur in the DMSO-PESf-58 membrane, as the faster polymer precipitation will prevent this diffusion-based growth.

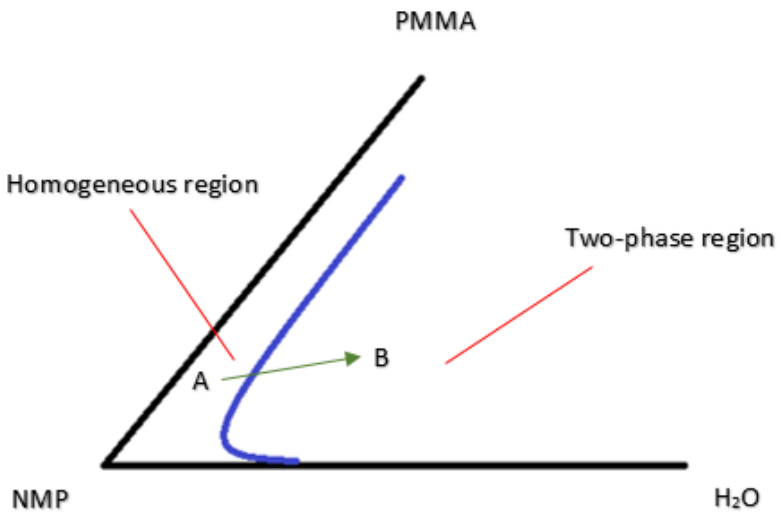

Figure 6.3 Simple schematic diagram of a ternary phase diagram for a NMP/PMMA/water system

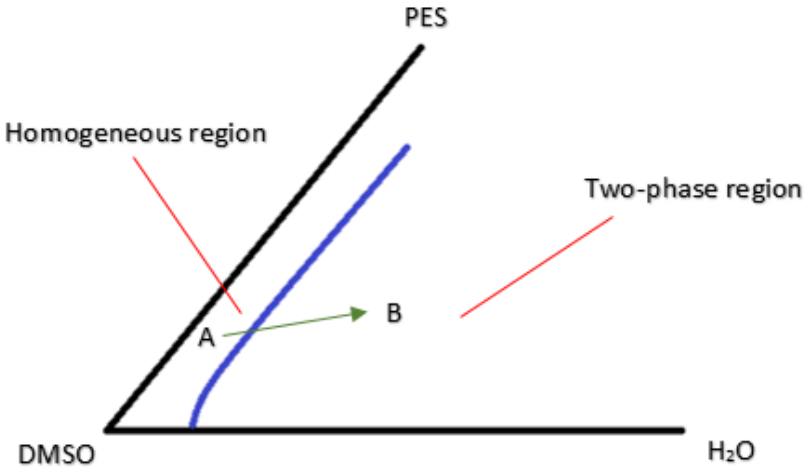

Figure 6.4 Simple schematic diagram of a ternary phase diagram for a DMSO/PES/water system

Unfortunately, after ordering new Al_2O_3 powder for the fabrication of the membranes, the DMSO/PESf-based membranes failed to provide any microstructure, and instead exhibited a uniform sponge-like layer throughout the whole cross-section of the membrane. The reason for this was unclear and DMSO-PESf-based membranes were not pursued further. This was unfortunate, as these membranes provided a radically different microstructure to NMP/PMMA-based membranes, whilst having a higher density of channels in the bottom third of the membrane, providing more channels for catalytic membrane operation. Therefore, efforts were directed at altering the microstructure of the NMP-PMMA membranes to reduce channel diameter and increase channel density in the mid to bottom thirds of the membranes by altering the parameters of the precursor suspension. The channel morphology of NMP-PMMA-based membranes can be altered quite dramatically.

NMP-PMMA-based membranes with two distinct cross-sectional morphologies were prepared to test as forced-through contactor catalytic membranes in FTS. Two different precursor suspensions were prepared to create flat disc membranes through the phase-inversion assisted process. The precursor suspensions for the two membranes, NMP-PMMA-56 and NMP-PMMA-60, can be seen in Table 6.3 and Table 6.4, respectively.

Table 6.3 Precursor suspension composition for the NMP-PMMA-56 membranes

Component	**g**	**Wt%**
NMP	86.8	32.4
α-Al_2O_3	150.0	56.0
PMMA	30.0	11.2
A135	1.1	0.4

Table 6.4 Precursor suspension composition for NMP-PMMA-60 membrane

Component	**g**	**Wt%**
NMP/DMSO	84.0	33.6
α-Al_2O_3	150.0	60.0
PMMA	15.0	6.0
A135	1.1	0.4

Compared to the NMP-PMMA-58 membrane, decreasing the ceramic/polymer ratio of the NMP-PMMA-56 membrane from 10 to 5, which doubles the amount of polymer in the precursor suspension, was done to reduce the micro-channel diameter. By increasing the amount of polymer in the solvent, the solution will be closer to its cloud point. When the suspension comes into contact with the coagulant and phase inversion occurs, the polymer will precipitate faster. As a result, a faster increase in viscosity at the micro-channel wall will constrain its radial growth and form thinner micro-channels, as opposed to bell-shaped micro-channels with large diameters. To offset the increase in viscosity of suspension at the micro-channel head during micro-channel formation, which could impede the axial growth, the wt% of α-alumina was decreased from 58 to 56 wt% by increasing the solvent amount. The NMP-PMMA-60 membrane had the same composition as the NMP-PMMA-58 membrane, except the weight percentage of α-alumina was increased slightly by decreasing the amount of solvent. This adjustment was made in response to the new α-Al_2O_3 powder to create the large-diameter channels.

Figure 6.5 Digital microscope image of the cross-section of the NMP-PMMA-56 membrane with top and bottom skin-layers removed

Figure 6.6 Digital microscope image of the cross-section of the NMP-PMMA-60 membrane with top and bottom skin-layers removed

The effect of this can be seen in Figure 6.5, which shows the NMP-PMMA-56 membrane with the top-surface sanded away. A significantly different micro-structure is present compared to the NMP-PMMA-60 membrane shown in Figure 6.6, with straight channels of approximately 100 µm. In order to study the effect of the micro-structure in FTS, a comparison between two radically different micro-structure is preferred. It can be seen that the lower ceramic/polymer ratio in the NMP-MMA-56 membrane leads to the reduction in channel diameter due to the faster precipitation of polymer at the channel wall. The NMP-PMMA-60 membrane in Figure 6.6 shows larger micro-channels than the NMP-PMMA-56 membrane, with a diameter over 100 µm, and lower finger density, with 9 channels counted in the

mid-section of the sanded membrane, compared to about 29 channels for the same-sized membrane cross-section in the NMP-PMMA-56 membrane.

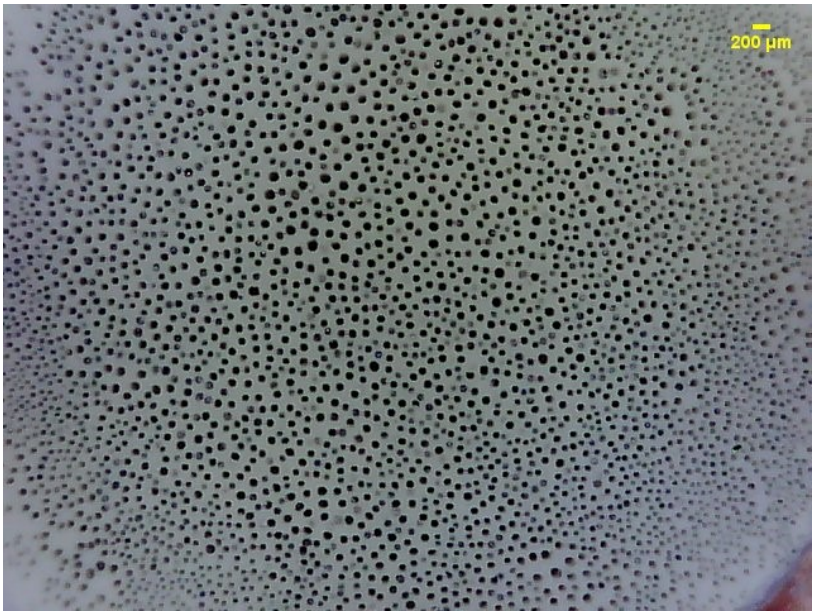

Figure 6.7 Digital microscope image of the top-surface of the sanded NMP-PMMA-56 membrane

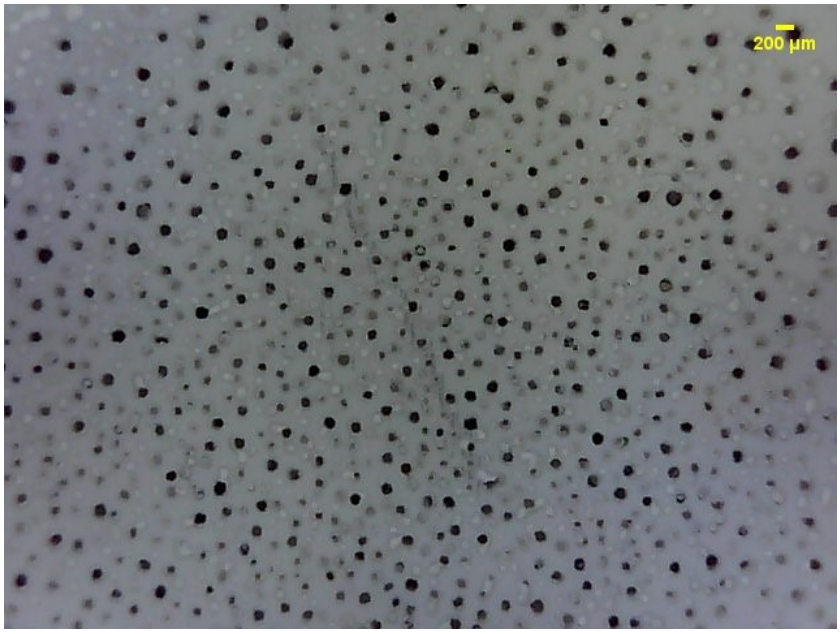

Figure 6.8 Digital microscope image of the top-surface of the sanded NMP-PMMA-60 membrane

Figure 6.7 shows the top-surface of the NMP-PMMA-56 membrane after removal of the top skin-layer by sanding. Each membrane was reduced in thickness from 3 mm to 1.3 to 1.7 mm in order to remove the top and bottom skin-layer. The skin-layer of is often critical for separation processes, as it acts as the separation layer, whilst the larger micro-channels act as a support. However, it is not necessary for this application. The top surface shows a high density of similarly sized channels, with largest channels show a diameter of approximately 100 µm or less. In comparison, the top-surface of the NMP-PMMA-60 membrane shows a lower channel density with a fairly uniform channel diameter of around 100 µm. Figure 6.9 shows the bottom surface of the NMP-PMMA-56 membrane, which shows a lower channel density with a larger channel diameter, with many channels larger than 200 µm. This shows that not all the channels are able to penetrate deep into the membrane and it is expected that more channels would be exposed with a greater degree of sanding. However, to ensure the structural integrity of the membrane, this extent of sanding is limited. As the bottom surface channels shows a greater diameter, it is clear that the channel increases with length. Although the cross-section shows fairly straight channels for the NMP-PMMA-56 membrane, it is impossible to prevent the radial growth of the micro-channel to a certain degree, as the viscosity increase at the channel wall cannot be instantaneous. Figure 6.10 shows the bottom surface of the NMP-PMMA-60 membrane. A significantly lower channel density is present, whilst the channel bottom shows a dramatic increase in diameter, with many channel openings showing a diameter of around 400 µm. It appears like a channel within the channel, where the diameter becomes constricted to about 100 µm in the upper regions.

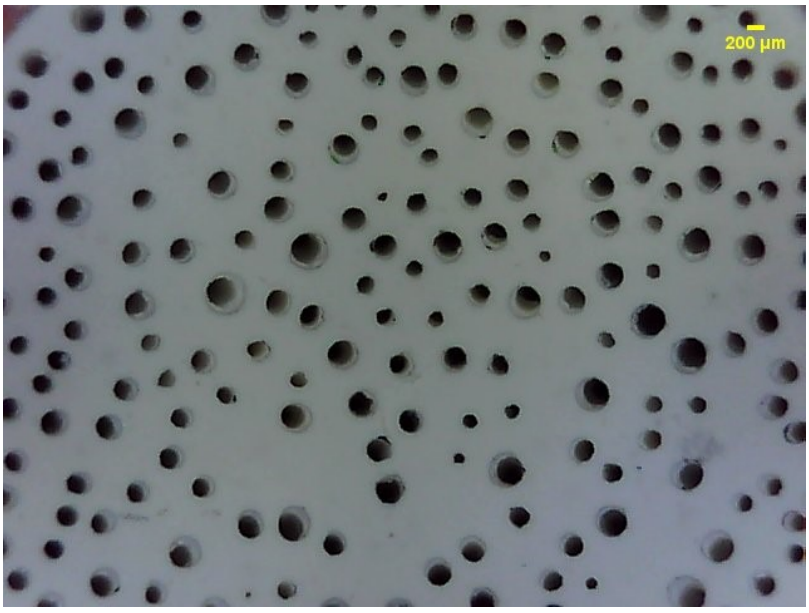

Figure 6.9 Digital microscope image of the bottom-surface of the NMP-PMMA-56 membrane

Figure 6.10 Digital microscope image of the bottom-surface of the NMP-PMMA-60 membrane

Figure 6.11 Digital microscope image of the NMP-PMMA-56 spent membrane cross-section

Figure 6.12 Digital microscope image of the NMP-PMMA-60 spent membrane cross-section

Figure 6.11 and Figure 6.12 show the spent membrane cross-section of the NMP-PMMA-56 and NMP-PMMA-60 catalytic membranes after reaction. It is clear compared to the images of the unimpregnated membrane in Figure 6.5 and Figure 6.6 that the Co was deposited inside the membrane micro-channels. The amount of Co in the channels does not seem to be uniformly dispersed, and the amount seems to vary between channels. Also, some of the Co seems to be deposited on the sponge-like layer separating the channels. However, it is not clear whether this Co settled here after breaking the membrane, or whether it was a result of the impregnation process. It can be seen that the Co on the sponge-like layer is localised, and not dispersed throughout the membrane cross-section.

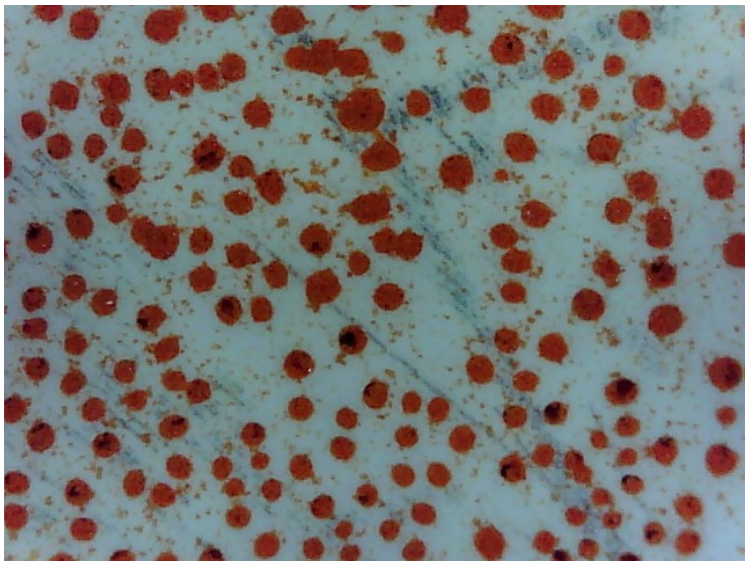

Figure 6.13 Top surface of an NMP-PMMA-56 membrane after deposition with Co-MOF-74

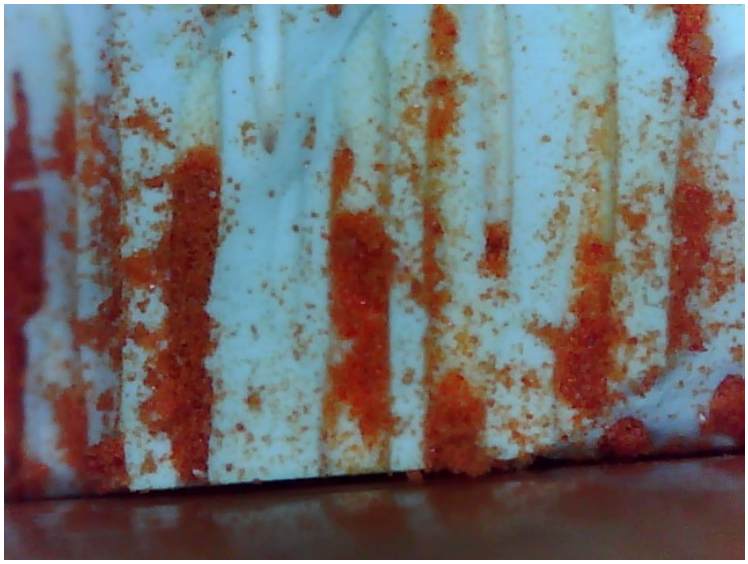

Figure 6.14 Cross-section of an NMP-PMMA-56 membrane after deposition with Co-MOF-74

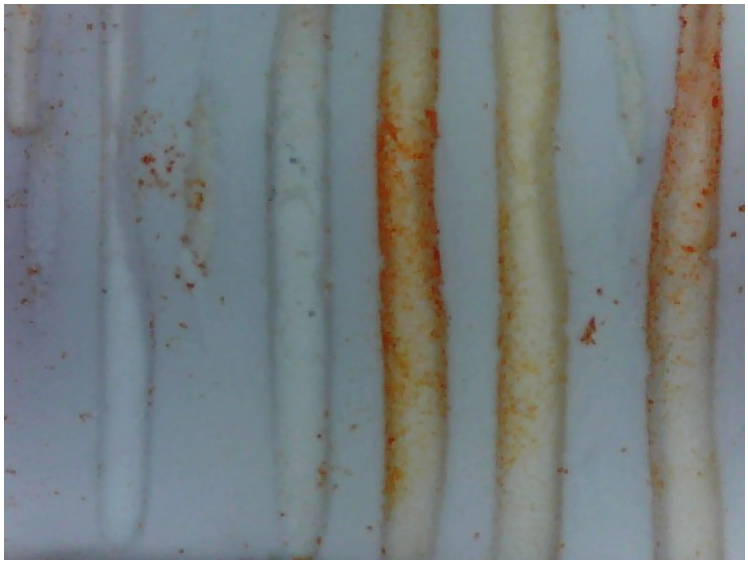

Figure 6.15 Cross-section of an NMP-PMMA-56 membrane after deposition with Co-MOF-74

Figure 6.13 shows the top-surface of an NMP-PMMA-56 membrane after deposition with Co-MOF-74, whilst Figure 6.14 and Figure 6.15 show the cross-section. It is clearly shown that the Co-MOF-74 can settle inside the channel, but it is difficult to achieve uniformly dispersed Co-MOF-74, with some channels showing very little of the MOF and others showing abundant amounts.

SEM-EDX

An SEM microscope with EDX was used to provide more detailed characterisation of the membrane, and the spent catalytic membrane after reaction. The membranes underwent impregnation with a solution of cobalt acetate, before drying and undergoing calcination in air and reduction in the reactor to attain the metallic Co, the details of which are included in Chapter 3. After reaction, the spent catalytic membranes were removed for characterisation. Figure 6.16 shows an SEM of the top-surface of the membrane before impregnation. This image more clearly shows the micro channel morphology, where the channel diameter can be estimated more accurately to be between 50 and 100 µm. There are also a number of channels that seem blocked, or exhibit the outline of a channel but without a hollow void. These channels may be filled with debris form the sanding procedure, which is difficult to remove. In some cases, the top-surface has not been sanded deep enough, meaning these channels are still covered by thin skin-layer. Figure 6.17 shows an example of the micro-channel opening of the top-surface at a greater magnification, showing well-formed micro-channels with a diameter of approximately 50 µm. The image in Figure 6.18 shows an SEM image of the bottom surface of the NMP-PMMA-56 membrane, and it can be clearly seen by comparing to Figure 6.16 that there is a lower channel density and larger channel diameter, with many channels showing a diameter of over 100 µm.

Figure 6.19 shows an SEM image of the top-surface of the NMP-PMMA-60 membrane after sanding the top-surface. Channel opening with varying diameters are shown, with the largest channels showing diameters of approximately 80 µm, whilst the smallest channels show diameters of about 30 µm. By comparing to the top-surface of the NMP-PMMA-56 membrane in Figure 6.16, a slightly less uniform channel diameter is present, whilst similar signs of blocked channels are displayed. A magnified view of the channel opening can be seen in Figure 6.20, where a clear difference in channel morphology can is present compared to the NMP-PMMA-56 membrane in Figure 6.17. As opposed to displaying a well-formed, cylindrical channel, a jagged misshaped channel is shown with a diameter of about 20 µm. The most obvious difference is displayed in Figure 6.21, which shows a magnified SEM of the bottom surface of the NMP-PMMA-60 membrane. A drastic change in channel morphology is shown compared to the top surface of the NMP-PMMA-60 membrane and the bottom surface of the NMP-PMMA-56 membrane. An increase in channel diameter is shown, with a channel diameter of about 200 µm, whilst the channel opening shows a misshapen morphology, likely due to the slower rate of precipitation.

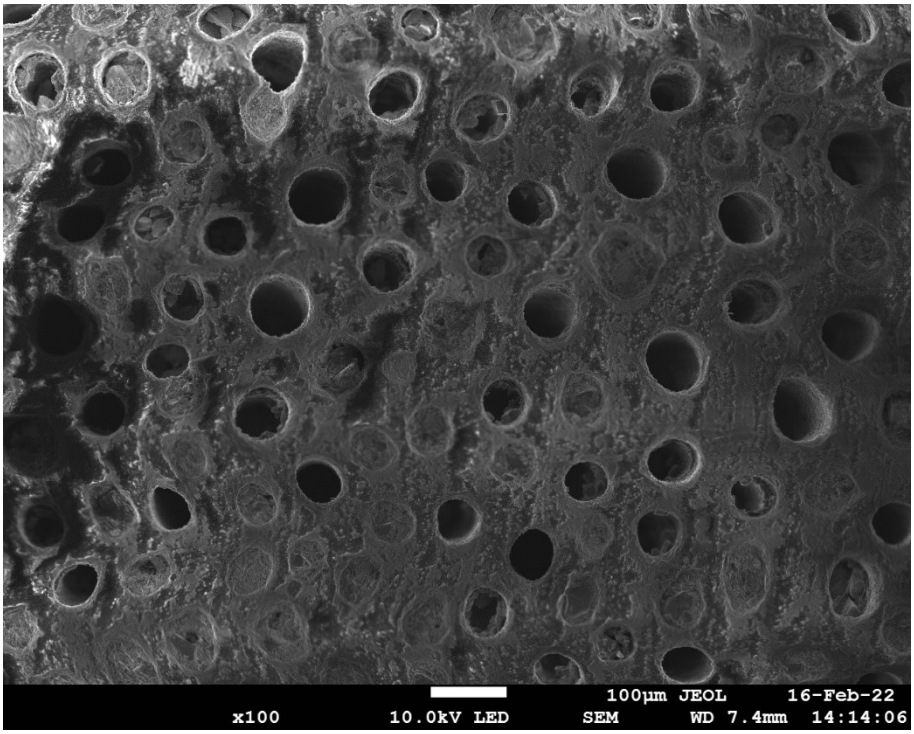

Figure 6.16 SEM image of the NMP-PMMA-56 top-surface before impregnation

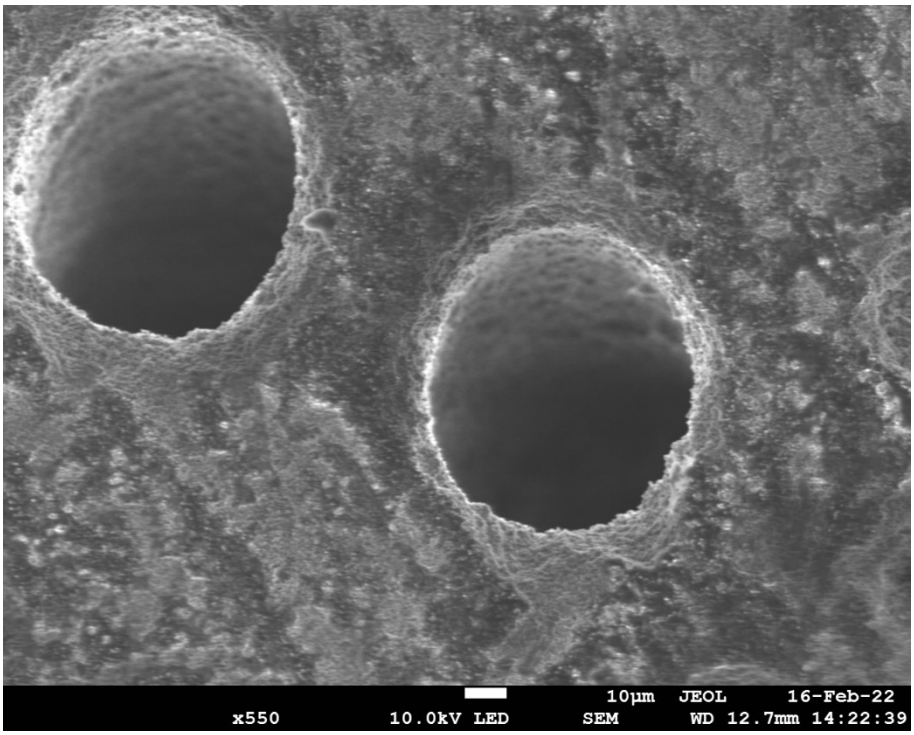

Figure 6.17 Top-Surface of the NMP-PMMA-56 membrane before impregnation

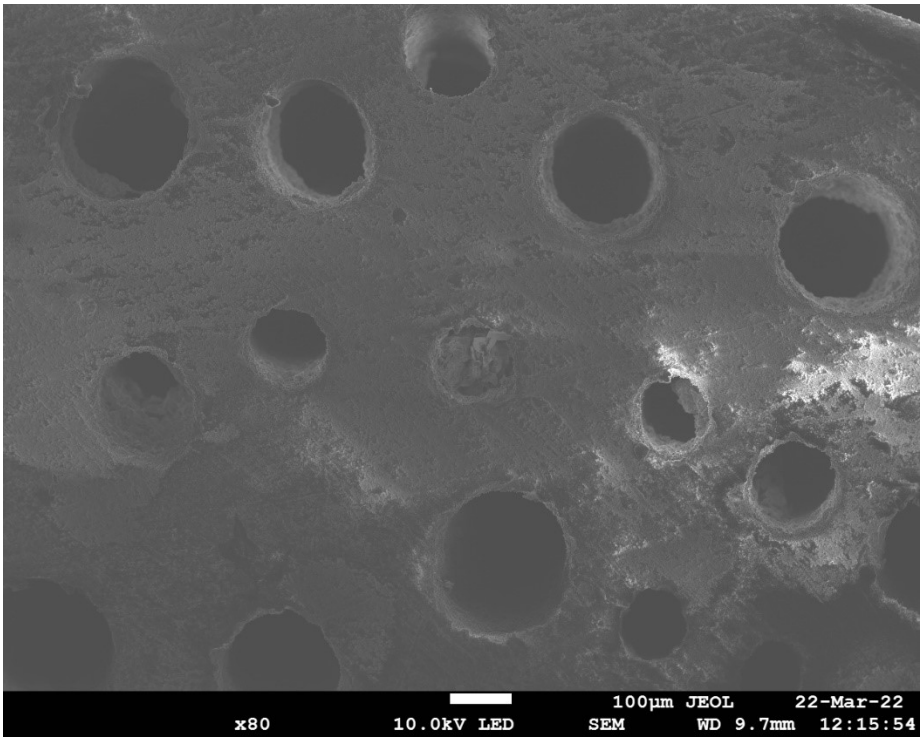

Figure 6.18 SEM of the bottom surface of the NMP-PMMA-56 membrane before impregnation

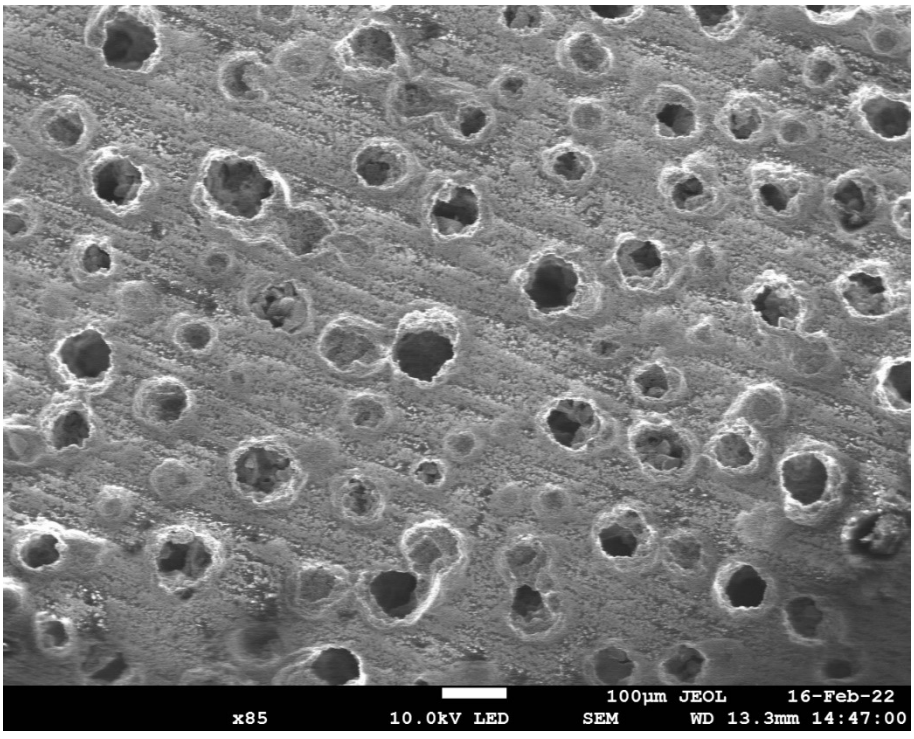

Figure 6.19 SEM image of the top-surface of the NMP-PMMA-60 membrane before impregnation

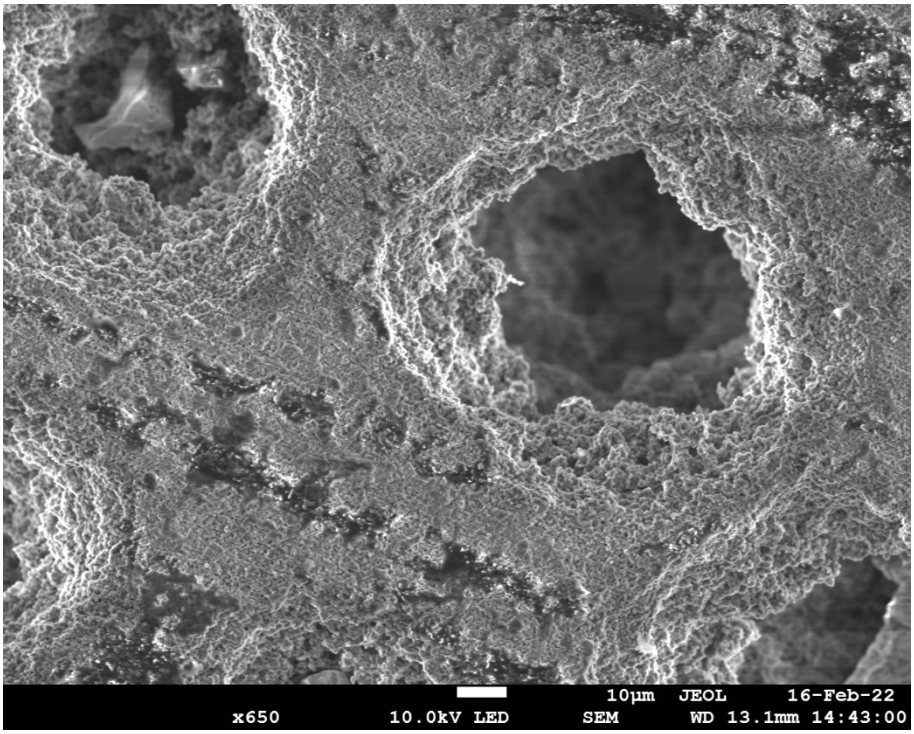

Figure 6.20 SEM image of the top-surface of the NMP-PMMA-60 membrane before impregnation

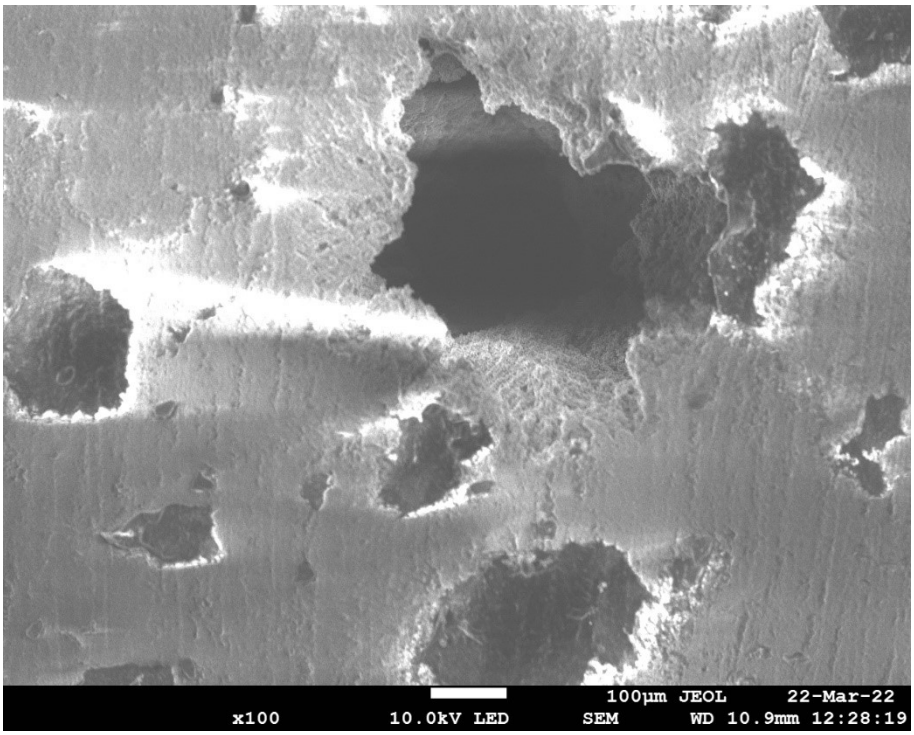

Figure 6.21 SEM image of the bottom-surface of the NMP-PMMA-60 membrane

Figure 6.22 shows the cross-section of the NMP-PMMA-56 spent catalytic membrane. It is clearer from this image that the channel diameter of the cross-section is approximately 80-100 µm and there is little increase is channel diameter with channel length. Conversely, the cross section of the spent NMP-PMMA-60 membrane in Figure 6.23 shows a much larger and less well-defined channel, with increasing diameter with length. The top section of the channel has a diameter of approximately 50 µm, whereas the diameter at the very bottom is over 200 µm.

Figure 6.24 shows a backscattered SEM image taken of the cross-section of the NMP-PMMA-56 membrane after reaction, in order to highlight the different elements that may be present. It can be clearly seen that shades of lighter coloured material are present, which likely represents the Co, due to its higher atomic mass. The light-coloured material is shown to occupy almost the whole of one micro-channel in large amounts, whereas it is present in significantly smaller amounts in other channels, but small light-coloured spots are still present. This is possible evidence that Co is present inside the channel, whilst also showing that the Co is not distributed in even amounts among the channels. Figure 6.25 shows the top-surface of the NMP-PMMA-60 spent membrane. On the surface, a light-coloured material can be seen, which represents a material change and is likely to be Co. This is confirmed by the EDX mapping in Figure 6.26, which clearly shows Co distributed on the surface of the membrane. It can be seen from both images can Co is present in large agglomerations near some of the channel openings, whilst also present as much smaller particles distributed on the surface. From Figure 6.25, the agglomerates can be as large as approximately 30 µm in diameter, whilst much smaller Co particles are present which are less than 10 µm and some even in the range of 1 µm. Considering the magnification of the image, it is difficult to see much smaller Co particles. Figure 6.27 shows the single element EDX mapping of Co and Al. It is clearer from this image that Co is distributed across the whole top-surface of the membrane. Although large agglomerates are present, the average Co particle size is likely to be much smaller. But considering the size of agglomerates and other larger particles seen in this image, it is highly likely that the average particle sizes is much larger than the Co-MOF-74-derived catalysts, and possibly larger than the Co/Al_2O_3 catalysts, due to the highly concentrated impregnation solution used.

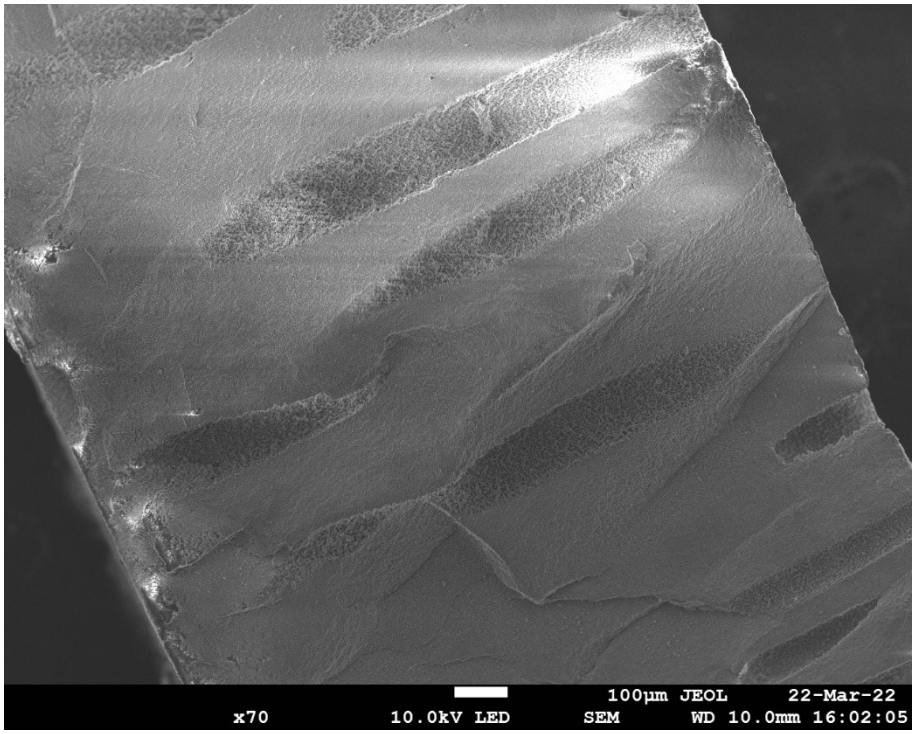

Figure 6.22 SEM image of the cross-section of the spent NMP-PMMA-56 membrane after reaction

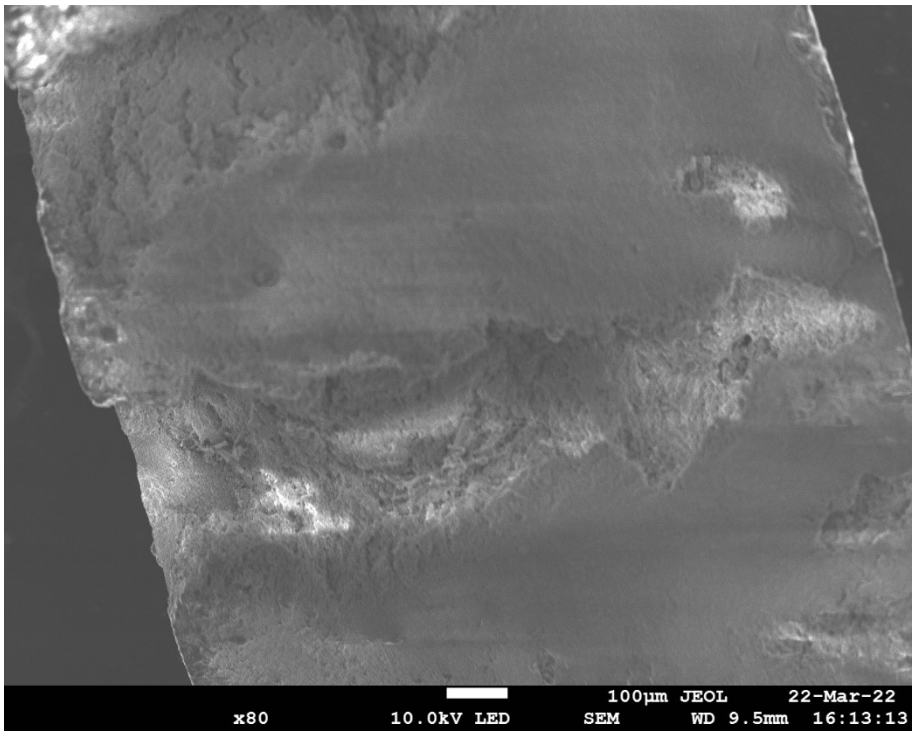

Figure 6.23 SEM image of the cross-section of the spent NMP-PMMA-60 membrane after reaction

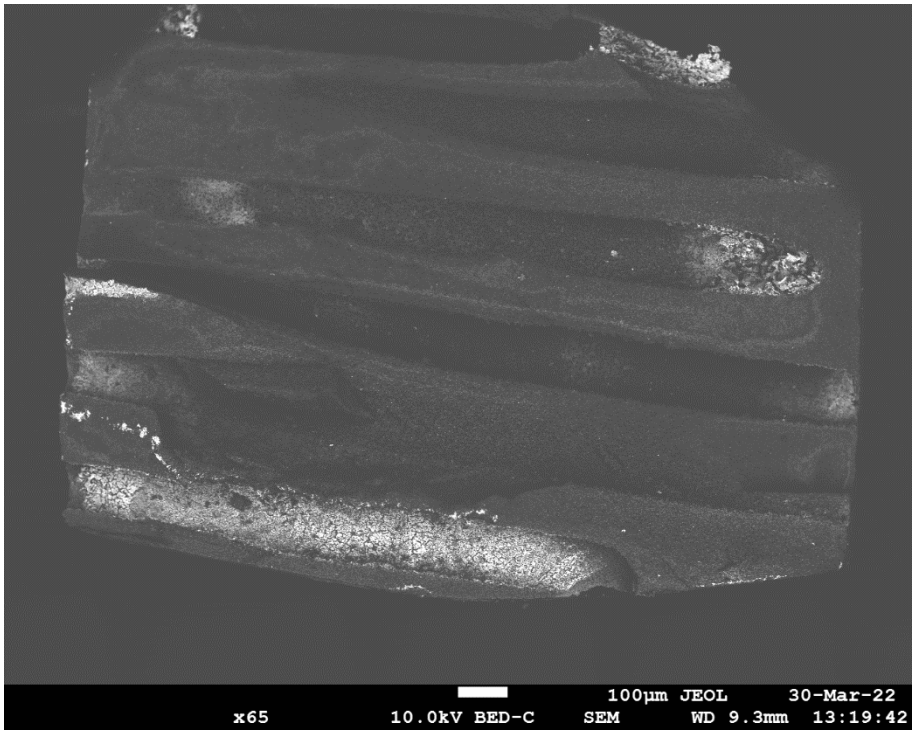

Figure 6.24 Backscattered electron SEM image of the spent NMP-PMMA-56 membrane cross-section after reaction

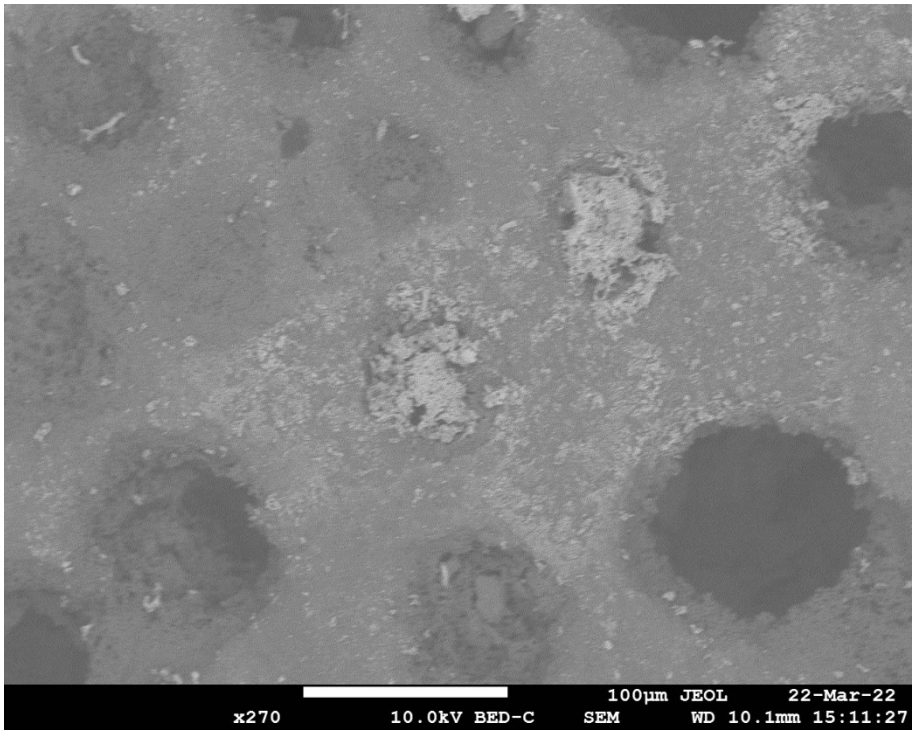

Figure 6.25 SEM image of the top-surface of the NMP-PMMA-60 spent membrane after reaction

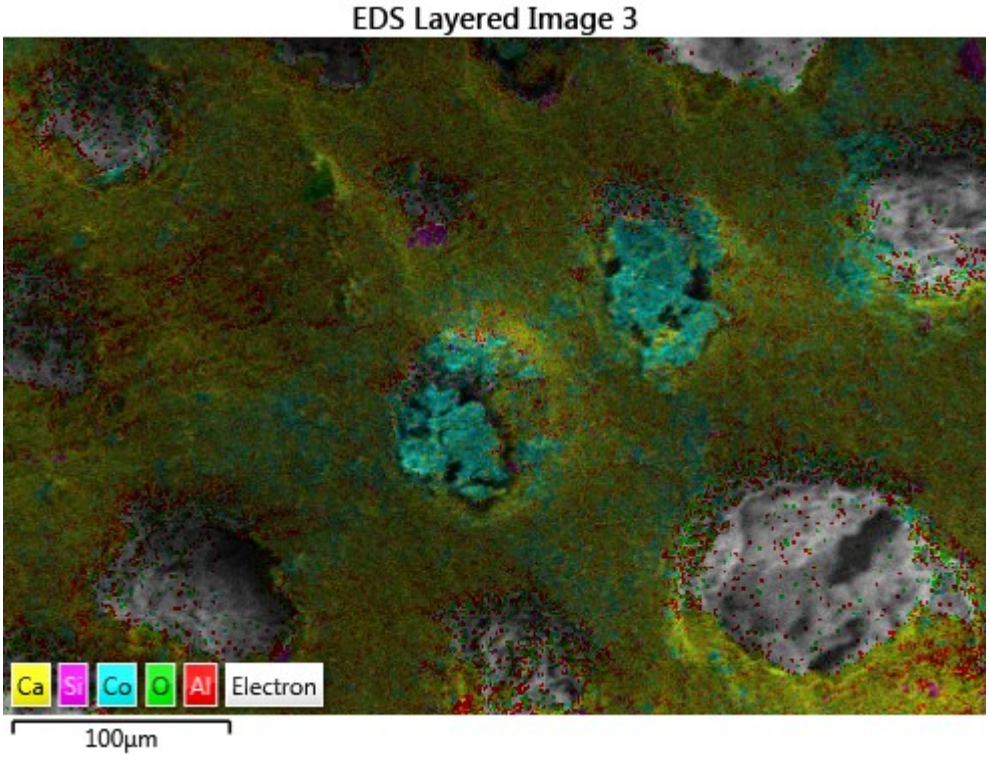

Figure 6.26 SEM-EDX mapping image of the top-surface of the spent NMP-PMMA-60 membrane after reaction

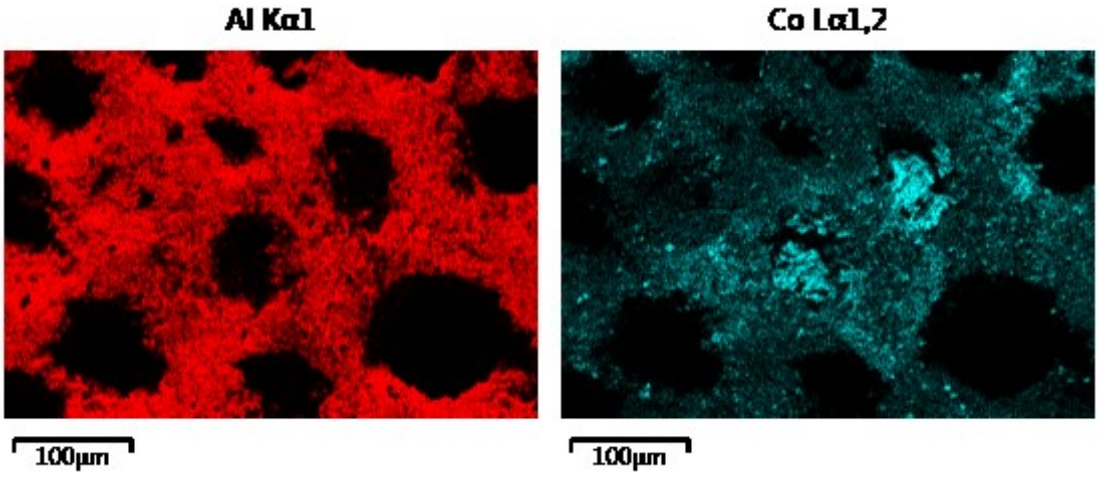

Figure 6.27 EDX element mapping of Al (left) and Co (right) on the top-surface of the spent NMP-PMMA-60 membrane

XRD

In order to estimate the average Co nanoparticle size using the Scherrer equation, the membranes were ground into powder and analysed using XRD. However, as can be seen from the XRD spectra of the ground NMP-PMMA-56 and ground NMP-PMMA-60 membranes in Figure 6.28 and Figure 6.29, respectively, the only obvious peaks shown are those of the α-alumina. The peaks at approximately 2θ = 25 °, 35°, 38°, 43.4 °, 52.5 °, 57 °, 61 °, 66 °, 68 ° and 77 ° show the 012, 104, 110, 113, 024, 116, 018, 024, 030, 119 lattice planes of α-Al_2O_3 [115, 116]. It is likely that the FCC Co peaks normally observed at 2θ = 44.3 °, 51 ° and 77 ° are obscured by the 113, 024 and 119 peaks of α-Al_2O_3, as they appear at very similar, almost identical, 2θ values. A very small peak around 2θ = 44.3 ° occurs, but this is also shown on one of the reference spectra. The only peak that isn't found in the reference α-Al_2O_3 spectra is the peak located at approximately 2θ = 30. However, this peak does not correspond to any cobalt or cobalt oxide lattice plane [78].

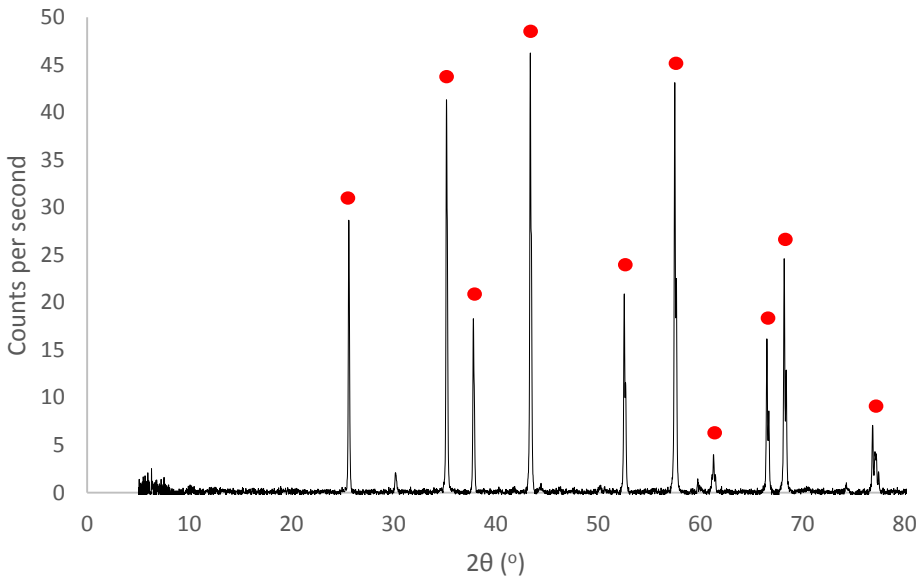

Figure 6.28 XRD spectrum of the ground NMP-PMMA-56 spent membrane after reaction. ● = α-Al_2O_3 peaks

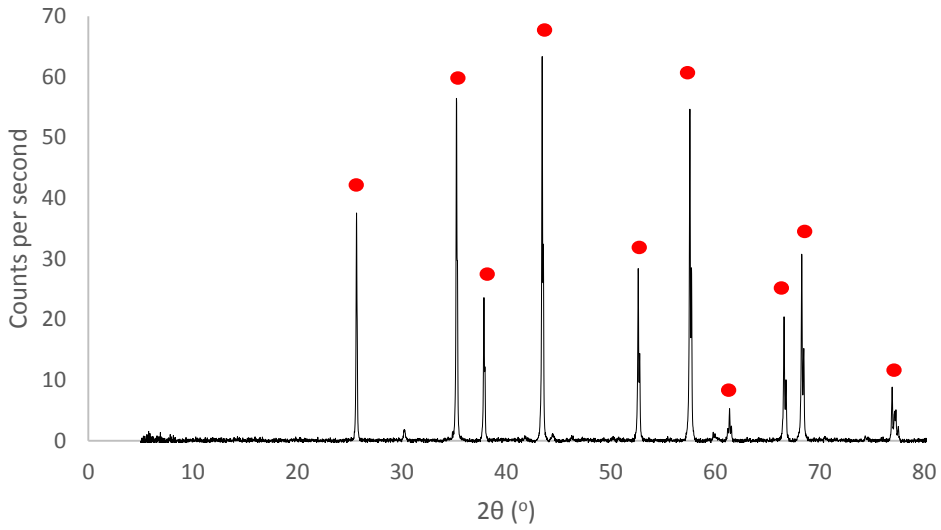

Figure 6.29 XRD spectrum of the ground NMP-PMMA-60 membrane spent membrane after reaction. ● = α-Al_2O_3 peaks

Mercury Intrusion

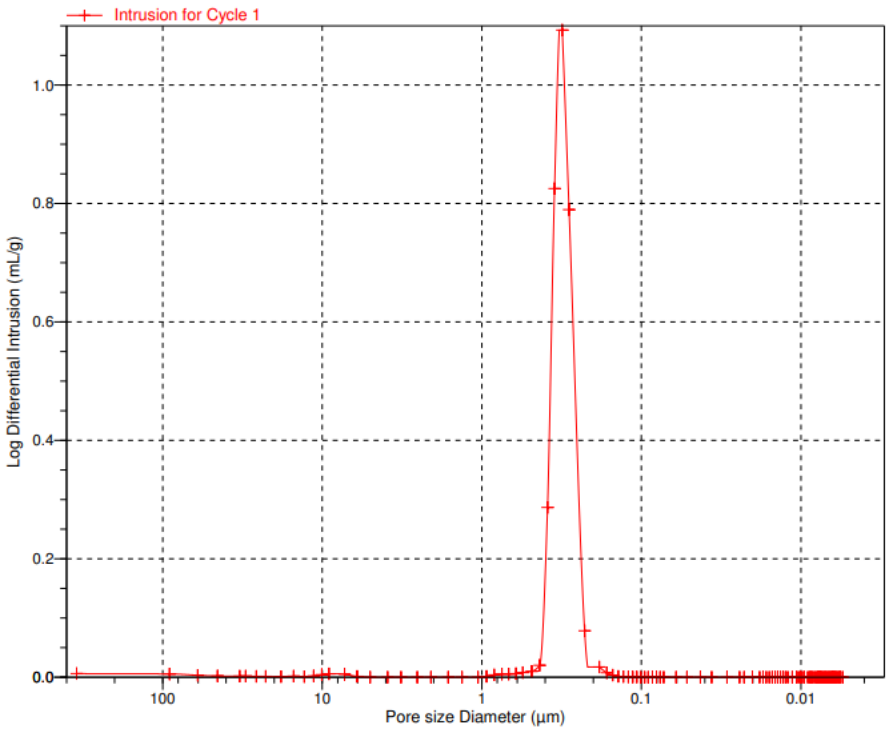

Figure 6.30 Plot of pore size diameter and log differential intrusion from mercury intrusion of the NMP-PMMA-56 membrane before impregnation

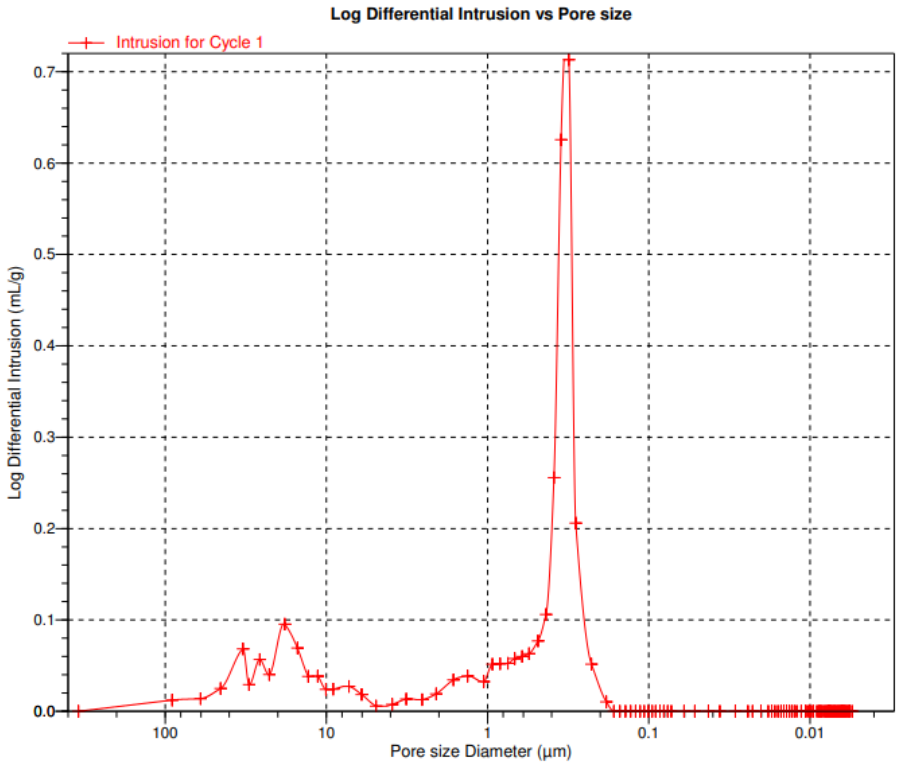

Figure 6.31 Plot of pore size diameter and log differential intrusion from mercury intrusion of the NMP-PMMA-60 membrane before impregnation

Figure 6.30 and Figure 6.31 show the mercury intrusion plots of the NMP-PMMA-56 and NMP-PMMA-60 membranes, respectively. The mercury intrusion was performed with the top surface still present. From Figure 6.30, a large peak at around 0.7 µm represents the sponge-like layer that separates the micro-channels and makes up the skin-layer. This shows that pore diameter of sintered the α-alumina sponge-like layer is very large compared to that of the MOF-derived and γ-alumina based catalysts. The peak around 10 µm represents the micro-channels. A similar peak for the sponge-like layer is observed in Figure 6.31, however much larger peaks at larger pore size diameters are noticeable for the micro-channels. This shows the much larger pore diameter and volume of the NMP-PMMA-60 membrane.

6.4 Results and Discussion

Table 6.5 shows the reactions results for each catalyst in Chapter 6, where each catalyst was run at three different cobalt space velocities. The Co/Al_2O_3 catalyst has also been included from Chapter 5, to show a comparison between powder, pellet and membrane-based Co catalysts. Figure 6.32 shows the relationship between space velocity and conversion for all results, excluding the MOF/NMP-PMMA-56 run, which will be discussed separately. It can be seen that conversion increases with decreasing space velocity for all the catalysts aside from the Co/NMP-PMMA-60 catalyst, which shows the highest conversion of 0.46 at a space velocity of 652 $cm^{-3}\,min^{-1}\,g_{Co}^{-1}$. The general decrease in conversion with space velocity can be explained by the fact that conversion is inversely proportional to the flowrate, as shown in Equation 5.2. It is also acknowledged in literature that increasing space velocity results in decreased conversion in FTS reactions [89]. The Co/AL_2O_3 – P shows the highest conversion at the space velocities of 652 and 943 $cm^{-3}\,min^{-1}\,g_{Co}^{-1}$ and displayed the highest conversion of all the catalysts at a space velocity of 652 $cm^{-3}\,min^{-1}\,g_{Co}^{-1}$ with a value of 0.65. The Co/NMP-PMMA-56 catalyst shows the lowest conversions at each space velocity point, with values between 0.22 and 0.41, whilst the Co/Al_2O_3 catalyst shows slightly higher conversion at each point, between 0.28 and 0.5.

Table 6.5 Chapter 6 reaction results

Catalyst	**Space Velocity ($cm^3\ min^{-1}\ g_{Co}^{-1}$)**	**X_{CO}**	**CTY ($mol_{CO}\ g_{Co}^{-1}\ h^{-1}$)**	**S_{CH4} (%)**	**S_{C2+}**	**S_{C2-C6} (%)**	**S_{5+} (%)**	**S_{C7+} (%)**	**S_{C10+} (%)**	**S_{CO2} (%)**
Co/Al_2O_3	403	0.50	0.169	33.1	66.6	26.9	41.1	39.7	28.0	0.3
	652	0.45	0.243	45.8	51.4	36.7	15.0	14.6	9.6	2.9
	943	0.28	0.223	44.4	55.7	27.6	28.9	28.0	18.3	<0.1
Co/Al_2O_3 - P	652	0.65	0.352	27.0	71.1	54.4	18.7	16.8	9.0	1.84
	943	0.32	0.254	42.8	57.2	34.8	23.0	22.4	14.2	<0.1
Co/NMP-PMMA -56	404	0.41	0.139	28.6	71.4	42.0	29.6	29.4	22.0	<0.1
	651	0.29	0.160	41.0	59.0	32.1	27.2	26.9	19.0	<0.1
	943	0.22	0.171	43.7	56.4	29.4	27.2	26.9	19.4	<0.1
Co/NMP-PMMA-60	512	0.34	0.147	40.5	59.5	31.5	28.1	28.0	22.3	<0.1
	654	0.46	0.248	28.6	71.4	57.2	14.3	14.2	11.0	<0.1
	944	0.28	0.227	37.3	62.7	38.6	24.1	24.1	20.7	<0.1
MOF/NMP-PMMA-56	871	0.24	0.175	83.8	16.2	-	-	-	-	<0.1

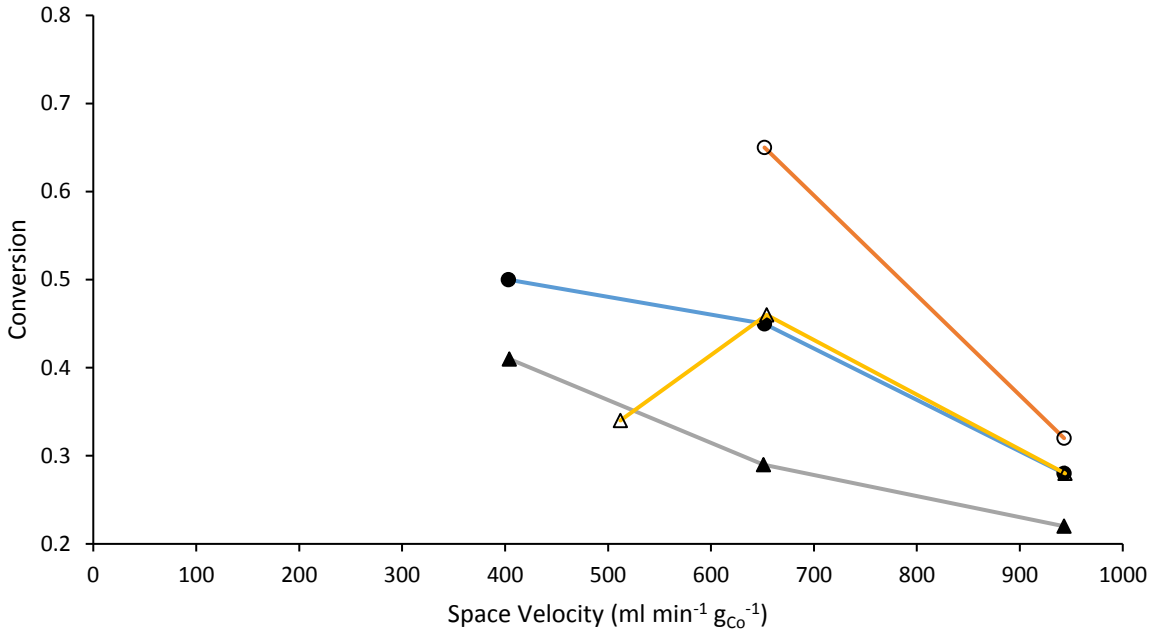

Figure 6.32 Effect of space velocity on conversion. ● = Co/Al_2O_3, ○ = Co/AL_2O_3 – P, ▲ = Co/NMP-PMMA-56, △ = Co/NMP-PMMA-60

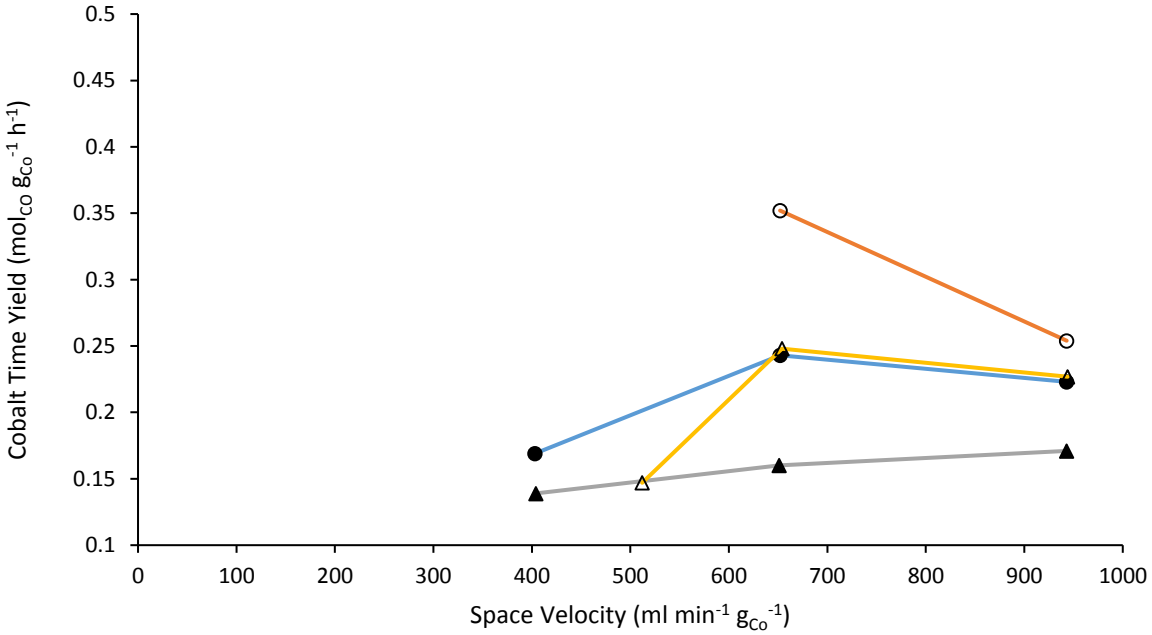

Figure 6.33 Effect of space velocity on activity. ● = Co/Al_2O_3 ○ = Co/Al_2O_3 – P, ▲ = Co/NMP-PMMA-56, △ = Co/NMP-PMMA-60

From Figure 6.33 it is evident that the cobalt time yield increases with space velocity for the Co/NMP-PMMA-56 catalysts, which shows the lowest activity of all the catalysts at each space velocity point. The catalyst Co/Al_2O_3 and Co/NMP-PMMA-60 show very similar activity to each other at each space velocity point. Both catalysts show an increased cobalt time yield from about 0.15 to 0.25 $mol_{CO}\ g_{CO}^{-1}\ h^{-1}$ from a space velocity of around 400-500 to 652 $cm^3\ min^{-1}\ g_{Co}^{-1}$, until the activity shows signs of levelling off at around 952 $mol_{CO}\ g_{CO}^{-1}\ h^{-1}$. The Co/AL2O3 – P shows a decrease in activity from 0.352 to 0.254 $mol_{CO}\ g_{CO}^{-1}\ h^{-1}$,when space velocity is increased from 652 to 943 $cm^3\ min^{-1}\ g_{Co}^{-1}$. This is not expected, as a decrease in activity is not expected with increasing space velocity, rather a levelling of activity is anticipated. However, this may be explained by a minor variations in the data. Catalysts were run in the space velocity order of 652, 943, 403 $cm^3\ g_{Co}^{-1}\ min^{-1}$. In the case of the pellet, being the first of these catalysts to be tested at these space velocities, was run in the order of 652, 1300 and 943 $cm^3\ g_{Co}^{-1}\ min^{-1}$. This makes it possible that some deactivation may have occurred and reduced the activity, but the overall picture of reaction is unlikely to be affected. However, the catalyst still displays the highest activity of all catalysts at comparable space velocities.

The higher activity of the Co/Al_2O_3 and Co/Al_2O_3 – P catalyst is expected, as the porous γ-alumina support provides a much higher BET surface area of 249.5 $m^2\ g^{-1}$, compared to BET surface areas close to 0 for both in the NMP-PMMA-56 membrane and NMP-PMMA-60 membranes, meaning less surface area for the dispersion of the active phase. The mercury intrusion data does suggest that the sponge-like layer is porous, but the pores are very large compared to γ-alumina and MOF-based catalysts, which is why no BET surface area is detected. Although in Chapter 5 it was shown that the BJH average pore diameter of the γ-alumina pellet is smaller than the estimated nanoparticle size, a common occurrence in catalysis, it is likely the active metal cobalt crystallites are still present in the disordered porous network [110]. Whereas the NMP-PMMA-56 only has the active metal dispersupon a much lower surface area, leaving a lower dispersion of active phase, and less sites for reaction. Therefore, the activity of the membrane catalyst if far higher in terms of activity per surface area. It is also possible that Co particle size plays a role, as the particle may be larger in the membrane, as suggested by large Co clusters observed in the Figure 6.26 and Figure 6.27, compared to those shown in Figure 5.5 and Figure 5.6 in Chapter 5 for the Co/Al_2O_3. The increased crystallite size suggests decreased dispersion in the membrane, indicating less sites accessible for reaction, leading to lower conversion. However, without further characterisation to confirm the average Co particle size and number of active sites, such as H_2 chemisorption, ICP-OES and TEM, it is difficult to quantitatively confirm this. The NMP-PMMA-60 membrane shows similar activity to the ground Co/Al_2O_3 catalyst and better activity than the NMP-PMMA-56 membrane. Both membrane catalysts and ground Co/Al_2O_3 should have negligible diffusion effects, which means the difference can only be accounted for by the accessibility of active

sites or Co particle size effects. In the case of the Co particle size, it would be thought that there is no difference between both membrane catalysts as they underwent the same impregnation procedure. It may It is possible surface area is greater in the NMP-PMMA-60 membrane, or the active phase has dispersed more effectively in the larger channels during the impregnation. However, more evidence is needed to confirm this.

The Co/Al_2O_3 – P shows better activity and conversion out of all catalysts at the space velocity points of 652 and 943 $cm^3\ min^{-1}\ g_{Co}^{-1}$. This is not in line with studies by Post et al, who showed that decreasing particle diameter increased FTS reaction rates on Co catalysts [33]. But this was in contrast to findings by Iglesia et al, who found that FTS reaction rate, expressed as cobalt time yield, was not influenced by pellet size [40, 117]. The current phenomenon has been observed previously by Fratalocchi et al, who observed higher conversions in eggshell catalysts of 600 µm diameter with a 75 µm thick shell region, compared to the same catalyst crushed into a particle size range of 75-100 µm, which has the same chemical and physical properties apart from the characteristic length of diffusion [40]. When run at the same conditions, the eggshell catalyst showed conversion of 42 % compared to 34 %. This was explained by considering the FTS kinetics are positive order with respect to H_2 and negative order with respect to CO, whilst the different molecular diffusivities of H_2 and CO in the liquid filling the pores result in H_2/CO ratios higher in close proximity of the catalyst active centre than the bulk phase. It may be typical of reactions with kinetics having negative dependencies on the concentration of the limiting reactant to have an effectiveness factor greater than 1 in a range of Thiele modulus values around ϕ = 1 [40]. Similarly, in this experiment the Co/Al_2O_3 – P and Co/Al_2O_3 catalysts share identical physical and chemical properties, except the Co/Al_2O_3 – P catalyst has a pellet diameter of approximately 3 mm compared to less than 180 µm for the Co/Al_2O_3. This is significantly larger than the diffusion lengths mentioned by Fratalocchi et al, whilst the Thiele modulus value for such a large catalyst pellet is likely to be significantly larger than ϕ = 1. In this case, the difference in mass transport limitations is thought to be much larger, however the experiment is well controlled with respect to the conditions and catalyst properties, and a higher activity is still shown in the pellet-based catalyst. Also, the Yang et al also showed that a larger catalyst pellets showed higher conversion than smaller ones [70]. It may be useful to investigate this occurrence further by repeating the experiment to gauge the effect of system error, whilst also running the Co/Al_2O_3 – P catalyst at a space velocity of 403 $cm^3\ min^{-1}\ g_{Co}^{-1}$.

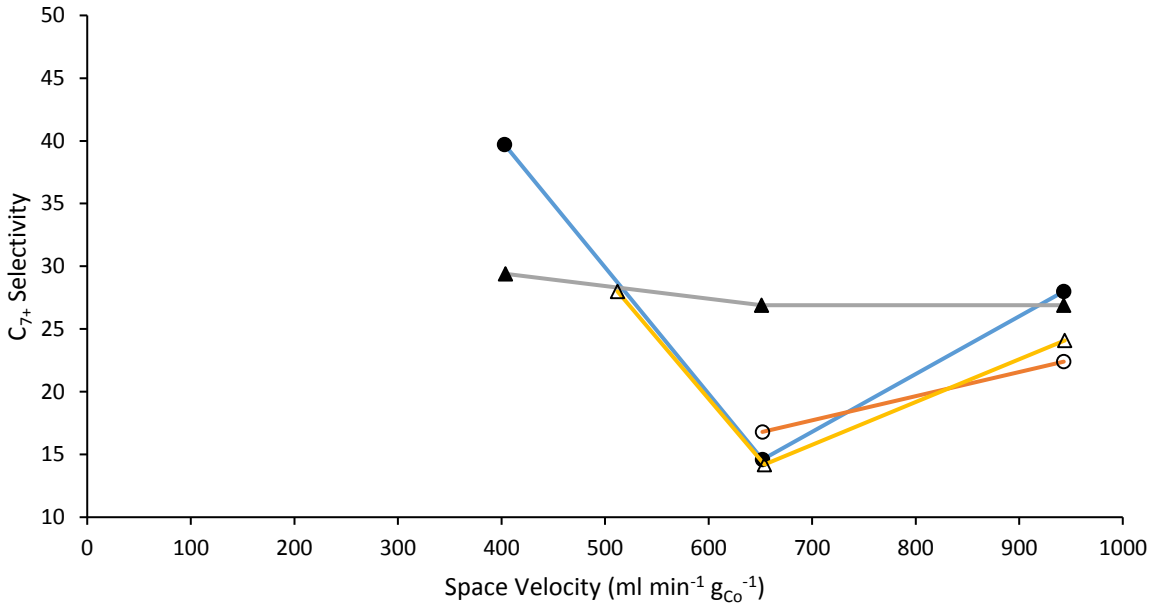

Figure 6.34 Effect of space velocity on C_{7+} selectivity. ● = Co/Al_2O_3, ○ = Co/Al_2O_3 – P, ▲ = Co/NMP-PMMA-56, △ = Co/NMP-PMMA-60

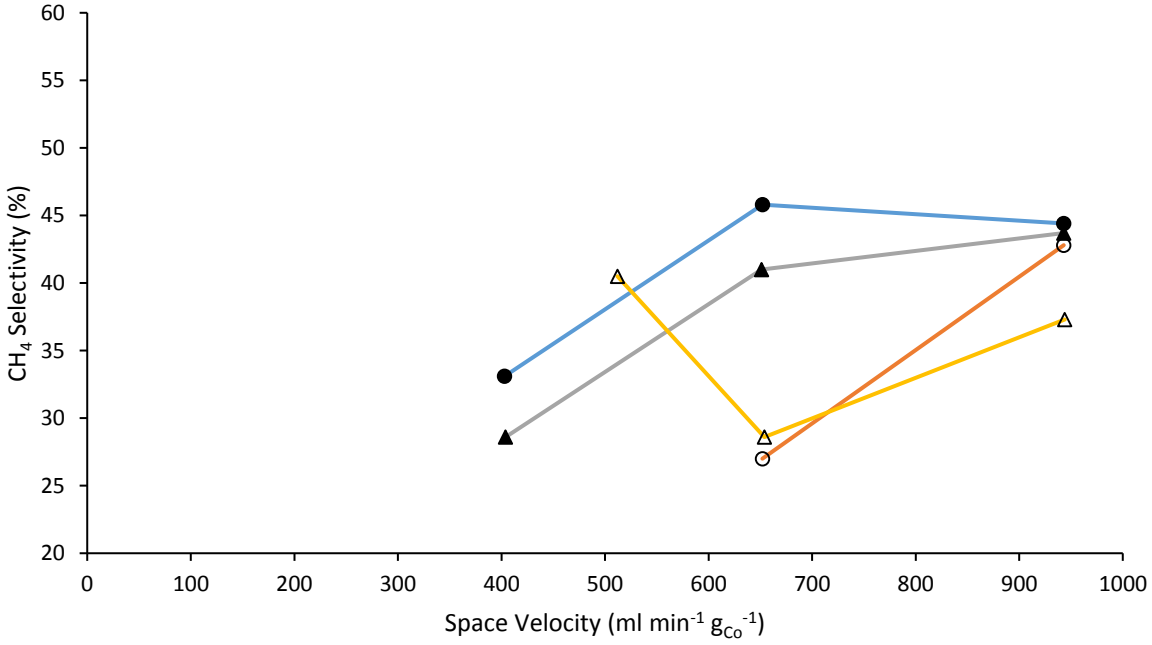

Figure 6.35 Effect of space velocity on methane selectivity. ● = Co/Al_2O_3, ○ = Co/Al_2O_3 – P, ▲ = Co/NMP-PMMA-56, △ = Co/NMP-PMMA-60

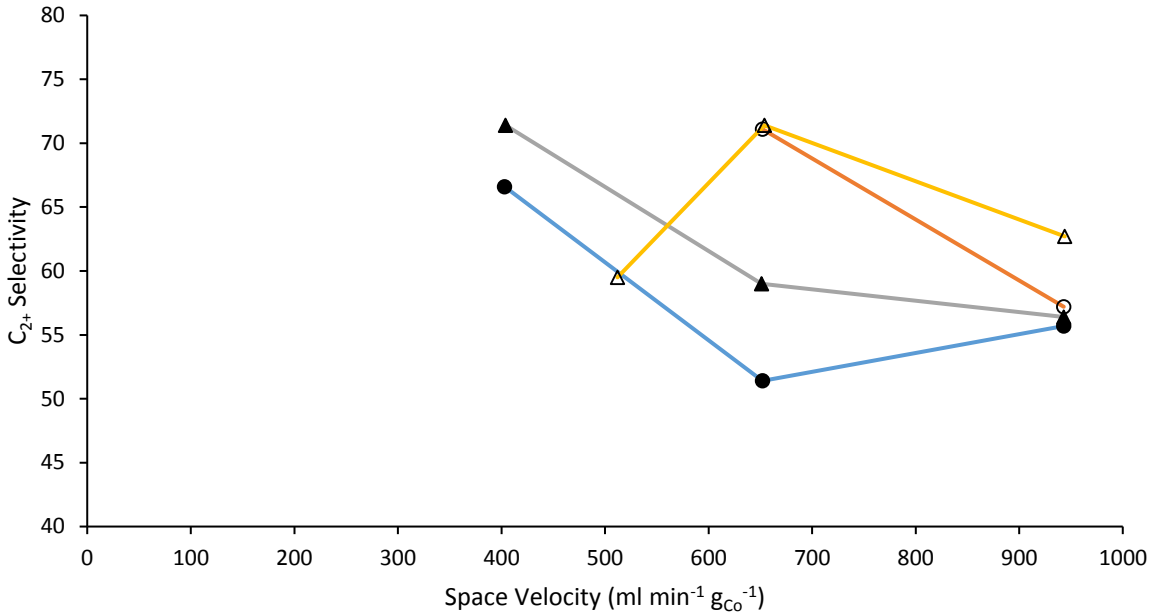

Figure 6.36 Effect of space velocity on C_{2+} selectivity. ● = Co/Al_2O_3, ○ = Co/Al_2O_3 – P, ▲ = Co/NMP-PMMA-56, △ = Co/NMP-PMMA-60

From Figure 6.34, it can be seen that similar general trends related to conversion and selectivity observed in Chapter 5 apply here. Again, the selectivity is low for Co catalysts compared to many literatures, but this is likely to be due to the high temperature and lower pressure used in these experiments compared to other LTFT studies. Lower space velocity result in higher conversions, which has been shown to correlate to higher C_{5+} selectivity in multiple studies until conversions of around 0.8 are reached, at which point significant WGS activity is induced resulting in high methane selectivity [95]. For example, the Co/Al_2O_3, NMP-PMMA-56 and NMP-PMMA-60 catalysts all show higher C_{7+} selectivity at the lowest space velocity point than the highest space velocity point, although the difference is not large, only a few percent, with the largest difference of 10 % occurring for the Co/Al_2O_3, which shows the highest C_{7+} selectivity out of all the catalysts at the lowest space velocity point. From Figure 6.36 it can be seen that the C_{2+} selectivity was also correlated to the space velocity, and hence the conversion. For each catalyst, the highest C_{2+} selectivity was recorded at the highest conversion excluding for the NMP-PMMA-60 catalyst, which showed the highest conversion at a space velocity of 652 cm^3 min^{-1} g_{Co}^{-1}. This is unexpected, as increasing space velocity should lower the conversion. The space velocity order in which each catalyst was run was 652, 943, 403-512 cm^3 min^{-1} g_{Co}^{-1}. Also, considering the space velocity difference between medium and low points of 654 and 512 cm^3 min^{-1} g_{Co}^{-1} is slightly closer for the Co/NMP-PMMA-60 than the other catalysts, a period of

deactivation may account for a lower conversion at the space velocity at 512 $cm^3\ min^{-1}\ g_{Co}^{-1}$. Figure 6.35 shows the trends in methane selectivity, which generally shows an increase in methane selectivity with increasing space velocity, due to the lower conversion, except for the NMP-PMMA-60 catalyst, which shows similar methane selectivity of around 40 % percent at the lowest and highest space velocity points, but shows a dramatic decrease at a space velocity of 652 $cm^3\ min^{-1}\ g_{Co}^{-1}$. It is also noticeable that the Co/Al_2O_3 – P shows comparatively low methane selectivity, which does not fit with explanation of mass transport limitations distorting the H_2/CO ratio, as higher methane selectivity would be expected compared to other catalysts, especially the Co/Al_2O_3 catalyst, where the chemical and physical properties have been carefully controlled aside from particle diameter.

At the lowest cobalt space velocities, between 652 and 512 $cm^3\ min^{-1}\ g_{Co}^{-1}$, the Co/Al_2O_3 catalyst shows the highest C_{7+} selectivity, around 41 %, compared to around 30 % for the NMP-PMMA-56 and NMP-PMMA-60 membranes. The higher selectivity to higher length hydrocarbons is difficult to explain, as none of these catalysts should exhibit significant mass transport limitations, due to the small catalyst particle size of the Co/Al_2O_3 and the direct contact between the reactants and active phase in the NMP-PMMA catalytic membranes. One reason may be the particle size effect of the Co nanoparticles. But based on the characterisation, the NMP-PMMA catalytic membranes have been shown to have quite large Co agglomerates, and although the average Co particle size has not been quantified rigorously, it is unlikely that the NMP-PMMA catalytic membranes have a particle size small enough to negatively affect selectivity, which normally occurs below Co nanoparticle sizes of below 8 nm [103]. One possibility is that, although mass transport phenomena should be minimal at Co/Al_2O_3 catalyst particle sizes less than 180 µm, if some modest transport restrictions do exist, they may have the effect of increasing C_{7+} selectivity through the olefin reabsorption side reaction. Iglesia et al discusses the effect of the characteristic length of diffusion (δ) on LTFT. By comparing the performance of Co/SiO_2 spherical catalysts with different diameters (from 130 to 1500 µm) it was observed that C_{5+} selectivity increased with pellet size until reaching a maximum at 360 µm (δ = 60 µm). It was suggested that the C_{5+} selectivity increases as the result of α-olefin readsorption resulting in increased chain growth probability. After this point, larger pellets will become depleted of CO enhancing hydrogenation, increasing the methane selectivity and decreasing C_{5+} selectivity [40, 117]. It may be possible that the incremental increase in mass transport restriction imposed by the pellet of 180 µm in the Co/Al_2O_3 catalyst leads to a greater extent of olefin re-adsorption compared to the membrane catalyst with no diffusional restrictions. This is similar to the χ parameter from Equation 2.8, later proposed by Iglesia et al [37]. χ depends only on the number of sites available for chain desorption and readsorption, and on the average distance that molecules must diffuse within the intrapellet liquid phase before they are removed. It is based on the structural parameters of the catalyst pellet and the Co site density: the

average radius of the catalyst pellet (R_o), the density of Co sites per unit area (θ_{Co}), the void fraction (ε) and the average pore radius (r_p) of the metal oxide support. An increase in the χ parameter leads to an increase in C_{5+} selectivity, which peaks values of around 100 x 10^{-16}, after which a decline in C_{5+} selectivity is observed. However, without being able to accurately estimate the density of Co sites per unit area, it is difficult to calculate the χ parameter.

$$\phi_n = \left(\frac{k_{r,n}}{D_n}\right) \times \left(\frac{R_o^2 \varepsilon \theta_{Co}}{r_p}\right) = \psi_n \times (\chi) \qquad \text{(Equation 2.9)}$$

By comparing the C_{7+} selectivity of the catalysts at the space velocity of 943 $cm^3\ min^{-1}\ g_{Co}^{-1}$, the Co/Al_2O_3 – P has the lowest C_{7+} selectivity of 22.4 %, compared to 28 % for the similar Co/Al_2O_3 catalyst, and 26.9 and 24.1 % for the NMP-PMMA-56 and NMP-PMMA-60 catalysts, respectively. This may be a result of higher mass transport limitations due to the large particle diameter of the Co/Al_2O_3 – P catalyst, and modest transport restrictions enhancing the selectivity of the Co/Al_2O_3 catalyst, whilst the elimination of transport restrictions for the membrane-based catalyst improve the selectivity over a pellet-based catalyst, but do not benefit from olefin-readsorption enhanced selectivity. Although the highest methane selectivity would be expected for the Co/Al_2O_3 – P catalyst.

Table 6.6 Approximate reactor bed specifications at 943 $cm^3\ min^{-1}\ g_{Co}^{-1}$ (Volumetric flowrate is based on the inlet flowrate at 100 kPa and 20 ^oC)

Catalyst	**Bed Length (cm)**	**Volumetric Flowrate of Reactants ($cm^3\ min^{-1}$)**	**Reactor Superficial Gas Velocity ($cm\ s^{-1}$)**	**Bed Cobalt Density ($g_{Co}\ cm^{-3}$)**	**Superficial Residence Time (s)**
Co/Al_2O_3	4.1	84.9	0.53	0.050	7.74
Co/Al_2O_3-P	5.8	84.9	0.53	0.037	10.94
Co/NMP-PMMA-56	2.4	52.8	0.33	0.053	7.27
Co/NMP-PMMA-60	2	38.7	0.24	0.046	8.34

It is possible that some of the results may have been affected by factors related to the properties of the fixed bed which can be seen in Table 6.6. As the membrane-based catalysts had significantly lower Co loading, a reduced flowrate was required in order to operate at comparable space velocity. Consequently, this results in different residence times and gas velocities for each catalyst, despite the flowrate per gram of Co being comparable. For example, the Co/Al_2O_3-P has the greatest residence time compared to the other catalysts. Therefore, it is possible that potential transport restrictions imposed by the large pellet size can be offset by the longer time that the reactants spend inside the catalyst bed, which may explain the higher activity compared to other catalysts. Also, as this catalyst has the lowest Co density, the effect of bed temperature effects may be lessened as a result of the highly exothermic FTS reaction. Similarly, the membrane-based catalysts, due to the lower loading, have a much lower superficial gas velocity inside the reactor. This may affect external mass transfer between the bulk and active sites in a negative way, as lower superficial gas velocity is related to greater external mass transfer restrictions [70]. Ultimately, it is difficult to control all aspects of the experiment, especially when catalysts with different loadings and morphologies are involved.

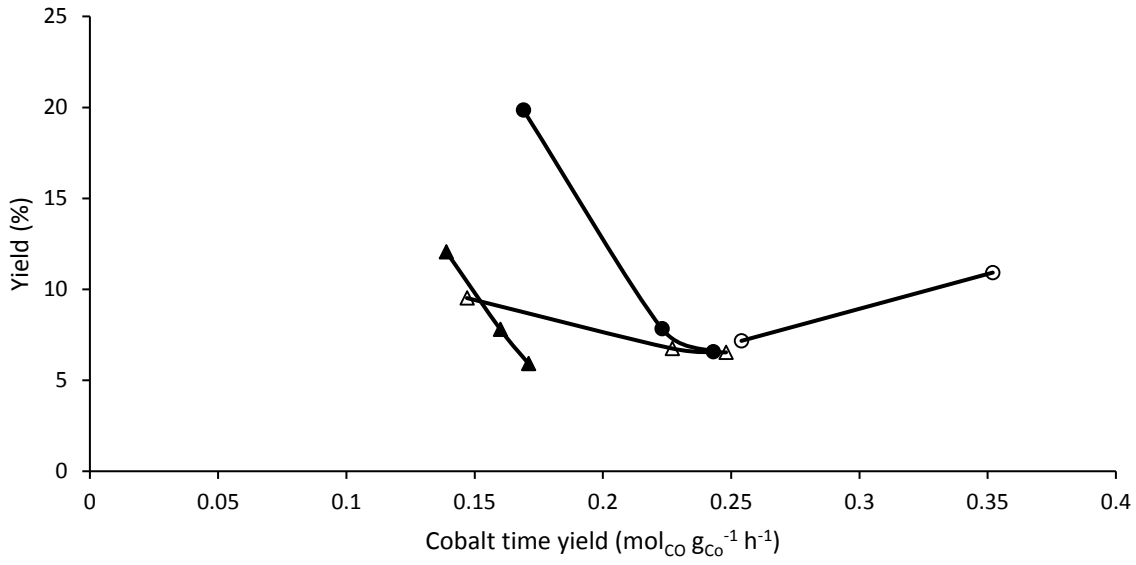

Figure 6.37 Effect of cobalt time yield on the yield of C_{7+} products. ● = Co/Al_2O_3, ○ = Co/Al_2O_3 – P, ▲ = Co/NMP-PMMA-56, △ = Co/NMP-PMMA-60

Figure 6.37 shows the effect of activity on the percentage yield of C_{7+} products. It can be observed from looking up from the x-axis at a cobalt time yield of about 0.157 mol$_{CO}$ g$_{Co}^{-1}$ min^{-1} that the C_{7+} yield

of the Co/Al_2O_3 catalyst is a lot larger than those for the membrane-based catalysts, with a yield of 20 % compared to 6 %. One reason for this occurrence may be related to the heat effect of the highly exothermic FTS reaction inside the membrane. The catalytic membranes and Co/Al_2O_3 catalyst have similar cobalt density per bed volume, but in the case of the membrane almost all of this cobalt is likely to be concentrated in the micro-channel or on the surface of the membrane, essentially less uniformly dispersed throughout the bed compared to the Co/Al_2O_3. Therefore, hotspots may occur inside the membrane channels, whilst high temperatures lead to lighter product formation [67]. To compound this, low superficial gas velocity has been shown to cause increased temperature in the reactor [70]. It is noticeable that the performance of the NMP-PMMA-60 shows a lesser decline in C_{7+} yields at comparable activity in comparison to the NMP-PMMA-56 membrane. This may be due to the wider channels relieving some of the heat effects. The Co/Al_2O_3, Co/Al_2O_3-P and NMP-PMMA-60 membrane catalyst also show very similar yield at the same activity around 0.25 $mol_{CO}\ g_{Co}^{-1}\ min^{-1}$, suggesting that all these are equally affected by the heat effect at this activity. However, the pellet seems to show a slight increase in yield with increasing activity, but as the other catalysts were unable to achieve the same kind of activity, it is difficult to make a comparison.

Table 6.5 also shows the reaction result of the MOF/NMP-PMMA-56 catalyst, which contains the MOF on the surface and within the channels of the NMP-PMMA-56 membrane. The result in this case is very strange. Comparable conversion and activity are shown at a space velocity of 871 $cm^3\ min^{-1}\ g_{Co}^{-1}$ compared to the other catalysts run at 943 $cm^3\ min^{-1}\ g_{Co}^{-1}$, with values of 0.24 and 0.175 $mol_{CO}\ g_{Co}^{-1}\ h^{-1}$. However, there is an extremely high selectivity to methane of 83.8 % and very low selectivity to C_{2+} hydrocarbons, with a value of 16.2 %, making it difficult to extract the liquid product for analysis. This result is peculiar, as previous MOF-derived catalyst experiments in Chapter 4 showed extremely high WGS shift activity, which could account for extremely high methane selectivity in the range of 60 %. This was likely caused by the high bed temperature leading to high conversions over 0.8 inducing significant WGS activity. However, in this case, barely any WGS activity is shown, evidenced by the low CO_2 selectivity below 0.1 %, making this explanation unlikely. XRD of some of the spent Co-MOF-74 derived catalyst, which underwent in-situ pyrolysis inside the membranes at the same conditions as the MOF/Al_2O_3 catalyst in Chapter 5, showed a comparable spectra with a broad peak at $2\theta = 44.3^{o}$, indicating the presence of metallic Co [72]. Using the Scherrer equation, the Co nanoparticle size can be estimated to be 11.7, which in the range observed for Co-MOF-74 derived catalysts in this work. The lack of discrepancies in XRD spectra suggest there was no problem with the decomposition of the Co-MOF-74 into a Co containing catalyst, and no evidence of additional compounds can be observed from the XRD spectra. The purpose of applying the Co-MOF-74 derived catalyst to the membrane was to investigate whether this reactor configuration would have a similar effect, or even enhanced effects,

compared to diluting the MOF precursor, such as reducing temperature effects to avoid WGS activity. Originally, in-situ impregnation of the Co-MOF-74 onto the membrane, by impregnating the membrane with the Co-MOF-74 precursor solutions and placing the impregnated membrane into the autoclave with the remaining solution for synthesis, was preferred. This way, the MOF is deposited on the channel walls and not filling the channels in a powdered form, meaning the membrane can act as a support for a catalyst that is difficult to be used in industrial reactor operation due to its powdered form. However, the low loading made this difficult considering the lower flowrate limit of the mass flow controller, as there would not be sufficient Co in the reactor to achieve measurable conversion. Instead, the ex-situ approach was taken, as extra loading could be applied by depositing a layer of MOF on each membrane surface. The experiment seems successful in eliminating the high WGS activity. However, the extremely high selectivity to methane is difficult to explain and may be linked to the temperature effect in the small membrane channel promoting methanation. This suggests that MOF-derived catalysts are perhaps unsuitable for membrane application.

6.5 Conclusion

Chapter 6 shows the fabrication and characterisation of two types of ceramic flat disc membranes with different microstructures. Cobalt was applied to both membranes, and they were successfully tested in FTS reaction, along with a conventionally prepared γ-alumina supported cobalt catalyst in a pellet form with a diameter of about 3 mm. By including the data obtained from the ground γ-alumina supported cobalt catalyst Chapter 5, a comparison in reactor performance can be drawn between cobalt-based catalyst in the ground particle form, pellet form, and two distinct micro-structured ceramic catalytic membranes. The pellet-based catalyst showed the highest activity, which may be linked to the mass transport restrictions increasing the H_2/CO ratio and favouring reaction kinetics. Another possible reason is the configuration of the bed, as the long bed means that the gas residence time is longer compared to the other catalysts. The ground Co/Al_2O_3 catalyst displays the highest selectivity at the lowest and highest space velocity points, which may be related to weak mass transport limitations favouring the olefin readsorption, which can increase C_{7+} selectivity. The membrane based catalysts did not perform as well as expected. The removal of diffusion limitations was expected to have the effect of enhancing selectivity and activity. However, difficulty in dispersing the cobalt occurred as evidenced by large cobalt agglomerates, which may lower activity. Also, the heat effect of the highly exothermic FTS reaction taking place in micro-channels with a high density of cobalt may favour lighter product formation. Other negative effects may be the lower gas velocity,

which can further increase the temperature. However, there is evidence to suggest that the NMP-PMMA-60 membrane shows improved performance over the NMP-PMMA-56 membrane, which may be due to the better dispersion of cobalt or lesser heat effect in the wider micro-channels.

Chapter 7

Conclusion

The early part of this thesis focused on the preparation and testing of Co-MOF-74-derived catalysts to investigate the performance improvement in FTS reaction. Initially, variation in the pyrolysis procedure and reaction conditions were explored. The catalysts prepared at different pyrolysis dwell times of 1 and 5 hours showed similar characteristics, such as average Co nanoparticle grain size and BET surface area, which concurred with those published in the literature. The Co-MOF-74 was packed directly into the reactor for in-situ pyrolysis before reaction. Abnormal reaction results were observed, which were very different to those in similar studies. The catalyst showed extremely high activity, very high methane selectivity, very low C_{2+} selectivity, and very high CO_2 selectivity, with little variation in the result despite changes in temperature, pressure, pyrolysis dwell time and heating rate. The only observable trend was a decrease in conversion and mild increase in C_{2+} selectivity with increasing pressure. The high CO_2 selectivity indicates the high WGS activity, which is thought to contribute to the high methane selectivity and low selectivity to higher hydrocarbons. The extremely high conversions results in high partial pressure of water which increases WGS activity, and H_2 and H_2O compete to react with CO. The result is a distorted H_2/CO ratio, much higher than the original ratio of 2, which favours hydrogenation and methane formation.

In order to rectify the performance of the Co-MOF-74-derived catalysts, when the original Co-MOF-74 was packed into the reactor before pyrolysis, it was first diluted with ground γ-alumina particles. This had a quite dramatic effect on the performance, showing greatly increased selectivity to higher hydrocarbons and significantly lower methane selectivity compared to undiluted catalysts. This is likely due to the dilution reducing the extremely high local bed temperature induced by having such a highly loaded MOF-based catalyst in a very exothermic reaction. The high temperature favour the formation of methane, whilst water from the high conversion induce significant WGS activity which contributes to further methane formation and the formation of CO_2. Chemical vapour deposition of acetylene was also applied to further improve the performance of the Co-MOF-74-derived catalyst, whilst a conventionally prepared, ground γ-alumina supported cobalt catalyst was tested as a performance comparison. The conventionally prepared Co/Al_2O_3 showed lower activity but greater selectivity at comparable space velocity compared to the MOF-based catalysts, and this was thought to be due to the Co nanoparticle size effect leading to lower activity and a lower local temperature at the active sites, favouring higher hydrocarbon formation. However, at comparable activities the MOF-derived catalysts demonstrated significantly higher C_{7+} percentage yields, showing greater selectivity of the

MOF-derived catalyst when taking activity, and hence local active site temperature, into account. The porous carbon support formed from the organic ligand in the original Co-MOF-74 may play a key role in improving the selectivity, whilst chemical vapour deposition of ethyne showed enhanced performance which may be related to the formation of graphene layers on the cobalt nanoparticles.

Two difference types of micro-structured flat disc ceramic membranes were fabricated by altering the parameters of the precursor suspension. Cobalt was applied to both membranes through an impregnation process, and they were successfully tested in FTS reaction, along with a conventionally prepared γ-alumina supported cobalt catalyst in a pellet form with a diameter of approximately 3 mm. By including the ground γ-alumina supported cobalt catalyst, a comparison of FTS reactor performance could be drawn across different fixed-bed reactor configurations and catalyst geometries. The pellet-based catalyst showed the highest activity, which may be linked to the mass transport restrictions increasing the H_2/CO ratio and favouring reaction kinetics. However, this may also be linked to the geometry, due to a longer bed and longer residence time. The ground catalyst displays slightly higher activity, possibly due to the weak mass transport limitation resulting in enhanced α-olefin readsorption, but this change is not significant and the pellet-based catalyst is still a more sensible and feasible choice for industrial operation. The membrane-based catalysts did not perform as well as expected. Difficulty in dispersing the cobalt and the heat effect of the highly exothermic FTS reaction taking place in micro-channels with a high density of cobalt may favour lighter product formation. However, a performance improvement was noticed in the wider-channelled NMP-PMMA-60 membrane at similar activities, possibly due to the lesser effect of the local temperature in the wider micro-channels. Also, the application of the Co-MOF-74-derived catalyst to the membrane resulted in extremely high methane selectivity, which is undesirable for FTS.

Overall, Co-MOF-74-derived catalysts are more active and selective than conventionally prepared cobalt-based γ-Al_2O_3 based catalysts. However, due to the extremely high activity of the Co-MOF-74-derived catalyst and the very exothermic nature of FTS, excellent reactor temperature control is needed to gain optimum performance. Ceramic membrane reactors with channel diameters of around 100 µm resulted in poorer performance than conventionally prepared γ-alumina supported cobalt catalysts, possibly as a result of local temperature effects at the active sites inside the channels. Pellet based catalyst remain the most sensible option for industrial LTFT operation.

Chapter 8

Recommendations for Future Work

There are several improvements that can be made to the methodology. Being able to run the reaction at higher pressure may be helpful, as many FTS studies in the literature are undertaken at pressures of 20-30 bar. This will make it easier to compare the experimental results to those in literature, to generate better understanding of data trends and generate more fruitful discussion. Also, running the FTS reaction for at least 50 hours would be desired. This is useful for several reasons, such as to ensure steady state operation before taking reaction data points and allowing operation at the lower temperatures of 200-230 ^{o}C, whilst still having enough time to accumulate liquid product. Having a larger amount of liquid product will reduce errors in measurement when separating the two liquid phases. Another useful change to the method would be the addition of on an online gas chromatograph. This would allow monitoring of conversion and product gas composition across an extended time period whilst also enable the user to run the experiments at specified conversions, so the effect of conversion or activity can be equalised across all experiments. Also, more efficient reactor temperature control would be useful, such as a water-cooled system, as isothermal control in FTS can be challenging.

There are multiple characterisation techniques that would be helpful in this kind of project. High resolution transmission electron microscope (HR-TEM) analysis would be helpful for analysing the metal nanoparticle size, as obtaining the nanoparticle grain size from XRD is sometimes challenging. Also, this would allow for the investigation of the carbon support in MOF-derived catalysts, which may play a role in improving FTS selectivity. H_2 chemisorption would be helpful for obtaining the number of active sites, and therefore a site time yield can be calculated. Whilst temperature-programmed reduction (TPR) can help show the extent of reduction of the cobalt oxide. ICP-OES will also more accurately determine the cobalt content of MOF-derived catalysts.

Further study of the carbon support in MOF-derived catalysts, and the effect that the chemical vapour deposition of acetylene has on the support and nanoparticles would be useful. Although a performance improvement is noticed, the exact reasons for this have not been explicitly identified. Further reaction study and characterisation may be needed to improve the understanding. Also, whilst the micro-structured flat disc ceramic membrane seemed unsuitable for FTS in this work, the application of a wash-coated layer to the membrane may benefit the performance as it allows for much greater dispersion of the active metal.

List of References

1. U.S Energy Information Administration, International Energy Outlook, May 2016.

2. U.S Energy Information Administration, International Energy Outlook, October 6 2021.

3. BP, Statistical Review of World Energy, 2021.

4. Moulijn, J.A., M. Makkee, and A.E. van Diepen, Chemical Process Technology. 2013, Wiley.

5. Takeshita, T. and K. Yamaji, Important roles of Fischer–Tropsch synfuels in the global energy future. Energy Policy, 2008. **36**(8): p. 2773-2784.

6. van de Loosdrecht, J., et al., Fischer–Tropsch Synthesis: Catalysts and Chemistry. 2013: p. 525-557.

7. Rauch, R., A. Kiennemann, and A. Sauciuc, Fischer-Tropsch Synthesis to Biofuels (BtL Process), in The Role of Catalysis for the Sustainable Production of Bio-fuels and Bio-chemicals. 2013. p. 397-443.

8. Konarova, M., W. Aslam, and G. Perkins, Chapter 3 - Fischer-Tropsch synthesis to hydrocarbon biofuels: Present status and challenges involved, in Hydrocarbon Biorefinery, S.K. Maity, K. Gayen, and T.K. Bhowmick, Editors. 2022, Elsevier. p. 77-96.

9. Ramberg, D.J., et al., The economic viability of gas-to-liquids technology and the crude oil–natural gas price relationship. Energy Economics, 2017. **63**: p. 13-21.

10. Saeidi, S., et al., Recent advances in reactors for low-temperature Fischer-Tropsch synthesis: process intensification perspective %J Reviews in Chemical Engineering. 2015. **31**(3): p. 209-238.

11. Guettel, R., U. Kunz, and T. Turek, Reactors for Fischer-Tropsch Synthesis. Chemical Engineering & Technology, 2008. **31**(5): p. 746-754.

12. Wang, Z., et al., Syngas composition study. Frontiers of Energy and Power Engineering in China, 2009. **3**(3): p. 369-372.

13. Rafati, M., et al., Techno-economic analysis of production of Fischer-Tropsch liquids via biomass gasification: The effects of Fischer-Tropsch catalysts and natural gas co-feeding. Energy Conversion and Management, 2017. **133**: p. 153-166.

14. Jahangiri, H., et al., A review of advanced catalyst development for Fischer–Tropsch synthesis of hydrocarbons from biomass derived syn-gas. Catal. Sci. Technol., 2014. **4**(8): p. 2210-2229.

15. Han, J., et al., The effect of syngas composition on the Fischer Tropsch synthesis over three-dimensionally ordered macro-porous iron based catalyst. Molecular Catalysis, 2017. **440**: p. 175-183.

16. Riedel, T., et al., Comparative study of Fischer–Tropsch synthesis with H2/CO and H2/CO2 syngas using Fe- and Co-based catalysts. Applied Catalysis A: General, 1999. **186**(1): p. 201-213.

17. Ma, T., et al., Synthesis of Hydrocarbons from H2-Deficient Syngas in Fischer-Tropsch Synthesis over Co-Based Catalyst Coupled with Fe-Based Catalyst as Water-Gas Shift Reaction. Journal of Nanomaterials, 2015. **2015**: p. 10.

18. Jean Marie, C. and R. Iulian, Syngas production via methane steam reforming with oxygen: plasma reactors versus chemical reactors. Journal of Physics D: Applied Physics, 2001. **34**(18): p. 2798.

19. Fahim, M.A., T.A. Alsahhaf, and A. Elkilani, Chapter 12 - Clean Fuels, in Fundamentals of Petroleum Refining. 2010, Elsevier: Amsterdam. p. 303-324.

20. Mehariya, S., et al., Chapter 7 - Fischer–Tropsch synthesis of syngas to liquid hydrocarbons, in Lignocellulosic Biomass to Liquid Biofuels, A. Yousuf, D. Pirozzi, and F. Sannino, Editors. 2020, Academic Press. p. 217-248.

21. Adesina, A.A., Hydrocarbon synthesis via Fischer-Tropsch reaction: travails and triumphs. Applied Catalysis A: General, 1996. **138**(2): p. 345-367.

22. van Santen, R.A. and A.J. Markvoort, Chain Growth by CO Insertion in the Fischer Tropsch Reaction. ChemCatChem, 2013. **5**.

23. Perego, C., R. Bortolo, and R. Zennaro, Gas to liquids technologies for natural gas reserves valorization: The Eni experience. Catalysis Today, 2009. **142**(1-2): p. 9-16.

24. F. Fischer, H.T., Chem. Ber. 59 (1926) 830–836.

25. Zhou, L., et al., Chain Propagation Mechanism of Fischer–Tropsch Synthesis: Experimental Evidence by Aldehyde, Alcohol and Alkene Addition. Reactions, 2021. **2**(2): p. 161-174.

26. Jacobs, G. and B.H. Davis, Applications of isotopic tracers in Fischer–Tropsch synthesis. Catal. Sci. Technol., 2014. **4**(11): p. 3927-3944.

27. Perego, C., Development of a Fischer-Tropsch catalyst: From laboratory to commercial scale demonstration. Rendiconti Lincei, 2007. **18**(4): p. 305.

28. Filot, I.A.W., et al., Kinetic aspects of chain growth in Fischer-Tropsch synthesis. Faraday Discuss, 2017. **197**: p. 153-164.

29. Tavakoli, A., M. Sohrabi, and A. Kargari, Application of Anderson–Schulz–Flory (ASF) equation in the product distribution of slurry phase FT synthesis with nanosized iron catalysts. Chemical Engineering Journal, 2008. **136**(2-3): p. 358-363.

30. Bezemer, G.L., Advances in Gas-to-Liquids Technology at Shell. 12th Natural Gas Conversion Symposium

31. Espinoza, R.L., et al., Low temperature Fischer–Tropsch synthesis from a Sasol perspective. Applied Catalysis A: General, 1999. **186**(1): p. 13-26.

32. Schanke, D., M. Wagner, and P. Taylor, Scale-up and Demonstration of Fischer-Tropsch Technology, in Proceedings of the 1st Annual Gas Processing Symposium, H.E. Alfadala, G.V. Rex Reklaitis, and M.M. El-Halwagi, Editors. 2009, Elsevier: Amsterdam. p. 370-377.

33. Post, M.F.M., et al., Diffusion Limitations in Fischer-Tropsch Catalysts. AIChE Journal, 1989. **35**(7): p. 1107-1114.

34. Madon, R.J., S.C. Reyes, and E. Iglesia, Primary and secondary reaction pathways in ruthenium-catalyzed hydrocarbon synthesis. The Journal of Physical Chemistry, 1991. **95**(20): p. 7795-7804.

35. Li, H., et al., Effects of macropores on reducing internal diffusion limitations in Fischer–Tropsch synthesis using a hierarchical cobalt catalyst. RSC Advances, 2017. **7**(16): p. 9436-9445.

36. Madon, R.J. and E. Iglesia, Hydrogen and CO Intrapellet Diffusion Effects in Ruthenium-Catalyzed Hydrocarbon Synthesis. Journal of Catalysis, 1994. **149**(2): p. 428-437.

37. Iglesia, E., Design, synthesis, and use of cobalt-based Fischer-Tropsch synthesis catalysts. Applied Catalysis A: General, 1997. **161**(1): p. 59-78.

38. Maatman, R. and C. Prater, Adsorption and exclusion in impregnation of porous catalytic supports. Industrial & Engineering Chemistry, 1957. **49**(2): p. 253-257.

39. Iglesia, E., et al., Synthesis and Catalytic Properties of Eggshell Cobalt Catalysts for the Fischer-Tropsch Synthesis. Journal of Catalysis, 1995. **153**(1): p. 108-122.

40. Fratalocchi, L., et al., Exploiting the effects of mass transfer to boost the performances of Co/γ-Al 2 O 3 eggshell catalysts for the Fischer–Tropsch synthesis. Applied Catalysis A: General, 2016. **512**: p. 36-42.

41. Becker, H., R. Güttel, and T. Turek, Optimization of Catalysts for Fischer-Tropsch Synthesis by Introduction of Transport Pores. Chemie Ingenieur Technik, 2014. **86**(4): p. 544-549.

42. Becker, H., R. Güttel, and T. Turek, Enhancing internal mass transport in Fischer–Tropsch catalyst layers utilizing transport pores. Catalysis Science & Technology, 2016. **6**(1): p. 275-287.

43. Mandić, M., et al., Effects of Catalyst Activity, Particle Size and Shape, and Process Conditions on Catalyst Effectiveness and Methane Selectivity for Fischer–Tropsch Reaction: A Modeling Study. Industrial & Engineering Chemistry Research, 2017. **56**(10): p. 2733-2745.

44. Fogler, H.S., Elements of Chemical Reaction Engineering. 2006: Prentice Hall PTR.

45. Bukur, D.B., et al., Pore diffusion effects on catalyst effectiveness and selectivity of cobalt based Fischer-Tropsch catalyst. Catalysis Today, 2020. **343**: p. 146-155.

46. Almeida, L.C., et al., Microchannel reactor for Fischer–Tropsch synthesis: Adaptation of a commercial unit for testing microchannel blocks. Fuel, 2013. **110**: p. 171-177.

47. Cao, C., et al., Intensified Fischer–Tropsch synthesis process with microchannel catalytic reactors. Catalysis Today, 2009. **140**(3-4): p. 149-156.

48. Ronde, M.P., et al., Fischer-Tropsch synthesis with in-situ H 2O removal by a new hydrophilic membrane - An experimental and modelling study. DGMK Tagungsbericht, 2006: p. 215-222.

49. Rohde, M.P., D. Unruh, and G. Schaub, Membrane application in Fischer–Tropsch synthesis reactors—Overview of concepts. Catalysis Today, 2005. **106**(1-4): p. 143-148.

50. Khassin, A.A., et al., Performance of a catalytic membrane reactor for the Fischer–Tropsch synthesis. Catalysis Today, 2005. **105**(3-4): p. 362-366.

51. Bradford, M.C.J., M. Te, and A. Pollack, Monolith loop catalytic membrane reactor for Fischer–Tropsch synthesis. Applied Catalysis A: General, 2005. **283**(1-2): p. 39-46.

52. Sondhi, R., R. Bhave, and G. Jung, Applications and benefits of ceramic membranes. Membrane Technology, 2003. **2003**(11): p. 5-8.

53. Asif, M.B. and Z. Zhang, Ceramic membrane technology for water and wastewater treatment: A critical review of performance, full-scale applications, membrane fouling and prospects. Chemical Engineering Journal, 2021. **418**: p. 129481.

54. Lee, M., Z. Wu, and K. Li, Advances in ceramic membranes for water treatment. 2015: p. 43-82.

55. Choi, I.-H., et al., Preparation and characterization of ultrathin alumina hollow fiber microfiltration membrane. Desalination, 2006. **193**(1-3): p. 256-259.

56. Kingsbury, B.F.K. and K. Li, A morphological study of ceramic hollow fibre membranes. Journal of Membrane Science, 2009. **328**(1-2): p. 134-140.

57. Lee, M., et al., Formation of micro-channels in ceramic membranes – Spatial structure, simulation, and potential use in water treatment. Journal of Membrane Science, 2015. **483**: p. 1-14.

58. Oar-Arteta, L., et al., Metal organic frameworks as precursors for the manufacture of advanced catalytic materials. Materials Chemistry Frontiers, 2017. **1**(9): p. 1709-1745.

59. Sun, X., et al., Manufacture of highly loaded silica-supported cobalt Fischer-Tropsch catalysts from a metal organic framework. Nat Commun, 2017. **8**(1): p. 1680.

60. Zhou, H.-C., J.R. Long, and O.M. Yaghi, Introduction to Metal–Organic Frameworks. Chemical Reviews, 2012. **112**(2): p. 673-674.

61. Rangnekar, N., et al., Zeolite membranes - a review and comparison with MOFs. Chem Soc Rev, 2015. **44**(20): p. 7128-54.

62. Jiang, H., et al., MOF-74 as an Efficient Catalyst for the Low-Temperature Selective Catalytic Reduction of NOx with NH3. ACS Appl Mater Interfaces, 2016. **8**(40): p. 26817-26826.

63. Valvekens, P., F. Vermoortele, and D. De Vos, Metal–organic frameworks as catalysts: the role of metal active sites. Catalysis Science & Technology, 2013. **3**(6): p. 1435.

64. Luo, Q.-X., et al., Cobalt nanoparticles confined in carbon matrix for probing the size dependence in Fischer-Tropsch synthesis. Journal of Catalysis, 2019. **369**: p. 143-156.

65. Li, N., et al., Low-cost preparation of carbon-supported cobalt catalysts from MOFs and their performance in CO hydrogenation. Journal of Fuel Chemistry and Technology, 2019. **47**(4): p. 428-437.

66. Qiu, B., et al., Highly dispersed Co-based Fischer–Tropsch synthesis catalysts from metal–organic frameworks. Journal of Materials Chemistry A, 2017. **5**(17): p. 8081-8086.

67. Zhang, C., et al., Ethyne-Reducing Metal–Organic Frameworks to Control Fabrications of Core/shell Nanoparticles as Catalysts. ACS Catalysis, 2018. **8**(8): p. 7120-7130.

68. Snavely, K. and B.J.J.o.C.S. Subramaniam, Thermal Conductivity Detector Analysis of Hydrogen Using Helium Carrier Gas and HayeSep® D Columns. 1998. **36**: p. 191-196.

69. Shafer, W., et al., Fischer–Tropsch: Product Selectivity–The Fingerprint of Synthetic Fuels. Catalysts, 2019. **9**(3): p. 259.

70. Yang, J.H., et al., Mass transfer limitations on fixed-bed reactor for Fischer–Tropsch synthesis. Fuel Processing Technology, 2010. **91**(3): p. 285-289.

71. Dietzel, P.D.C., et al., An In Situ High-Temperature Single-Crystal Investigation of a Dehydrated Metal-Organic Framework Compound and Field-Induced Magnetization of One-Dimensional Metal-Oxygen Chains. Angewandte Chemie, 2005. **117**(39): p. 6512-6516.

72. Pei, Y., Z. Li, and Y. Li, Highly active and selective Co-based Fischer-Tropsch catalysts derived from metal-organic frameworks. AIChE Journal, 2017. **63**(7): p. 2935-2944.

73. Otun, K.O., X. Liu, and D. Hildebrandt, Metal-organic framework (MOF)-derived catalysts for Fischer-Tropsch synthesis: Recent progress and future perspectives. Journal of Energy Chemistry, 2020. **51**: p. 230-245.

74. S.J. Tauster, S.C. Fung, R.T. Baker, J.A. Horsley. Science, 211 (4487) (1981), pp. 1121-1125.

75. Jiang, H., et al., MOF-74 as an Efficient Catalyst for the Low-Temperature Selective Catalytic Reduction of NOx with NH3 Supporting Information. ACS Applied Materials & Interfaces, 2016. **8**(40): p. 26817-26826.

76. Wang, K., et al., Porous Co-C Core-Shell Nanocomposites Derived from Co-MOF-74 with Enhanced Electromagnetic Wave Absorption Performance. ACS Appl Mater Interfaces, 2018. **10**(13): p. 11333-11342.

77. Mujtaba, J., et al., Nanoparticle Decorated Ultrathin Porous Nanosheets as Hierarchical Co3O4 Nanostructures for Lithium Ion Battery Anode Materials. Sci Rep, 2016. **6**: p. 20592.

78. Montazerozohori, M., et al., Sonochemical synthesis of a new cobalt(II) complex: Crystal structure, thermal behavior, Hirshfeld surface analysis and its usage as precursor for preparation of CoO/Co3O4 nanoparticles. Ultrason Sonochem, 2017. **38**: p. 134-144.

79. Ravindra, A.V., B.C. Behera, and P. Padhan, Laser induced structural phase transformation of cobalt oxides nanostructures. J Nanosci Nanotechnol, 2014. **14**(7): p. 5591-5.

80. Chang, S.S., et al., Mesoporosity as a new parameter for understanding tension stress generation in trees. J Exp Bot, 2009. **60**(11): p. 3023-30.

81. Q. F. Wang, W. Xia, W. H Guo, L. An, D. G Xia and R. Q. Zou, Chem.–Asian J., 2013, 8, 1879–1885.

82. Putz, A.M., et al., Ultrasonic preparation of mesoporous silica using pyridinium ionic liquid. Korean Journal of Chemical Engineering, 2016. **33**(3): p. 749-754.

83. Iqbal, S., et al., Fischer Tropsch Synthesis using promoted cobalt-based catalysts. Catalysis Today, 2016. **272**: p. 74-79.

84. Khodakov, A.Y., et al., Pore Size Effects in Fischer Tropsch Synthesis over Cobalt-Supported Mesoporous Silicas. Journal of Catalysis, 2002. **206**(2): p. 230-241.

85. Schulz, H., Comparing Fischer-Tropsch Synthesis on Iron- and Cobalt Catalysts: The dynamics of structure and function, in Studies in Surface Science and Catalysis, B.H. Davis and M.L. Occelli, Editors. 2007, Elsevier. p. 177-199.

86. Wolf, M., et al., Synthesis, characterisation and water-gas shift activity of nano-particulate mixed-metal (Al, Ti) cobalt oxides. Dalton Trans, 2019. **48**(36): p. 13858-13868.

87. Marion, M.-C. and F. Hugues, Modification of cobalt catalyst selectivity according to fischer-tropsch process conditions, in Studies in Surface Science and Catalysis, F. Bellot Noronha, M. Schmal, and E. Falabella Sousa-Aguiar, Editors. 2007, Elsevier. p. 91-96.

88. Gavrilović, L., et al., Fischer-Tropsch synthesis over an alumina-supported cobalt catalyst in a fixed bed reactor – Effect of process parameters. Catalysis Today, 2020.

89. Gorimbo, J., et al., Fischer–Tropsch synthesis: product distribution, operating conditions, iron catalyst deactivation and catalyst speciation. International Journal of Industrial Chemistry, 2018. **9**(4): p. 317-333.

90. Ebrahimi, P., A. Kumar, and M. Khraisheh, A review of recent advances in water-gas shift catalysis for hydrogen production. Emergent Materials, 2020. **3**(6): p. 881-917.

91. Schanke, D., et al., Reoxidation and Deactivation of Supported Cobalt Fischer−Tropsch Catalysts. Energy & Fuels, 1996. **10**(4): p. 867-872.

92. Ma, W., et al., Fischer–Tropsch Synthesis: Influence of CO Conversion on Selectivities, H2/CO Usage Ratios, and Catalyst Stability for a Ru Promoted Co/Al2O3 Catalyst Using a Slurry Phase Reactor. Topics in Catalysis, 2011. **54**(13-15): p. 757-767.

93. Tompkins, H.G. and J.A. Augis, The oxidation of cobalt in air from room temperature to 467°C. Oxidation of Metals, 1981. **16**(5): p. 355-369.

94. Melaet, G., et al., Evidence of Highly Active Cobalt Oxide Catalyst for the Fischer–Tropsch Synthesis and CO2 Hydrogenation. Journal of the American Chemical Society, 2014. **136**(6): p. 2260-2263.

95. Yang, J., et al., Fischer–Tropsch synthesis: A review of the effect of CO conversion on methane selectivity. Applied Catalysis A: General, 2014. **470**: p. 250-260.

96. Carter, J.L., J.A. Cusumano, and J.H. Sinfelt, Effect of Crystallite size on the Catalytic Activity of Nickel. J Phys Chem, 1966. **70**(2257).

97. Iglesia, E., Design, synthesis, and use of cobalt-based Fischer-Tropsch synthesis catalysts. Applied Catalysis a-General, 1997. **161**(1-2): p. 59-78.

98. Bezemer, G.L., et al., Cobalt particle size effects in the Fischer-Tropsch reaction studied with carbon nanofiber supported catalysts. J Am Chem Soc., (0002-7863).

99. Liu, J.-X., et al., Particle Size and Crystal Phase Effects in Fischer-Tropsch Catalysts. Engineering, 2017. **3**(4): p. 467-476.

100. den Breejen, J.P., et al., On the Origin of the Cobalt Particle Size Effects in Fischer−Tropsch Catalysis. Journal of the American Chemical Society, 2009. **131**(20): p. 7197-7203.

101. Herranz, T., et al., Influence of the Cobalt Particle Size in the CO Hydrogenation Reaction Studied by In Situ X-Ray Absorption Spectroscopy. The Journal of Physical Chemistry B, 2009. **113**(31): p. 10721-10727.

102. Tuxen, A., et al., Size-dependent dissociation of carbon monoxide on cobalt nanoparticles. J Am Chem Soc, 2013. **135**(6): p. 2273-8.

103. Borg, O., et al., Fischer–Tropsch synthesis: Cobalt particle size and support effects on intrinsic activity and product distribution. Journal of Catalysis, 2008. **259**(2): p. 161-164.

104. Rane, S., et al., Relation between hydrocarbon selectivity and cobalt particle size for alumina supported cobalt Fischer–Tropsch catalysts. Applied Catalysis A: General, 2012. **437-438**: p. 10-17.

105. Melaet, G., A.E. Lindeman, and G.A. Somorjai, Cobalt Particle Size Effects in the Fischer–Tropsch Synthesis and in the Hydrogenation of CO2 Studied with Nanoparticle Model Catalysts on Silica. Topics in Catalysis, 2013. **57**(6-9): p. 500-507.

106. Nabaho, D., et al., Hydrogen spillover in the Fischer–Tropsch synthesis: An analysis of platinum as a promoter for cobalt–alumina catalysts. Catalysis Today, 2016. **261**: p. 17-27.

107. Soulantica, K., et al., Hydrogen Spillover in the Fischer-Tropsch Synthesis on Carbon-supported Cobalt Catalysts. ChemCatChem, 2019. **12**.

108. Bezemer, G.L., et al., Cobalt Particle Size Effects in the Fischer−Tropsch Reaction Studied with Carbon Nanofiber Supported Catalysts. Journal of the American Chemical Society, 2006. **128**(12): p. 3956-3964.

109. Rahmanpour, O., A. Shariati, and M.R.K. Nikou, New Method for Synthesis Nano Size γ-Al2O3 Catalyst for Dehydration of Methanol to Dimethyl Ether. International Journal of Chemical Engineering and Applications, 2012: p. 125-128.

110. Borg, O., et al., Fischer–Tropsch synthesis over γ-alumina-supported cobalt catalysts: Effect of support variables. Journal of Catalysis, 2007. **248**(1): p. 89-100.

111. Gupta, M. and J.J. Spivey, Catalytic Processes for the Production of Clean Fuels, in New and Future Developments in Catalysis. 2013. p. 87-126.

112. Xie, J., et al., Promoted cobalt metal catalysts suitable for the production of lower olefins from natural gas. Nat Commun, 2019. **10**(1): p. 167.

113. Su, S.-L., D.-M. Wang, and J.-Y. Lai, Critical residence time in metastable region – a time scale determining the demixing mechanism of nonsolvent induced phase separation. Journal of Membrane Science, 2017. **529**: p. 35-46.

114. Mohsenpour, S., et al., Effect of graphene oxide in the formation of polymeric asymmetric membranes via phase inversion. Journal of Membrane Science, 2022. **641**.

115. Chauruka, S.R., et al., Effect of mill type on the size reduction and phase transformation of gamma alumina. Chemical Engineering Science, 2015. **134**: p. 774-783.

116. Mulpur, P., et al., Surface plasmon coupled emission studies on engineered thin film hybrids of nano α−Al2O3 on silver. 2014. p. 22-24.

117. Iglesia, E., et al., Selectivity Control and Catalyst Design in the Fischer-Tropsch Synthesis: Sites, Pellets, and Reactors, in Advances in Catalysis, D.D. Eley, H. Pines, and P.B. Weisz, Editors. 1993, Academic Press. p. 221-302.

Appendix

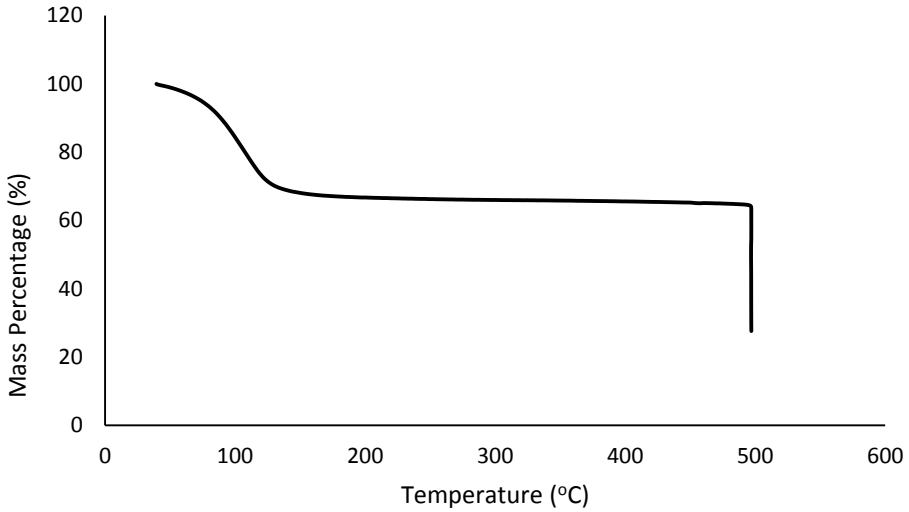

A1 TGA data of Co-MOF-74 at a ramp of 8 °C min^{-1} to 500 °C for 1 h

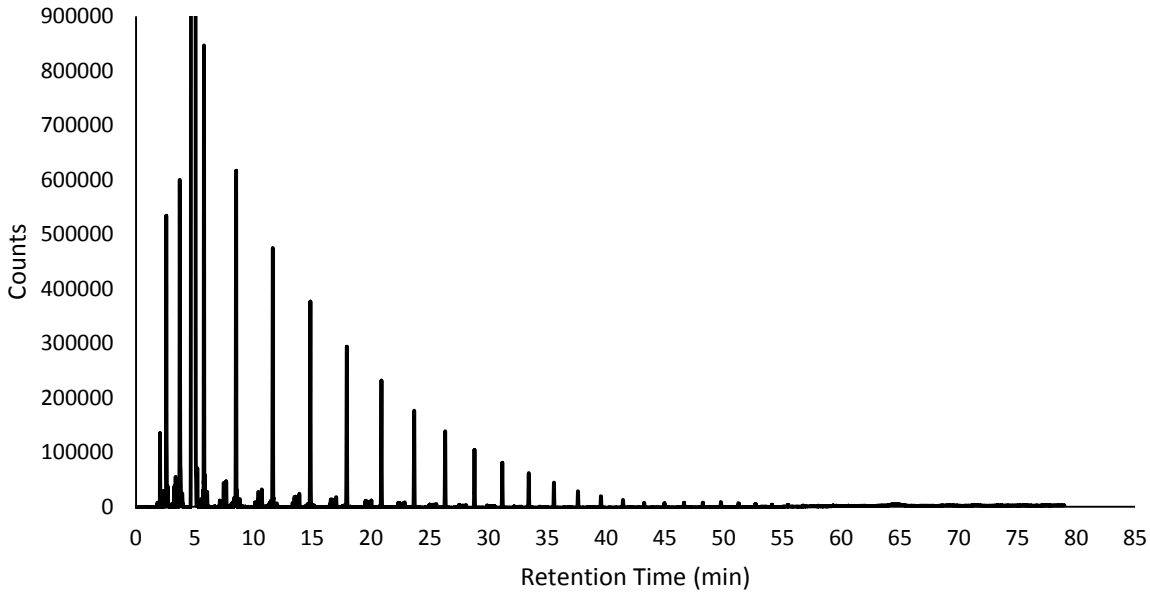

A2 GC-FID chromatogram of the oil product of the Co/Al_2O_3-P catalyst at a space velocity of 652 cm^3 g_{Co}^{-1} min^{-1}